



JAEA-Conf
2006-009
INDC(JPN)-196/U

Proceedings of the 2005 Symposium on Nuclear Data
February 2-3, 2006, JAEA, Tokai, Japan

(Eds.) Yoshihisa TAHARA* and Tokio FUKAHORI

Nuclear Data Center
Nuclear Science and Engineering Directorate

November 2006

Japan Atomic Energy Agency

日本原子力研究開発機構

JAEA-Conf

本レポートは日本原子力研究開発機構が不定期に発行する成果報告書です。
本レポートの入手並びに著作権利用に関するお問い合わせは、下記あてにお問い合わせ下さい。
なお、本レポートの全文は日本原子力研究開発機構ホームページ (<http://www.jaea.go.jp/index.shtml>)
より発信されています。このほか財団法人原子力弘済会資料センター*では実費による複写頒布を行っ
ております。

〒319-1195 茨城県那珂郡東海村白方白根 2 番地 4
日本原子力研究開発機構 研究技術情報部 研究技術情報課
電話 029-282—6387, Fax 029-282-5920

*〒319-1195 茨城県那珂郡東海村白方白根 2 番地 4 日本原子力研究開発機構内

This report is issued irregularly by Japan Atomic Energy Agency
Inquiries about availability and/or copyright of this report should be addressed to
Intellectual Resources Section, Intellectual Resources Department,
Japan Atomic Energy Agency
2-4 Shirakata Shirane, Tokai-mura, Naka-gun, Ibaraki-ken 319-1195 Japan
Tel +81-29-282-6387, Fax +81-29-282-5901

Proceedings of the 2005 Symposium on Nuclear Data
February 2-3, 2006, JAEA, Tokai, Japan

(Eds.) Yoshihisa TAHARA* and Tokio FUKAHORI

Division of Nuclear Data and Reactor Engineering
Nuclear Science and Engineering Directorate
Japan Atomic Energy Agency
Tokai-mura, Naka-gun, Ibaraki-ken

(Received October 13, 2006)

The 2005 Symposium on Nuclear Data was held at Nuclear Science Research Institute in Tokai Research and Development Center, Japan Atomic Energy Agency (JAEA), on 2nd and 3rd of February 2006. Japanese Nuclear Data Committee and Nuclear Data Center, JAEA organized this symposium. In the oral sessions, presented were 16 papers on topics of nuclear data for the innovative reactor development and upgrade of current light water reactor, the past and future of nuclear data research, capability of the latest evaluated nuclear data files, and recent cross section measurements. In the poster session, presented were 21 papers concerning experiments, evaluations, benchmark tests, applications and so on. A part of those presented papers are compiled in this proceedings.

Keywords: Nuclear Data, Symposium, Proceedings, Nuclear Reaction, JENDL, Experiment, Evaluation, Benchmark Test, Cross Section, Nuclear Fuel Cycle.

*Engineering Development Co., Ltd.

2005 年度核データ研究会報文集
2006 年 2 月 2 日～3 日，原子力科学研究所，東海村

日本原子力研究開発機構 原子力基礎工学研究部門 核工学・炉工学ユニット
(編) 田原 義壽*・深堀 智生

(2006 年 10 月 13 日受理)

2005 年度核データ研究会が、2006 年 2 月 2 日と 3 日の両日、日本原子力研究開発機構原子力科学研究所において開催された。この研究会は、日本原子力研究開発機構の核データ評価研究グループとシグマ研究委員会が主催して開いたものである。口頭発表では、革新炉開発および現行炉高度化のための核データ、核データ研究の過去と未来、最新評価済み核データの現状と性能分析、最新の核データ測定についての 16 件の報告があった。ポスター発表では、21 件の発表があり、それらは、核データの測定、評価や評価済み核データのベンチマークテスト及び応用等に関するものであった。本報文集は、それらの論文の一部をまとめたものである。

原子力科学研究所（駐在）：〒319-1195 茨城県那珂郡東海村白方白根 2-4

* エンジニアリング開発株式会社

Program Committee

Yoshihisa TAHARA (Chairman)	Engineering Development Co., Ltd.
Satoshi CHIBA	Japan Atomic Energy Agency
Tokio FUKAHORI	Japan Atomic Energy Agency
Kazuyoshi FURUTAKA	Japan Atomic Energy Agency
Makoto ISHIKAWA	Japan Atomic Energy Agency
Osamu IWAMOTO	Japan Atomic Energy Agency
Shin-ya KOSAKA	TEPSYS
Toshiro OHSAKI	Tokyo Institute of Technology
Kazuhiro OYAMATSU	Aichi-Shukutoku University
Shoji NAKAMURA	Japan Atomic Energy Agency
Hiroshi NAKASHIMA	Japan Atomic Energy Agency
Satoshi SHIMAKAWA	Japan Atomic Energy Agency
Kazufumi TSUJIMOTO	Japan Atomic Energy Agency

プログラム委員会

田原 義壽 (委員長)	エンジニアリング開発 (株)
千葉 敏	日本原子力研究開発機構
深堀 智生	日本原子力研究開発機構
古高 和禎	日本原子力研究開発機構
石川 眞	日本原子力研究開発機構
岩本 修	日本原子力研究開発機構
小坂 進矢	(株) テプコシステムズ
大崎 敏郎	東京工業大学
親松 和浩	愛知淑徳大学
中村 詔司	日本原子力研究開発機構
中島 宏	日本原子力研究開発機構
島川 聡司	日本原子力研究開発機構
辻本 和文	日本原子力研究開発機構

Contents

1. Introduction	1
2. Papers Presented at Oral Sessions	5
2.1 Nuclear Data for Innovative Reactor Developments and Further Developments of Current Reactors	7
2.1.1 Analysis of Core Physics Experiments of High Moderation Full MOX LWR	7
T. Yamamoto	
2.1.2 Nuclear Data for Design of Reduced Moderation Light Water Reactor	14
H. Akie	
2.1.3 Nuclear Data for Non-refueling Core Design	20
T. Matsumura, Y. Nauchi, N. Ueda, S. Okajima and T. Takeda	
2.1.4 Impact of Nuclear Data on Design Work for High Temperature Gas-cooled Reactors (paper not available)	25
S. Shimakawa, M. Goto and Y. Nagaya	
2.2 Past and Future of Nuclear Data Research	26
2.2.1 Japanese Nuclear Data Activities in the Last 40 Years	26
T. Nakagawa	
2.2.2 Nuclear Data Evaluation Activities in JAEA and the Mid-term Plan	30
J. Katakura	
2.3 Panel Discussion – Future of Nuclear Data Research –	34
2.3.1 Expectation for Nuclear Data Development (I)	34
K. Tsujimoto	
2.3.2 Expectation for Nuclear Data Development (paper not available)	39
A. Zukeran	
2.3.3 Future for Nuclear Data Research – Human Resources –	40
M. Baba	
2.3.4 A Proposal for New Treatment of Radiation Behavior with Combination of Nuclear Data and Reaction Model (paper not available)	43
K. Niita	
2.4 Status and Performance of Latest Evaluated Nuclear Data Files	44

2.4.1	Comparison of Major Nuclear Data Libraries – JENDL-3.3, ENDF/B-VI.8, ENDF/B-VIIβ1.2 and JEFF-3.1– K. Shibata	44
2.4.2	Integral Comparison of Library Performance T. Mori	52
2.4.3	Nuclear Data Library in Design Calculation G. Hirano and S. Kosaka	58
2.5	Latest Nuclear Data Measurements	64
2.5.1	Utilization of J-PARC – Research Plan with Neutron-nucleus Reaction Measurement Facilities – (paper not available) M. Igashira	64
2.5.2	Measurement of Neutron Capture Cross Sections (paper not available) S. Nakamura, A. Laptev, M. Ohta, H. Harada, T. Fujii and H. Yamana	65
2.5.3	Photoneutron Cross Section Measurement for ⁹⁴ Zr Using Laser Inverse Compton γ Rays S. Hohara, S. Goko, A. Makinaga, T. Kaihori, H. Toyokawa, H. Utsunomiya, K.Y. Hara, F. Kitatani, H. Harada, T. Matsumoto and H. Harano	66
3.	Papers Presented at Poster Sessions	71
3.1	The Investigation of Deuteron Production Double Differential Cross Section Induced by 392 MeV Protons T. Kin, M. Nakano, M. Imamura, Y. Yamashita, H. Iwamoto, N. Koba, Y. Koba, H. Fukuda, G. Wakabayashi, Y. Uozumi, N. Ikeda, N. Koori and M. Matoba	73
3.2	Measurements of Double Differential Fragment Production Cross Sections of Silicon for 70 MeV Protons M. Hagiwara, T. Oishi, S. Kamada, M. Baba, T. Sanami, M. Takada and N. Miyahara	78
3.3	Measurement of Double-differential Cross Section of Fragments on C, Al, Cu, Ag Induced by 400 MeV Helium T. Sanami, H. Matsumura, M. Takada and T. Murakami	84
3.4	Measurements of Cross-sections of Producing Short-lived Nuclei with 14 MeV Neutrons $^{27}\text{Al}(n,\alpha)^{24\text{m}}\text{Na}$, $^{144}\text{Sm}(n,2n)^{143\text{m}}\text{Sm}$, $^{206}\text{Pb}(n,2n)^{205\text{m}}\text{Pb}$, $^{208}\text{Pb}(n,2n)^{207\text{m}}\text{Pb}$ – K. Arakita, T. Shimizu, K. Kawade, M. Shibata, K. Ochiai and T. Nishitani	89
3.5	Measurement of Angle-correlated Differential (n,2n) Reaction Cross Section with Pencil-beam DT Neutron Source	95

S. Takaki, K. Kondo, S. Shido, H. Miyamaru, I. Murata, K. Ochiai
and T. Nishitani

3.6	Study on keV-neutron Capture Cross Sections and Capture γ -ray Spectra of $^{117,119}\text{Sn}$	101
	J. Nishiyama, M. Igashira, T. Ohsaki, G.N. Kim, W.C. Chung and T.I. Ro	
3.7	Measurement of Fission Cross-sections with Lead Slowing-down Spectrometer using Digital Signal Processing	106
	W. Takahashi, T. Oishi, M. Nakhostin, T. Yamauchi, M. Baba, J. Hori, H. Yuki and T. Ohtsuki	
3.8	Effect of ^{140}Ba Fission Yield on Fission Rate Distribution Measurements in UO ₂ -MOX Mixed Core of REBUS Program	112
	T. Yamamoto, K. Kawashima and K. Kamimura	
3.9	Measurement of Neutron Production Spectra at the Forward Direction from Thick Graphite, Aluminum, Iron and Lead Targets Bombarded by 250 MeV Protons	118
	Y. Iwamoto, S. Taniguchi, N. Nakao, T. Itoga, T. Nakamura, Y. Nakane, H. Nakashima, D. Satoh, H. Yashima, H. Yamakawa, K. Oishi, A. Tamii and K. Hatanaka	
3.10	Measurement of 40 MeV Deuteron Induced Reaction on Fe and Ta for Neutron Emission Spectrum and Activation Cross Section	124
	T. Itoga, M. Hagiwara, T. Oishi, S. Kamada and M. Baba	
3.11	Analysis of Induced-radioactivity using DCHAIN-SP for Iron, Copper and Niobium at a Mercury Target Irradiated by 2.83 and 24 GeV Protons	130
	T. Kai, Y. Kasugai, F. Maekawa, S. Meigo, H. Takada and Y. Ikeda	
3.12	Analysis of Induced-radioactivity using DCHAIN-SP for Pb and Hg at a Mercury Target Irradiated by 2.8 and 24 GeV Protons	136
	Y. Kasugai, T. Kai, F. Maekawa, S. Meigo, H. Takada and Y. Ikeda	
3.13	Resonance Analysis Combined with Optical Model	141
	T. Murata and T. Nakagawa	
3.14	Analysis of Fission with Selective Channel Scission Model	145
	M. Ohta and S. Nakamura	
3.15	Investigation of Nuclear Reaction Data for Analyses of Single-event Effects in Semiconductor Devices	151
	A. Kodama, K. Nishijima and Y. Watanabe	
3.16	Improvement of Prediction Power of FP Summation Calculations by Use of the TAGS Experimental Data	157
	N. Hagura, T. Yoshida and M. Katsuma	
3.17	Density Distributions and Form Factors in Neutron-rich Nuclei	163
	A.N. Antonov, D.N. Kadrev, M.K. Gaidarov, E. Moya de Guerra,	

	P. Sarriguren, J.M. Udias, V.K. Lukyanov, E.V. Zemlyanaya and G.Z. Krumova	
3.18	Burn-up Calculation of Fusion-fission Hybrid Reactor Using Thorium Cycle	169
	S. Shido, Y. Yamamoto, M. Matsunaka, K. Kondo and I. Murata	
3.19	Database Retrieval Systems for Nuclear and Astronomical Data	175
	T. Suda, N. Otuka, S. Korenov, S. Yamada, Y. Katsuta, A. Ohnishi, K. Kato and M.Y. Fujimoto	
3.20	Development of the Measurement System of the $^{189}\text{Os}(n,n'\gamma)$ Cross Section and Re/Os Chronometer	181
	Y. Temma, M. Segawa, Y. Nagai, T. Ohta, A. Nakayoshi, S. Fujimoto, H. Ueda, T. Shima, M. Igashira, T. Ohsaki, J. Nishiyama and T. Masaki	
3.21	Analysis of Continuum Spectra for Proton Induced Reactions on ^{27}Al , ^{58}Ni , ^{90}Zr , ^{197}Au and ^{209}Bi at Incident Energies 42 and 68 MeV-direct Reaction Model Analysis	185
	S.A. Sultana, T. Kin, G. Wakabayashi, Y. Uozumi, N. Ikeda, M. Matoba and Y. Watanabe	
Appendix : Participant Lists		191

目 次

1. はじめに	1
2. 口頭発表論文	5
2.1 革新炉開発及び現行炉高度化のための核データ	7
2.1.1 高減速全MOX軽水炉心炉物理試験の解析	7
山本 徹	
2.1.2 低減速軽水炉設計における核データ	14
秋江 拓志	
2.1.3 小型高速炉（4S）設計のための核データ	20
松村 哲夫、名内 泰志、植田 伸幸、岡嶋 成晃、 竹田 敏一	
2.1.4 高温ガス炉設計における断面積の影響	25
島川 聡司、後藤 実、長家 康展	
2.2 核データ研究の過去と未来	26
2.2.1 わが国における過去の核データ評価体制	26
中川 庸雄	
2.2.2 新法人としての核データ活動の新体制と中期計画	30
片倉 純一	
2.3 パネルディスカッション –核データ研究の未来–	34
2.3.1 核データ研究への期待	34
辻本 和文	
2.3.2 核データ研究への期待.....	39
瑞慶覧 篤	
2.3.3 人材育成	40
馬場 護	
2.3.4 核データと核反応モデルの結合による新しい放射線挙動の取り 扱いについての提言	43
仁井田 浩二	
2.4 最新評価済核データの現状と性能分析	44
2.4.1 主要核データライブラリの比較 –JENDL-3.3, ENDF/B-VI.8, ENDF/B-VIIβ1.2, JEFF-3.1–	44
柴田 恵一	

2.4.2	積分実験解析による性能比較	52
	森 貴正	
2.4.3	設計計算における核データライブラリーの利用	58
	平野 豪、小坂 進矢	
2.5	最新の核データ測定	64
2.5.1	J-PARC の利用ー中性子核反応測定装置による研究計画ー	64
	井頭 政之	
2.5.2	中性子捕獲断面積の測定	65
	中村 詔司、A. Laptev、太田 雅之、原田 秀郎、 藤井 俊行、山名 元	
2.5.3	逆コンプトン γ 線による $^{94}\text{Zr}(\gamma,n)^{93}\text{Zr}$ 反応断面積の測定	66
	芳原 新也、後神 進史、牧永 あや乃、海堀 岳史、 豊川 弘之、宇都宮 弘章、原 かおる、北谷 文人、 原田 秀郎、松本 哲郎、原野 英樹	
3.	ポスター発表論文	71
3.1	392 MeV 陽子入射による重陽子生成二重微分断面積に関する研究	73
	金 政浩、中野 正博、今村 稔、山下 雄介、岩元 大樹、 古場 尚雅、古場 裕介、福田 博明、若林 源一郎、 魚住 裕介、池田 伸夫、桑折 範彦、的場 優	
3.2	70MeV 陽子入射反応におけるシリコンからのフラグメント生成二重 微分断面積の測定	78
	萩原 雅之、大石 卓司、鎌田 創、馬場 護、佐波 俊哉、 高田 真志、宮原 信幸	
3.3	400MeV He 入射による C, Al, Cu, Ag からのフラグメント生成二重微 分断面積の測定	84
	佐波 俊哉、松村 哲夫、高田 真志、村上 健	
3.4	14 MeV 中性子に対する短寿命核生成断面積の測定 - $^{27}\text{Al}(n,\alpha)^{24m}\text{Na}$, $^{144}\text{Sm}(n,2n)^{143m}\text{Sm}$, $^{206}\text{Pb}(n,2n)^{205m}\text{Pb}$, $^{208}\text{Pb}(n,2n)^{207m}\text{Pb}$ -	89
	荒木田 和正、清水 俊明、河出 清、柴田 理尋、 落合 謙太郎、西谷 健夫	
3.5	ビーム状 DT 中性子源による角度相関(n,2n)反応微分断面積の測定	95
	高木 智史、近藤 恵太郎、志度 彰一、宮丸 広幸、 村田 勲、落合 謙太郎、西谷 健夫	
3.6	Sn-117,119 の keV 中性子捕獲断面積及び捕獲ガンマ線スペクトルに関 する研究	101
	西山 潤、井頭 政之、大崎 敏郎、G.N. Kim、W.C. Chung、 T.I. Ro	

3.7 デジタル信号処理を利用した鉛スペクトロメータにおける核分裂 断面積測定	106
高橋 渉、大石 卓司、M. Nakhostin、山内 健、馬場 護、 堀 順一、結城 秀行、大槻 勤	
3.8 REBUS 計画の UO ₂ -MOX 混在炉心における核分裂分布測定での ¹⁴⁰ Ba 核分裂収率の影響.....	112
山本 徹、川島 克之、上村 勝一郎	
3.9 250 MeV 陽子入射による厚いグラファイト、アルミニウム、鉄及び鉛 ターゲットからの 0 度方向における中性子エネルギースペクトルの 測定.....	118
岩元 洋介、谷口 真吾、中尾 徳晶、糸賀 俊朗、 中村 尚司、中根 佳弘、中島 宏、佐藤 大樹、八島 浩、 山川 裕司、大石 晃嗣、民井 淳、畑中 吉治	
3.10 40 MeV 重陽子による Fe, Ta 厚いターゲットからの生成中性子スペク トルと放射化断面積の測定	124
糸賀 俊朗、萩原 雅之、大石 卓司、鎌田 創、馬場 護	
3.11 2.8 または 24 GeV 陽子で照射された水銀ターゲットの周辺の軽核の 誘導放射能に対する DCHAIN-SP を用いた解析	130
甲斐 哲也、春日井 好己、前川 藤夫、明午 伸一郎、 高田 弘、池田 裕二郎	
3.12 2.8 及び 24 GeV 陽子を入射した水銀ターゲット周りでの鉛及び水銀 試料に対する DCHAIN-SP を使った誘導放射能の解析	136
春日井 好己、甲斐 哲也、前川 藤夫、明午 伸一郎、 高田 弘、池田 裕二郎	
3.13 光学モデルを併用した共鳴解析	141
村田 徹、中川 庸雄	
3.14 選択チャンネル核分裂モデルによる核分裂の解析	145
太田 雅之、中村 詔司	
3.15 半導体デバイスのシングルイベント現象解析用核反応データの検討	151
児玉 章裕、西嶋 康太、渡辺 幸信	
3.16 TAGS 実験データを用いた FP 総和計算予測性能の改良.....	157
羽倉 尚人、吉田 正、勝間 正彦	
3.17 中性子過剰核の密度分布と形状因子	163
A.N. Antonov, D.N. Kadrev, M.K. Gaidarov, E. Moya de Guerra, P. Sarriguren, J.M. Udias, V.K. Lukyanov, E.V. Zemlyanaya and G.Z. Krumova	
3.18 トリウムを用いた核融合・核分裂ハイブリッド炉の燃焼計算	169
志度 彰一、山本 泰史、松中 允亨、近藤 恵太郎、村田 勲	

3.19 実験・評価済核データ、及び天文データに関するデータベース検索システム	175
須田 拓馬、大塚 直彦、S. Korennov、山田 志真子、 勝田 豊、大西 明、加藤 幾芳、藤本 正行	
3.20 $^{189}\text{Os}(n,n'\gamma)$ 断面積測定システム及び Re/Os 宇宙核時計の開発	181
天満 康之、瀬川 麻里子、永井 泰樹、太田 岳史、 仲吉 彬、藤本 臣哉、上田 仁、嶋 達志、井頭 政之、 大崎 敏郎、西山 潤、正木 智洋	
3.21 中高エネルギー領域の連続スペクトル解析 ー直接反応モデル解析ー	185
Sadia Afroze Sultana、金 政浩、若林 源一郎、魚住 裕介、 池田 伸夫、的場 優、渡辺 幸信	
付録：参加者リスト	191

1. Introduction

The 2005 Symposium on Nuclear Data was held at Nuclear Science Research Institute in Tokai Research and Development Center, Japan Atomic Energy Agency (JAEA), on 2nd and 3rd of February 2006, with about 90 participants. Japanese Nuclear Data Committee and Nuclear Data Center, JAEA organized this symposium.

The program of the symposium is listed below. In the oral sessions, presented were 16 papers on topics of nuclear data for the innovative reactor development and upgrade of current light water reactor, the past and future of nuclear data research, capability of the latest evaluated nuclear data files, and recent cross section measurements. In the poster session, presented were 21 papers concerning experiments, evaluations, benchmark tests, applications and so on. A part of those presented papers are compiled in this proceedings.

Program of Symposium on Nuclear Data 2005

Feb. 2 (Thu.)

9:50-10:00

1. Opening Address

A. Hasegawa (JAEA)

10:00-12:00

2. Nuclear Data for Innovative Reactor Developments and Further Developments of Current Reactors

【Chairperson: T. Yamamoto (Osaka Univ.)】

2.1 Analysis of Core Physics Experiments of High Moderation Full MOX LWR [25+5]

T. Yamamoto (JNES)

2.2 Nuclear Data for Design of Reduced Moderation Light Water Reactor [25+5]

H. Akie (JAEA)

2.3 Nuclear Data for Non-refueling Core Design [25+5]

T. Matsumura (CRIEPI)

2.4 Impact of Nuclear Data on Design Work for High Temperature Gas-cooled Reactors [25+5]

S. Shimakawa (JAEA)

12:00-13:00

Lunch

13:00-14:30

3. Poster Presentations (Odd Numbers)

14:30-15:30

4. Past and Future of Nuclear Data Research 【Chairperson: Y. Tahara (EDC)】

4.1 Past Organization for Nuclear Data Evaluation in Japan [25+5]

T. Nakagawa (JAEA)

4.2 Nuclear Data Evaluation Activities in JAEA and the Mid-Term Plan [15+10]

J. Katakura (JAEA)

15:30-15:50 Coffee Break

15:50-17:40

5. Panel Discussion - Future of Nuclear Data Research - 【Chairperson: T. Yoshida (Musashi Tech.)】

5.1 Expectation for Nuclear Data Development [20] (K. Tsujimoto, JAEA)

5.2 Expectation for Nuclear Data Development [20] (A. Zukeran, NAIS)

5.3 Human Resources [20] (M. Baba, Tohoku Univ.)

5.4 A Proposal for New Treatment of Radiation Behavior with Combination of
Nuclear Data and Reaction Model [20] (K. Niita, RIST)

18:00-20:30 Reception (Akogi-ga-ura Club)

Feb. 3 (Fri.)

9:45-11:15

6. Status and Performance of Latest Evaluated Nuclear Data Files

【Chairperson: T. Fukahori (JAEA)】

6.1 Comparison of Major Nuclear Data Libraries

- JENDL-3.3, ENDF/B-VI.8, ENDF/B-VII β 1.2, and JEFF-3.1 - [25+5] K. Shibata (JAEA)

6.2 Integral Comparison of Library Performance [25+5] T. Mori (JAEA)

6.3 Nuclear Data Library in Design Calculation [25+5] G. Hirano (TEPSYS)

11:15-11:45

7. Nuclear Data Needs and Activities in Abroad 【Chairperson: T. Ohsawa (Kinki Univ.)】

7.1 Present Status of CENDL Project [25+5] (canceled) YU Hongwei (CIAE)

11:45-12:00 Photo

12:00-13:00 Lunch

13:00-14:30

8. Poster Presentations (Even Numbers)

14:30-16:00

9. Latest Nuclear Data Measurements 【Chairperson: Y. Watanabe (Kyushu Univ.)】

- 9.1 Utilization of J-PARC --- Research Plan with Neutron-Nucleus Reaction
 Measurement Facilities --- [25+5] M. Igashira (TIT)
- 9.2 Measurement of Neutron Capture Cross Sections [25+5] S. Nakamura (JAEA)
- 9.3 Measurement of Cross Section for $^{94}\text{Zr}(\gamma, n)$ Reaction Using Laser Inverse
 Compton Gamma Rays [25+5] S. Hohara (ITRI)

16:00-16:10

10. Closing Session Y. Tahara (EDC)

Poster Presentations

Feb. 2 (Thu.) 13:00-14:30 (Odd Numbers)

Feb. 3 (Fri.) 13:00-14:30 (Even Numbers)

- P1. The Investigation of Deuteron Production Double Differential Cross Section
 Induced by 392 MeV Protons T. Kin (UOEH)
- P2. Measurement of Double Differential Fragment Production Cross Sections of
 Silicon for 70 MeV Protons T. Oishi (Tohoku Univ.)
- P3. Measurement of Double-differential Cross Section of Fragments on C, Al, Cu, Ag
 Induced by 400 MeV Helium T. Sanami (KEK)
- P4. Measurements of Cross-sections of Producing Short-lived Nuclei with 14 MeV Neutrons
 $^{27}\text{Al}(n, \alpha)^{24\text{m}}\text{Na}$, $^{144}\text{Sm}(n, 2n)^{143\text{m}}\text{Sm}$, $^{206}\text{Pb}(n, 2n)^{205\text{m}}\text{Pb}$, $^{208}\text{Pb}(n, 2n)^{207\text{m}}\text{Pb}$ -
K. Arakita (Nagoya Univ.)
- P5. Measurement of Angle-correlated Differential (n,2n) Reaction Cross Section with
 Pencil-beam DT Neutron Source S. Takaki (Osaka Univ.)
- P6. Study on keV-neutron Capture Cross Sections and Capture Gamma-ray Spectra of
 $^{117,119}\text{Sn}$ J. Nishiyama (TIT)
- P7. Measurement of Fission Cross-sections with Lead Slowing-down Spectrometer
 using Digital Signal Processing W. Takahashi (Tohoku Univ.)
- P8. Effect of ^{140}Ba Fission Yield on Fission Rate Distribution Measurements in
 UO₂-MOX Mixed Core of REBUS Program T. Yamamoto (JNES)
- P9. Measurement of Neutron Production Spectra at the Forward Direction from Thick

- Graphite, Aluminum, Iron and Lead Targets Bombarded by 250 MeV Protons
Y. Iwamoto (JAEA)
- P10. Measurement of 40 MeV Deuteron Induced Reaction on Fe and Ta for Neutron
Emission Spectrum and Activation Cross Section
S. Kamata (Tohoku Univ.)
- P11. Analysis of Induced-radioactivity Using DCHAIN-SP for Light Nuclei at a
Mercury Target Irradiated by 2.8 or 24 GeV Protons
T. Kai (JAEA)
- P12. Analysis of Induced-radioactivity using DCHAIN-SP for Heavy Nuclei at a
Mercury Target Irradiated by 2.8 and 24 GeV Protons
Y. Kasugai (JAEA)
- P13. Resonance Analysis Combined with Optical Model
T. Murata (Aitel)
- P14. Analysis of Fission with Selective Channel Scission Model
M. Ohta (JAEA)
- P15. Investigation of Nuclear Reaction Data for Analyses of Single-event Effects in
Semiconductor Devices
A. Kodama (Kyushu Univ.)
- P16. Improvement of Prediction Power of FP Summation Calculations by Use of the
TAGS Experimental Data
N. Hagura (Musashi Tech.)
- P17. Density Distributions and Form Factors in Neutron-rich Nuclei
D.N. Kadrev (Kyushu Univ.)
- P18. Burn-up Calculation of Fusion-fission Hybrid Reactor Using Thorium Cycle
S. Shido (Osaka Univ.)
- P19. Database Retrieval Systems for Nuclear and Astronomical Data
T. Suda (Hokkaido Univ.)
- P20. Development for the Measurement System of the $^{189}\text{Os}(n,n'\gamma)$ Cross Section and
Re/Os Chronometer
Y. Temma (Osaka Univ.)
- P21. Some Calculated Results of the Cell Parameters for the Dalat Nuclear Research Reactor
HOANG Duc Huynh (INST)
- P22. Analysis of Continuum Spectra for Proton Induced Reactions on ^{27}Al , ^{58}Ni , ^{90}Zr ,
 ^{197}Au and ^{209}Bi at 42 and 68 MeV –Direct Reaction Model Analysis
Sadia Afroze Sultana (Kyushu Univ.)

2. Papers Presented at Oral Sessions

2.1 Nuclear Data for Innovative Reactor Developments and Further Developments of Current Reactors

2.1.1 Analysis of Core Physics Experiments of High Moderation Full MOX LWR

Toru YAMAMOTO

Reactor Core and Fuel Reliability Group, Safety Standard Division

Japan Nuclear Energy Safety Organization (JNES)

Fujita Kanko Toranomom Bldg. 7F, 3-17-1, Toranomom, Minato-ku, Tokyo 105-0001

E-mail: yamamoto-toru@jnes.go.jp

NUPEC carried out an core physics experimental programs called MISTRAL and BASALA in order to obtain the major physics characteristics of the high moderation full MOX LWR cores from 1996 to 2002. In addition to those data, NUPEC also obtained a part of experimental results of the EPICURE program that CEA had conducted for 30 % Pu recycling in French PWRs. The analysis of those experimental data was also performed by NUPEC with SRAC, a deterministic code system for pin cell and core calculations, and MVP, a continuous energy Monte Carlo calculation code, based on a common nuclear data library, JENDL-3.2. A part of analysis was also done with JENDL-3.3, ENDF/B-VI and JEF-2.2 This paper summarizes the analysis results of those MOX core physics experiments referring to the published papers etc..

1. Introduction

Full MOX LWR cores are favorable since they enable a large amount of plutonium to be loaded in a small number of reactors. Higher moderation LWR cores are also favorable to enhance the consumption of plutonium and reduce the residual plutonium in burned MOX fuel. Nuclear Power Engineering Corporation (NUPEC) studied such high moderation full MOX cores¹⁻³⁾ as a part of advanced LWR core concept studies from 1994 to 2003 supported by the Ministry of Economy, Trade and Industry. In order to obtain the major physics characteristics of this advanced MOX cores, high moderation full MOX LWR cores, NUPEC carried out the core physics experimental programs called MISTRAL⁴⁻⁷⁾ and BASALA^{8,9)} in collaboration with CEA in the EOLE critical facility of the Cadarache Center from 1996 to 2002. NUPEC also obtained a part of experimental data of the EPICURE program¹⁰⁾ that CEA had conducted for 30 % Pu recycling in French PWRs under the collaboration with French industrial partners. Those experimental data was transferred to Japan Nuclear Energy Safety Organization (JNES) by March 2005 for further effective utilization.

The analysis of the experimental data was performed by NUPEC from 1996 to 2003 with SRAC¹¹⁾, a deterministic code system for pin cell and core calculations, and MVP¹²⁾, a continuous energy Monte Carlo calculation code, based on a common nuclear data library, JENDL-3.2.¹³⁾ A part of analysis was also done with JENDL-3.3,¹⁴⁾ ENDF/B-VI and JEF-2.2.

This paper summarizes the analysis results of those MOX core physics experiments that have been published in a large number of papers⁴⁻⁹⁾ and others.¹⁵⁾

2. Outline of Core Physics Experimental Programs

An outline of core configurations and measurement items of EPICURE, MISTRAL and BASALA programs is shown in Table 1 and Fig. 1. The UO₂ and MOX fuel rods used for the experiments other than 11 wt% MOX fuel rods have the same geometry of the standard PWR 17x17 assembly with Zry-4 claddings of an outer diameter of 9.5 mm except for the fuel effective length, about 800 mm. Those rods are sealed by Aluminum over-claddings for adjusting the core moderation ratio and protecting the rods in handling. The MOX pellets except for the 11% MOX fuel are composed of typical reactor grade plutonium with a fissile plutonium content of 60 to 70% and ²⁴⁰Pu content larger than 20% in a depleted UO₂ matrix. The total Plutonium contents of the MOX pellets are 3.0, 4.3, 7.0 and 8.7wt%.

3. Analysis Results and Discussion

Table 2 shows a summary of major analysis results obtained with SRAC-CITATION (Diffusion) and/or -TWORAN (Sn Transport) based on JENDL-3.2. Fig. 2 shows the values of critical keff of MVP with different nuclear data libraries in the order of MOX fraction in the core.

3.1 Criticality

UO₂ vs MOX cores: As shown in Table 2 and Fig. 2, it is seen that the values of keff of JENDL-3.3 increase with the fraction of MOX in the core. This trend is also seen for the other libraries. The critical keff in full MOX cores seems to increase with the date of critical measurements that cause a Pu composition change by decaying of ²⁴¹Pu and piling of ²⁴¹Am in MOX fuel rods. Fig. 3 shows a correlation between the critical keff and absorption fraction of ²⁴¹Am in MVP analysis.

Moderation ratio: This effect is less than 0.1 %dk from comparison between MISTRAL Core 2 (H/HM=5.1) and 3 (H/HM=6.2), and BASALA Core1 (H/HM=5.0) and 2 (H/HM=9.0).

Homogeneous and Mockup: The effect in the PWR cores is 0.2 to 0.3 %dk in the from comparison between MISTRAL Core 3 (homogeneous) and 4 (mock up). The effect in BWR cores is less than 0.1 %dk as seen in MISTRAL Core 2 (homogeneous) and BASALA Core 1 (mock up).

3.2 Other Characteristics

The power distributions calculated by SRAC-CITATION with JENDL-3.2 agree well with the measurements almost within the measurement errors of 1 to 2 % in the same manner for the UO₂ and the MOX cores, the conventional and the high moderation cores, the homogeneous and the mockup cores. The influence of the nuclear data libraries on the analysis results of the power distributions was surveyed with MVP for several cores and it turned out the influence is negligibly small.

The trend of C/E of spectrum index for MH1.2 is different from that of the MISTRAL cores, which may be caused from systematic error in the measurements in MH1.2.

Analysis of reactivity worth with SRAC-TWOTRAN generally shows better C/E than that of SRAC-CITATION for the absorbers, the burnable poisons, the control cluster, the control blade, the water hole/rod and the void burnable poison.

Table 1 Core configurations and measurements of EPICURE, MISTRAL and BASALA programs (M: measured item, blank: not measured)

Program	EPICURE			MISTRAL				BASALA			
	UH1.2	MH1.2	UM17x17 /7%	UM17x17 /11%	Core 1	Core 2	Core 3	Core4 Full MOX	Core4 UO2 zone	Core 1	Core 2
Core Config-ration	UO2 Homogeneous	Partial MOX Homogeneous	Partial MOX 17x17 Mockup	Partial MOX 17x17 Mockup	UO2 Homogeneous	Full MOX Homogeneous	Full MOX Homogeneous	Full MOX 17x17 Mockup	UO2 17x17 Mockup in MOX	Full MOX BWR Mockup	Full MOX BWR Mockup
-Vm/Vf*1	1.3	1.3	1.3	1.3*3	1.8	1.8	2.1	2.0	2.0	1.7	3.1
-H/HM*2	3.7	3.7	3.7	3.7*3	5.1	5.1	6.2	5.8	5.8	5.0	9.0
-Fuel pitch cm	1.26	1.26	1.26	1.26	1.32	1.32	1.39	1.32	1.32	1.13 (in Assembly)	1.35 (in Assembly)
-Fuel rod type	UO2-3.7%	MOX-7.0% UO2-3.7%	MOX-7.0% UO2-3.7%	MOX-11% UO2-3.7%	UO2-3.7%	MOX-7.0, 8.7%	MOX-7.0%	MOX-7.0%	MOX-7.0% UO2-3.7%	MOX-3.0, 4.3,7.0,8.7%	MOX-3.0, 4.3,7.0,8.7%
-Core size*4	D=54cm	D=69cm	D=58cm	D=55cm	D=41cm	D=60cm	D=59cm	D=62cm	D=52cm	XY=61cm	XY=47cm
Measurement											
-Critical mass	M	M	M	M	M	M	M	M	M	M	M
-Critical boron	M	M	M	M	M	0 ppm	M	M	M	0 ppm	0 ppm
-Buckling*5	M	M	M	M	M	M	M	M	M		
-Spec. Index	M	M	M	M	M	M	M	M	M		
-Rad.&Axial, Distribution	M	M	M	M	M	M	M	M	M	M	M
-ITC*6					M	M	M				M
-Boron*7	M	M	M	M	M	M	M	M	M		M
-Absorber rod	M	M	M	M	M	M	M			M	M
-Control Cluster								M	M		
-Control blade											M
-Water hole					M	M				M	
-Void	M	M	M	M			M			M	
-Beta effective					M	M					

*1 Volumetric ratio of moderator to fuel pellet, *2 Hydrogen to heavy metal atomic ratio, *3 Vm/Vf=1.7, H/HM=4.9 for 17x17 MOX region, *4 "D" means effective diameter of cylindrical core and "XY" side length of square core, *5 Radial buckling, *6 Iso-thermal temperature coefficient, *7 Differential and/or integral boron worth

Table 2 Summary of Analysis Results by SRAC and JENDL-3.2¹⁵⁾

Measurement Item	EPICURE			MISTRAL				BASALA			
	UHL.2	MHL.2	UM17×17 /7%	UM17×17 /11%	Core 1	Core 2	Core 3	Core 4 Full_MOX	Core 4 I02_zone	Core 1	Core 2
(a) Referenc core											
- keff (C-E, Δk, CITATION/TWOTRAN)	-0.44%/+0.07%	+0.27%/+0.13%	-0.25%/+0.07%	-0.25%/+0.31%	-0.97%/-0.19%	+0.48%/+0.41%	+0.49%/+0.42%	+0.74%/+0.74%	-0.10%/+0.24%	+0.39%/+0.78%	+0.47%/+0.41%
- Power (RMS of (C-E)/E, CITATION)	0.8% (1.0%)	0.9% (1.5%)	1.1% (1.5%)	1.1% (1.5%)	2.0% (1.0%)	1.1% (1.5%)	1.3% (1.5%)	1.0% (1.5%)	1.5% (2.2%)	1.8% (1.5%)	1.6% (1.5%)
- Spectrum Index (C/E, Pij)											
U238/U235		2.45 (3%)			0.67 (10%)	0.91 (7%)	-				
Pu239/U235		1.05 (2%)			1.01 (2%)	1.04 (2%)	1.03 (2%)				
Pu238/Pu239		0.89 (3%)			-	0.94 (1.4%)	-				
Pu240/Pu239		0.81 (3%)			0.95 (8%)	0.83 (6%)	-				
Pu241/Pu239		0.92 (2%)			0.99 (3%)	0.98 (3%)	0.98 (3%)				
Pu242/Pu239		0.17 (3%)			-	0.98 (8%)	-				
Np237/Pu239		-			0.76 (3%)	0.90 (3%)	0.90 (3%)				
- Conversion fact. (C/E, Pij)		-			1.02 (3%)	1.01 (1%)	1.02 (1%)				
(b) Boron worth (C/E, CITATION)											
- Differential					1.09 (11%)	1.08 (4%)	1.12 (4%)	0.90 (5%)			
- Integral (Av. C/E)					-	1.00 (4%)	1.01 (5%)	1.07 (6%)			0.98 (5%)
(c) Iso-thermal Temp. Co. (C-E, ×10 ⁻⁵ Δk/kk/°C, CITATION)					-2.0 (1.7)	-1.0 (0.9)	-1.3 (1.1)				-0.8 (1.9)
(d) Absorber/Control Cluster Worth (C/E, CITATION/TWOTRAN)								(Cluster)	(Cluster)	(Burnable Poison)	
UO ₂ Gd ₂ O ₃		1.07/1.06 (7%)			(Absorber)	1.10/1.09 (7%)	1.15/1.13 (8%)	-	-	1.04/0.99 (6%)	1.08/1.03 (6%)
AlC	1.16/1.12 (5%)	1.13/1.05 (5%)			1.06/1.04 (12%)	1.07/1.03 (8%)	-	1.07/1.02 (6%)	-	-	(Control Blade)
Hf					-	-	-	1.06/1.02 (6%)	-	-	1.09/0.91 (6%)
natB ₄ C	1.09/1.06 (4%)	1.03/0.99 (4%)			1.08/1.04 (12%)	1.01/1.00 (7%)	-	-	-	-	1.07/0.97 (6%)
90%EnrichB ₄ C					1.11/1.05 (12%)	0.97/0.98 (7%)	1.01/1.04 (6%)	1.08/1.00 (6%)	1.06/0.98 (6%)		
(f) Water Hole/Rod Worth (C/E, CITATION/TWOTRAN)					(Water Hole)					(Water Rod)	
					0.84/1.02 (7%)	1.04/1.02 (6%)				1.12/1.12 (5%)	
(g) Void Worth (C/E, CITATION/TWOTRAN)	1.05/- (~10%) (2D Void)	1.05/- (~7%) (2D Void)	1.13/0.97 (~12%) (2D Void)	1.20/1.08 (13%) (3D Void)			1.09/1.05 (6%) (2D Void)			1.14/1.01 (6%) (2D Void)	
(h) Eff. Delayed Neutron Fraction (C/E, CITATION)					0.99 (2%)	0.98 (2%)					

Note: Bracket shows measurement error % (Iso-thermal Temp. Co. : measurement error in x10⁻⁵ Δk/kk/°C)

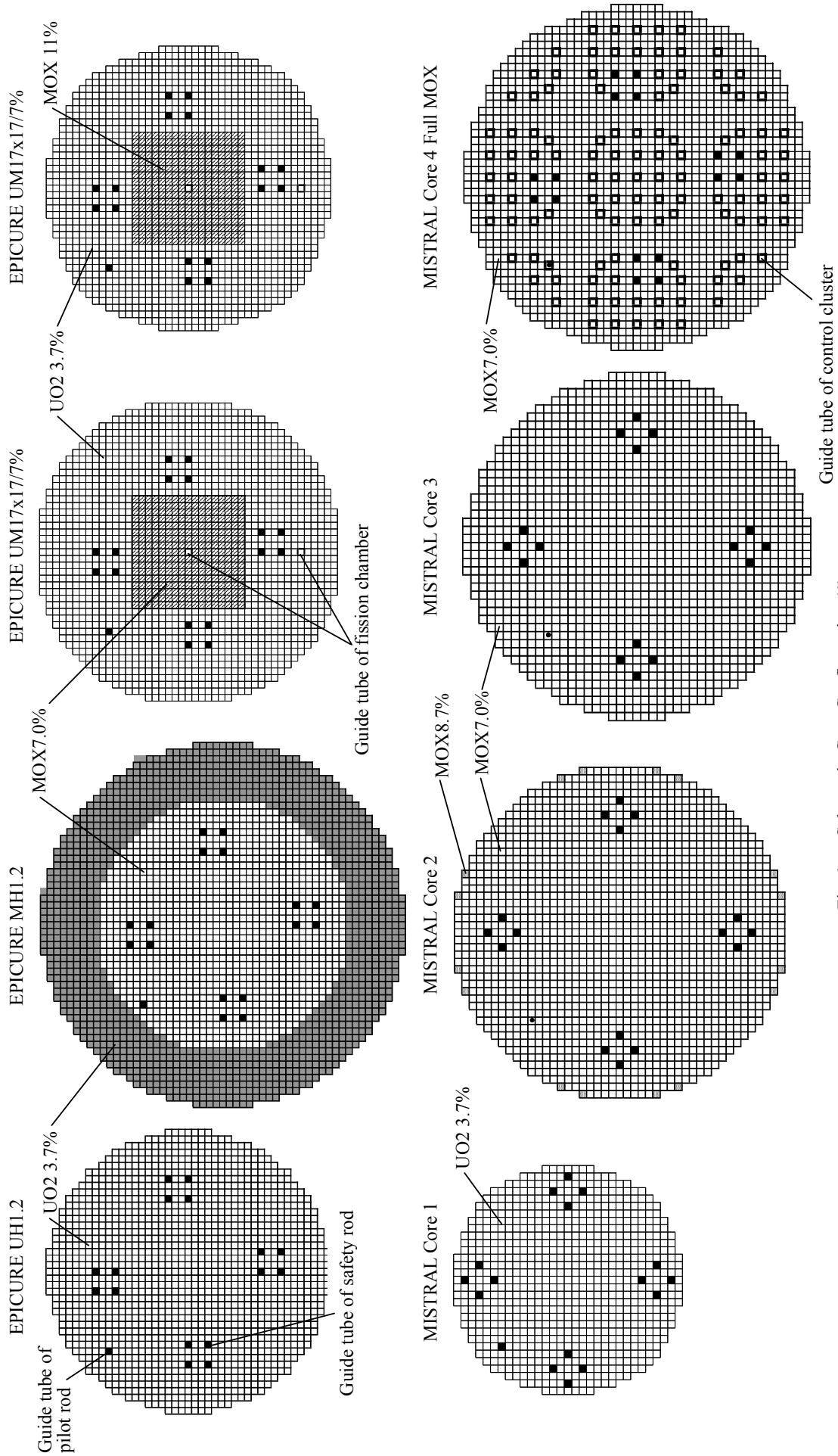


Fig. 1a Schematic Core Configuration (I)

References

- 1) T. Kanagawa *et al.*, "Study of Advanced LWR Cores for Effective Use of Plutonium," Proc. Int. Conf. on Future Nuclear Systems, Global'97, Yokohama, Japan, Oct. 5-10, 1997, Vol. 1, p.281 (1997).
- 2) K. Sakurada *et al.*, "Studies on Advanced LWR Cores for Effective Use of Plutonium and Analysis of MOX Physics Experiments," Proc. Int. Conf. on Future Nuclear Systems, Global'99, Jackson Hole, U.S.A., Aug.29-Sept.3, 1999 (1999).
- 3) R. Kanda *et al.*, "Effective Use of Plutonium through its Multi-Recycling with High Moderation LWRs," Proc. Int. Conf. on Advanced Nuclear Power Plants (ICAPP), Hollywood, Florida, U.S.A, June 9-13, 2002 (2002).
- 4) S. Cathalau *et al.*, "MISTRAL : an Experimental Programme in the EOLE facility devoted to MOX core physics," Proc. Int. Conf. on Physics of Reactor, Physor'96, Mito, Japan, Sept. 16-20, 1996, Vol. H, p.84 (1996).
- 5) K. Hibi *et al.*, "Analyses of MISTRAL and EPICURE Experiments with SRAC and MVP Code Systems," Proc. Int. Topical Meeting on Advances in Reactor Physics and Math. and Comp. into the Next Millenium, Physor2000, Pittsburg, USA, May 7-12, 2000, p.IX.E-5 (2000).
- 6) T. Yamamoto *et al.*, "Analysis of MISTRAL Experiments with JENDL-3.2," Int. Conf. on Nuclear Data for Science and Technology (ND2001), Tsukuba, Japan, Oct. 7-12, 2001, *J. Nucl. Sci. Technol.*, Supplement 2, 864 (2002).
- 7) K. Ishii *et al.*, "Analysis of MOX Core Physics Experiments MISTRAL," *Trans. At. Energy Soc. Japan*, **2**, 39 (2003) [Japanese].
- 8) T. Yamamoto *et al.*, " Core Physics Experiments and Their Analyses of High Moderation Full MOX BWR," Proc. of GENES4/ANP2003, Sep. 15-19, 2003, Kyoto, Japan.
- 9) K. Ishii *et al.*, "Analysis of High Moderation Full MOX BWR Core Physics Experiments BASALA," *Trans. At. Energy Soc. Japan*, **4**, 45 (2005) [Japanese].
- 10) J.P. Chauvin *et al.*, "EPICURE: an Experimental Programme Devoted to the Validation of the Calculational Schemes for Plutonium Recycling in PWR," Int. Conf. on Physics of Reactors: Operation, Design and Computation, PHYSOR 1990, Marseille, France, April 23-27, 1990.
- 11) K. Tsuchihashi, Y. Ishiguro, K. Kaneko, M. Ido, Revised SRAC Code System, JAERI-1302, Japan Atomic Energy Research Institute (JAERI), (1986).
- 12) T. Mori, M. Nakagawa, M. Sasaki, Vectorization of continuous energy Monte Carlo method for neutron transport calculation, *J. Nucl. Sci. Technol.*, **29**, 325 (1992).
- 13) T. Nakagawa, K. Shibata, S. Chiba, *et al.*, "Japanese Evaluated Nuclear Data Library Version 3 Revision-2," *J. Nucl. Sci. Technol.*, **32**, 1259 (1995).
- 14) K. Shibata, *et al.*, "Japanese Evaluated Nuclear Data Library Version 3 Revision-3: JENDL-3.3," *J. Nucl. Sci. Technol.*, **39**, 1125 (2002).
- 15) "Research Report on Safety Evaluation of Plutonium Effective Utilization LWR cores," Nuclear Power Engineering Corporation, March 2004 [Japanese].

2.1.2 Nuclear Data for Design of Reduced Moderation Light Water Reactor

Hiroshi AKIE
 Japan Atomic Energy Agency
 Tokai-mura, Ibaraki-ken, 319-1195, Japan
 e-mail : akie.hiroshi@jaea.go.jp

Reduced Moderation Water Reactor (RMWR) is a MOX fueled light water reactor (LWR) which can realize a higher conversion ratio than 1.0 by reducing moderator to fuel ratio than the current LWR. Neutronically, the reactor has intermediate neutron spectrum between conventional LWR and fast reactor (FR). To study the effect of nuclear data uncertainty on the physics behavior of RMWR, by using a simple benchmark calculation model, reactor physics characteristics were estimated with the different nuclear data libraries JENDL-3.3, ENDF/B-VI.8 and JEFF-3.0. As a result, for the precise estimation of the important integral parameters such as multiplication factor, void reactivity and conversion ratio, the nuclear data in all fast, resonance and thermal energy regions are found to be important. The most important difference in multiplication factor and void reactivity between ENDF/B-VI.8 and JENDL-3.3 was shown to be caused from the difference in the fast neutron spectrum mainly due to the difference in ^{238}U inelastic scattering cross section.

1. Introduction

For the efficient utilization of uranium resources based on the well experienced light water reactor (LWR) technology, Reduced Moderation Water Reactor (RMWR) concept has been studied in Japan Atomic Energy Agency (JAEA). In RMWR, it is possible to achieve the conversion ratio of higher than 1.0 and to keep the quality of plutonium (ratio of fissile to total plutonium) after burnup. The reactor can therefore sustainably supply energy for a long term through plutonium multiple recycling.

The current RMWR design is a boiling water reactor (BWR) type, and a high conversion ratio is realized by reducing the moderator to fuel ratio with a triangular tight pitched fuel lattice and a higher core averaged moderator void fraction than the existing BWR. In Fig. 1 are compared the neutron spectra in the current standard axially heterogeneous RMWR core with those in LWR and fast reactor (FR). In both upper and lower core regions in RMWR with different moderator void fraction, the neutron spectrum is intermediate between conventional LWR and FR as shown in this figure, and the neutronic characteristics of RMWR are different both from current LWR and FR. To study the effect of nuclear data uncertainty on the reactor physics characteristics of RMWR, by using a 1-dimensional simplified benchmark calculation model on the axially heterogeneous RMWR core, reactor physics characteristics such as multiplication factor, void reactivity and conversion ratio were estimated with the different nuclear data libraries JENDL-3.3, ENDF/B-VI.8 and JEFF-3.0.

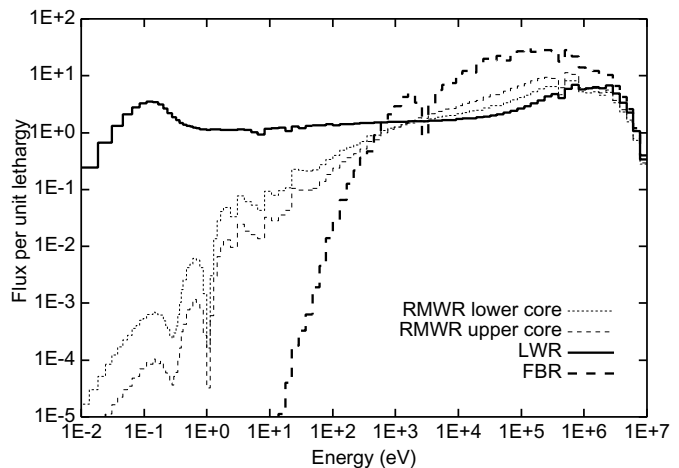


Fig. 1 Neutron spectrum in LWR, RMWR and FR.

2. Calculation model and method

One-dimensional slab geometry benchmark calculation model is considered based on the current standard axially heterogeneous RMWR design. The model consists of two MOX fueled core regions of 23cm height and 18 wt.% fissile Pu, 20cm height upper and lower blanket and 40 cm height inner blanket

regions with depleted UO_2 and upper and lower reflector regions. moderator void fraction increases from 0% in lower reflector region to 85% in upper blanket and reflector regions.

Cross sections in the core and the blanket regions are to be obtained by the cell calculations on a cylindrical pin cell model. The cell model is consisted of the fuel pin of the pin diameter of 13mm with the zircaloy cladding of 0.83mm thickness surrounded by the H_2O coolant region of the cell diameter of 15.016mm. This cylindrical cell diameter corresponds to the fuel pin pitch of 14.3mm in hexagonal pin cell.

The cell calculations were performed with the collision probability method by using the SRAC95 code system [1], and the 1-D core calculation based on the diffusion method also by using the SRAC95 and COREBN95 [1] system.

3. Integral parameters of RMWR core

3.1 Effective multiplication factor

Effective multiplication factors of 1-dimensional axially heterogeneous RMWR core model calculated with nuclear data libraries ENDF/B-VI.8 and JEFF-3.0 as a difference from JENDL-3.3 are compared in Fig. 2. As shown in this figure, ENDF/B-VI.8 was found to give $\sim 1.5\%$ larger multiplication factor than JENDL-3.3 and JEFF-3.0. This difference corresponds to, in terms of burnup period, about 500days or $>5\text{GWd/t}$. This is a very big difference from the viewpoint of reactor core design to precisely estimate the discharge burnup of RMWR.

3.2 Void reactivity

Moderator void reactivities were estimated both for the 5% void fraction increase from the nominal condition, and for the void change from nominal to 100% void. In both cases, more positive side void reactivities were obtained with ENDF/B-VI.8 data library than the other libraries.

For the 100% void case, void reactivity difference from the JENDL-3.3 result is shown in Fig. 3, and the difference between ENDF/B-VI.8 and the other libraries corresponds to about $1.5 \times 10^{-4} \text{dk/k}$ in terms of void reactivity coefficient. Almost the same difference in void coefficient is also observed in the +5% void case. The prediction of void coefficient, if it is to be negative or not, is very important in RMWR design study. As the negative void coefficient of current standard RMWR design is in the order of 10^{-4}dk/k , above shown difference between nuclear data libraries is also very large.

3.3 Conversion ratio

In contrast with the multiplication factor and void reactivity cases, the difference in conversion ratio between the results with different nuclear data libraries is not so large. It was found ENDF-B-VI.8 gives 0.5% larger conversion ratio at the beginning of burnup life (BOL) and 0.5% smaller at the end of burnup life (EOL) than JENDL-3.3 and JEFF-3.0.

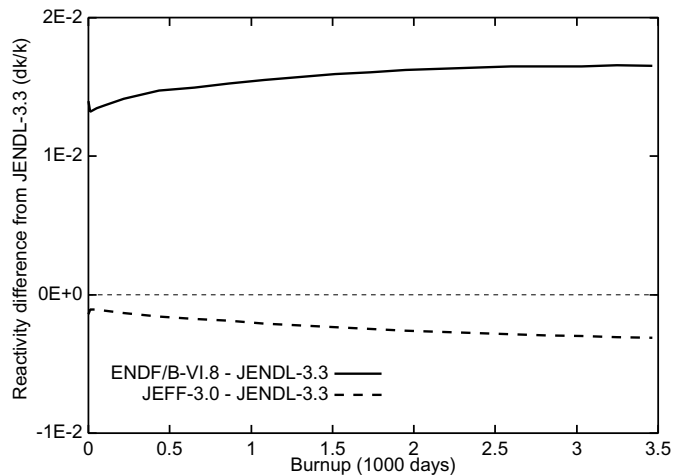


Fig. 2 Calculated multiplication factor difference from JENDL-3.3 of 1-d axially heterogeneous RMWR core model.

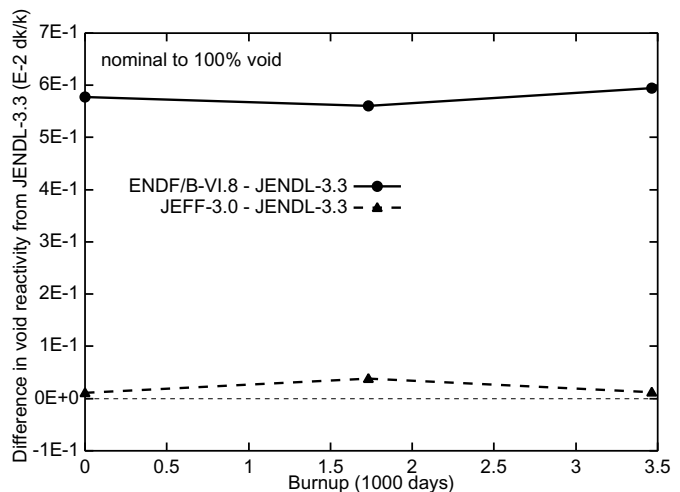


Fig. 3 Void reactivity difference from JENDL-3.3 of RMWR core calculated for nominal to 100% void fraction change.

4. Nuclide-wise and energy group-wise breakdown of the difference in integral parameters
4.1 Multiplication factor difference

To understand the cause of the difference in integral parameters estimated with different nuclear data libraries, nuclide-wise and energy group-wise contributions to the difference were next compared. Figure 4 shows the neutron production and absorption reaction rate differences between ENDF/B-VI.8 and JENDL-3.3 in the lower core region cell both at BOL and EOL. These reaction rate differences show the contribution of each nuclide to the difference in multiplication factor. This figure indicates that the most important contributions are from the production rates of ^{238}U , ^{239}Pu and ^{240}Pu both at BOL and EOL. Similar contributions were observed also in the upper core cell.

From the energy group-wise comparison of the production rates of ^{238}U , ^{239}Pu and ^{240}Pu , all the contributions of these reactions to the multiplication factor difference were shown to come from the fast energy range above 10^5eV (Fig. 5). Furthermore from the comparison of the cross sections, no significant difference in fission cross sections between ENDF/B-VI.8 and JENDL-3.3 was found in the energy region of $10^5 < E < 10^7\text{eV}$, and only slight difference in ν values without such strong energy dependence as in Fig. 5. The difference in the production rates of these nuclides in the fast energy region is mainly caused from the neutron spectrum difference calculated with ENDF/B-VI.8 and JENDL-3.3, as shown in Fig. 6.

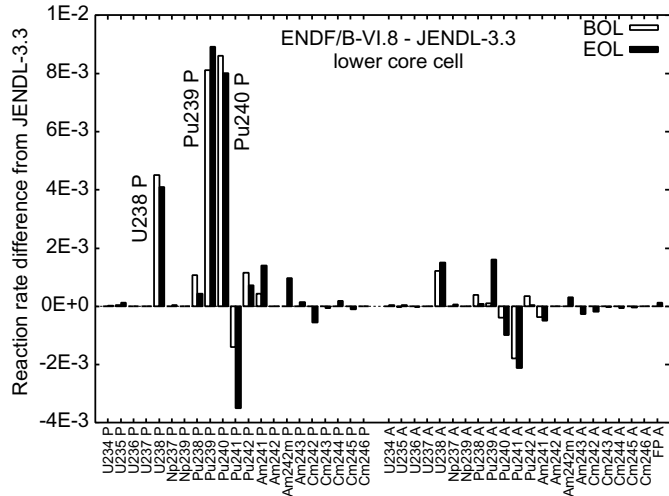


Fig. 4 Nuclide-wise contribution to the difference of multiplication factor in lower core cell calculated with ENDF/B-VI.8 from JENDL-3.3 (P : production rate, and A : absorption rate of nuclides).

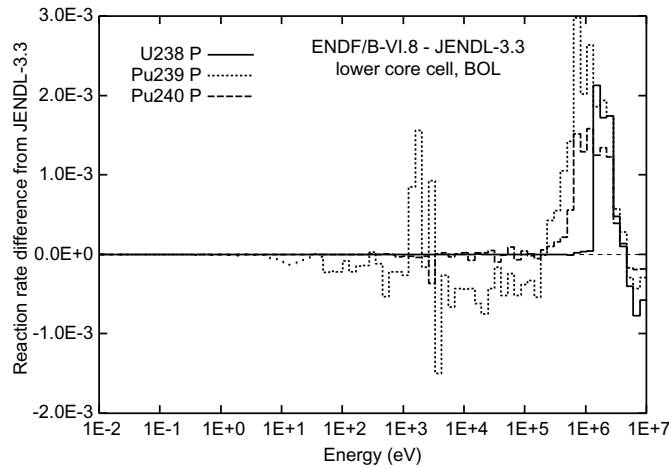


Fig. 5 Energy dependency of the difference in production rates between ENDF/B-VI.8 and JENDL-3.3.

4.2 Void reactivity difference

Similarly to the multiplication factor case, the difference between ENDF/B-VI.8 and JENDL-3.3 is mainly caused from the production rates of ^{238}U , ^{239}Pu and ^{240}Pu , due to the difference in the fast energy range of the neutron spectrum change from nominal to voided state.

4.3 Conversion ratio difference

Table 1 summarizes the conversion ratio in each region of the axially heterogeneous core calculated with ENDF/B-VI.8 and JEFF-3.0 in comparison with the JENDL-3.3 results. The conversion ratios of the whole core do not differ very much each other between the libraries, but there are found several larger differences in the region-wise conversion ratio. In the core regions, ENDF/B-VI.8 and JEFF-3.0 give smaller conversion ratio than JENDL-3.3, and the difference between ENDF/B-VI.8 and JENDL-3.3 is larger. In the blanket regions, ENDF/B-VI.8 and JEFF-3.0 both give similarly larger conversion ratio than JENDL-3.3.

In the core regions, the difference is mainly contributed by ^{240}Pu capture rate especially in resonance energy region around $E \sim 10^3\text{eV}$ (Fig. 7). The difference is mainly due to ^{240}Pu capture cross section around 1keV. While in the blanket regions, the conversion ratios calculated with ENDF/B-VI.8 and JEFF-3.0 are larger than the JENDL-3.3 case because the absorption rate of ^{235}U is smaller than JENDL-3.3. But from the viewpoint of the ^{239}Pu production in the blanket regions, the difference in the ^{238}U capture rate between the libraries is large and important. The difference comes from all fast to thermal energy regions, particularly in the lower blanket region (Fig. 8), where the neutron spectrum is much softer than the other regions. The difference is due to both the ^{238}U capture cross section and the neutron spectrum.

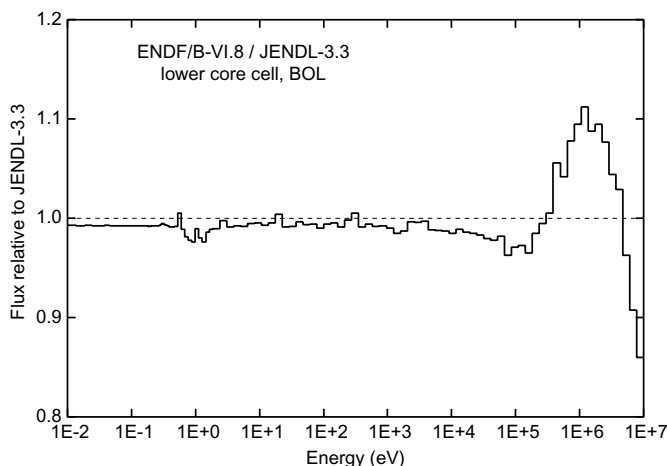


Fig. 6 Neutron spectrum in the lower core cell calculated with ENDF/B-VI.8 relative to the spectrum calculated with JENDL-3.3.

Table 1 Conversion ratio in each region

region		JENDL-3.3	ENDF/B-VI.8	JEFF-3.0
whole core	BOL	1.164	(+0.5%)	(+0.0%)
	EOL	1.085	(-0.4%)	(+0.0%)
lower blanket	BOL	6.051	(+0.2%)	(+0.2%)
	EOL	1.477	(+0.3%)	(+0.1%)
lower core	BOL	0.4524	(-1.1%)	(-0.51%)
	EOL	0.6687	(-1.0%)	(-0.09%)
inner blanket	BOL	11.85	(+0.3%)	(+0.3%)
	EOL	1.610	(+0.7%)	(+0.3%)
upper core	BOL	0.4494	(-1.4%)	(-0.60%)
	EOL	0.6642	(-1.3%)	(-0.14%)
upper blanket	BOL	17.96	(+0.2%)	(+0.3%)
	EOL	1.650	(+0.8%)	(+0.4%)

() : difference from JENDL-3.3

5. Library effect on multiplication factor and void reactivity

The difference in multiplication factor and void reactivity between ENDF/B-VI.8 and JENDL-3.3 is very important from the RMWR core design point of view. It seems necessary to further investigate the cause of the difference, i.e., what kind of cross section difference results in the neutron spectrum difference such that is shown in Fig. 6.

Since the main contributing nuclides to the difference are ^{238}U , ^{239}Pu and ^{240}Pu , the calculations were firstly carried out by using the three data libraries based on ENDF/B-VI.8 but the data for ^{238}U , ^{239}Pu or ^{240}Pu are from JENDL-3.3, respectively. As a result, the data replacement of ^{239}Pu and ^{240}Pu does not have an effect at all on multiplication factor and void reactivity. On the other hand, by replacing ENDF/B-VI.8 ^{238}U data by JENDL-3.3, both multiplication factor and void reactivity values approach

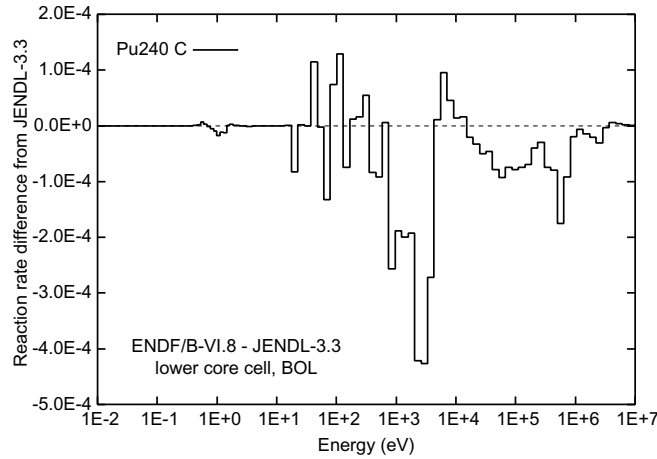


Fig. 7 ^{240}Pu capture rate difference between ENDF/B-VI.8 and JENDL-3.3 in lower core cell.

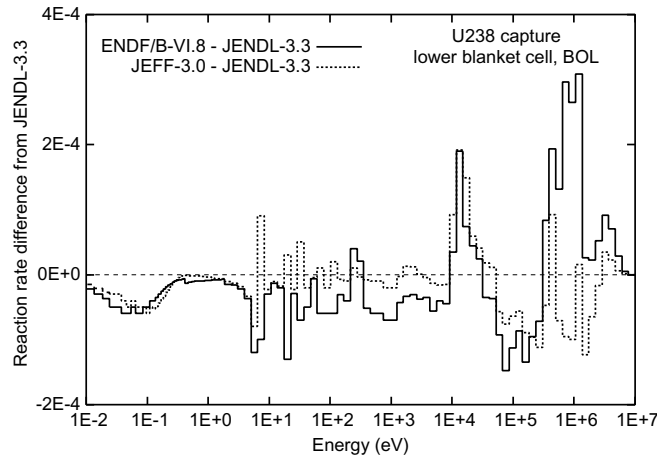


Fig. 8 ^{238}U capture rate difference between the nuclear data libraries in lower blanket cell.

to a large extent to the JENDL-3.3 results : The multiplication factor becomes about 1% smaller by using JENDL-3.3 ^{238}U data, and the void reactivity coefficient by about $1 \times 10^{-4} \text{dk/k/\%void}$ more negative.

From these results, the fast neutron spectrum difference between ENDF/B-VI.8 and JENDL-3.3 calculations seems to be caused mainly by the ^{238}U data. The calculation was next made by using such library that is based on ENDF/B-VI.8 and only the inelastic scattering cross section of ^{238}U is replaced by JENDL-3.3 data. Figures 9 and 10 show the calculated multiplication factor and void reactivity as a difference from JENDL-3.3 in the lower core cell by using this library ("ENDF/B-VI.8 + U8inJ33") in comparison with those obtained with the libraries based on ENDF/B-VI.8 and ENDF/B-VI.8 but for

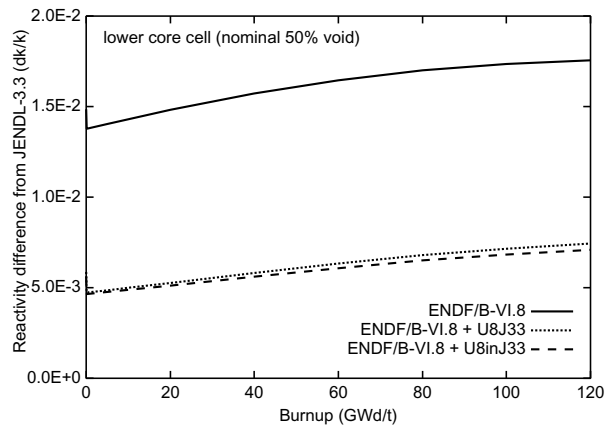


Fig. 9 Infinite multiplication factor difference from JENDL-3.3 in lower core cell calculated with different nuclear data libraries for ^{238}U .

^{238}U from JENDL-3.3 ("ENDF/B-VI.8 + U8J33"). In these figures, the effect of ^{238}U data on multiplication factor and void reactivity is shown to totally come from inelastic scattering cross section. The neutron spectrum difference between ENDF/B-VI.8 and JENDL-3.3 calculations at around 1MeV also decreases very much by replacing ^{238}U inelastic scattering cross section (Fig. 11).

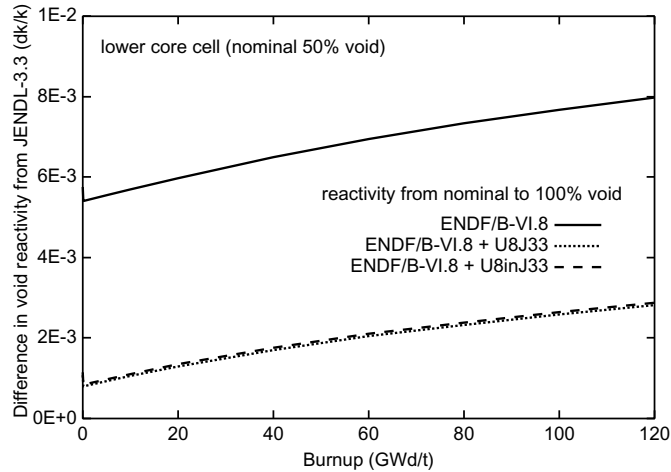


Fig. 10 Void reactivity difference from JENDL-3.3 in lower core cell for nominal to 100% void fraction change calculated with different nuclear data libraries for ^{238}U .

6. Summary

Reactor physics characteristics were calculated on the 1-dimensional axially heterogeneous Reduced Moderation Water Reactor (RMWR) core model by using the nuclear data libraries JENDL-3.3, ENDF/B-VI.8 and JEFF-3.0, and the effect of nuclear data uncertainty was studied.

As a result, ENDF/B-VI.8 was found to give nearly 1.5% larger effective multiplication factor, and more positive void reactivity coefficient by about $1.5 \times 10^{-4} \text{dk/k/\%void}$, than JENDL-3.3. The differences are very important in the RMWR core design study, and caused mainly due to the difference in the fast neutron spectrum calculated with ENDF/B-VI.8 and JENDL-3.3. The difference in conversion ratio calculated with the libraries is not so large as in the multiplication factor and void reactivity cases, but the source of the difference seems to be in all fast to thermal energy regions.

From the results obtained here, it can be said that the nuclear data in all fast, resonance and thermal energy regions are important in the RMWR core design study for a precise estimation of the important integral parameters such as multiplication factor, void reactivity and conversion ratio.

From the library effect study on the most important differences in multiplication factor and void reactivity between ENDF/B-VI.8 and JENDL-3.3, the main cause was found to be the inelastic scattering cross section of ^{238}U .

References

[1] K. Okumura, K. Kaneko and K. Tsuchihashi : "SRAC95; General Purpose Neutronics Code System", JAERI-Data/Code 96-015 (1996) [in Japanese].

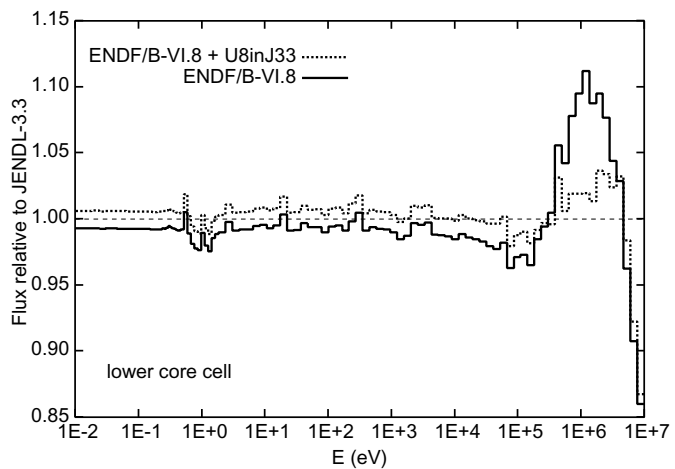


Fig. 11 Neutron spectrum in lower core cell calculated with different nuclear data libraries for ^{238}U , relative to the spectrum obtained with JENDL-3.3.

2.1.3 Nuclear data for Non-refueling core design

Tetsuo MATSUMURA¹, Yasushi NAUCHI¹, Nobuyuki UEDA¹, Shigeaki OKAJIMA²
and Toshikazu TAKEDA³

¹Central Research Institute of Electric Power Industry (CRIEPI)

2-11-1, Iwado Kita, Komae-shi, Tokyo 201-8511 JAPAN, matsu-t@criepi.denken.or.jp

²Japan Atomic Energy Agency (JAEA)

Tokai-mura, Naka-gun, Ibaraki-ken, 319-1195, JAPAN, okajima.shigeaki@jaea.go.jp

³Osaka University

Yamada-oka, 2-1, Suita Osaka 565-0871, JAPAN, takeda@nucl.eng.osaka-u.ac.jp

For design of innovative control system and safety characteristic of the Non-refueling core design of long life, a series of critical experiments is conducted at the fast critical facility, FCA of JAEA-Tokai. To quantitatively estimate the uncertainty reduction through critical experiments, an uncertainty reduction ratio (UR) is introduced, using the cross section error. Additionally with sensitivity analysis of the cross sections, important cross sections are clarified for burn-up calculation.

1. Introduction

The 4S, Super Safe, Small and Simple, reactor (Fig.1) is a kind of fast reactor core in which burn-up reactivity loss is compensated by decrement of neutron leakage probability with movement of reflector. For extending core life of the Non-refueling core up to 30 years generating 30MW thermal power, a core of 2.5m height has been designed and studied in which 21%/24%-Pu-enriched Pu-U-Zr metallic fuel pins are loaded (Fig.2) [1,2].

Present document is based on extractions from papers of authors [3,4].

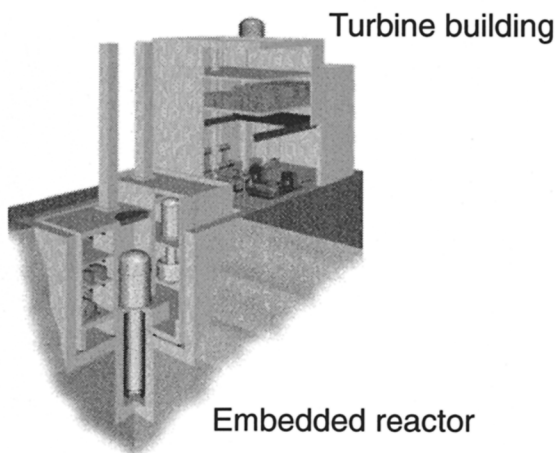


Fig. 1 Overview of 4S Reactor

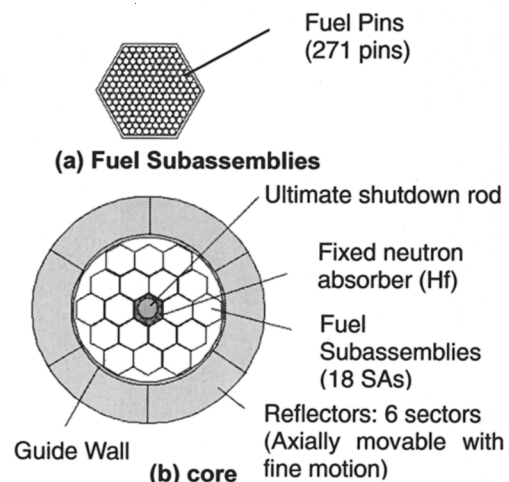


Fig. 2 Design of the Non-refueling core

2. Critical experiments [3].

For design of innovative control system and safety characteristic of the Non-refueling core of long life, we have to verify and improve neutronics calculation methods. However, there are few experimental data focused on reflector reactivity, small (zero or negative) Na void reactivity etc.. For the verification of the design methods, a series of critical experiments is conducted at the fast critical facility, FCA of JAEA-Tokai. A core of metallic fuels of Pu and Pu+U surrounded by massive reflector of stainless steel has been mocked up and measurements of several kinds of reactivity and reaction rate distribution have been conducted. The measured data have been analyzed by conventional deterministic diffusion/transport codes and continuous energy Monte Carlo codes. By the comparison of calculated one to the data, prediction accuracies of neutronics codes have been clarified.

The experimental core (FCA XXIII core) was constructed to focus on the behavior of neutron leakage in radial direction and the neutron spectrum. As shown in Fig. 3, the core has a core region (about 30 cm in radius and 111 cm in height) with a sodium (Na) channel (about 9 cm in radius) along the center axis. The core region is divided into two zones, the inner zone and the outer zone. The inner zone is composed of Pu fuel plates, natural U plates, Zr plates and Na plates to simulate the composition of the Non-refueling core. The composition of the outer zone is slightly different from that of the inner zone; enriched U plates instead of some of Pu plates were used because of the insufficient inventory of fissile materials. The core region is surrounded by the Na region of 5cm thickness and the reflector region of 33cm thickness.

Measurements have been made for criticality (k_{eff}), central reaction rate ratios, reaction rate distributions, Na void reactivity worth and reflector reactivity worth. Especially, to get the leakage and no-leakage information in the Na void reactivity worth, the detailed distribution of the Na void reactivity worth has been measured. The experimental core first went critical in July 2004.

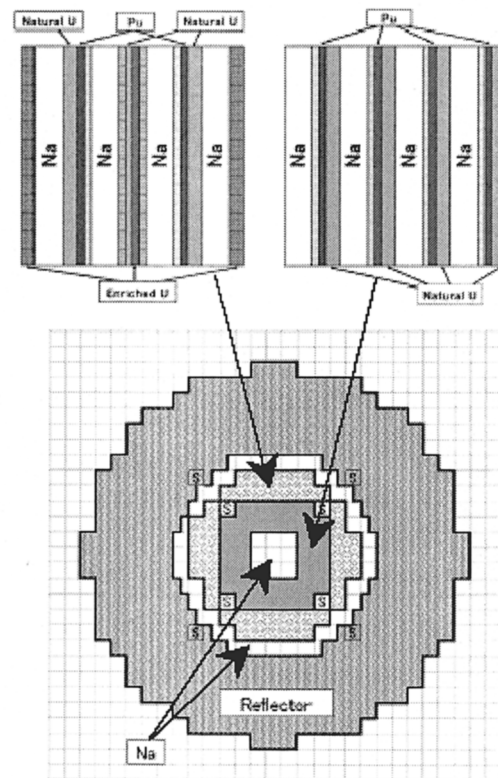


Fig. 3 Cross sectional view of the experimental core (FCA XXIII core)

3. Neutronic uncertainty reduction technique [4].

Using the experimental data, the bias factor, the ratio of measured neutronics characteristics to the calculated ones, is obtained. The uncertainty of this bias factor is also calculated. To quantitatively estimate the uncertainty reduction through critical experiments, an uncertainty reduction ratio (UR) is introduced, using the cross section error. By using UR, better experimental core can be mocked up and required accuracy for experiments have been identified to reduce the uncertainty of the bias factor, i.e., to improve the accuracy of design calculation of the target the Non-refueling core. [5,6].

As an example, let us show the uncertainty reduction (UR) for the conversion ratio. The UR is obtained for the inner core (IC) and the outer core (OC) in the Non-refueling core as a function of the experimental error as shown in Fig.4.

The UR is almost 0.85 when experimental error is zero. This means that the uncertainty is reduced by 85% when using the critical experiment. The measurement with more than 5% error is meaningless for the reduction of the uncertainty of the target Non-refueling core. Therefore, accurate measurement is necessary. The large UR is caused by the fact that they have very similar nuclide-wise component of uncertainty (S^tVS) due to the cross section error as shown in Fig. 5. Here S and V denote the sensitivity coefficient and cross section covariance matrices, and superscript t shows the transpose of the matrix. As shown in Fig. 5, ^{238}U and ^{239}Pu are the main component in S^tVS for the case of conversion ratio. The similar trend for these components leads to the satisfactory reduction of uncertainty.

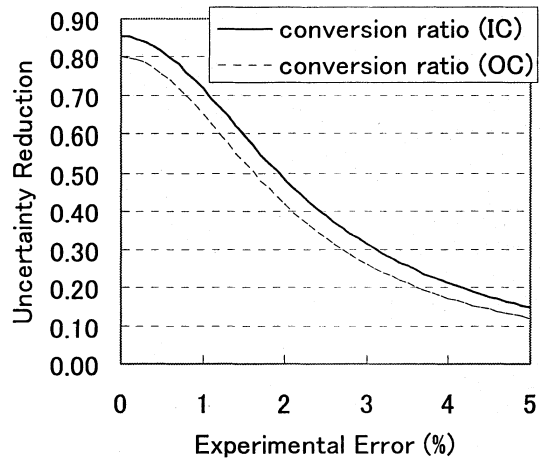


Fig. 4 UR vs. experimental error (conversion ratio)

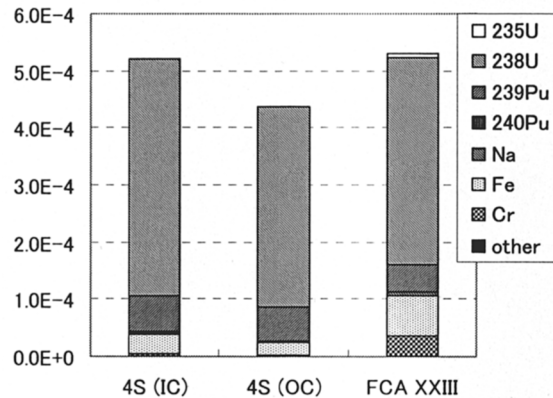


Fig. 5 Nuclide-wise component of SVS (conversion ratio)

4. Sensitivity analysis of burn-up depletion

For achievement of long core life of 30 years without refueling, prediction of burn-up reactivity depletion is important. With sensitivity analysis of the cross sections, important cross sections are clarified for burn-up calculation.

Calculations are carried out with 2-dimensional (R-Z) diffusion code with 70 energy group

JFS-3-J3.3 library (added lumped FP data of JFS-3-J32R library on it). Seven group effective cross-sections were created, and burn-up calculation was performed. Sensitivity coefficients are calculated directly with fluctuation of burn-up depletion reactivity resulting from small change of seven group effective cross-sections.

Sensitivity coefficients of the fission cross section of ^{235}U , ^{239}Pu , and ^{241}Pu (fissile nuclides) are positive (when the cross-section is increased, depletion reactivity is also increased), and a fertile nuclides have negative values. Sensitivity coefficients of the capture cross section of ^{238}U and ^{240}Pu (fertile nuclides) are negative, and the sensitivity coefficient of ^{239}Pu capture cross section is positive. These results are due to accumulation of fissile nuclides. Important nuclides and reactions are fission cross section of ^{239}Pu and capture cross section of ^{238}U (Fig. 6) [7].

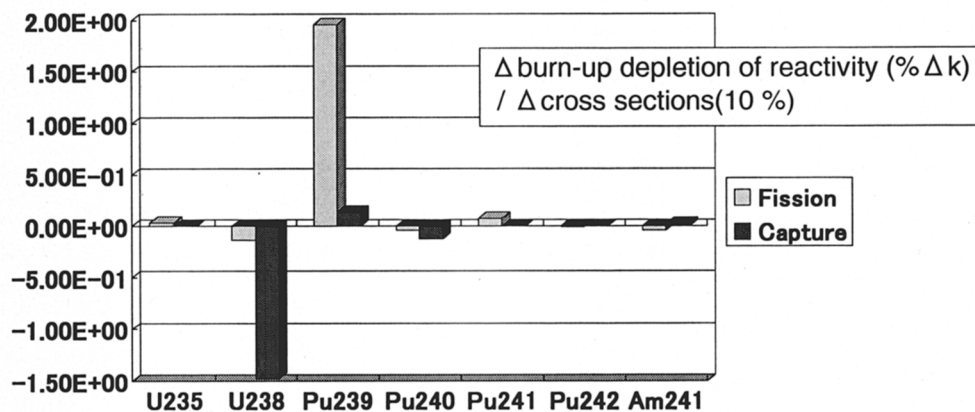


Fig. 6 Sensitivity coefficients of buru-up depletion reactivity

5. Summary

- In the Non-refueling core, burn-up reactivity loss of 30 years is compensated by decrement of neutron leakage probability with movement of reflector. And small (zero or negative) Na void reactivity is important for safety core characteristics of the Non-refueling core.
- For the verification of the design methods, series of critical experiments is conducted at FCA.
- To quantitatively estimate the uncertainty reduction through critical experiments, an uncertainty reduction ratio (UR) is introduced, using the cross section error.
- With sensitivity analysis of the cross sections, important cross sections are clarified for burn-up calculation

Acknowledgements

The present study is the results of "Development of Advanced Controlling System for Non-Refueling Reactor Core" in fiscal year 2003 and 2004 entrusted by Ministry of Education,

Culture, Sports, Science and Technology (MEXT) to Central Research Institute of Electric Power Industry (CRIEPI).

Present work is completed under several discussions with Dr. M. Yamaoka, Dr. M. Kawashima (Toshiba) and other members.

References

- [1] N. UEDA, et al.: "Passive Reactor Dynamics and Load Following Characteristics of Sodium Cooled Super-Safe Small and Simple Reactor.", Procedure of the 11th ASME-JSME International Conference on Nuclear Engineering (ICONE-11), 36539, Tokyo, April 14-18 (2003).
- [2] N. UEDA and I. KINOSHITA: "Development of an extrapolation method for longer metallic fuel pin for Non-refueling Core", ANS Winter Meeting, Washington D.C. (2005).
- [3] S. Okajima, M. Fukushima and T. Takeda: "Development of Neutronics Analysis Technique for Non-refueling Core (Part 1: Critical Experiment)", ANS Winter Meeting, Washington D.C. (2005).
- [4] T. Takeda, T. Kitada and S. Okajima: "Development of Neutronic Analysis Technique for Non-refueling Core Part2: Method", ANS Winter Meeting, Washington D.C. (2005).
- [5] T. Takeda, et al.: "New Uncertainty Reduction Method of Na Void Worth in Long-Life Small Fast Reactor.", Proceedings of ICAPP'04, 4154, Pittsburgh, PA USA, June 13-17 (2004)
- [6] T. Takeda et al., "Application of Uncertainty Reduction Factor for Determining Critical Mockup of An Innovative Long-Life Fast Reactor", Proceedings of ICAPP'05, Seoul, KOREA, May 15-19(2005).
- [7] T. Matsumura et al.: "Development of Neutronic Analysis Technique for Non-refueling Reactor Core(6) -Sensitivity evaluation of cross sections for burn-up reactivity depletion-" AESJ Autumn meeting, C44, Kyoto, (2004) [in Japanese].

2.1.4 Impact of Nuclear Data on Design Work for High Temperature Gas-cooled Reactors

Satoshi SHIMAKAWA, Minoru GOTO and Yasunobu NAGAYA

Nuclear Science and Energy Directorate,

Japan Atomic Energy Agency

4002 Oarai-machi, Higashi-ibaraki-gun, Ibaraki-ken 311-1393

e-mail: shimakawa.satoshi@jaea.go.jp

Concerning to nuclear design for the high temperature gas-cooled reactors (HTGRs), the calculation method has been improved with experimental data of the research reactors, such as the HTTR in Japan and the HTR-10 in China. One of the HTGRs type with very high temperature, called VHTR, has been proposed in the Generation IV International Forum.

In nuclear design of HTGRs, several cross sections were interested to characterize the criticality and burn-up situations.

- U-235, Pu-241: (n,f) and (n,g) reactions
- U-239, Pu-239, Pu-240 : (n,g) reaction
- C : elastic and (n,g) reactions
- MAs and LLFPs: generation and transformation

From the recent studies, it is indicated that JENDL-3.3 gives the k_{eff} agreement with the experiments within 1.5% Δk , JENDL-3.2 gives within 1.7% Δk , and ENDF/B-IV.8 and JEFF-3.0 give within 1.8% Δk for the some HTTR core conditions. The k_{eff} discrepancy between JENDL-3.3 and JENDL-3.2 is caused by difference of U-235 fission data and its ratio of (n,f)/(n,g) reaction in neutron energy range of 0.1-1.0eV. There is no discrepancy of k_{eff} value between ENDF/B- IV.8 and JEFF-3.0.

In thermal energy range, the capture cross section of carbon in the nuclear library JENDL is about 4% larger than those of ENDF/B and JEF. From the calculation results of the HTR-10 and HTTR, it was found that the reactivity discrepancy by the carbon capture data is about 0.6% $\Delta k/k$ for criticality analysis, although the section is very small as about 3mb at 2200m/s.

The influence of cross sections of carbon and impact for design work of HTGRs will be cleared by the neutronics calculation using the Monte Carlo code MVP and the diffusion code system SRAC.

2.2 Past and Future of Nuclear Data Research

2.2.1 Japanese Nuclear Data Activities in the Last 40 Years

Tsuneo NAKAGAWA

Nuclear Data Center, Japan Atomic Energy Agency

Tokai-mura, Naka-gun, Ibaraki-ken 319-1195

e-mail: nakagawa.tsuneo@jaea.go.jp

Nuclear data activities in Japan were started in 1963 by organizing Japanese Nuclear Data Committee (JNDC). Since then, JNDC and Nuclear Data Center which was established in Japan Atomic Energy Research Institute as Nuclear Data Laboratory in 1968 have made efforts to provide various kinds of information on nuclear data and to develop Japanese own evaluated nuclear data library (JENDL). Especially various versions of JENDL and JENDL special purpose files are excellent products of Japanese nuclear data activities.

The nuclear data activities in Japan started about 40 years ago. In 1963, two Japanese Nuclear Data Committees (JNDC) were organized in Japan Atomic Energy Research Institute (JAERI) and Atomic Energy Society of Japan (AESJ). They started work to develop theoretical calculation codes for unknown cross sections, and collaborations with international organizations. The optical model code ELIESE-1[1] is a result of the code development.

The Nuclear Data Laboratory which was a precursor of Nuclear Data Center (NDC) was established in JAERI in 1968. Full-scale evaluation work was started in 1970. In 1971, they discussed eagerly if they need their own evaluated nuclear data libraries. After long discussion, they decided to make own data library, Japanese Evaluated Nuclear Data Library (JENDL). A trial of data compilation began in the next year. During the test compilation of evaluated nuclear data file, computer codes needed for the compilation were developed.

The compilation work of JENDL-1 started in 1974. Results of nuclear data evaluation work made in JNDC were compiled in the ENDF format. JENDL-1 [2] was completed in 1976 and released in 1977 after benchmark tests. Since then, several versions of JENDL were released as listed in **Table 1**. Special purpose files listed in **Table 2** were also released so far. Nuclear data evaluation for those JENDL files was successfully performed under the collaboration among JAERI NDC and JNDC.

JNDC has a few subcommittees which consist of several working groups (WG). An example of JNDC structure is given in **Fig.1**, which is a JNDC in 1992 when they were making JENDL-3.2 [3]. The evaluation work was made by the WG's of the Nuclear Data Subcommittee, such as FP Nuclear Data WG, Heavy Nuclear Data WG and Gamma-ray Production Data WG. Those of Data for fusion reactors, Activation cross sections, PKA Spectra, Charged particles and Photonuclear data were organized for JENDL special purpose files. Benchmark tests of JENDL files were performed by WG's of the Reactor Constant Subcommittee.

For example, FP Nuclear Data WG made evaluation of nuclear data of FP nuclides; 28 nuclides for JENDL-1, 100 nuclides for JENDL-2, 172 nuclides for JENDL-3.1, and 63 nuclides for

JENDL-3.2. The WG members from NDC mainly performed jobs of theoretical calculations, comparison of calculated cross sections with experimental data, data compilations in the ENDF format and maintenance of computer codes. Other members made evaluation of resonance parameters, determination of model parameters, and benchmark tests.

The structure of JNDC was changed often to meet the circumstances. The number of JNDC members has been also changed as is shown in Fig. 1. It has a peak around 1990 to 1997, and has decreased recently. The number of JNDC meetings also has the same tendency. When JAERI dissolved at the end of last September, JNDC also disappeared once. New JNDC is going to be organized in Japan Atomic Energy Agency (JAEA). The new JNDC will be expected to be as quite active as old JNDC in the past.

References

- [1] Japanese Nuclear Data Committee; "Program ELIESE-1, FORTRAN-II Program for Analyses of Elastic and Inelastic Scattering Cross Sections," JAERI 1096 (1965).
- [2] S. Igarasi, et al.; "Japanese Evaluated Nuclear Data Library, Version-1, -- JENDL-1 --," JAERI 1261 (1979).
- [3] T. Nakagawa, et al.; *J. Nucl. Sci. Technol.*, **32**, 1259 (1995).
- [4] T. Nakagawa; "Summary of JENDL-2 General Purpose File," JAERI-M 84-103 (1984).
- [5] K. Shibata, et al.; "Japanese Evaluated Nuclear Data Library, Version-3, -- JENDL-3 --," JAERI 1319 (1990).
- [6] M. Kawai, et al.; *J. Nucl. Sci. Technol.*, **29**, 195 (1992).
- [7] K. Shibata, et al.; *J. Nucl. Sci. Technol.*, **39**, 1125 (2002).
- [8] M. Nakazawa, et al.; "JENDL Dosimetry File," JAERI 1325 (1992).
- [9] K. Kobayashi, et al.; "JENDL Dosimetry File 99 (JENDL/D-99)," JAERI 1344 (2002).
- [10] Y. Nakajima, et al.; "JENDL Activation Cross Section File," Proc. the 1990 Symposium on Nuclear Data, JAERI-M 91-032, p. 43 (1991).
- [11] S. Chiba, et al.; *J. Nucl. Sci. Technol.*, **39**, 187 (2002).
- [12] J. Katakura, et al.; "JENDL FP Decay Data File 2000," JAERI 1343 (2001).
- [13] Y. Watanabe, et al.; "Nuclear Data Evaluation for JENDL High-Energy File," Proc. International Conference on Nuclear Data for Science and Technology, Santa Fe, New Mexico, USA, Sep. 26 - Oct. 1, 2004, Vol. 1, p.326 (2004).
- [14] N. Kishida, et al.; "JENDL Photonuclear Data File," Proc. International Conference on Nuclear Data for Science and Technology, Santa Fe, New Mexico, USA, Sep. 26 - Oct. 1, 2004, Vol. 1, p.199 (2004).
- [15] T. Murata and K. Shibata; *J. Nucl. Sci. Technol.*, Suppl. 2, Vol.1, 76 (2002).

Table 1 JENDL general purpose files

Version	Year of release	Number of nuclides
JENDL-1 [1]	1977	72
JENDL-2 [4]	1982/1985	181
(JENDL-3 [5])	1989	171
JENDL-3.1 [5,6]	1990	304
JENDL-3.2 [3]	1994	340
JENDL-3.3 [7]	2002	337

Table 2 JENDL special purpose files

File name	JNDC WG*	Working year	Total years
Dosimetry File 91 [8]	○	1987~1991	4
Dosimetry File 99 [9]	○	1990~1999	9
Activation Cross Section File 96 [10]	○	1988~1996	8
Fusion File 99 [11]	none	1990~1999	9
FP Decay Data File 2000 [12]	○	~2000	
High-energy Files 2004 [13]	○	1993~2004	11
Photoreaction File 2004 [14]	○	1988~2004	16
(α,n) Data Files 2003 [15]	○	1988~2003	15
(α,n) Data Files 2005	none	2003~2005	2

*) WG for data evaluation. ○ means a WG worked for the evaluation.

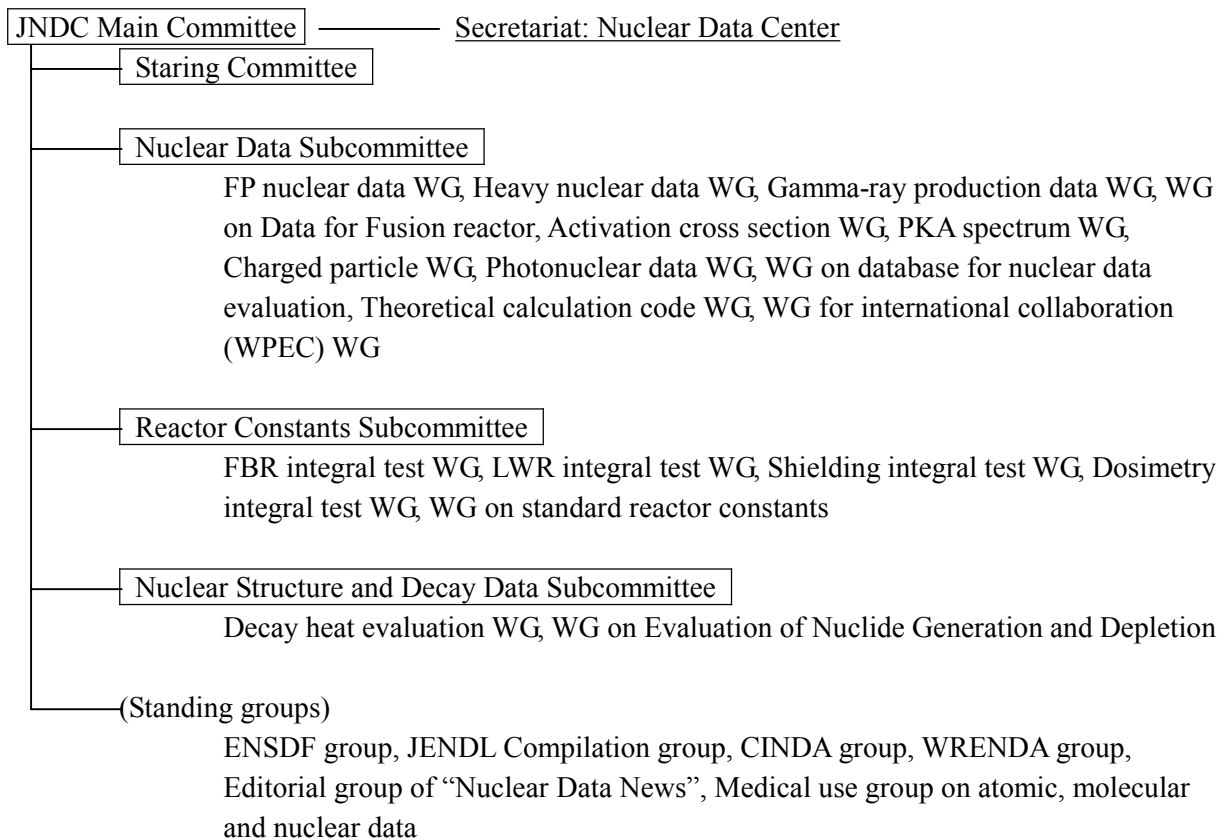


Fig.1 JNDC in 1992

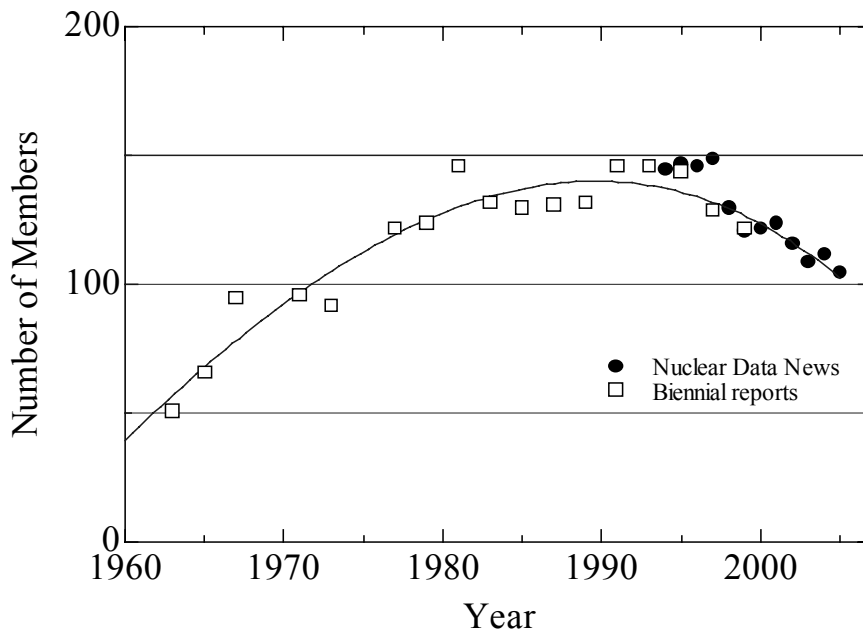


Fig.2 Numbers JNDC members

Data were taken from “Nuclear Data News” and biennial reports of JNDC.

2.2.2 Nuclear Data Evaluation Activities in JAEA and the Mid-Term Plan

J. Katakura
Nuclear Data Center
Nuclear Science and Engineering Directorate
Japan Atomic Energy Agency
Tokai-mura, Naka-gun, Ibaraki-ken 319-1195
e-mail: katakura.junichi@jaea.go.jp

Japan Atomic Energy Agency (JAEA) was established at October 1, 2005. The activities relating to nuclear data evaluation in JAEA are described.

1. Introduction

Japan Atomic Energy Agency (JAEA) was established at October 1, 2005 after the merger of Japan Atomic Energy Research Institute (JAERI) and Japan Nuclear Cycle Development Institute (JNC). Missions of JAEA are described as followings: (1) Establishment of nuclear fuel cycles, (2) Research and development of nuclear fusion energy, (3) Contribution to hydrogen economy by nuclear process heat, (4) Quantum beam technology, (5) Research on nuclear safety, (6) Non-proliferation and safeguards technology, (7) Decommissioning of nuclear facilities, treatment and disposal of low level waste, (8) Cooperation with academic and industrial communities/ international collaboration/ human resource development/ atomic energy information and (9) Basic nuclear engineering research, advanced basic research. The nuclear data evaluation activities are included in the mission of (1) and (9). In order to perform the missions, the nuclear data evaluation work is carried out in JAEA.

2. Mid-term plan

When JAEA was established, the mid-term plan was issued to the Minister

of Education, Culture, Sports, Science and Technology and was approved by the minister. The mid-term plan is the work list JAEA promises to perform during the mid-term from October 1, 2005 through March 31, 2010. In the mid-term plan the nuclear data activities are written in two parts. One is the activities relating to the development of nuclear conversion system including FBR and ADS systems. In the part nuclear data evaluation is written as “Design precision will be enhanced by establishing nuclear data for nuclear conversion target MA and LLFP, establishing nuclear design code, and conducting reactor physics experiment. Through the acquisition of physical property of fuel containing MA, and test production of target containing LLFP, we will contribute to building a base for nuclear conversion technology”. (From the JAEA English home page. <http://www.jaea.go.jp/english/index.shtml>). The second one is relating to the basic nuclear engineering research. In the part it is written that “With fuel burn-up rate becoming higher, FP and MA nuclide will be playing increasingly important role. Thus, efforts will be made to mainly assess such nuclear data, and to complete JENDL-4, the General-Purpose, Pre-Assessed Nuclear Data Library featuring expansive error data, so to enhance the reliability of nuclear calculation.” (From the JAEA English home page. <http://www.jaea.go.jp/english/index.shtml>). So the missions of Nuclear Data Center are to complete the Japanese Evaluated Nuclear Data Library JENDL-4 (Japanese Evaluated Nuclear Data Library) and to provide the nuclear data for development of nuclear conversion system until the end of the mid-term.

3. Nuclear Data Evaluation Activities

Although we have a mission to provide the necessary nuclear data for development of nuclear conversion system, we consider that the primary purpose of our group is to complete JENDL-4. The main effort to compile the JENDL-4 library focus on the nuclear data evaluation of minor actinide (MA) nuclides and fission product (FP) nuclides and the provision of more covariance data than the present evaluated nuclear data library JENDL-3.3. The planned schedule for the development of JENDL including the development of high energy relating files is shown in Fig. 1.

Time Schedule of JENDL

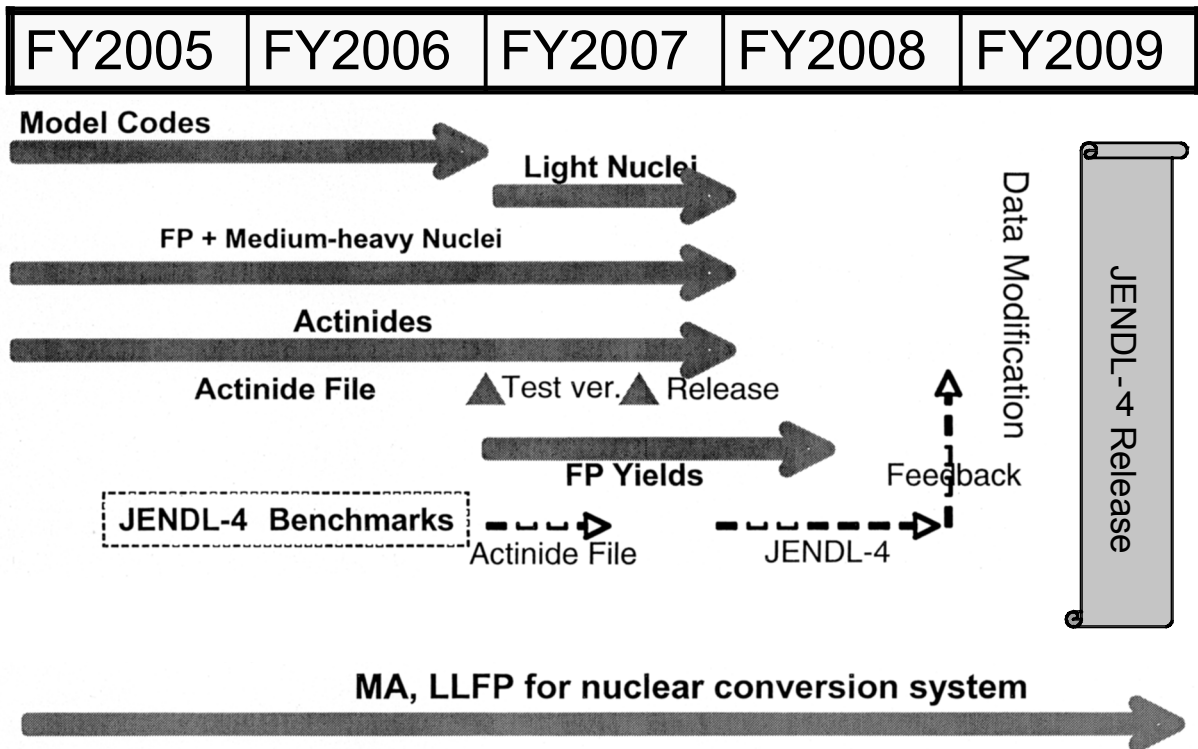


Fig. 1 Planned Time Schedule of JENDL Development

As seen in Fig. 1, benchmark tests of JENDL-4 are indispensable to ensure the performance of the nuclear data included. We have to cooperate for the tests with reactor engineers who have the activities to perform the calculation using the nuclear data. The benchmark tests will be performed by not only other research groups in JAEA but also the groups outside JAEA.

In JAEA there is a research group which has the activity of nuclear data measurement. The group has the plan to obtain the measured data of minor actinide and long-lived FP nuclides. Nuclear data center keeps close contact with the group to obtain the up-to-date measured data. When new measured data are obtained we are going to use them for new evaluation.

4. Summary

Under the new organization, Japan Atomic Energy Agency, the nuclear data evaluation is performed based on the mid-term plan which is approved by the Minister of Education, Culture, Sports, Science and Technology. In the plan, the

goal of the nuclear data evaluation work is to complete the JENDL-4 library until the end of the term. In the work of the JENDL-4 compilation, main effort focuses on the evaluation of MA and FP nuclides and covariance data in addition to solving the problems of the JENDL-3.3 nuclear data.

The Nuclear Data Center in JAEA continue the effort to compile and to maintain the Japanese Evaluated Nuclear Data Library JENDL.

2.3 Panel Discussion - Future of Nuclear Data Research -

2.3.1 Expectation for Nuclear Data Development (I)

Kasufumi TSUJIMOTO

Transmutation Experimental Facility Group, Japan Atomic Energy Agency
Tokai-mura, Naka-gun, Ibaraki-ken 319-1195
e-mail : tsujimoto.kazufumi@jaea.go.jp

The nuclear data has a crucial role in development of nuclear power systems. From a point of view for future nuclear systems, expectation for nuclear data development is discussed in this paper. The purpose of this paper is to give some proposal for the future improvement of nuclear data.

1. Introduction

The nuclear data has played an important role in the development of the nuclear power development. There is no practical meaning in the reactor physics without the nuclear data. It provides a fundamental database for various research fields, such as astrophysics. However, will it continue to play a crucial role in the development of future nuclear system? Many nuclear plants are now operated in the world. Some people say that the current data has sufficient accuracy. In this paper, from the view point of future nuclear system, expectation for the nuclear data development will be discussed.

2. Future Nuclear Power System

In the development of future nuclear power system, first of all, it is necessary to think about extrapolation of the present nuclear power plant, such as high-burn up and recycling of Pu. For the reactor performance, nuclear data of the higher actinides will become increasingly essential to reduce the potential uncertainties. As far as the fuel cycle, it will be desired to reduce the uncertainties of the isotope contents of the discharged fuel from viewpoint of critical safety issues.

One of the most important issues for sustainable utilization of nuclear energy is steady implementation of High Level Waste (HLW) disposal. The long-term radio-toxicity of the HLW is mainly dominated by the minor actinides (MA). The Partitioning and Transmutation (P&T) technology is aiming at the reduction of the radio-toxicity by transmuting MA and other long-lived fission products. Various P&T conceptual studies were performed over the past dozen years or so. The Japan Atomic Energy Agency (JAEA) has developed a concept of double-strata fuel cycle, in which P&T is carried out in a dedicated and small-scale fuel cycle attached to the commercial fuel cycle¹⁾. For a dedicated transmutation system, JAEA has been proceeding with the research and development on accelerator-driven subcritical system (ADS)²⁾. In this concept, the ADS loaded with MA nitride fuel is considered as the most powerful tool for transmutation because such dedicated fuel cannot be loaded in critical nuclear reactors for safety reasons.

For the future systems, it will be strongly desired by minimizing the long-lived radioactive waste. To develop future-generation nuclear systems, the Generation-IV International Forum (GIF) was launched in 2000 by US-DOE. The six systems, GFR, LFR, MSR, SFR, SCWR, and VHTR, were selected as Generation-IV systems to be developed. Three out of the six concepts in Gen-IV foresee the full TRU recycling in Fast Reactors (FR) in order to meet the requirement for waste minimization.

As described above, the nuclear data, especially neutron cross-sections, of MA will play important role in future nuclear systems. The present status and the potential needs for nuclear data of

MA are discussed in following section.

3. Current Status and Data Needs

The reduction of analytical uncertainties for core parameters, such as subcriticality and burnup swing, are very important issues for design study of ADS. In the operation of ADS, the system must be subcritical in any case because there are no control rods in present design of ADS proposed by JAEA. Moreover, the proton beam current required to keep predefined power level is directly related to the subcriticality (k_{eff}). To indicate the current status for nuclear cross-section of MA, the results of the burnup calculations using JENDL-3.3, ENDF/B-VI and JEF-3.0 libraries, respectively, are presented in Fig.1(a). The calculated core was a Pb-Bi cooled ADS³⁾. For the core fuel, mixture of mono-nitride of MA (60%) and plutonium (40%) was used with an inert matrix, ZrN. The isotopic composition of MA and Pu were assumed as the spent PWR fuel of 50 GWd/t burnup. As shown in Fig.1, even at initial core, the difference among calculated k_{eff} is about 2%. The burnup reactivity swings also show very different trend with the libraries. To clear the reason of discrepancy for calculated results, contributions of each nuclide for difference of k_{eff} at initial state are shown in Fig.1(b). The results show that the discrepancy among the nuclear data libraries is mainly attributed to the uncertainties of MA cross-section data.

The sensitivity and uncertainty analysis are very strong tools to investigate the impact of nuclear data uncertainties on the core parameters. These analyses will help to indicate future direction for improvement of the nuclear data. For sound uncertainty studies, variance-covariance data to be associated to nuclear data library are absolutely essential. Recently, new evaluations for variance-covariance data for MA and other nuclides related to ADS were carried out by Nuclear Data Center in JAEA. The results of the uncertainty analysis for k_{eff} at initial state are given in Fig.2 together with main contributor for the total uncertainties. Total value is the square root of the sum of the squares. The total value ($\pm 0.9\%$) for k_{eff} is higher than corresponding values for critical fast reactor. The major contributor among the actinide nuclides is ²³⁷Np and ²⁴¹Am, and the capture cross-section of ²⁴¹Am especially has considerable impact. The variance data, diagonal section of covariance matrix, of capture cross section of ²⁴¹Am is shown in Fig.3 with differences between the corresponding values based on JENDL-3.3. The variance data for the capture cross section of ²⁴¹Am are relatively large in the energy region from 100keV to 1MeV because there is less experimental data in this energy domain.

As simply indicated in previous section, neutron cross-sections for MA are needed with improved accuracy for the development of the future nuclear system. Of course, other nuclear data, such as data related to delayed neutron and decay heat, are also important. To give the feedback to the nuclear data from the integral experiments, the sensitivity and uncertainty analysis provide strong tools. For this purpose, estimation of the variance-covariance data should be enhanced.

4. Conclusions

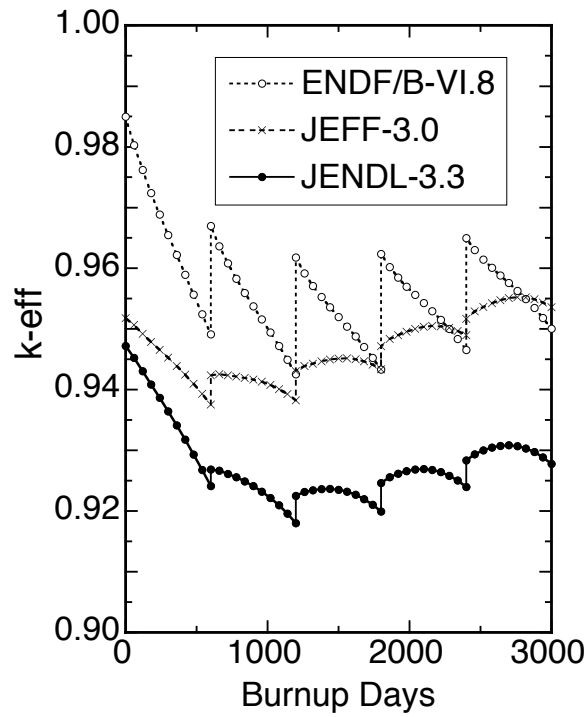
The nuclear data still play an important role in the future nuclear power development. The neutron cross-sections of MA, especially, will become key issues. Current status of MA nuclear data is not so satisfactory. What must be done for the future nuclear data? To improve the nuclear data for MA, significant efforts are needed not only to measure nuclear data but also to evaluate the reliability of existing data by using integral measurements. For this purpose, well-organized framework program with coordinating role will be necessary.

References

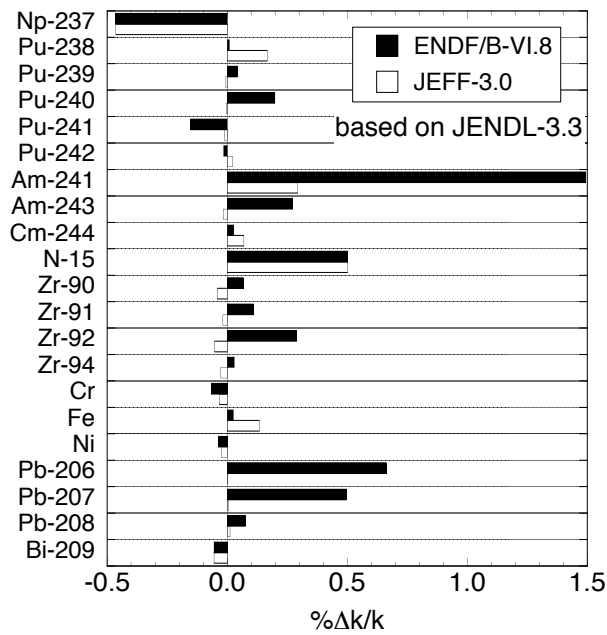
- [1] T. Mukaiyama, "Importance of Double Strata Fuel Cycle for Minor Actinide Transmutation," *Proc.*

OECD/NEA 3rd Information Exchange Meeting. on Actinide and Fission Product Partitioning and Transmutation, Cadarache, France, November 11-13, 1994, p. 30 (1994)

- [2] T. Mukaiyama, T. Takizuka, M. Mizumoto, Y. Ikeda, T. Ogawa, A. Hasegawa, H. Takada, and H. Takano : “Review of research and development of Accelerator-driven System in Japan for transmutation of long-lived nuclides,” *Prog. Nucl. Energy*, ADS special edition, **38**, No. 1-2, p.107, (2001).
- [3] Tsujimoto K., Sasa T., Nishihara K., Takizuka T., and Takano H.,:“Accelerator-Driven System for Transmutation of High-level Waste,” *Prog. Nucl. Energy*, **37**, No. 1-4, p. 339, (2000).
- [4] G. Chiba :“ERRORJ — Covariance Processing Code Version2.2”, JNC TN9520 2004-003 (2004).



(a) Burnup calculation results with different nuclear data libraries



(b) Contribution of each nuclide to the difference of k-eff at initial state

Fig.1 Burnup calculation results with different nuclear data libraries and contribution of each nuclide to the difference of k-eff at initial state. The calculations were performed for ADS proposed by JAEA.

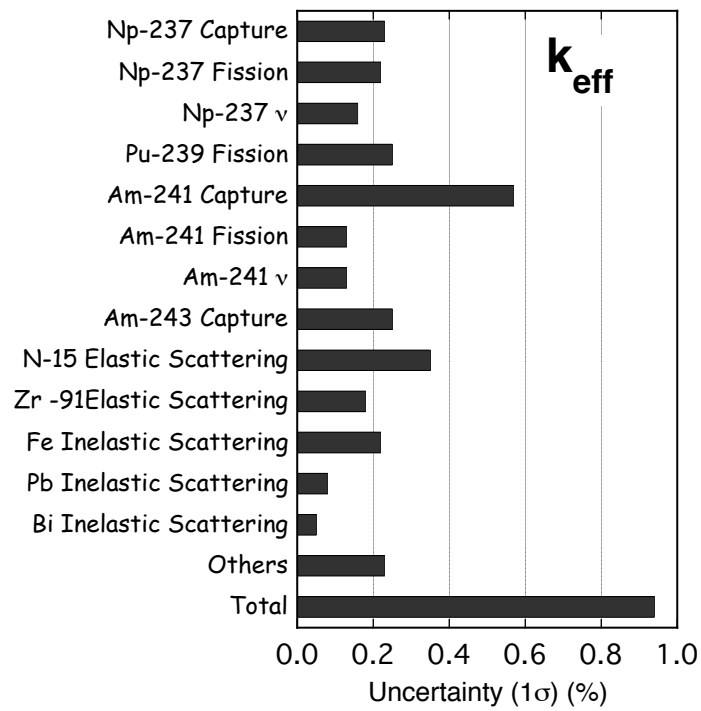


Fig.2 Uncertainty analysis results for k_{eff} at initial state of ADS

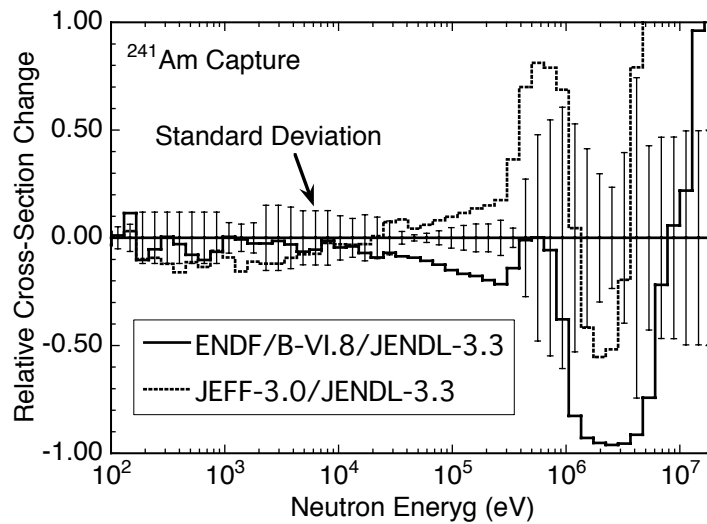


Fig.3 Variance data of capture cross section for ^{241}Am with difference between data in the nuclear data libraries. Variance data is diagonal data of covariance matrix proceeded by ERRORJ code⁴⁾.

2.3.2 Expectation for Nuclear Data Development

A. Zukeran
Nippon Advanced Information Service

2.3.3 Future for Nuclear Data Research — Human Resources —

M. Baba

Cyclotron and Radioisotope Center, Tohoku University

980-8578, Sendai Japan

e-mail: babam@cyric.tohoku.ac.jp

A comment is given on the problem of human resources to support the future nuclear data activity which will be indispensable for advanced utilization of nuclear energy and radiations. Emphasis is put in the importance of the functional organization among the nuclear data center (JAEA), industries and universities for provision of human resources.

1. Introduction

The nuclear data is a fundamental data base for nuclear technology and science. It has played a crucial role in the course of nuclear energy development of fission reactors and fusion reactors, and will be so also in the future because the nuclear power is expected to support the future human activity as the energy source with low load to nature such as a green room effect and chemical pollution. Nowadays, the data requirement is not restricted to nuclear energy but extending over various fields from basic to application areas such as astrophysics, space technology and medical application and so on [1].

Sometimes it is pointed out that the nuclear data reaches to “satisfactory level” both in quantity and quality. It may be partially true so long as the nuclear data for traditional fields is concerned. It should be noticed that, nevertheless, nuclear data requirement is extending to “exotic fields” like minor actinides, high energy region, basic fields and medical fields and so on to develop new concept and/or technology for advanced utilization of nuclear energy and radiations [2,3,4]. The nuclear data will continue to be a “fundamental infrastructure” for the modern society which utilizes nuclear energy and radiation. Recently, in particular, the nuclear data requirement in non-energy fields like radiation application to medicine, space and industries etc seems extending. Therefore, in the future, the field which nuclear data should cover will be much wider than in the past, covering atomic and molecular data and also a macroscopic material like radiation transport.

It is also true that, however, the man power and the funding for nuclear data activity is decreasing as the world wide trend [1]. Therefore, it is necessary to look for the way of effective organization of nuclear data activity and keep the human resources which is the most essential base for the activity.

2. Nuclear Data activity

The characteristic and important point of “nuclear data” is the “completeness of the data” which means the coverage of all the items required e.g., a type of cross sections/physical quantities, energy and nuclides in a consistent manner with accuracy as high as achievable. The accuracy required is very high, e.g., the accuracy required for fission cross section and number of prompt fission neutron of ^{235}U is as high as 1 %

or higher.

Such high performance of nuclear data has been achieved and maintained through well-organized collaboration among experiment/ measurement, evaluation and compilation, and the feed back from benchmark analysis. In Japan, systematic benchmark analyses were undertaken by reactor physicists/ engineers and radiation engineers to assess the accuracy and to pickup problems prior to the release of the file. Owing to the systematic work, JENDL has achieved highest quality-assurance among nuclear data libraries over the world. Therefore, one important point in the nuclear data activity is such collaboration among different fields. Such characteristics will be stronger in the future because of inter-disciplinary nature of the nuclear data.

In addition to such traditional and newly arising nuclear data, as proposed by Niita in the next talk [5], the problem of integral radiation transport should also be covered by the nuclear data because it is strongly correlated with the nuclear data itself. The unification of nuclear data and the particle transport through an appropriate computer code like PHITS [5] will provide various benefits to the user of both items and also a new “market” of the nuclear data.

3. Importance of human resources

To meet such a wide requirement with keeping the activity of nuclear data society, sew up of good human resources is most essential as well as effective organization among scientists or engineer who have motivation on nuclear data. Peoples who are expected to support nuclear data activity may be divided into three types: 1) experimenters who produce experimental data, 2) evaluators who produce evaluated data, and 3) bench-marker doing quality assurance of the evaluated data. As mentioned in sect. 2, evaluators are highly desired to cover the modeling and/or the development of computer codes treating radiation transport including new transport analysis schemes. To support such highly inter-disciplinary jobs, well-organized collaboration of peoples in different fields are required as well as supply of new human resources.

From the above mentioned view points, I would like to point out two recommendations;

One is the promotion of collaboration with peoples in nuclear physics, particle physics, mathematics and other related fields to promote the production of “exotic nuclear data” taking account of new models and theories developed in the physics fields. For the reason, establishment of an appropriate scheme is highly required to promote the collaboration in particular with young people. A good example of such collaboration can be seen in EU and USA; young peoples graduated from physics departments look to be working very actively in the nuclear data fields having challenging subjects [6]. This is also true for the experimental area for production of new nuclear data because experiments required for “exotic” data should be more complicated and comprehensive than in traditional nuclear data experiments. In such experiments, sophisticated detector and data acquisition systems which have been developed and employed in the physics filed will open a new possibility of nuclear data. Examples are seen in the n-TOF project in CERN [7] and Nuclear Data Project in Japan lead by Dr. Igashira [8] which enable new high sensitive and functional radiation detectors providing very detailed and redundant out put data.

The second one is to provide young people with opportunities to do nuclear data work like internship. Nuclear data research will be attractive for young peoples owing to its deep underlying contents on

nuclear/particle physics, nuclear engineering, data engineering, mathematics and computer technology and so on. The presently-carried out tutorial course on nuclear data and the seminar like one on PHITS seem very effective as well as the nuclear data symposium to encourage the young people and provide the chance to touch such a fascinating subject. They are expected to continue and even extended. Universities in the nuclear engineering field will be expected to encourage students to learn such subjects and nurture specialists with strong motivation on nuclear engineering. The problem is a very limited number of jobs after graduation, but such basic knowledge will be useful in any fields around nuclear engineering.

The nuclear data center JAEA and/or the Sigma Committee is expected to act as an organizer of collaboration with other fields including physics society and young people.

References:

1. T. Yoshida: JAERI-Conf 2004-005 p.111
2. T. Nakagawa; *ibid.*, p.9
3. M Baba; JAER-Conf. 2005-003, p.126
4. Y. Watanabe; *ibid.*, p.50
5. K. Niita, report in this symposium
6. M. Igashira, *ibid.*, p.118
7. Proc. Int. Conf., on Nuclear Data 2004, Santa Fe (American Institute of Physics, 2004)
8. M. Igashira, *ibid.*, p.601

2.3.4 A Proposal for New Treatment of Radiation Behavior with Combination of Nuclear Data and Reaction Model.

K. Niita

*Research Organization for Information Science & Technology,
Tokai, Naka, Ibaraki, 319-1106, Japan*

The nuclear data are extensively used in the Monte Carlo transport calculations to analyze the radiation behavior in various fields such as accelerator facilities, spacecrafts, and radiotherapy. Most of the Monte Carlo transport calculations are based on Boltzmann equation for one-body phase space distribution of the transport particles. By such transport calculations, particularly with the nuclear data, one could obtain only the mean value of the one-body observables in the phase space, e.g. heat, flux, and so on. We cannot calculate the fluctuations around the mean value, since the Boltzmann equation has no information for the two-body and higher order correlations which determine the fluctuation around the mean value.

Recently, however, the higher order quantities, i.e. the fluctuations around the mean values of the one-body observables are often required in a certain field. A typical example for such a correlated quantity is the deposit energy distribution in a cell, which is necessary for the estimation of the response function of the detector or a single event upset probability of a semiconductor memory cell. The solution of the Boltzmann equation cannot describe the distribution but only the mean value. Furthermore, Monte Carlo calculations by using the nuclear data cannot deal with these quantities, since the nuclear data includes only the inclusive one-body cross sections but no information of the correlations.

We have therefore developed a new treatment of radiation behavior in the transport calculations by combining the nuclear data with the reaction models so as to trace all higher correlations. We would like to discuss a possibility of this new treatment in the nuclear data field.

2.4 Status and Performance of Latest Evaluated Nuclear Data Files

2.4.1 Comparison of Major Nuclear Data Libraries

– JENDL-3.3, ENDF/B-VI.8, ENDF/B-VII β 1.2 and JEFF-3.1 –

Keiichi SHIBATA

Nuclear Data Center, Japan Atomic Energy Agency

Tokai-mura, Naka-gun, Ibraki-ken 319-1195, Japan

Compared are neutron-induced reaction data contained in major general-purpose libraries: major actinides, minor actinides, long-lived fission products, and structural materials in JENDL-3.3, ENDF/B-VI.8, ENDF/B-VII β 1.2, and JEFF-3.1. It is found from the comparison that there still exist large discrepancies among the cross sections in different libraries.

1. Introduction

Evaluations for JENDL-4 are in progress in order to improve fission product and minor actinide data in JENDL-3.3 [1]. In Europe, the OECD/NEA Data Bank released JEFF-3.1 [2] in 2005. Moreover, the National Nuclear Data Center in BNL, which released ENDF/B-VI.8 [3] in 2001, is now preparing for the release of ENDF/B-VII whose β version [4] is available on Web. It is worthwhile to compare the data in the existing major libraries including the β version ENDF/B-VII β 1.2 to clarify their differences. Comparisons were made for major actinides ($^{233, 235, 238}\text{U}$, $^{239, 240, 241}\text{Pu}$, ^{232}Th), minor actinides (^{237}Np , $^{241, 242g, 242m, 243}\text{Am}$, $^{242, 244, 245}\text{Cm}$), long-lived fission products (^{79}Se , ^{93}Zr , ^{99}Tc , ^{107}Pd , ^{126}Sn , ^{129}I , ^{135}Cs), and structural materials (Cr, Fe, Ni). The following sections describe the results of the comparisons.

2. Major Actinides

The same resolved resonance parameters of ^{235}U [5] were used for all libraries below 2.25 keV, which gives the same thermal behavior of the total, elastic scattering, fission and capture cross sections. In the energy region above 2.25 keV, the difference in the fission cross section of ^{235}U is small, i.e., several %, while the capture cross sections of JENDL-3.3 are about 10% larger than the other libraries in the region from 30 keV to 1 MeV as seen in Fig. 1. At thermal energy, there is little difference (0.02%) in the average number of prompt neutrons emitted in the $^{235}\text{U}(n,f)$ reaction, although several-percent difference can be seen in

the case of delayed neutrons. As for ^{238}U , JEFF-3.1 and ENDF/B-VII β 1.2 adopted the new resolved resonance parameters [6] evaluated in ORNL, which yield somewhat smaller thermal capture cross sections and capture resonance integrals than those of JENDL-3.3 and ENDF/B-VI.8, as seen in Table 1. It is found from Fig. 2 that the $^{238}\text{U}(n,n')$ cross section of ENDF/B-VII β 1.2 is close to that of JENDL-3.3 below 6 MeV. The ^{233}U data were completely revised for ENDF/B-VII β 1.2, whereas JEFF-3.1 adopted the ^{233}U data in JENDL-3.3.

The same resolved resonance parameters of ^{239}Pu [7] were adopted for all libraries below 2.5 keV, although background fission cross sections are contained in ENDF around 2 keV. It should be noted that all libraries but JENDL-3.3 adopted the evaluation of Fort et al. [8] for the average number of prompt neutrons emitted in the $^{239}\text{Pu}(n,f)$ reaction, which exhibits fluctuations in the region from 10 to 700 keV. Concerning ^{240}Pu , there is a question why ENDF/B-VII β 1.2 did not adopt the latest resolved resonance parameters evaluated by Bouland *et al.* [9]. Resolved resonance parameters of ^{241}Pu were revised for JEFF-3.1 and ENDF/B-VII β 1.2 below 20 eV.

As for the fission cross section of ^{232}Th , there is several-percent difference among libraries above 1 MeV.

3. Minor Actinides

Differences can be seen in the fission cross section of ^{237}Np below the sub-threshold between JENDL-3.3, JEFF-3.1 and the two ENDF libraries. Even at thermal energy, there is about 10% difference in the capture cross section of ^{237}Np .

The fission cross section of ^{241}Am in JEFF-3.1 deviates from those of the other libraries considerably below 1 eV. Figure 3 shows the isomeric ratio of the $^{241}\text{Am}(n,\gamma)$ reactions and it indicates that each evaluator has different views of measurements and nuclear model calculations. The $^{242g, 242m, 243}\text{Am}$ data of JEFF-3.1 were taken from JENDL-3.3, while the $^{242g, 242m}\text{Am}$ data of ENDF/B-VII β 1.2 were partly taken from JENDL-3.3.

Figure 4 shows the fission cross section of ^{242}Cm . In the energy region from 10 keV to 1 MeV, available measurements, which are not shown in the figure, support JENDL-3.3 and JEFF-3.1. The $^{244, 245}\text{Cm}$ data of JENDL-3.3 were adopted by ENDF/B-VII β 1.2, while the ^{245}Cm data of JEFF-3.1 were taken from JENDL-3.3.

4. Long-lived Fission Products

Only the capture cross sections of long-lived fission products (LLFPs) were examined in the present work.

As for ^{79}Se , ENDF/B-VI.8, ENDF/B-VII β 1.2 and JEFF-3.1 adopted JENDL-3.3 data. There exist no experimental data on ^{79}Se . No resolved resonance parameters are compiled in

the libraries. It is strongly recommended that measurements should be performed for this nucleus.

The ^{93}Zr data of ENDF/B-VI.8 contains no resolved resonance parameters, while there is only one resonance level in those of JEFF-3.1. The thermal capture cross section of ^{93}Zr in ENDF/B-VII β 1.2 is 70% smaller than that of JENDL-3.3, as seen in Fig. 5.

The difference in the capture cross section of ^{99}Tc among the libraries is smaller than that of ^{93}Zr . However, 10-20 % differences can be seen depending on energy region.

As for the capture cross section of ^{107}Pd , a large difference can be seen between JENDL-3.3 and JEFF-3.1 in the resonance region from 10 eV to 1 keV.

There are no experimental data on ^{126}Sn . The data of ENDF/B-VII β 1.2 were taken from JENDL-3.3, while those of JEFF-3.1 were taken from ENDF/B-VI.8. Measurements are also required for ^{126}Sn to produce reliable evaluated data.

Recently, Noguere *et al.* [10] evaluated the resolved resonance parameters of ^{129}I , and their parameters were adopted by JEFF-3.1. As shown in Fig. 6, there is a marked difference in the low energy tail of the lowest resonance of the $^{129}\text{I}(n,\gamma)$ cross section between JEFF-3.1 and JENDL-3.1. Preliminary data of the cross section measured by Kobayashi [11], which are not shown in the figure, seem to support the JEFF-3.1 data.

As for the capture cross section of ^{135}Cs , the resonant cross sections are discrepant among the libraries.

5. Structural Materials

Only the total cross sections of elemental Cr, Fe and Ni were examined in the present work. Maximum 20% differences are seen between JENDL-3.3 and ENDF-VII β 1.2 in Fig. 7, although the difference is about 2-3 % in the case of Fe and Ni. It is recommended to re-examine the resonance parameters of Cr isotopes for the JENDL-4 evaluation.

6. Conclusions

Major actinide, minor actinide, long-lived fission product and structural material data were compared among the existing major nuclear data libraries JENDL-3.3, ENDF/B-VI.8, ENDF/B-VII β 1.2 and JEFF-3.1. Even for major actinides, there still remain differences among the libraries. New measurements are required to resolve the differences. Moreover, re-analyses of old measurements are also encouraged with the aid of advanced theoretical techniques.

References

- [1] K. Shibata *et al.*: "Japanese Evaluated Nuclear Data Library Version 3 Revision-3: JENDL-3.3," *J. Nucl. Sci. Technol.*, **39**, 1125 (2002).

- [2] OECD/NEA Data Bank: <http://www.nea.fr/html/databank/>
- [3] H.D. Lemmel *et al.*: “ENDF/B-VI Release 8 (Last release for ENDF/B-VI) The U.S. Evaluated Nuclear Data Library for Neutron Reaction Data,” IAEA-NDS-100 (2001).
- [4] Cross Section Evaluation Working Group (CSEWG): http://www.nndc.bnl.gov/csewg_members/index_html, National Nuclear Data Center, BNL.
- [5] L.C. Leal *et al.*: “R-Matrix Analysis of ^{235}U Neutron Transmission and Cross-Section Measurements in the 0- to 2.25-keV Energy Range,” *Nucl. Sci. Eng.*, **131**, 230 (1999).
- [6] H. Derrien *et al.*: “Neutron Resonance Parameters of ^{238}U and the Calculated Cross Sections from the Reich-Moore Analysis of Experimental Data in the Neutron Energy Range from 0 keV to 20 keV,” ORNL/TM-2005 (2005).
- [7] H. Derrien: “R-Matrix Analysis of ^{239}Pu Neutron Transmissions and Fission Cross Sections in Energy Range from 1.0 keV to 2.5 keV,” *J. Nucl. Sci. Technol.*, **30**, 845 (1993).
- [8] E. Fort *et al.*: “Evaluation of ν_p for ^{239}Pu : Impact for Application of the Fluctuations at Low Energy,” *Nucl. Sci. Eng.*, **99**, 375 (1988).
- [9] O. Bouland *et al.*: “R-Matrix Analysis of the ^{240}Pu Neutron Cross Sections in the Thermal to 5700-eV Energy Range,” *Nucl. Sci. Eng.*, **127**, 105 (1997).
- [10] G. Noguere *et al.*: “Reich-Moore Analysis of the ^{127}I and ^{129}I Resolved Resonance Range,” Proc. Int. Conf. Nuclear Data for Science and Technology, Santa Fe 2004, p.1462 (2005).
- [11] K. Kobayashi: private communication (2002).
- [12] S.F. Mughabghab: “Thermal Neutron Capture Cross Sections, Resonance Integrals and g-Factors,” INDC(NDS)-440 (2003).

Table 1 Thermal capture cross sections (σ_c) and capture resonance integrals (I_c) of ^{238}U at 300 K

Library	σ_c (b)	I_c (b)*
JENDL-3.3	2.718	278.1
ENDF/B-VI.8	2.718	278.1
ENDF/B-VII β 1.2	2.684	275.3
JEFF-3.1	2.684	275.3
Mughabghab 2003 [12]	2.608 \pm 0.019	277 \pm 3

* Integration was performed from 0.5 eV to 20 MeV.

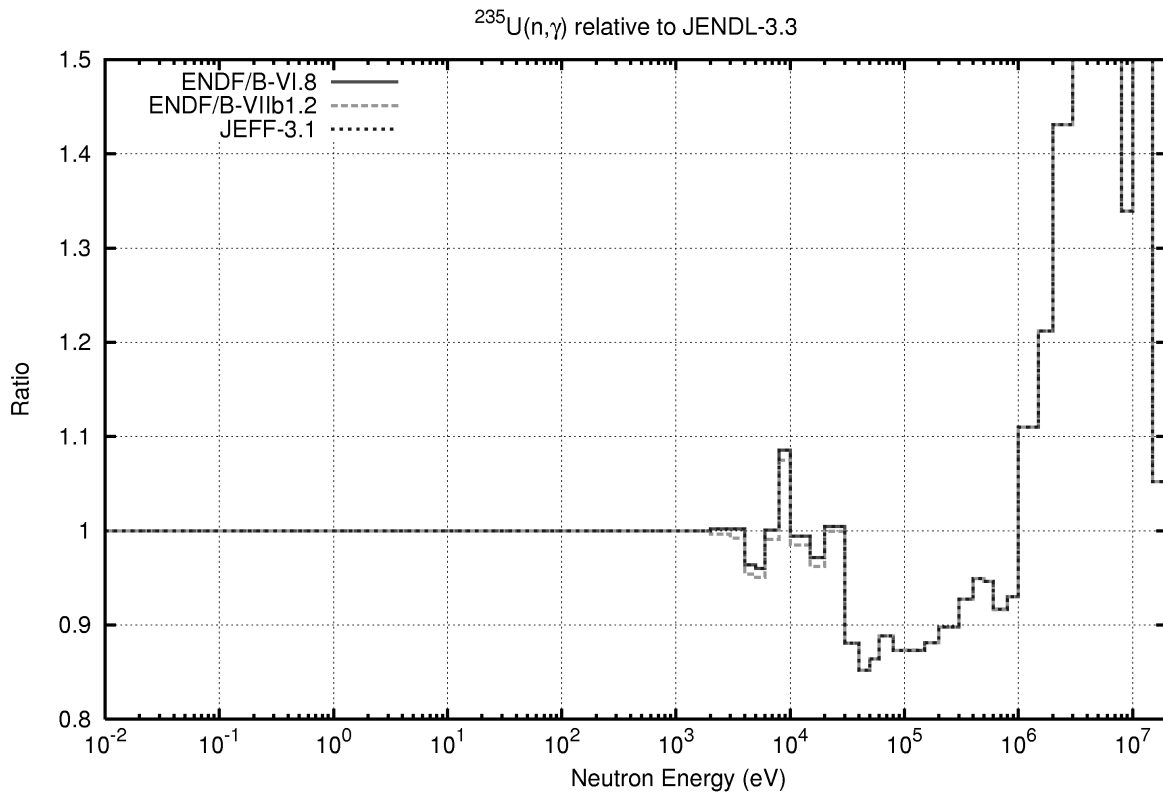


Fig. 1 Capture cross sections of ^{235}U relative to JENDL-3.3

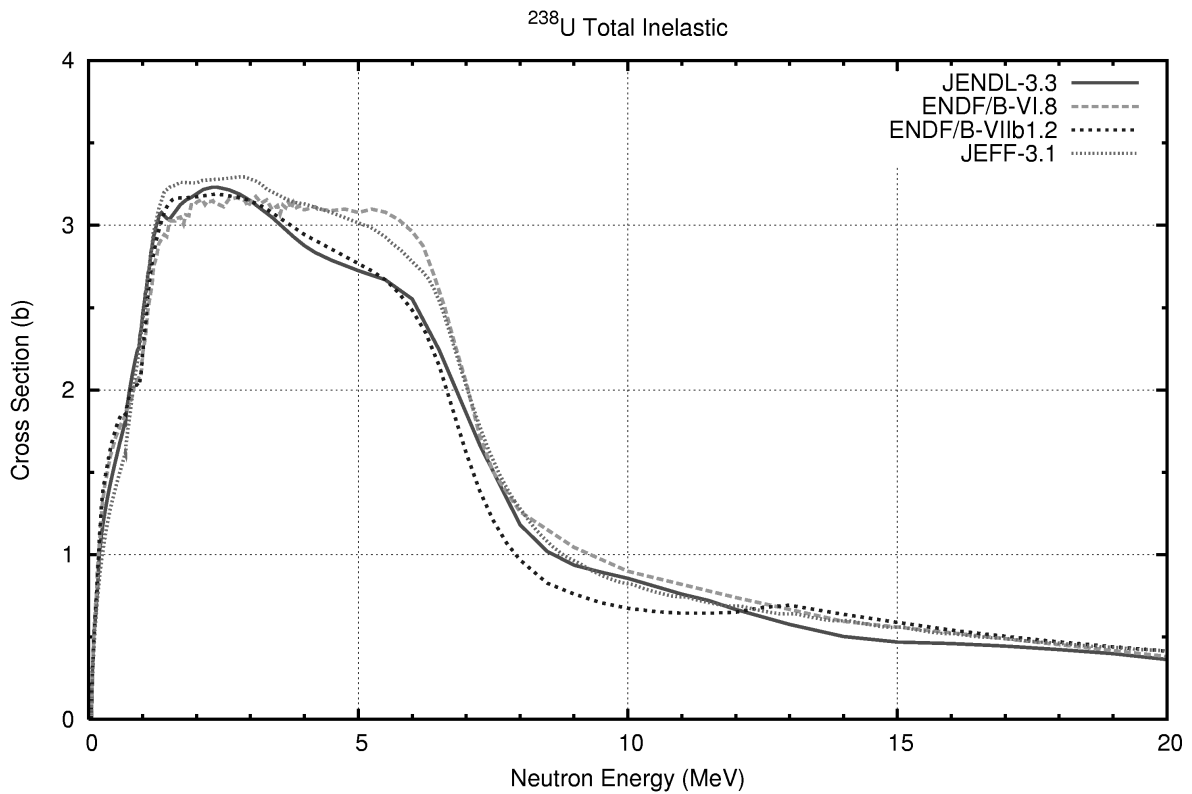


Fig. 2 Inelastic scattering cross sections of ^{238}U

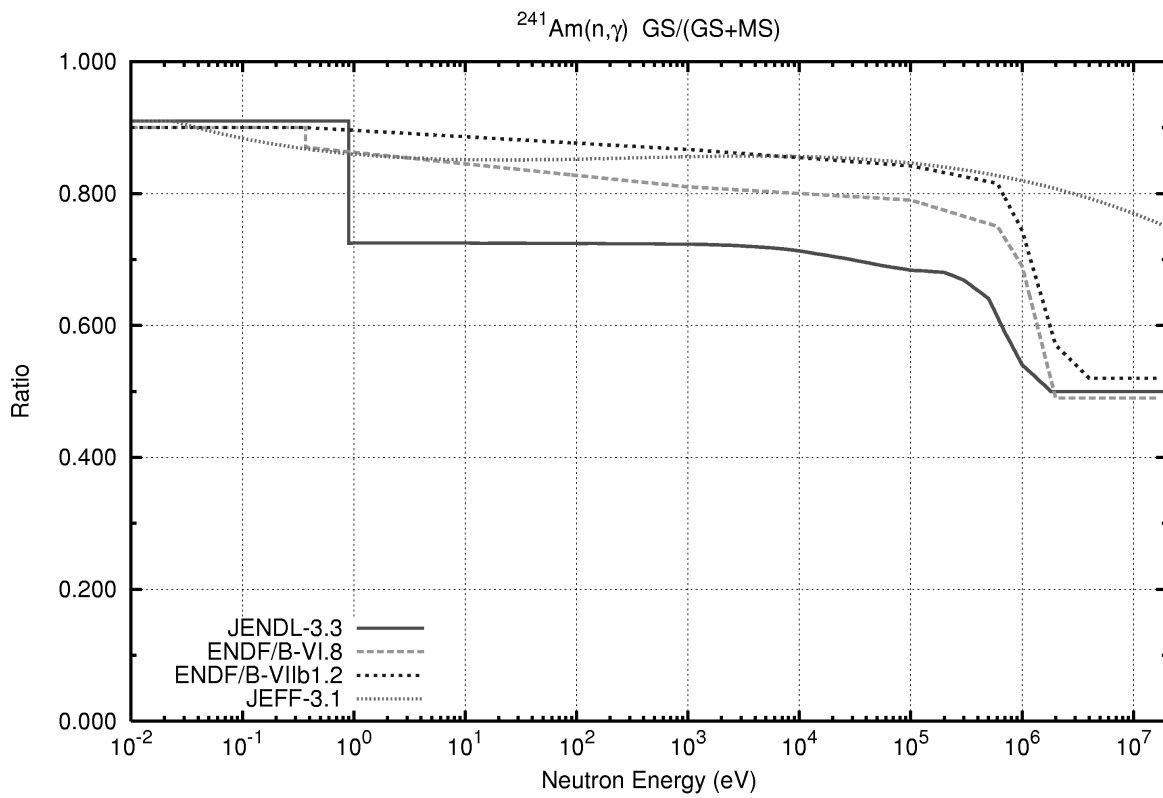


Fig. 3 Isomeric ratio of the $^{241}\text{Am}(n,\gamma)$ cross section

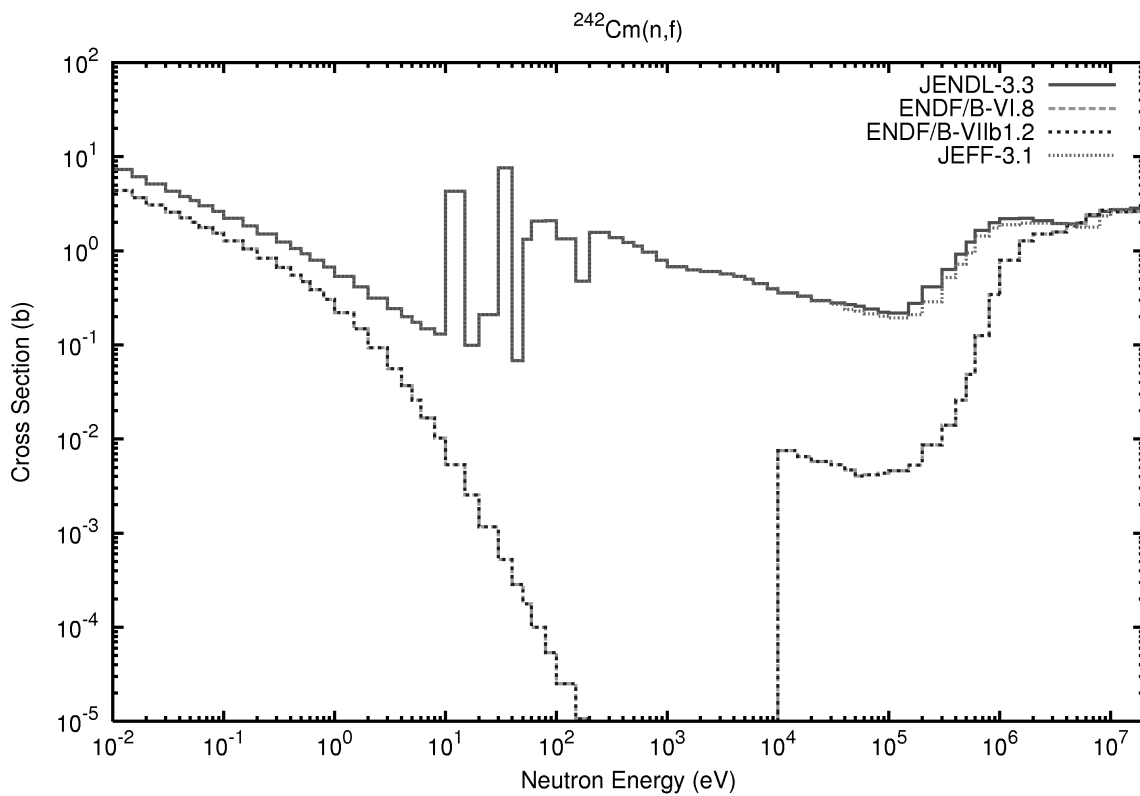


Fig. 4 Fission cross sections of ^{242}Cm

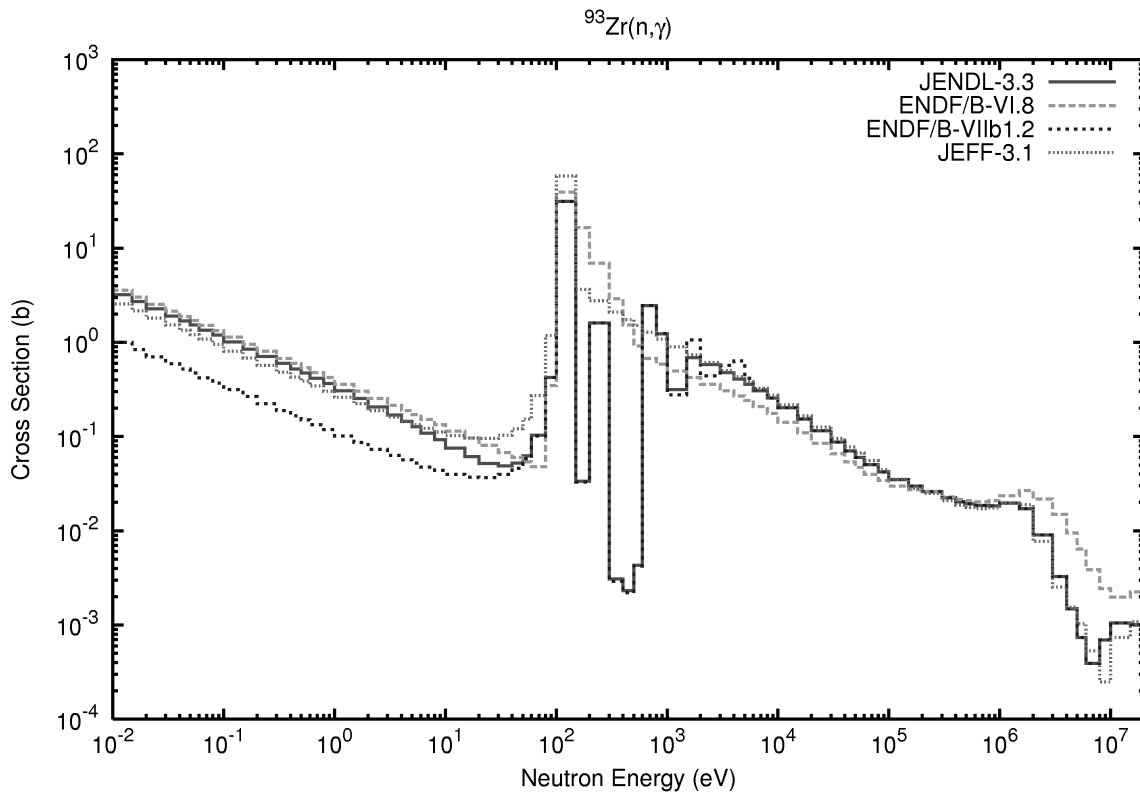


Fig. 5 Capture cross sections of ^{93}Zr

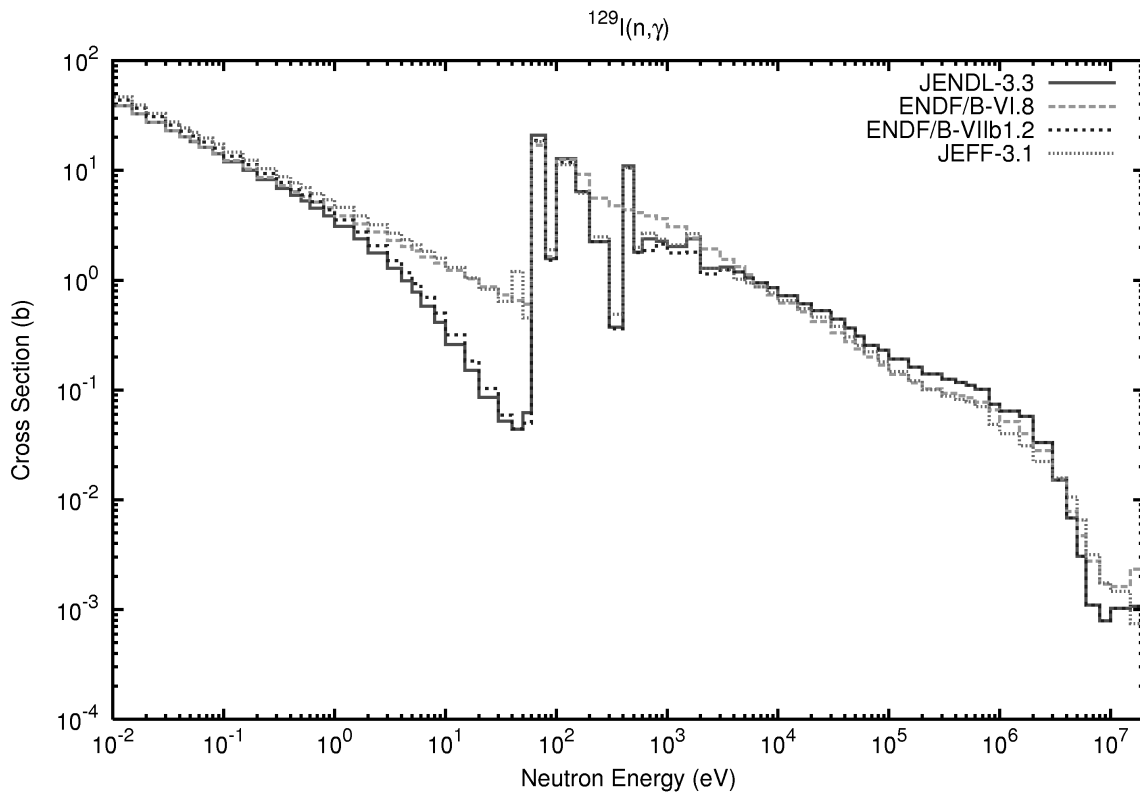


Fig. 6 Capture cross sections of ^{129}I

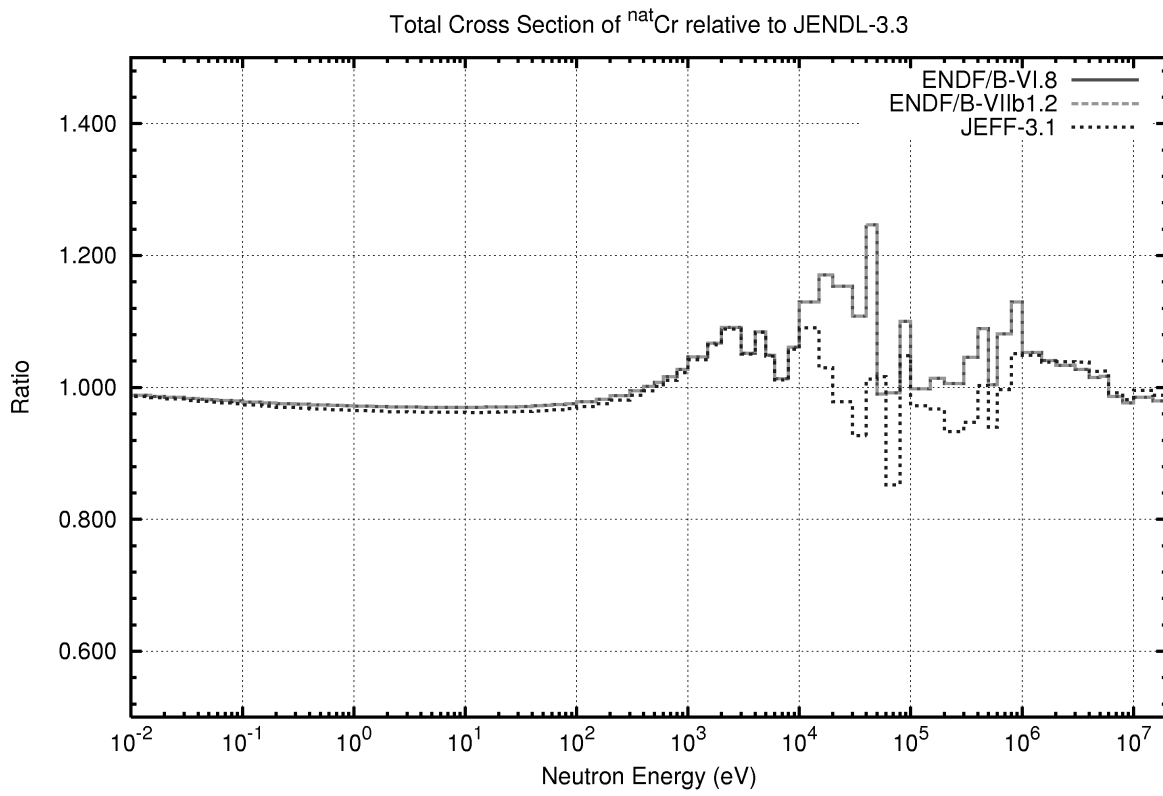


Fig. 7 Total cross sections of elemental Cr relative to JENDL-3.3

2.4.2 Integral Comparison of Library Performance

Takamasa MORI

Japan Atomic Energy Agency
Tokai-mura, Naka-gun, Ibaraki-ken 319-1195
e-mail: mori.takamasa@jaea.go.jp

The 2003-2004 activities of Reactor Integral Test WG under Subcommittee on Reactor Constants of Japanese Nuclear Data Committee are presented. During this period, the WG carried out integral tests of JENDL-3.3, ENDF/B-VI and JEF 2.2 (JEFF-3.0) for reactor applications. Some results of integral tests for other latest libraries, JEFF-3.1 and ENDF/B-VII are also presented.

1. Introduction

The latest version of Japanese Evaluated Nuclear Data Library (JENDL-3.3) [1] was released in May, 2002. After the release of JENDL-3.3, the activities of Reactor Integral Test Working Group under Subcommittee on Reactor Constants of Japanese Nuclear Data Committee have been concentrated on the benchmark testing of JENDL-3.3 and other recent libraries to improve JENDL-3.3 for the next version, JENDL-4. This paper summarizes the 2003-2004 activities of the WG*. During this period, the WG discussed on the following topics:

- Benchmark analysis for thermal systems
- Analysis of LWR MOX physics experiments MISTRAL/BASALA
- Sensitivity analysis for thermal systems
-Dependence of criticality prediction accuracy on U-235 enrichment-
- Integral test for fast reactors at JNC with BFS, MOZART, SEFOR experiments
- PIE and burn-up calculation for MA irradiated at PFR
- Applicability of JENDL-3.3 to MOX critical experiments
- FUBILA project for full-MOX BWR and its preliminary analysis
- FCA Benchmark for JENDL-3.3 and ENDF/B-VII Preliminary
- Benchmark system for JENDL-4

Among these topics, the following 4 topics are briefly reported in this paper.

1. Integral test of JENDL-3.3 in U-fueled thermal reactors by K. Okumura (JAEA),
2. Integral test for FCA cores by S. Okajima (JAEA),
3. Integral test of latest libraries by K. Okumura (JAEA), and
4. Action plans now underway by Reactor Integral Test WG chaired by M. Ishikawa

* Members of Reactor Integral Test WG(2003-2004): T.Iwasaki (Tohoku Univ.), H. Unesaki (Kyoto Univ.), T. Kitada, T. Takeda (Osaka Univ.), K. Ikeda, Y. Tahara (MHI), M. Yamamoto (GNF-J), T. Sanda (JAPC), K. Ishii, A. Zukeran (Hitachi), H. Akie, M. Ishikawa, H. Oigawa, S. Okajima, K. Okumura, H. Takano, Y. Nakano, T. Hazama, A. Hasegawa, Y. Miyoshi, T. Mori (JAEA)

2. Integral Test of JENDL-3.3 in U-fueled Thermal Reactors by K. Okumura

Extended benchmark tests were carried out by K. Okumura for light water moderated uranium fueled systems, aiming at investigating dependence of criticality evaluation accuracy on U-235 enrichment. The benchmark cores selected are shown in Table 1. All the benchmark calculations were performed by using a continuous-energy Monte Carlo code MVP [2] and its four different nuclear data libraries generated from JENDL-3.2 [3], JENDL-3.3, JEF-2.2 [4] and ENDF/B-VI (R8) [5].

The results are summarized in Figs.1-4. The dependence of C/E values on U-235 enrichment is apparently seen in Fig.2 (JENDL-3.3) and Fig.3 (all nuclear data). The C/E values for all nuclear data increase with the enrichment. However, the U-235 enrichments for C/E value ~1.0 vary from 2.5% to 10%, depending on the libraries as shown in Fig.4. No apparent dependence of prediction accuracy is observed for other parameters such as H/U ratio and leakage. In order to solve the systematic dependence on U-235 enrichment, 4 factors of k_{∞} were evaluated for the benchmark cores with MVP and JENDL-3.3. Only the η -value showed a similar dependence on the U-235 enrichment, as shown in Fig.5. It was concluded from this fact and some consideration that 3% decrease of $\sigma_{\gamma}^{238} / \sigma_a^{235}$ solves the dependence of prediction accuracy on u-235 enrichment.

Table 1 List of benchmark cores for integral test of JENDL-3.3 in U-fueled thermal reactors

No	Core	U-235/U	H/U	Remarks
1	TRX-1	1.3	3.3	Metal-U, Hexagonal lattice, Al clad. (11.506mm ϕ)
2	TRX-2	1.3	5.6	Metal-U, Hexagonal lattice, Al clad. (11.506mm ϕ)
3	KRITZ2:1	1.89	3.4	Zry-2 clad (12.25mm ϕ), Boron:218ppm
4	KRITZ2:13	1.89	5.0	Zry-2 clad (12.25mm ϕ), Boron:452ppm
5	B&W-XI*	2.46	5.4	Al-6061 clad (12.06mm ϕ), Boron:1511ppm
6-8	TCA-1.50U*	2.6	4.3	3 cases of different loading patterns, Al clad (14.17mm ϕ)
9-13	TCA-1.83U*	2.6	5.3	5 cases of different loading patterns, Al clad (14.17mm ϕ)
14-18	TCA-2.48U*	2.6	7.2	5 cases of different loading patterns, Al clad (14.17mm ϕ)
19-23	TCA-3.00U*	2.6	8.6	5 cases of different loading patterns, Al clad (14.17mm ϕ)
24	DIMPLE3*	3.0	3.0	SS clad (10.937mm ϕ)
25	MISTRAL-C1	3.7	5.1	By NUPEC, Zry-4 clad (9.5mm ϕ), Boron:300ppm
26	DIMPLE7*	7.0	8.4	SS clad (8.324mm ϕ)
27-33	STACY* 001-007	10.0	72~ 103	Nitrate solution in water reflected 600mm ϕ cylindrical tank, 7 cases of different U concentrations: 310.1~225.3 gU/liter,
34	TRACY	10.0	7.2	Nitrate solution, 430g/liter, critical level:45.3cm with CR
35	JRR4-U20	20.0	-	U ₃ Si ₂ -Al dispersed fuel, minimum critical core (12 elements)
36	JRR4-U93	93.0	-	U-Al alloy, minimum critical core (12 elements)
37	KUCA-B(1:1)	5.4	9.56	EU:NU=1:1, B3/8”P33EU-NU-NU-EU(5)
38	KUCA-B(1:1)	9.6	13.4	EU:NU=2:1, B3/8”P36EU-NU-NU-EU(3)
39	KUCA-B(1:1)	93.0	9.3	EU:NU=1:0, B1/8”P80EU(2)

*Experimental data and benchmark models are taken from the ICSBEP Handbook[6]

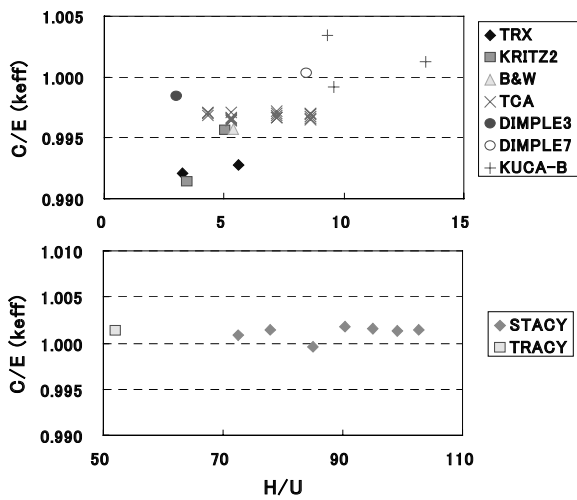


Fig.1 Prediction accuracy of keff vs. H/U ratio (JENDL-3.3)

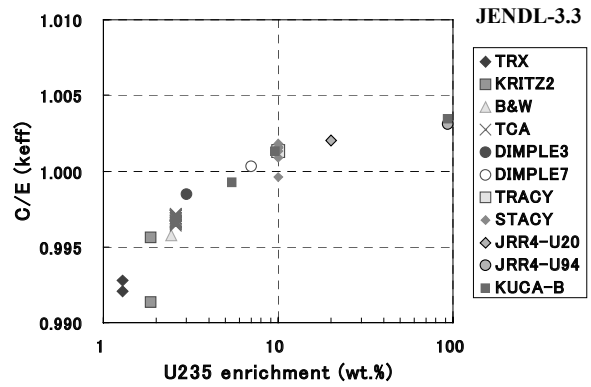


Fig.2 Prediction accuracy of keff vs. U-235 enrichment (JENDL-3.3)

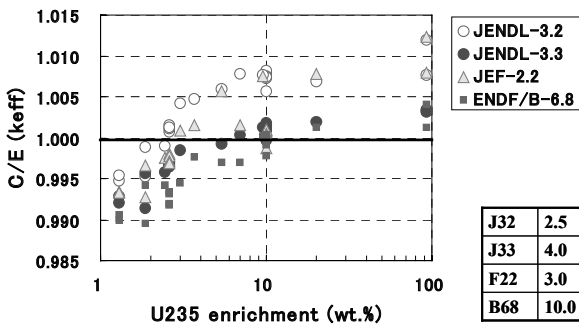


Fig.3 Comparison of 4 libraries (keff vs. U-235 enrichment)

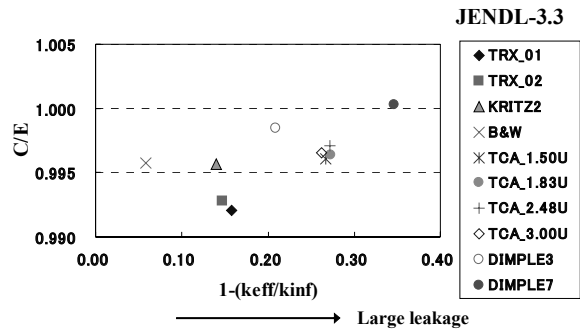


Fig.4 Prediction accuracy of keff vs. leakage (JENDL-3.3)

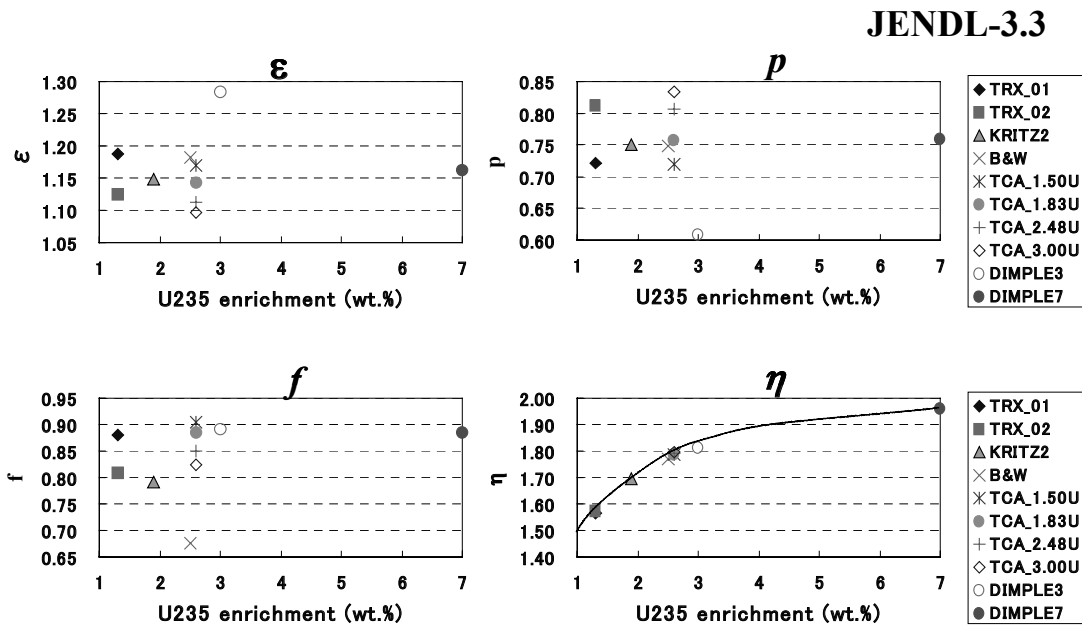


Fig.5 4 factors of k_{∞} evaluated with MVP and JENDL-3.3

3. Integral Test for FCA Cores by S. Okajima

Eight different FCA cores were selected from a viewpoint of benchmark test for the main revision in JENDL-3.3: the IX-1 to IX-6, X-1 and X-2 cores. These cores were simple in geometry. Each core was composed of a core region and axial and radial blanket regions. The characteristics of these cores were summarized in Table 2.

The IX series cores were constructed for the integral test of actinide nuclides cross sections. Figure 6 shows the calculated neutron spectra at the core center. The spectrum is soft in the IX-1 core and becomes harder for a core of later number.

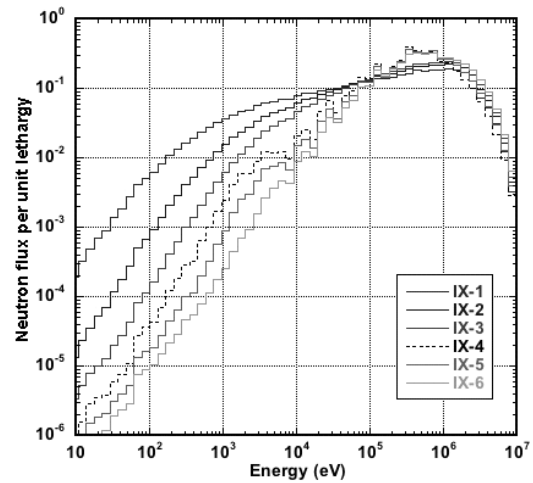


Fig.6 Neutron spectra in FCA IX cores

The X-1 and X-2 cores were constructed for the mockup experiment of the Fast Experimental Reactor “JOYO” Mark II Core. The X-1 core had a cylindrical core surrounded by a depleted uranium blanket, while the X-2 core consisted of the core and reflector regions comprised of sodium and stainless steel. Both cores had a similar geometry and fuel configuration in core cells.

Table 2 Characteristics of the FCA cores for a benchmark test

Core name		IX-1	IX-2	IX-3	IX-4	IX-5	IX-6	X-1	X-2	
Geometry	Core (cm)	Radius	30.4	23.1	17.9	27.6	20.4	22.9	28.6	28.0
		Height	61.0	40.6	35.6	50.8	40.6	40.6	50.8	50.8
dimension	Blanket thickness	Radial	31.2	35.1	39.6	32.5	37.1	36.0	33.1	33.8*
		Axial	35.6	35.6	35.6	35.6	35.6	35.6	30.5	35.6*
Fuel material (Enrichment)		EU (93%)	EU (93%)	EU (93%)	EU (93%)	EU (93%)	EU (93%)	Pu+EU (35%)	Pu+EU (35%)	
Principal diluent material		C	C	C	SUS [†]	SUS [†]	SUS [†]	Na	Na	
Volume fraction of fuel		0.06	0.13	0.19	0.13	0.19	0.19	0.5	0.5	

* : Reflector thickness, † : Stainless steel

Figure 7 compares calculated results (C/E values for criticality) between JENDL-3.3 and JENDL-3.2. No large discrepancy is seen between both the libraries, except for IX-1 to -3 cores. For IX-1 to -3 cores, neutron spectrum dependence is observed in the results with JENDL-3.3, while no spectrum dependence is seen in JENDL-3.2. This tendency is caused by the revised capture cross section of U-235.

In Fig.8, calculated results are compared between ENDF/B-VI.8 and JEFF-3.0, together with JENDL-3.3. Both libraries give a similar tendency of C/E values. The ENDF/B-VI.8 gives C/E values of 0.999 ~ 1.017, while the JEFF-3.0 results are 0.996 ~ 1.010. In the IX-1 to -3 cores, similar spectral dependence is found among the three libraries including JENDL-3.3. On the other hand, spectral dependence in the IX-4 to -6 cores, which is found in the JENDL-3.3 results, is not observed in the

ENDF/B-VI.8 and JEFF-3.0 results.

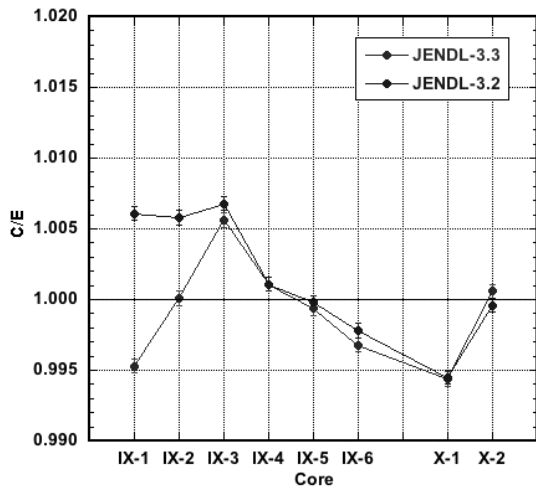


Fig.7 Comparison between JENDL-3.3 and JENDL-3.2

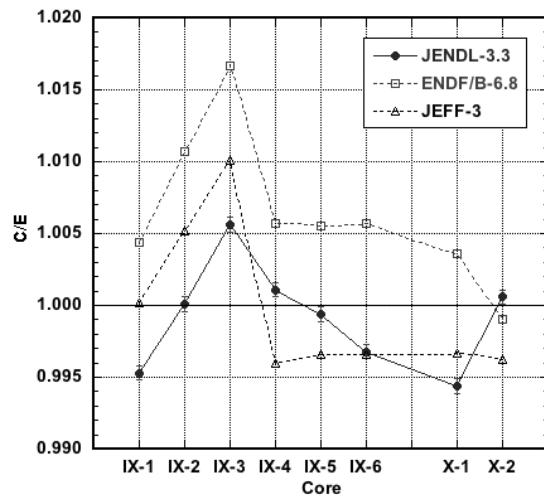


Fig.8 Comparison between ENDF/B-VI.8, JEFF-3.0 and JENDL-3.3 and JENDL-3.2

4. Integral Test of Latest Libraries by K. Okumura

Benchmark test of latest libraries JEFF-3.1[7] and ENDF/B-VIIβ1.2[8] were carried out by K. Okumura with the MVP code for typical thermal and fast cores with U or Pu fuel. The results are shown in Fig.9, together with those of JENDL-3.3 and ENDF/B-VI.8. As for the thermal systems with U fuels, both the latest libraries improve the U-235 enrichment dependence of prediction accuracy. However, the underestimate in lower enrichment remains.

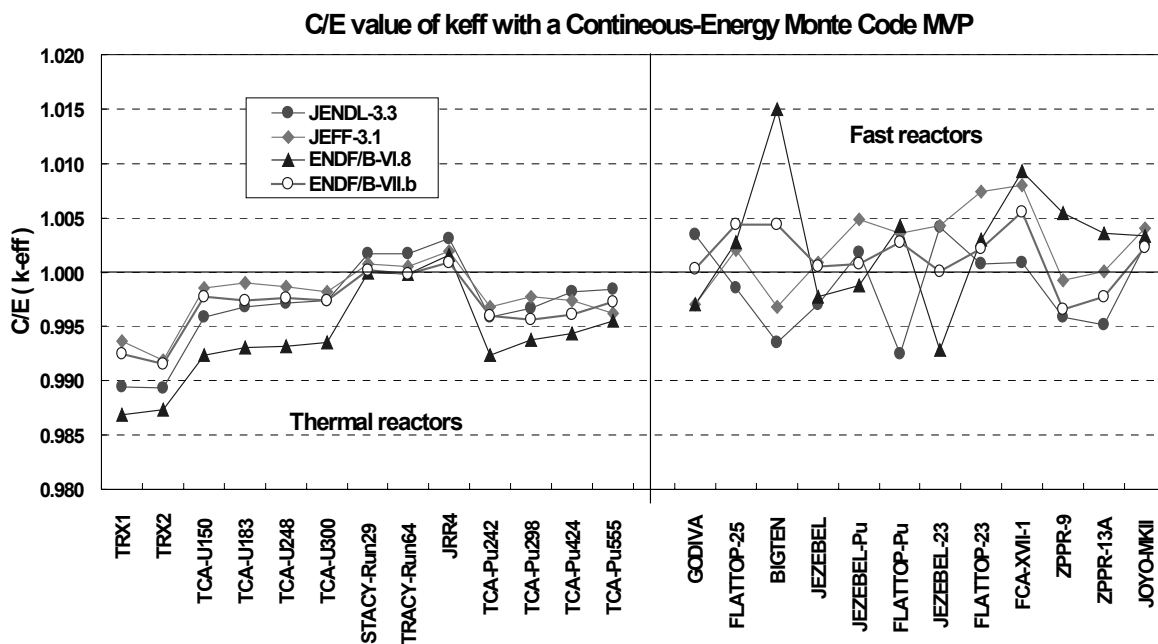


Fig.9 C/E values of k_{eff} with the latest libraries, JEFF-3.1, ENDF/B-VIIβ1.2, together with those with JENDL-3.3 and ENDF/B-VI.8

5. Action Plans Now Underway by Reactor Integral Test WG Chaired by M. Ishikawa

The Reactor Integral Test WG has been chaired by M. Ishikawa since FY2005. It is carrying out extended benchmark tests for JEFF-3.1, ENDF/B-VII, JENDL-3.3. etc. to clarify problems in current nuclear data and to give recommendation to the evaluation work for JENDL-4. For this purpose, the following benchmark cores are selected:

- FUBILA and REBUS experiments with JEFF-3.1
- NCA
- Small fast cores: FCA-IX-1, -2, -3, -4, -5, -6, -7, FCA-X-1, -2
- Benchmark cores with metal or oxide fuel: FCA-XVI-1, -2, FCA-XVII-1
- Large Na-MOX cores: ZPPR-9 ~ -19B (19 cores)
- Large Na-UO₂ cores: BFS-62-1~5, BFS-66-1 (6 cores)
- JOYO MK-I, -II
- Experiments in ICEBEP
- etc.

References

- [1] K. Shibata, *et al.*: “Japanese Evaluated Nuclear Data Library Version 3 Revision-3: JENDL-3.3,” J. Nucl. Sci. Technol. **39**, 1125, (2002).
- [2] Nagaya Y., et al.: “MVP/GMVP II: General Purpose Monte Carlo Codes for Neutron and Photon Transport Calculations based on Continuous Energy and Multigroup Methods,” JAERI 1348, JAERI (2005).
- [3] T. Nakagawa, K. Shibata and S. Chiba: “Japanese Evaluated Nuclear Data Library version 3 revision-2: JENDL-3.2,” J. Nucl. Sci. Technol. **32**, 1259, (1995).
- [4] C. Nordborg and M. Salvatore: “Status of the JEF evaluated data library,” Proc. Int. Conf. on Nuclear Data for Science and Technology, Gatlinburg 1994, Vol.2, p.680 (1994).
- [5] Cross Section Evaluation Working Group: “ENDF/B-VI Summary Documentation,” BNL-NCS-17541 (ENDF-201) (1991).
- [6] NEA Nuclear Science Committee: “International Handbook of Evaluated Criticality Safety Benchmark Experiments,” NEA/NSC/DOC(95)03, September, 2004 Edition (2004).
- [7] OECD/NEA Data Bank Web site (<http://www.nea.fr/html/dbdata/JEFF/>).
- [8] Cross Section Evaluation Working Group (CSEWG), National Nuclear Data Center, Broohaven National Laboratory, http://www.nndc.bnl.gov/csewg_members/index.html.

2.4.3 Nuclear data library in design calculation

Go Hirano , Shinya Kosaka
TEPSYS
2-37-28 EITAI KOTO-KU TOKYO 135-0034
e-mail: gou-hirano@tepsys.co.jp

Abstract

In core design calculation, nuclear data takes part as multi group cross section library during the assembly calculation, which is the first stage of a core design calculation. This report summarizes the multi group cross section libraries used in assembly calculations and also presents the methods adopted for resonance and assembly calculation.

1. Nuclear data library in light-water reactor core design calculation

The current core design calculation does not treat whole core heterogeneous geometry of a reactor directly (for instance, the actual shape of a fuel assembly). Instead, the calculation is first done at an assembly level, and then to a reactor level. The assembly calculation is executed using multi group cross section data prepared beforehand from the nuclear data library, which then provides a few group cross section library to be used for the reactor calculation. The reactor calculation is then performed using this few group library to evaluate core characteristics such as eigenvalue or flux distribution.

Since a few group cross section library used in the reactor calculation consists of collapsed energy groups and homogenized spatial geometry, the characteristics of nuclear data library in reactor calculation is less obvious compared to that of assembly calculations which utilizes finer multi group cross section and more detailed geometry information. Therefore, this paper will focus on the assembly calculation and will present base library and neutronic calculation methods adapted in its calculation.

2. Present Design Assembly Code

The assembly codes were first introduced into Japan by nuclear fuel vendors such as WH (Westinghouse) or GE (General Electric) at the same time when light-water reactors were introduced. These assembly codes are based on ENDF/B-4/5 library, which have been constantly improved and updated. They are widely used now for a commercial core design.

Some of the features of assembly calculation codes for a core design calculation are noted as follows.

2.1 PHENIX-P(PWR) [1],[2]

PHENIX-P has been used for PWR fuel assemblies at MHI (Mitsubishi Heavy Industries). It was developed with WH and was released for design use in 1987. It employs a 42-group cross-section library based on ENDF/B-V. The resonance calculation method is based on IR approximation. The assembly calculation employs S_4 using energy-condensed 6-group cross-section data as a transport solver. The 6-group cross-section data is collapsed in energy and space by using 42 energy groups flux distribution which is obtained by Node Joined Method. The heterogeneous neutron flux distribution of the fuel cells in the assembly is evaluated by combining the heterogeneous flux of the fuel cells obtained by the Node Joined Method with the homogeneous flux of the fuel cells obtained by the assembly calculation.

2.2 Improved NULIF(PWR) [3],[4]

Improved NULIF(PWR) has been used for PWR fuel assemblies at NFI (Nuclear Fuel Industries). It was developed by NFI and was released for design use in 1988. It employs a 99-group cross-section library based on ENDF/B-V. The resonance calculation method is based on NR approximation and NRIA (Narrow Resonance Infinite Absorber). The assembly calculation is based on diffusion theory, and uses energy-condensed 3-group cross-section data. One of the remarks for Improved NULIF is very short run time, which makes the generation of few-group cross-section library easy.

2.3 CASMO(PWR/BWR) [5]

CASMO was developed by Studsvik of America (now Studsvik Scandpower), and has been used as a nuclear design code for PWR fuel assemblies at NEL (Nuclear Engineering Ltd.) and for BWR fuel assemblies at TEPSYS (Tepco Systems). It usually employs a 70-group cross-section library based on ENDF/B-IV and V. The resonance calculation method is based on IR approximation. Method of characteristic (MOC) is applied with energy-condensed 7-group cross-section data as a neutron transport solver. The explicit geometry of an assembly can be treated.

2.4 TGBLA(BWR) [6],[7],[8]

TGBLA has been used for BWR fuel assemblies at GNF-J (Global Nuclear Fuel Japan). It was developed by GE and Toshiba and was released for design use in 1982. It employs a 98-group cross-section library based on ENDF/B-4 and 5. The resonance calculation method is based on IR approximation and IRCM^[9] code. The assembly calculation is based on diffusion theory, and uses energy-condensed 3-group cross-section data.

2.5 HINES(BWR)

HINES has been used for BWR fuel assemblies at GNF-J. It was developed by Hitachi and was released for design use in 1982. It employs a 98-group cross-section library based on ENDF/B-IV and V. The resonance calculation method is based on IR approximation. The assembly calculation is based on diffusion theory, and uses energy-condensed 3-group

cross-section data.

2.6 NEUPHYS(BWR)[10]

NEUPHYS has been used for BWR fuel assemblies at NFI. It was developed by NFI and was released for design use in 1985. It employs a 98-group cross-section library based on ENDF/B-IV. The resonance calculation is based on IR approximation. The assembly calculation is based on diffusion theory, and uses energy-condensed 3-group cross-section data.

3) Next Generation Design Assembly Code

Decades have passed since the introduction of assembly codes, and domestic vendors are now developing next generation assembly codes. The next generation assembly codes feature improved accuracy with more explicit treatment of geometry and more energy groups. Some domestic vendors have started employing JENDL series (3.2/3.3) as one of the main nuclear data besides ENDF series.

3-1) PARAGON(PWR)[11]

PARAGON has been in development at WH and MHI for PWR fuel assemblies. For Core design calculation, it usually employs a 70-group cross-section library based on ENDF/B-VI. For research purposes, some multi-group cross-section libraries such as a 187-group based on JENDL-3.3 can be applied optionally. The resonance calculation is based on IR approximation with spatially dependent Dancoff method ^[12]. Current-coupling collision probability methods (CCCP methods)^[13] with 70-group cross-section data is utilized in PARAGON as a neutron transport solver.

3-2) AEGIS(PWR)[14]

AEGIS has been in development at NEL for PWR fuel assemblies. It employs three 172-group cross-section libraries made from ENDF/B-VI, ENDF/B-VII and JENDL 3.3. The resonance calculation is done in super fine groups. MOC is currently applied with 172-group cross-section data as a neutron transport solver. It can treat the large-scale calculation with explicit geometry, higher order anisotropic scattering, and resonance shielding effect.

3-3) LANCER(BWR)[15]

LANCER has already been developed for BWR fuel assemblies at GNF-J. It was developed by GNF-J and was released for design use in 2005. It employs a 190-group cross-section library based on ENDF/B-VI. The resonance calculation method is based on F-table. CCCP methods used energy-condensed 35-group cross-section data is utilized in LANCER as a neutron transport solver in the assembly calculation.

3-4) Improved NEUPHYS(BWR)[16]

Improved NEUPHYS has been in development at NFI for BWR fuel assemblies. It employs a 98-group cross-section library based on JENDL 3.2. The resonance calculation is based on

IR approximation. MOC with energy-condensed 20-group cross-section data is utilized in Improved NEUPHYS as a neutron transport solver. It can treat the large-scale calculation with explicit geometry.

4) Summary

The features of assembly codes are summarized in Table 1. The present assembly codes mainly employ the library based on ENDF/B-IV or V. On the other hand, some assembly codes have started employing JENDL series (3.2/3.3) as one of the main nuclide data besides ENDF series. The assembly codes are providing more accurate results, which makes the role of the nuclear library in the calculation more prominent.

5) Acknowledgment

I am greatly indebted to H. Matsumoto and K. Yamaji (MHD) for the information about PHOENIX-P and PARAGON, M. Tatsumi and H. Hyoudou(NFI) on Improved NULIF, M. Yamamoto(GNF-J) on TGBLA, HINES and LANCER, T. Ito(NFI) on NEUPHYS and Improved NEUPHYS.

Reference

- [1] MAPI-1087 rev.6 (2004) [in Japanese]
- [2] R.J.J.Stamm'ler, M.J.Abbate, "Method of Steady-state Reactor Physics in Nuclear Design," Academic Press, London, (1983)
- [3] NFK.8102 [in Japanese]
- [4] NFK.8113 rev.2 [in Japanese]
- [5] BTN-0204036 [in Japanese]
- [6] M. Yamamoto, et al. "Development and Validation of TGBLA Lattice Physics Methods". *In proceedings of the Topical Meeting on Reactor Physics and Shielding*, Chicago, USA, September 17-19 1984.
- [7] M. Yamamoto, et al. "Recent Developments in TGBLA Lattice Physics Code". *In Proceedings of the International Topical Meeting on Advances Reactor Physics, Mathematics and Computation*, Paris, France, April 27-30 1987.
- [8] M. Yamamoto, et al. "New Physics Models Recently Incorporated in TGBLA". *In Proceedings of the International Topical Meeting on Advances Reactor Physics, Mathematics and Computation*, Pittsburgh, USA, April 28-May2 1991.
- [9] JAERI 1134
- [10] NLR-01[in Japanese]
- [11] M. Ouisloumen, et al., "The New Lattice Code PARAGON and Its Qualification for Nuclear Applications", *Proc. International Conference on Supercomputing in Nuclear*

Applications, SNA' 2003, September 2003, Paris, France(2003)

[12] H. Matsumoto, et al., "Development of Spatially Dependent Resonance Shielding Method", *Journal of NUCLEAR SCIENCE and TECHNOLOGY*, Vol. 42, No.8, p.688-694(2005)

[13] E. A. Villarino, et al. "HELIOS: Angularly Dependent Collision Probabilities", *Nuc. Sci. Eng.*, 112,16(1992)

[14] N. Sugimura, et al., "Development of Advanced Neutronics Design System of Next Generation, AEGIS", *Proc. Mathematics and Computation, Supercomputing, Reactor Physics and Nuclear Biological Application*, Avignon, France, September 12-15 (2005)

[15] K. Azekura, et al. "Development of a BWR Lattice Analysis Code LANCER Based on an Improved CCCP Method". *Advances in Nuclear Fuel Management III*, HiltonHead Island, South Carolina, USA, October 5-8, 2003

[16] Y. Kanayama, et al., "An Applicability of the Advanced Fuel Assembly Design Code NEUPHYS for LWR Next Generation Fuels", GENES4/ANP2003, Kyoto, Japan, September 15-19 (2003)

Table 1 Summary of the Features of Assembly Codes

	Code Name	Base Library	Year	Developer	Group Structure	Resonance Calculation	Assembly Calculation	Remarks
PWR	PHOENIX-P	ENDF/B-5	1987	WH/MHI	42	IR	6G Transport (S4)	Hetero-42G Flux
	Improved NULLIF	ENDF/B-5	1988	NFI	99	NR/NRIA	5G Diffusion	Short Run Time
	CASMO	ENDF/B-4 and 5	—	SSP	70	IR	7G Transport (MOC)	Explicit Geometry
Present Assembly Codes	TGBLA	ENDF/B-4 and 5	1982	GE/Toshiba	98	IR/RICM	3G Diffusion	Short Run Time
	HINES	ENDF/B-4 and 5	1982	Hitachi	98	IR	3G Diffusion	Trabsport Correction
	LANCER	ENDF/B-6	2005	GNF-J	190	F-table	35G Transport (CCCP)	Explicit Geometry
	NEUPHYS	ENDF/B-4	1985	NFI	98	IR	3G Diffusion	Short Run Time
	CASMO	ENDF/B-4 and 5	—	SSP	70	IR	7G Transport (MOC)	Explicit Geometry
PWR	PARAGON	ENDF/B-6	—	WH/MHI	70	IR+SDDM	70G Transport (CCCP)	2D-Full Core, Inner Rod γ -Transport
	AEGIS	ENDF/B-6,7 and JENDL-3.3	—	NEL	172	Super Fine Group	172G Transport (MOC)	Large-Scale Calculation with Explicit Geometry
BWR	LANCER	ENDF/B-6	2005	GNF-J	190	F-table	35G Transport (CCCP)	38 Fuel Nuclides and 136 Fission Product
	Improved NEUPHYS	JENDL-3.2	—	NFI	96	IR	20G Transport (MOC)	Large-Scale Calculation with Explicit Geometry

2.5 Latest Nuclear Data Measurements

2.5.1 Utilization of J-PARC -Research Plan with Neutron-Nucleus Reaction Measurement Facilities-

Masayuki Igashira

*Research Laboratory for Nuclear Reactors, Tokyo Institute of Technology
2-12-1, N1-26 O-okayama, Meguro-ku, Tokyo 152-8550, Japan*

We proposed installing “Neutron-Nucleus Reaction Measurement Facilities” in the Materials and Life Science Facility (MLF) in the High-Intensity Proton Accelerator Project (J-PARC: Japan Proton Accelerator Research Complex) in 2002 to conduct three research projects: (1) fast-neutron reaction and nuclear astrophysics, (2) neutron nuclear data on minor actinides and long-lived fission products, and (3) all-elements simultaneous, non-destructive and high-sensitivity nuclide-quantification. Fortunately, the proposal was approved in 2004. MLF will receive the first 3-GeV proton beam by the end of 2007, and will provide test neutron beams for users in 2008. In this contribution, the research plan with our facilities will be presented.

2.5.2 Measurement of Neutron Capture Cross Sections

Shoji NAKAMURA ^{*1)}, Alexander LAPTEV ¹⁾, Masayuki OHTA ¹⁾, Hideo HARADA ¹⁾,
Toshiyuki FUJII ²⁾ and Hajimu YAMANA ²⁾

1) Japan Atomic Energy Agency, 2-4Shirane, Shirakata, Tokai-mura, Naka-gun, Ibaraki-ken 319-1195

2) Kyoto University Research Reactor Institute, Kumatori-cho Sennan-gun, Osaka 590-0494

*E-mail: nakamura.shoji@jaea.go.jp

The social acceptability of nuclear power reactors is related to the waste management of long-lived fission products (FP) and Minor Actinides (MA) during the burn-up of nuclear fuel. The transmutation is one of ways to reduce the radio toxicity of nuclear waste. In the transmutation study of FP's and MA's, the accurate data of neutron capture cross sections are necessary to evaluate reaction rates by reactor neutrons. In this view point, the cross section measurements have been made by an activation method, neutron time-of-flight (TOF) method and so on.

As for neutron TOF measurement, a high-speed data acquisition system has been developed, which comprising two parallel channels with a flash-ADC shown in Fig.1. One channel is intended for measuring fast neutrons, of which energies range from 10 eV up to several keV. The sampling rate is 40 MHz. The other is operated at a 4 MHz sampling rate for measuring slow neutrons of which energies range down to a few 10 eV. Laboratory tests for the developed system were performed, and the good efficiencies for the incoming counting rate were obtained.

The ²⁴¹Am and ²⁴³Am nuclides are important in the nuclear waste management, since the presence of these nuclides in the nuclear waste induce long-term radio toxicity because of long-lived alpha emitters. However, there are discrepancies among the reported data for the thermal neutron capture cross section σ_0 of ²⁴¹Am, which reach more than 20%. In addition, there is a discrepancy among the values for ²⁴³Am(n, γ) reaction cross section, which reaches about 10%. In these problems, the cross section measurements were made for the ²⁴¹Am(n, γ), ²⁴²Am and ²⁴³Am(n, γ)-^{244m+g}Am reactions.

In the session, the recent activities of cross section measurements will be presented as well as the details of the experiments and the tentative results.

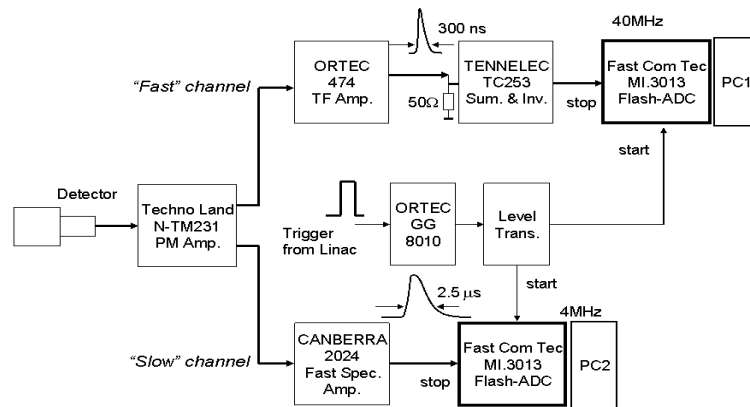


Fig. 1 Block diagram of the data acquisition system with two parallel F-ADC's

2.5.3 Photoneutron Cross Section Measurement for ^{94}Zr Using Laser Inverse Compton γ Rays

Sin-ya Hohara*^{1),2)}, Shinji Goko¹⁾, Ayano Makinaga¹⁾, Takeshi Kaihori¹⁾,
Hiroyuki Toyokawa²⁾, Hiroaki Utsunomiya¹⁾, Kaoru Y. Hara³⁾, Fumito Kitatani³⁾, Hideo Harada³⁾
Tetsuro Matsumoto²⁾, Hideki Harano²⁾

1) Konan Univ. / 8-9-1 Okamoto, Higashinada-ku, Kobe, Hyogo

2) National Institute of Advanced Industrial Science and Technology / AIST Tsukuba Central
2, Tsukuba, Ibaraki

3) Japan Atomic Energy Agency / 2-4 Shirane, Shirakata, Tokai-mura, Naka-gun, Ibaraki

* E-mail: s.hohara@aist.go.jp

Abstract

Quasi-monoenergetic γ rays produced in laser inverse Compton scattering (LCS) were used to measure photoneutron cross sections for ^{94}Zr near neutron threshold. The photodisintegration measurement is expected to probe neutron capture for ^{93}Zr (a long-lived fission product) within the framework of the statistical model. Measured cross sections are reported.

1. Introduction

In recent years, nuclear transmutation of minor actinides (MA) and long-lived fission products (LLFP) has promoted direct measurements of neutron capture cross sections for MA and LLFP [1,2]. However, the direct measurement is feasible only at dedicated facilities, for example, CERN n-TOF [1] and J-PARC [2], where strong neutron sources are/will be available. Yet preparation of radioactive samples is very difficult if not impossible.

Photodisintegration serves as an indirect probe of neutron capture because photoneutron cross sections can be used as constraints on the E1 γ strength function in the statistical model to predict neutron capture cross sections. Quasi-monoenergetic γ rays produced in laser inverse Compton scattering (LCS) at the National Institute of Advanced Industrial Science and Technology (AIST) are an ideal photon source for photodisintegration measurements. The present work represents a photodisintegration measurement for ^{94}Zr as a probe of neutron capture for ^{93}Zr ($t_{1/2} = 1.53 \times 10^6$ years) among other LLFP (^{80}Se , ^{108}Pd , etc.).

2. Experiment

Quasi-monoenergetic γ rays were generated in head-on collisions of laser photons from the INAZUMA laser system on relativistic electrons in the storage ring TERAS. The INAZUMA (a fiber-coupled diode-pumped Q-switch Nd: YVO₄ laser) was operated in the fundamental mode ($\lambda = 1054$ nm) at 20 kHz with the maximum power of 24 W. The beam line of the laser inverse Compton scattering (LCS) is shown in Fig. 1. Laser photons were led to a region of interaction with electrons through a laser optics consisting of an expander, a lens, and a mirror. The energy of the LCS γ rays was changed from 8.4 MeV to 9.8 MeV by adjusting the electron beam energy. Pencil-like beams of the LCS γ rays in 2mm diameter were produced with a 20cm lead collimator. A macro-time structure was generated in the LCS γ -ray beam by applying a 10 Hz external gate with 80 ms ON and 20 ms OFF to the laser system as shown in Fig. 2.

The LCS beam was used to irradiate a ^{94}Zr target mounted at the center of a neutron detector. The target was oxide powder (ZrO_2) with 99.60% in isotopic purity and 99.942% in chemical purity. The powder was encapsulated in an aluminum container. Fig. 3 shows the neutron detector consisting of twenty ^3He proportional counters (CANBERRA/ Dextray: Eurisys Mesures) embedded in a polyethylene moderator. The ^3He counter is 25mm in diameter and 500mm in length. The polyethylene moderator is 360mm in height, 360mm in width and 500mm in length. Three concentric rings of 4 (inner), 8 (middle), and 8 (outer) ^3He counters mounted at distances of 76mm, 140mm and 200mm from the beam axis, respectively, provide high detection efficiencies (60 – 70%)

for moderated neutrons. The electronic circuit for the triple-ring neutron detector is shown in Fig. 4. Signals from the ^3He counters in each ring were processed by an AMP-Discriminator module that is composed of 10 sets of pre-amplifiers, main amplifiers and pulse-height discriminators. The OR signal for the individual ring of ^3He counters was generated with a FANIN/OUT module. The beam ON and OFF gates were applied to the OR signals in a coincidence module to select events of reaction plus background neutrons and background neutrons, respectively.

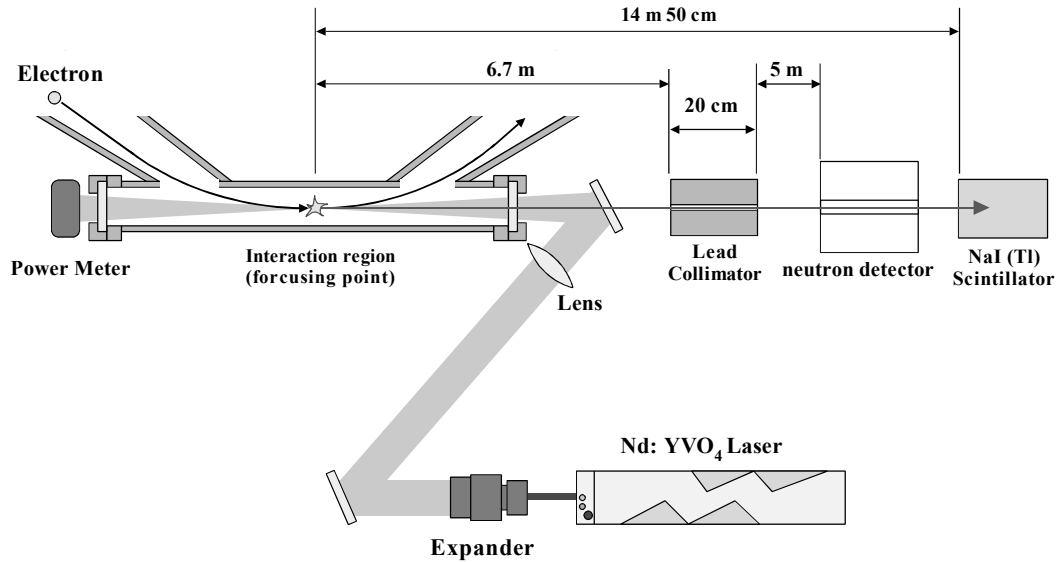


Fig. 1 Schematic view of the LCS γ -ray beam line.

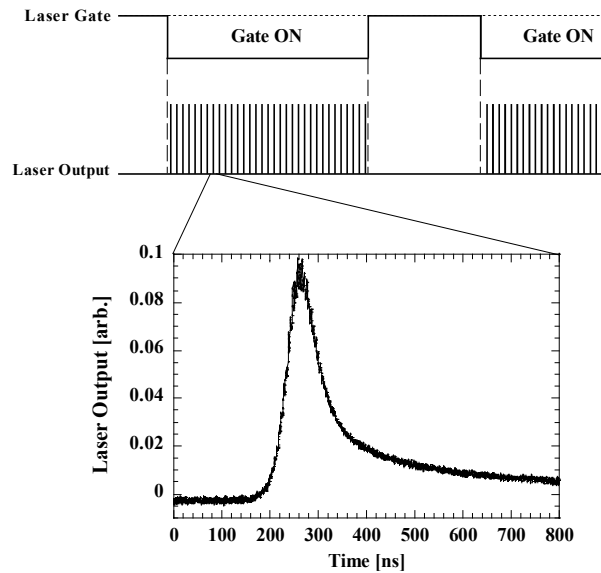


Fig. 2 Macro (upper) and micro (lower) time structures of the Nd:YVO₄ laser power (INAZUMA: Spectra-Physics)

The LCS γ ray was measured with a 120% high-purity germanium detector. The response function of the Ge detector to the LCS γ rays was analyzed in EGS4 Monte Carlo simulations to obtain the energy distribution of the LCS γ beam [3]. A typical response function of the Ge detector and energy spectrum of the LCS γ rays are shown in Fig. 5. Obviously γ rays above the neutron

threshold induced photoreactions. The LCS γ beam was monitored with a large volume NaI(Tl) detector (20cm in diameter and 30cm in length). A pile-up spectrum of the LCS γ rays from the NaI(Tl) detector is shown in Fig. 6. The pile-up spectrum was analyzed to obtain the number of incident γ rays [3].

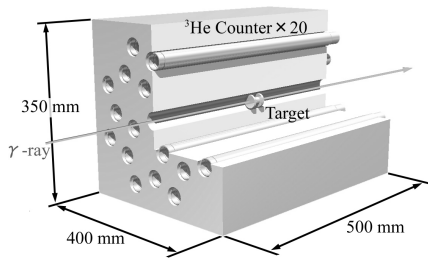


Fig. 3 Schematic view of the triple-ring neutron detector

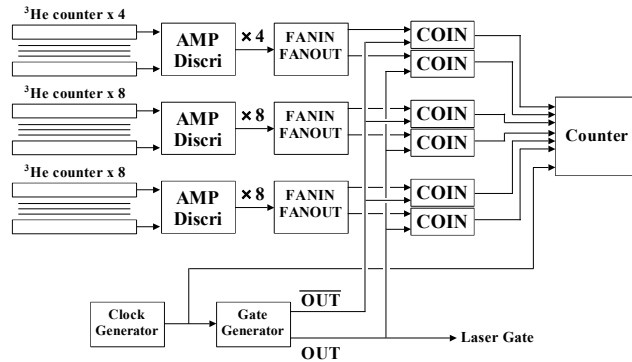


Fig. 4 Electronic circuit for the triple-ring neutron detector

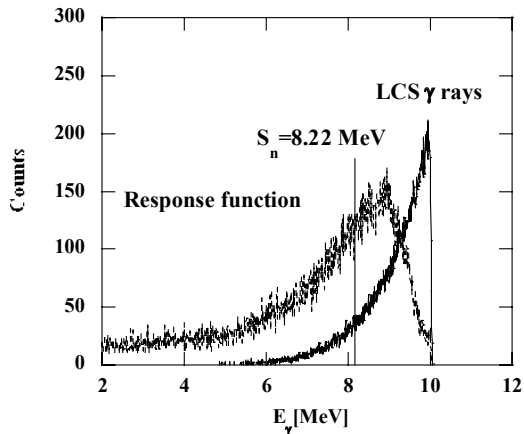


Fig. 5 Response function of the germanium detector and the energy distribution of the LCS γ rays

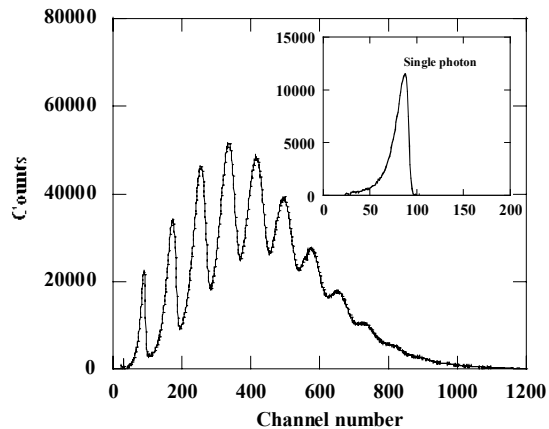


Fig. 6 Pile-up spectrum of the LCS γ -ray beam from the NaI(Tl) detector. A single photon response of the detector is also shown.

3. Analysis and Result

Photoneutron cross sections were experimentally determined at the average γ -ray energies in the monochromatic approximation from $\sigma(E_\gamma) = N_n / (N_t N_\gamma(E_\gamma) \epsilon_n f)$, where N_n is the number of neutrons detected, N_t is the number of target nuclei per unit area, $N_\gamma(E_\gamma)$ is the number of incident γ rays, ϵ_n is the neutron detection efficiency, and f is a correction factor for the present thick-target measurement. The correction factor is given by $f = (1 - e^{-\mu t}) / \mu t$ with the linear attenuation coefficient of γ rays μ and target thickness t [4]. The detection efficiency was determined from ring ratios [3,5], where three ring ratios were averaged with weights being proportional to the inverse of the square of associated statistical uncertainties. It is to be noted that the monochromatic approximation provides cross sections near the neutron threshold within typical uncertainties of a few percents [6].

Fig. 7 shows the present result of photoneutron cross sections for ^{94}Zr . The statistical error bars

are smaller than the size of the data points. The data of Berman et al. [5] are also shown for comparison. The present data are consistent with the previous data above neutron threshold, whereas non-vanishing cross sections below neutron threshold obtained in the previous measurement are apparently problematic.

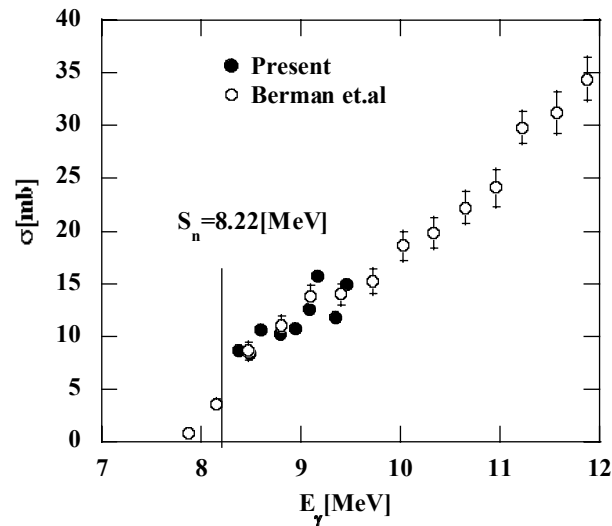


Fig. 7 Photoneutron cross sections for ^{94}Zr in comparison with those obtained previously [5].

4. Summary

We measured (γ, n) reaction cross section for ^{94}Zr with the LCS γ -ray beam at AIST. The present result is consistent with that of Berman et al. [5] above neutron threshold. However, the non-vanishing cross sections of the previous measurement below neutron threshold are apparently problematic. The present result exhibits a large cross section even at 8.36 MeV which is already very close to the threshold. The threshold behavior of the photoneutron cross section needs to be studied carefully further.

Reference

- [1] <http://pceet075.cern.ch/>
- [2] <http://jkj.tokai.jaeri.go.jp/Transmutation/en/ads/html>
- [3] H. Utsunomiya et al., Phys. Rev. C 67, 015807 (2003).
- [4] <http://physics.nist.gov/PhysReData/XrayMassCoef/>
- [5] B. L. Berman, J. T. Caldwell, R. R. Harvey, M. A. Kelly, R. L. Bramblett, S. C. Fultz, Phys. Rev. 162, 1098 (1967).
- [6] P. Mohr et al., Phys. Rev. C 69, 032801(R) (2004).

3. Papers Presented at Poster Sessions

3.1 The investigation of deuteron production double differential cross section induced by 392 MeV protons

Tadahiro KIN^{1,*}, Masahiro NAKANO¹, Minoru IMAMURA²,
 Yusuke YAMASHITA², Hiroki IWAMOTO², Naoya KOBA²,
 Yusuke KOBA², Hiroaki FUKUDA²,
 Genichiro WAKABAYASHI², Yusuke UOZUMI², Nobuo IKEDA²,
 Norihiko KOORI³, and Masaru MATOBA⁴

¹University of Occupational and Environmental Health, Fukuoka 807-8555, Japan

²Department of Applied Quantum Physics and Nuclear Engineering, Kyushu University, Fukuoka 812-8581, Japan

³Faculty of Integrated Arts and Sciences, University of Tokushima, Tokushima 770-8502, Japan

⁴Faculty of Engineering, Department of Biorobotics, Kyushu Sangyo University, Fukuoka 813-8503, Japan

We have investigated the deuteron productions from 392 MeV proton induced reaction for target nuclei of ¹²C, ²⁷Al, ⁹³Nb. Deuteron production double differential cross sections were determined over a broad energy range and scattered angles from 20 to 105 degrees in laboratory system. Those spectra were compared with two theoretical models; Quantum Molecular Dynamics model and Intranuclear Cascade model. We developed the code of Intra Nuclear Cascade model and we've got good results to reproduce the experimental data.

KEYWORDS: *intermediate energy, deuteron production cross section, double differential cross section, ¹²C, ²⁷Al, ⁹³Nb, QMD, INC*

I. Introduction

The data of nuclear reactions induced by intermediate-energy charged particles are important for variety of sciences and technologies. We have reported about proton induced proton production double differential cross section (DDX) already.¹⁾ Many kinds of charged particles are produced by proton induced reactions. Proton production events are the largest and the second-largest events are deuteron production. The cross section of deuteron production is about 10% compared with protons. We can't ignore such a large number of events, because deuterons possess high energy and cause much effect in materials. Therefore, deuteron production DDX data induced by intermediate energy protons are very important.

On the other hand, the simulation codes based on physical theories are necessary to evaluate the nuclear data. We also need these codes to know the reactions that cannot be measured easily by experiment. There are many models of nuclear reaction calculation codes. We adopted Quantum Molecular Dynamics (QMD)^{2,3)} and Intranuclear Cascade (INC)⁴⁻¹⁰⁾ models. These models are widely used for cross section calculations in an intermediate energy region.

We measured the deuteron production cross sections for reactions induced by 392 MeV protons as the data of this energy region. And we compared them with the QMD and the INC model calculations.

II. Experiment

Measurements of deuteron production reactions were carried out at the Research Center for Nuclear Physics, Osaka University. Proton beams were accelerated by the ring-cyclotron up to 392 MeV, and bombarded a target located in a vacuum chamber of 800-mm outer diameter. Target foils were mounted on a ladder, which was located at the center of the chamber. The targets were CD₂, ¹²C, ²⁷Al and ⁹³Nb. We used CD₂ target for taking quasi-monochromatic peaks for energy calibration. Other targets were used for measurements of DDX induced by 392 MeV protons. Energy spectra of emitted deuterons were measured by using stacked GSO(Ce) scintillators detectors^{11,12)} placed out of the chamber. A sketch of detectors is given in Fig. 1 and the size of each scintillator is shown in Table 1. The outline of the experimental setup is shown in Fig. 2.

* Corresponding author, Tel. +81-92-642-3764, Fax. +81- 92-642-3800, E-mail: kinnya@nucl.kyushu-u.ac.jp

Table 1 The Size of Detectors of stacked scintillators detectors

Detector	intended purpose	Size	Number
Plastic Scintillators	Active Collimator	44×44×5 mm ³	2
Plastic Scintillators	ΔE Detector	20×30×0.5 mm ³	2
Plastic Scintillators	ΔE Detector	20×30×2 mm ³	2
GSO(Ce) Scintillators	ΔE and E Detector	43×43×43 mm ³	5
GSO(Ce) Scintillator	E Detector	φ 62×120 mm	1

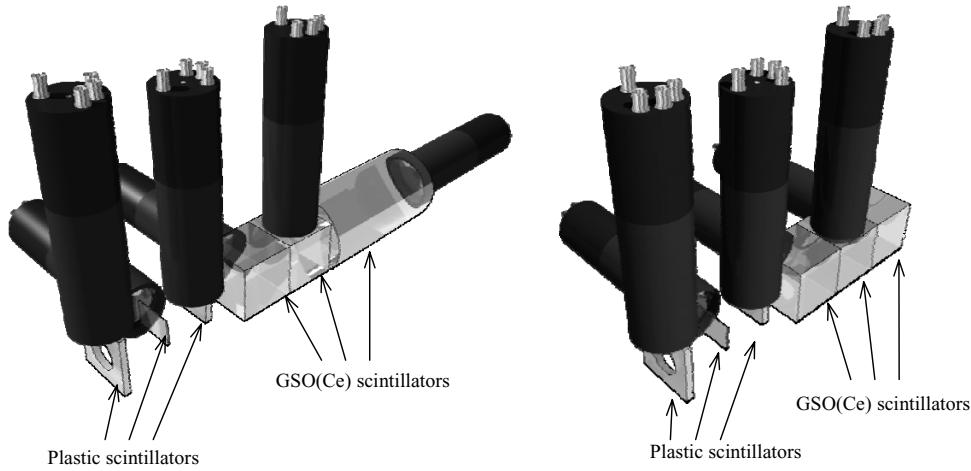


Fig. 1 Stacked GSO(Ce) spectrometers. The long one (left) and the short one (right).

The detectors are most suitable for investigating gross structures of energy spectra. Measurements were made at seven laboratory angles from 20 deg. to 105 deg.

Double differential cross sections were determined through off-line analyses. Pulse heights of signals were converted into particle energy using the light output and non-linearity^{12,13)} took into accounts. Then, the particle identification was carried out by using the parameter PI :¹⁴⁾

$$PI = E_{total}^b - (E_{total} - \Delta E)^b, \quad (1)$$

where b is the parameter representing the range of each particle, E_{total} the total energy deposited on the spectrometer, and the ΔE the amount of energy deposited on the transmission detector.

Figure. 3 shows a typical two-dimensional plot of PI versus particle energy for the 392-MeV proton induced reaction on ⁹³Nb at 20°. A value of 1.73 was employed for the parameter b , and the ΔE is the sum of deposit energies of deuteron for the two thin plastic scintillators. The thick belt lying at around $PI = 120$ corresponds to proton good events. The lower area is a group of the proton bad events, which accidentally underwent nuclear reactions with crystal elements or out-scattering from the crystal volume. Deuteron events that we want to focus distribute in the large PI area.

PI projection spectra were generated for each energy bin of a 10-MeV width. The deuteron events were separated from proton events in terms of PI for each of the spectra and then counted up by using Gaussian fittings. The number of deuteron event was corrected in terms of the peak efficiency that represents the good-to-total ratio. The peak efficiency for the spectrometers had been determined as a function of deuteron energy with both experiments and Monte Carlo calculations.¹²⁾ Finally, the double differential cross sections were determined for each energy bin through a correction for the dead time of the CAMAC-PC data acquisition system.

III. Results and discussion

The measured energy spectra were compared with the QMD and the INC models.

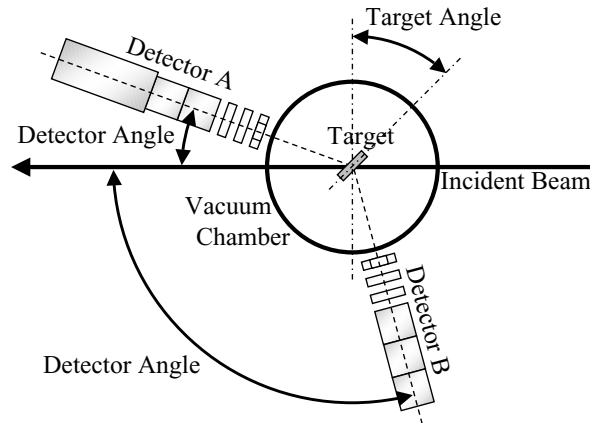


Fig. 2 Placement of the target, the chamber and detectors.

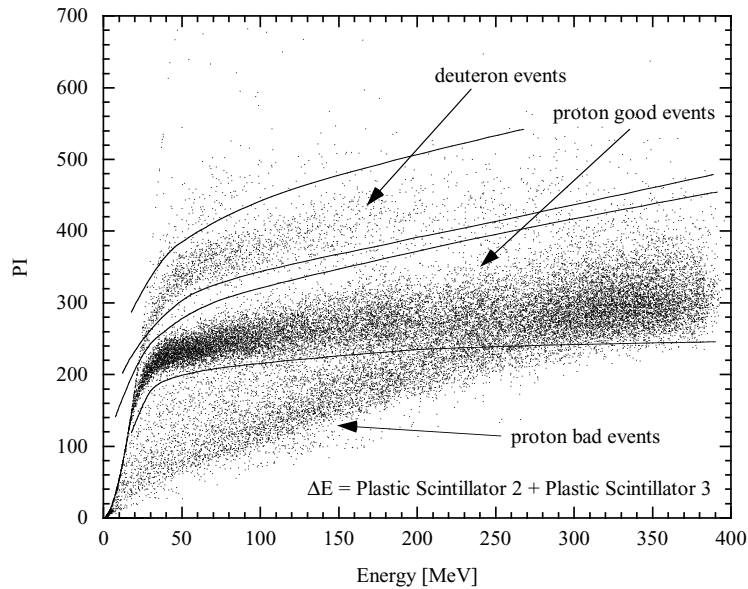


Fig. 3 Plot of PI versus deuteron kinetic energy obtained for the 392-MeV $^{93}\text{Nb}(p,dx)$ reaction at 20° .

The QMD model is a semi-classical simulation method, in which a Gaussian wave packet is used to express nucleon states. The time evolution of each nucleon is traced in event-by-event simulations through Newtonian equations of motion in the self-consistent mean field. In this work, we employed the JQMD code for the QMD model calculation. We also employed the SDM (Statistical Decay Model) code for the light particle evaporation and fission.

The INC model is based on two-body collisions and widely known to be a powerful tool to simulate a variety of nuclear reactions in an intermediate energy range. In this work, we have developed the INC code. The INC code is a semi-full-particle cascade model. It means the code make full particle ground state i.e. each nucleon has position and momentum. However, a nucleon keeps the ground state position before the first collision of it happens. The positions are determined to have Woods-Saxon type density distribution. The momenta are defined randomly to make sure that the nucleons energy is from 0 to 42 MeV. After the ground state is created, if there are proton and neutron that have short distance ($\leq 1.4\text{fm}$), we define the pair as a pre-formed deuteron. The number of deuterons in a target is about 10% (See Table 2).

There are two deuteron production processes. One is the knock-out process of pre-formed deuterons. The

other one is indirect pickup process. The deuteron from indirect pickup process is defined after the reaction by checking the distance and momentum of nucleons.

Table 2 The number of pre-formed deuterons in targets of ^{12}C , ^{27}Al and ^{93}Nb by the INC code.

Target	Number of Nucleons	Average Number of Deuterons
^{12}C	12	1.30
^{27}Al	27	2.98
^{93}Nb	93	10.94

The energy spectra of $^{12}\text{C}(p,dx)$, $^{27}\text{Al}(p,dx)$ and $^{93}\text{Nb}(p,dx)$ are shown in Fig. 4

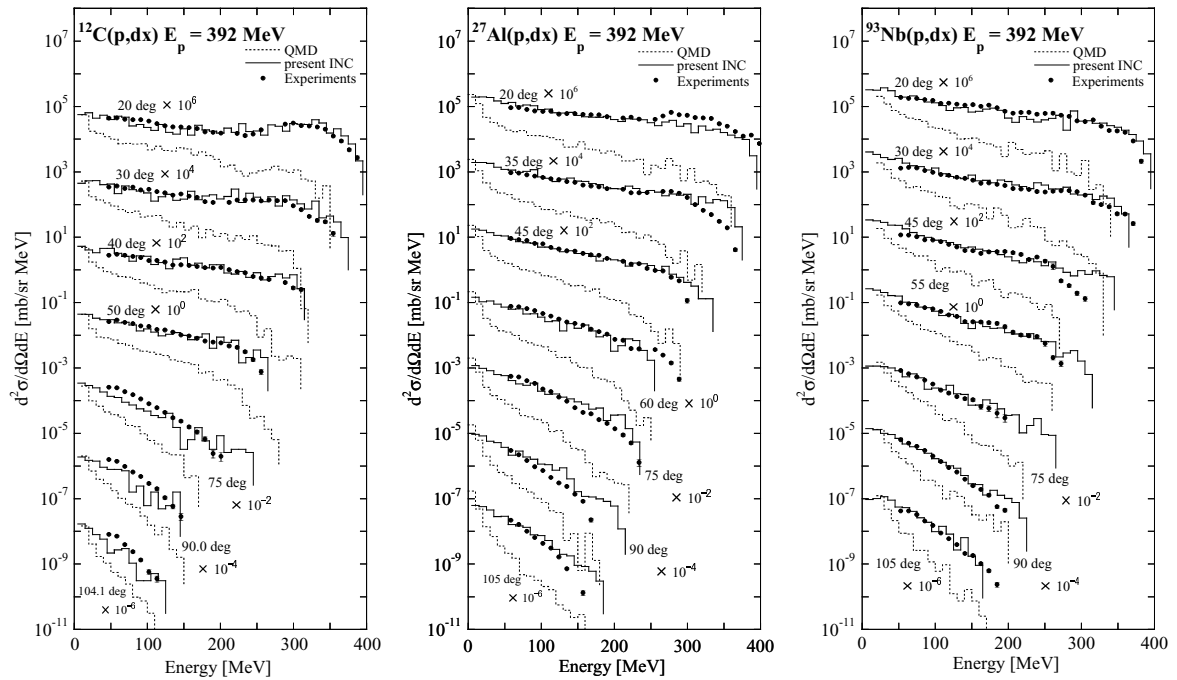


Fig. 4 Spectra of double differential cross section for (p,dx) at 392 MeV with the INC (solid) and the QMD+SDM (dotted).

The spectra by the QMD didn't have good reproducibility. At all angles about all targets, the simulated spectra were 10 times smaller than experimental ones. The INC spectra were very close to experimental ones. Most of the produced deuterons by the INC model are from the knock-out process. The QMD model doesn't have the knock-out process and fragments are determined by checking nucleons distance and momentum. The SDM calculation increased the DDX only around the low energy part of the spectra.

Without the knock-out process, the spectra by the INC model underestimated the experimental data as same as the QMD model. Therefore, we found the knockout processes of the pre-formed deuterons took main part of deuteron production.

IV. Conclusion

Experiments for double differential cross sections of (p,dx) reactions were conducted to facilitate compiling new nuclear data libraries for applications. Deuteron production DDX energy spectra were measured on $^{12}\text{C}(p,dx)$, $^{27}\text{Al}(p,dx)$ and ^{93}Nb at incident proton energy 392 MeV.

The results were compared with the INC and the QMD model calculations to check the reliability of these calculations.

Then, we found that the deuteron production reaction of intermediate-energy region can be simulated satisfactorily with the INC model that has the pre-formed deuterons knock-out and the indirect pickup processes.

References

- 1) T. Kin, F. Saiho, S. Hohara, K. Ikeda, K. Ichikawa, Y. Yamashita, M. Imamura, G. Wakabayashi, N. Ikeda, Y. Uozumi and M. Matoba *Phys. Rev. C* **72**, 014606 (2005).
- 2) J. Aichelin *Phys. Rep.* **202**, 233 (1991).
- 3) K. Niita, S. Chiba, T. Maruyama, H. Takada, T. Fukahori, Y. Nakahara and A. Iwamoto *Phys. Rev. C* **52**, 2620 (1995).
- 4) Y. Yariv and Z. Fraenkel, *Phys. Rev. C* **20**, 2227 (1979).
- 5) G. D. Harp, K. Chen, G. Friedlander, Z. Fraenkel and M. Miller *Phys. Rev. C* **8**, 581 (1973).
- 6) J. Cugnon, *ibid.* **22**, 1885 (1980).
- 7) A. Boudard, J. Cugnon, S. Leray and C. Volant *Phys. Rev. C* **66**, 044615 (2002).
- 8) H. W. Bertini *et al.*, *Phys. Rev.* **131**, 1801 (1963).
- 9) H. W. Bertini *et al.*, *Phys. Rev.* **188**, 1711 (1969).
- 10) H. W. Bertini *et al.*, *Phys. Rev. C* **6**, 660 (1972).
- 11) K. Anami, H. Yoshida, D. Konishi, H. Murohka, Y. Uozumi, G. Wakabayashi, A. Nohtomi, T. Sakae, M. Matoba, T. Maki and N. Koori *J. Nucl. Instrum. Methods Phys. Res. A* **404**, 327 (1998).
- 12) H. Yosida, D. Konishi, K. Anami, H. Murohka, Y. Uozumi, S. Aoki, T. Yamamoto, G. Wakabayashi, A. Nohtomi, T. Sakae, M. Matoba, T. Maki and N. Koori *J. Nucl. Instrum. Methods Phys. Res. A* **411**, 46 (1998).
- 13) F. Saiho, J. Tanaka, B. Cao, S. Aoki, Y. Uozumi, G. Wakabayashi, M. Matoba, T. Maki, M. Nakano and N. Koori *Proceeding of Symposium on Nuclear Data* **3.23**, (2000).
- 14) M. Makino, R. Eisberg, D. Ingham and C. Waddell *Nucl. Instr. Meth.* **81**, 125 (1970).

3.2 Measurements of double differential fragment production cross sections of silicon for 70 MeV protons

M. Hagiwara, T. Oishi, S. Kamada, M. Baba,
Cyclotron and Radioisotope Center, Tohoku University
 E-mail: *hagi@cyric.tohoku.ac.jp*
 T. Sanami
High Energy Accelerator Research Organization (KEK)
 M. Takada, N. Miyahara
National Institute of Radiological Sciences

Double-differential fragment production cross-sections of silicon are measured for 70 MeV proton with a specially designed Bragg curve counter (BCC). New method for particle identification and energy correction of range over fragments are applied to BCC and succeed in extension the energy dynamic range. The experimental results of double-differential cross-sections for Li, Be, B, C, N, O production are obtained at 30, 60, 90, 135 degree. The comparisons between the experimental data and theoretical calculations with different models clarified strong dependence of the fragment production on the intra-nuclear cascade model used in calculation.

1. INTRODUCTION

Single Event Effect (SEE) which is a radiation effect induced on a micro-electronics device by hitting of a single ion originated in cosmic radiation has been recognized as a serious problem which disturb the reliability of space technologies. Recently, with miniaturization of a micro-electronics device, SEE becomes a serious problem even on the ground level where there are terrestrial cosmic-rays composed mainly of secondary neutrons created by nuclear spallation reaction in the atmosphere. The most of SEE phenomena induced on the ground is caused by large LET (Linear Energy Transfer) secondary particles produced by the nuclear reaction in a device with the neutrons.

To analyze the SEE mechanism, information on the energy-angular double-differential cross-sections (DDX) of silicon which is main element of a semiconductor device are essential for secondary charged particles productions, especially for large LET secondary particles (called fragment thereafter) by ten's of MeV neutron. However, at present, there are no experimental DDX data for fragment production of silicon in ten's of MeV. Thereby theoretical models for fragment production DDXs have not been examined at all. It is important to accumulate reliable experimental DDX data for fragment production in ten's of MeV.

DDX data for neutrons are of prime importance to estimate SEE on the ground level. However the data are difficult to measure because an intense mono-energetic neutron source enough for the measurements of secondary fragment production which have usually very low cross-section ($\sim \mu\text{barn}$) is not available in ten's of MeV. To give information about fragment production reaction by ten's of MeV nucleon, DDX data for protons is useful in place of the data for neutrons. In the case of a proton experiment, beam intensity is enough to adopt the experiment. Our group has conducted the measurement of the DDX for fragment production reaction by proton using a Bragg curve counter (BCC) [1,2] and Energy Time-of-Flight (E-TOF) method [3,7]. In the previous study [4], DDXs were obtained for the C(p,x) and the Al(p,x) reaction ($E_p = 70 \text{ MeV}$) with the BCC and E-TOF method.

The present study aims to obtain DDX of silicon for 70 MeV proton. To improve energy dynamic range of DDX, new methods for particle identification and utilization of range over fragment are described. As a

result, DDXs for fragment production are obtained wide energy range. The DDXs by theoretical calculation with various models are compared with experimental data.

2. BRAGG CURVE COUNTER (BCC)

The details of Bragg curve counter (BCC) are described in the previous report [4]. The BCC is a cylindrical gridded ionization chamber [5,6] (300 mm ϕ x 360 mm long) filled with an Ar + 10%CH₄ gas at a pressure of ~200 torr. A fragment is identified from the transition of the anode signal which reflects the distribution of free electrons produced by the fragment. Since the distribution represents Bragg curve proper to the fragment, the fast part and the whole integration of the signal are proportional to the atomic number (Z) and energy of the fragment, respectively. The energy region which can be measured by the BCC (energy dynamic range) depends on gas pressure of detector and a species of fragment. The high energy limit is determined by maximum stopping energies in detector. In present detector configuration, the maximum stopping energies is 25 MeV for Beryllium, however maximum energy of Beryllium from 70 MeV proton induced reaction reaches 40 MeV. On the other hand, a fragment with energy lower than the energy of Bragg peak can not be identified because Bragg peak information is not included in the anode signal. The energy reaches more than 10 MeV for the fragments heavier than Carbon.

In this study, two new approaches are adopted to extend the energy dynamic range: 1) new identification scheme using a fragment range in place of Bragg peak, and 2) utilization of fragments which penetrate through BCC. For 1), the cathode electrode of BCC is designed to obtain the timing pulse which gives the timing of a fragment entering BCC. Since the anode signal gives the timing of free electron reaching at grid as shown in Fig.1, the time difference between the cathode and the anode shows inverse proportion to fragment range. By using the range, fragment can be identified with any energy, in principle. Thus, the threshold for particle identification is improved considerably. Besides, this method allows identification of not only Z number but also mass number. For 2), the energy of the fragment which penetrated through BCC is estimated from deposition energy in BCC. The relationships between deposition energy and incident energy are calculated by SRIM code for each fragment. The schematic view of this method is shown in Fig. 2. By combining these two approaches, the energy dynamic range of BCC covers almost all the energy of fragments from 70 MeV proton induced reactions.

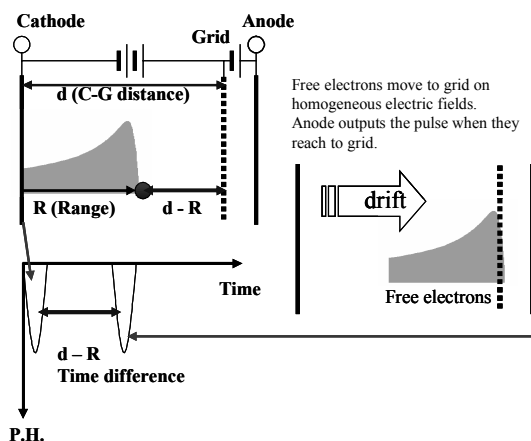


Fig.1. Schematic view of fragment identification from the time difference between the cathode and anode signal

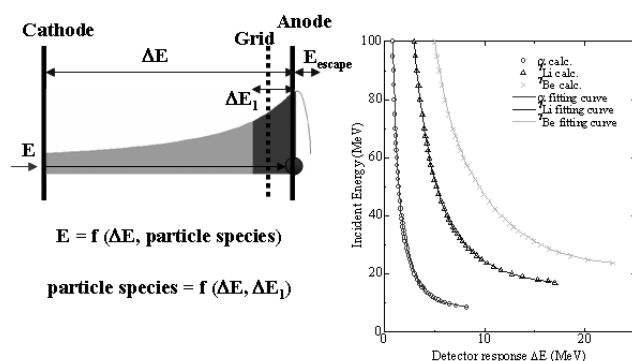


Fig.2. Detection scheme of particle which have the range longer than the detector length.

3. EXPERIMENTS

The experiment are performed using the AVF cyclotron at National Institute of Radiological Science (NIRS) with almost same apparatus as one employed in the previous measurement [4]. The silicon target of $310 \mu\text{g}/\text{cm}^2$ thick, which is deposited on a tantalum foil of $10 \mu\text{m}$ thick, is set at the center of a vacuum chamber and irradiated by 70 MeV proton beam with $\sim 30 \text{ nA}$. The effects of the tantalum foil are eliminated by subtracting background data obtained with a tantalum foil without silicon. The fragments from the targets are measured with BCC at 30, 60, 90, 135 degree. Owing to large solid angle of BCC, only 1 hour irradiation is enough for each measurement. At 30 degree, a counter telescope consisted of two SSD ($25 \mu\text{m}$ and $250 \mu\text{m}$ thickness) and 900 mm flight path is also employed to measure fragments based on E-TOF method. The results of E-TOF are used to evaluate the validity of BCC data.

Figures 3 and 4 show two-dimensional spectra on the energy vs. Bragg peak for silicon sample (Si ($310 \mu\text{g}/\text{cm}^2$) + Ta ($10 \mu\text{m}$)) and backing sample (Ta ($10 \mu\text{m}$)), respectively. Excellent separation of each fragment and S/N ratio are confirmed up to $Z = 8$ (Oxygen) for silicon sample in the energy region where particles are separated by the difference of Bragg peak value. As shown in Fig.4, background fragments heavier than lithium are less than 10 % compared with the foreground yields owing to the low fragment production cross-sections of tantalum. Identifications of the fragments were also performed by time difference between cathode and anode signals as shown in Fig 5 and the performances of two methods (Bragg peak and time difference method) are compared. As the results, identification with a time difference is better than with a Bragg peak on the point of lower energy limit to identify each fragment and isotope identification.

The turning blows at maximum energy point in Fig. 3 and 4 are caused by the fragments which have ranges longer than the cathode-grid distance (300 mm) which is the detector active region. In the past BCC method, the events were excluded from the energy spectra because the fragments are not fully deposit the energy to the detector and therefore become limitations of measurable detector energy in high energy. It is meaningful to extend the measurable energy range by developing a correction method for this effect from the information of the partial energy deposit (ΔE) In this study, the energy dynamic range of fragments was extended by introducing the energy correction method with the relation of E (energy which fragments have before the injection to detector) and ΔE (energy which fragments give to detector) calculated by SRIM code.

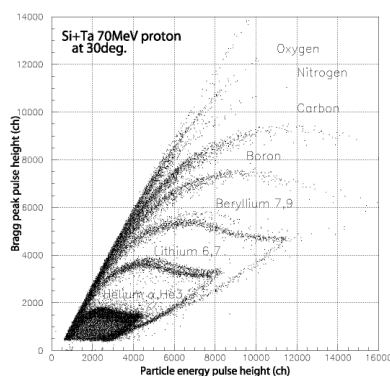


Fig.3 Two dimensional spectrum of energy vs. Bragg peak for silicon sample

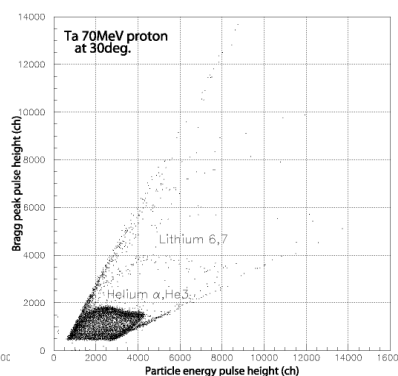


Fig.4 Two dimensional spectrum of energy vs. Bragg peak for tantalum backing

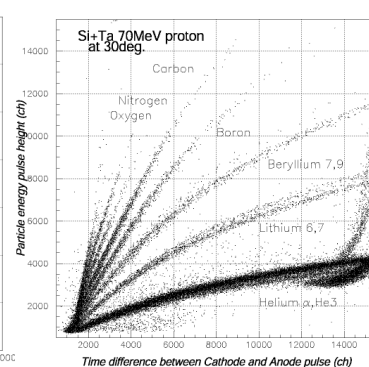


Fig.5 Two dimensional spectrum of time difference vs. energy for silicon sample

4. RESULTS AND DISCUSSION

Figure 6 shows the comparison of beryllium spectra with and without the energy correction for range over particle for example. The dynamic range of beryllium was extended reasonably by the corrections from around 25 to 38 MeV which is close to a kinematics maximum energy of beryllium.

Figure 7 shows the comparison between experimental data by BCC and ETOF with LA150[9]. The data by BCC are consistent with one by E-TOF in the overlapping region and are also consisted with one by LA150 which have been examined by another experiment. These facts confirm the method for absolute normalization and energy calibration of the data by BCC.

Figure 8 shows the Li, Be, B, C, N, O production double-differential cross-sections of silicon for 70 MeV proton at 30, 60, 90, 135 degree with the results of PHITS [10] calculations. The calculations carried out using three different intra-nuclear cascade models (ISOBAR, JQMD, Bertini) combined with one evaporation model (GEM). Considerable amount of fragments whose energy reaches to 20 MeV are observed as the results of 70 MeV proton induced reaction. The threshold energies of experimental data are determined from the thicknesses of sample and incident window. These thicknesses can be improved by the experimental setup focused at low energy fragments. The ISOBAR model generally reproduces experimental data except for the data of light fragments. The calculations with Bertini model show remarkable underestimates for all results. Therefore, to calculate correct deposition energy by a code in this energy range, we should pay much attention what model embedded in the code. At forward angle of lithium and beryllium DDXs, the experimental data show a different shape from the other data. This fact indicates that a new reaction mechanism is indispensable to reproduce these components. For the experimental data of ^7Be production cross-sections [12] and mass distribution [7] in this energy region, ISOBAR model underestimate the data, the discrepancies of which are similar trends for the present results as shown in Fig. 9. The models will be required for the improvements of the light cluster treatments to improve the calculation accuracy.

Figure 10 shows the comparison between DDXs of silicon and aluminum for He, Be, C and O at 30 degree. The magnitude and shape of fragment DDXs of aluminum are in good agreement with ones of silicon which are similar results in Fig. 9. Thus, the data of silicon can be estimate from ones of aluminum which can be obtained using a self-support sample. From an experimental point of view, it is important because a sample of aluminum is easy to fabricate in comparison with one of silicon.

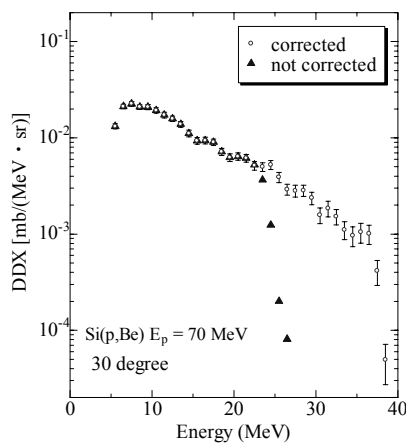


Fig.6 Comparison of beryllium spectra with/without the energy correction for range over events

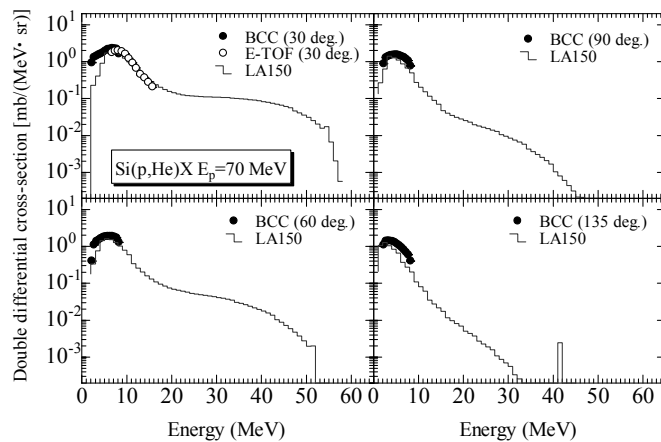


Fig.7 Comparison of DDX of Si(p, α) ($E_p = 70$ MeV) with LA150

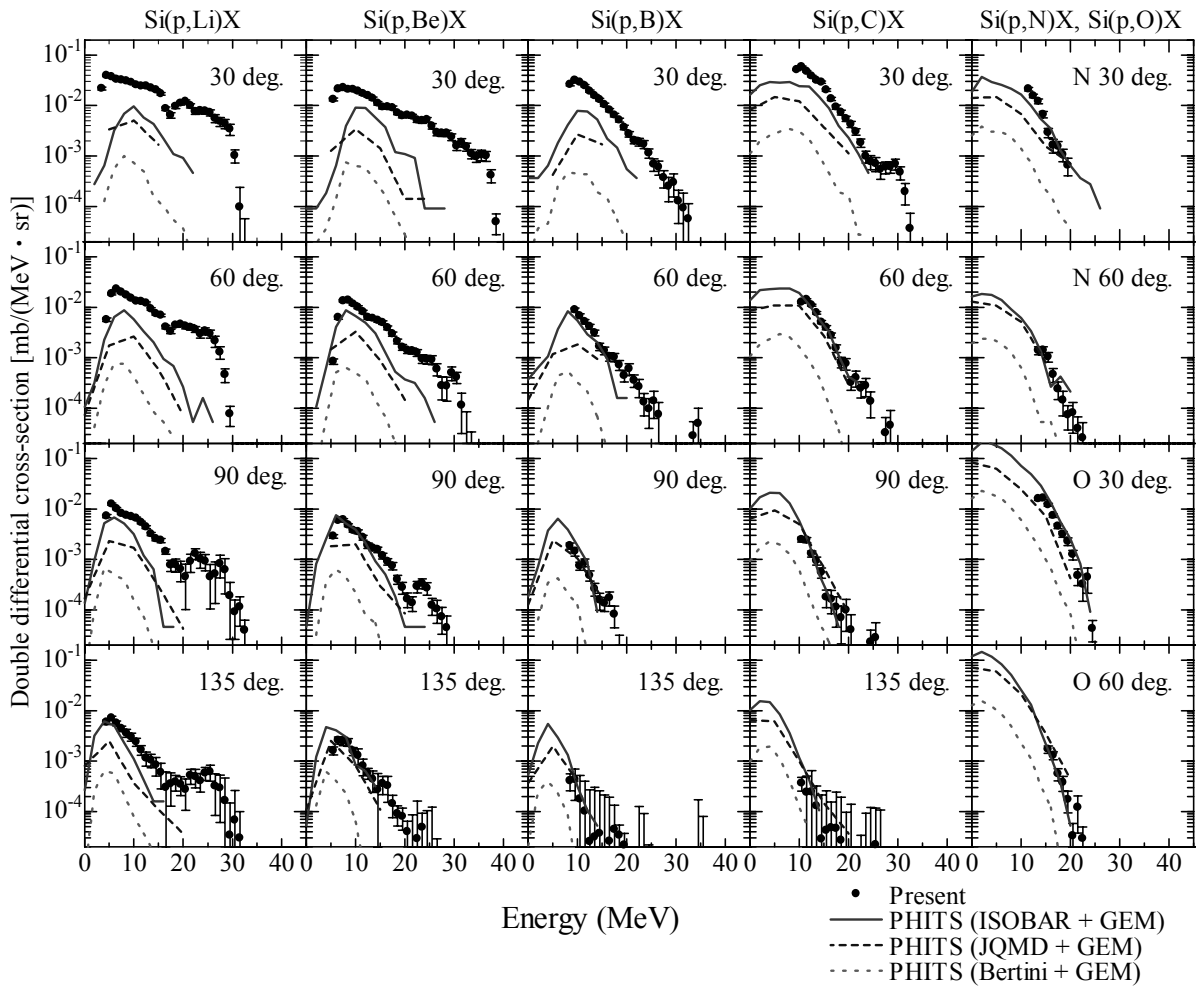


Fig.8 DDX of silicon for Li, Be, B, C, N, O production at 30, 60, 90, 135 degree from for 70 MeV proton reaction compared with the results of PHITS [10] calculations

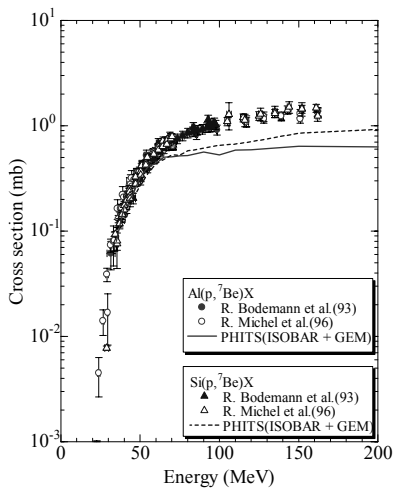


Fig.9 ⁷Be production cross-section [11,12] of Si and Al compared with PHITS

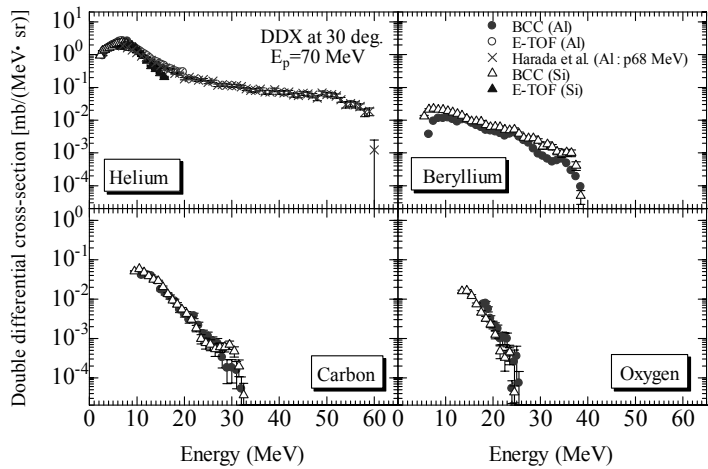


Fig.10 Comparison between DDXs of silicon and aluminum for He, Be, C and O at 30

5. CONCLUSION

Fragment production double-differential cross-sections of silicon for 70 MeV proton induced reaction are obtained using a specially designed BCC. The energy dynamic range of BCC is extended remarkably by a new identification scheme using particle range and a utilization of particles whose ranges are longer than the detector. The α -particle production double-differential cross-section data by the new methods are consistent with the data by E-TOF method and LA150. It becomes clear that considerable amount of fragments whose energy reaches to 20 MeV are produced from the Si(p,x) reaction in tens MeV region. By the comparison with theoretical calculations, the applicability of the calculation for fragment productions strongly depends on the model of an intra-nuclear cascade part. The ISOBAR model generally reproduces experimental data except for the data of light fragments. To reproduce these light fragment productions, a new reaction model will be indispensable. The comparison between results obtained with aluminum and silicon sample show that aluminum have similar DDXs for fragment production and can be substituted for silicon.

Our data will play important role in estimation of radiation effects on a silicon based semiconductor devices since this data set is only one data which describes fragment production rate and the energy spectra in this energy range. The data will be useful for not only benchmark data for the fragment production but also estimation of local charge density by proton in silicon. This data will be also useful for the estimation of neutron induced reaction by taking account of the coulomb contribution in the nuclear reaction.

ACKNOWLEDGEMENT

The authors express their thanks to the operation crew of the NIRS cyclotron for their cooperation. The authors wish to thank Dr. Sugai of KEK for his effort in fabrication of silicon samples with HIVAP method.

REFERENCES

- [1] C.R.Gruhn, M.Binimi, R.Legrain, R.Loveman, W.Pang, M.Roach, D.K.Scott, A.Shotter, T.J.Symons, J.Wouters, M.Zisman, R.Devries, Y.C.Peng and W.Sondheim, Nucl. Instrum. Methods, 196 (1982) 33
- [2] N.J.Shenhav and H.Stelzer, Nucl.Instrum.Meth. 228 (1985) 359
- [3] C.T.Roche, R.G.Clark, G.J.Mathews and V.E.Viola, Jr, Phys. Rev. C 14 (1976) 410
- [4] M. Hagiwara, T. Sanami, M. Baba, T. Oishi, N. Hirabayashi, M. Takada, H. Nakashima and S. Tanaka, Proc. of the international conference on Nuclear Data for Science and Technology ND2004, 769 (September 2004) 1031.
- [5] T. Sanami, M. Baba, M. Hagiwara, T.Hiroishi, M.Hosokawa, N.Kawata, N.Hirabayashi, T.Oishi, H.Nakashima and S.Tanaka. J. Nucl. Sci. and Tech. Suppl. 4 (2004) 502
- [6] T.Sanami, M.Baba, K.Saito, N.Hirakawa. Nucl. Instrum. Meth. A440 (2000) 403
- [7] K. Kwiatkowski, S. H. Zhou, T. E. Ward, et al., Phys. Rev. Lett. 50 (1983)1648
- [8] K.Omata and Y.Hujita, INS-Rep-884, Institute for Nuclear Study, University of Tokyo, 1991
- [9] M. B. Chadwick, P. G. Young, S. Chiba, S.C. Frankle, G. M. Hale, H. G. Hughes, A. J. Koning, R. C. Little, R. E. MacFarlane, R. E. Prael and L.S. Waters, Nucl. Sci. Eng., 1331 (1999) 293
- [10] H. Iwase, K. Niita, T. Nakamura, J. Nucl. Sci. and Tech. 39 No.11 (2002) 1142
- [11] R. Bodemann, H.-J. Lange, R. Michel, T. Schiekel et al., Nucl. Instr. Meth. B82 (1993) 9.
- [12] R. Michel, R. Bodemann, H. Busemann, R. Daunke et al., Nucl. Instr. and Meth. B129 (1997) 153

3.3 Measurement of Double-differential Cross Section of Fragments on C, Al, Cu, Ag Induced by 400 MeV Helium

T. Sanami, H. Matsumura
High energy accelerator research organization (KEK)
Oho 1-1, tsukuba, Ibaraki 305-0801, Japan
Email : toshiya.sanami@kek.jp

M. Takada, T. Murakami
National Institute of Radiological Science (NIRS)
Anagawa 4-9-1, Inage, Chiba 263-8555, Japan

An experimental setup is prepared for fragment spectroscopy and mass yield study in intermediate energy region. For fragment spectroscopy, fragment mass and Z number are identified simultaneously by time-of-flight and ΔE -E method using a counter telescope. Digital storage oscilloscope with segment transfer mode is used for determination of time-of-flight and pulse height from fast timing signals. Fragments from 400 MeV helium induced reaction on Al, Cu and Ag samples with 10 μm thickness are measured using this counter. The double differential cross sections from Lithium isotopes to Carbon isotopes from these samples at 30 degree laboratory angle are obtained with clear separation except for low energy region.

1. Introduction

A particle with energy ranging from several tens of MeV to a few GeV (intermediate energy) produces a fragment (products heavier than helium) through nuclear reaction. Energy and angular distribution of fragments still cannot be reproduced well because a theoretical model and its parameters are not specified. The fragment makes a considerable contribution in irradiation effects since it has large damage in a medium through energy deposit in a relatively short range. For example, to evaluate dose by intermediate energy neutron, production rate and energy distribution of reaction products, especially fragment, are indispensable. Evaluation of damage on devices, single event effect, is in same situation. Fragment production data are also important to estimate induced activity of materials around an accelerator, the power of which growth up in recent years. To evaluate not only a reaction model and its parameters but also an irradiation effect, experimental data set are important. The experiments of fragment production in this energy range divide broadly into two methods, a direct measurement and an activation method. The former can provide energy and angular distribution of fragment, the later high precise production cross section and mass yield data. To combine results by these two methods, the results of the direct measurement should be obtained separately about mass and Z since limited number of fragments can be measured by an activation method.

Experimental data of fragment energy and angular distribution with mass and Z separation are scarce except for data of 480 MeV $p + \text{Ag}$ [1]. As a result, there are a few calculation codes which can deal fragment production. To evaluate the theoretical model implemented in such codes, the experimental data for various incident particles, energies and target nuclides are useful. In addition, a reaction mechanism of fragment production will be obvious through this evaluation process. Recently, PISA project is started to gather fragment production data from 200 MeV to GeV proton induced reaction [2].

In this study, we designed an experimental setup for fragment spectroscopy and mass yield study in intermediate energy region. For spectroscopy, a ΔE -E TOF telescope with flight path is used to obtain fragment spectra with mass and Z separation. Detail of the telescope and first results of fragment spectra

are described in following sections.

2. Experimental

Experiments have carried out at HIMAC, NIRS. Figure 1 shows experimental arrangement. Incident particle is He 400 MeV (100 MeV/u). The intensity of helium beam is 1.2×10^{10} [pps]. The beam passes through 100 μm thick aluminum exit window, 1 cm thick air and a 100 μm thick aluminum incident window to enter a scattering chamber which equips a sample changer, an activation sample holder, Farady-cup and a detector telescope. The sample changer can mount 5 different samples with 16 mm ϕ , a ZnS viewer (EJ-440 by Eljen technology) and an α source (Am-241, 3.3 MBq). After pass through the sample, the incident helium beam enters to activation samples held the activation sample holder. The holder is placed at the entrance of Farady-cup which consists of a 1 m depth - 35 mm ϕ internal diameter stainless steel tube and an 80 mm thick graphite column. Samples are graphite 100 μm thick for checking the detector, and Al, Cu and Ag 10 μm thick. Beam profile at both samples, the center of the chamber and the entrance position of the Farady-cup, are confirmed to be less than 5 mm in diameter by using ZnS and polypropylene viewer. Fragments emitted from the sample mounted on the center enter the detector telescope at 30 degree with respect to the incident beam.

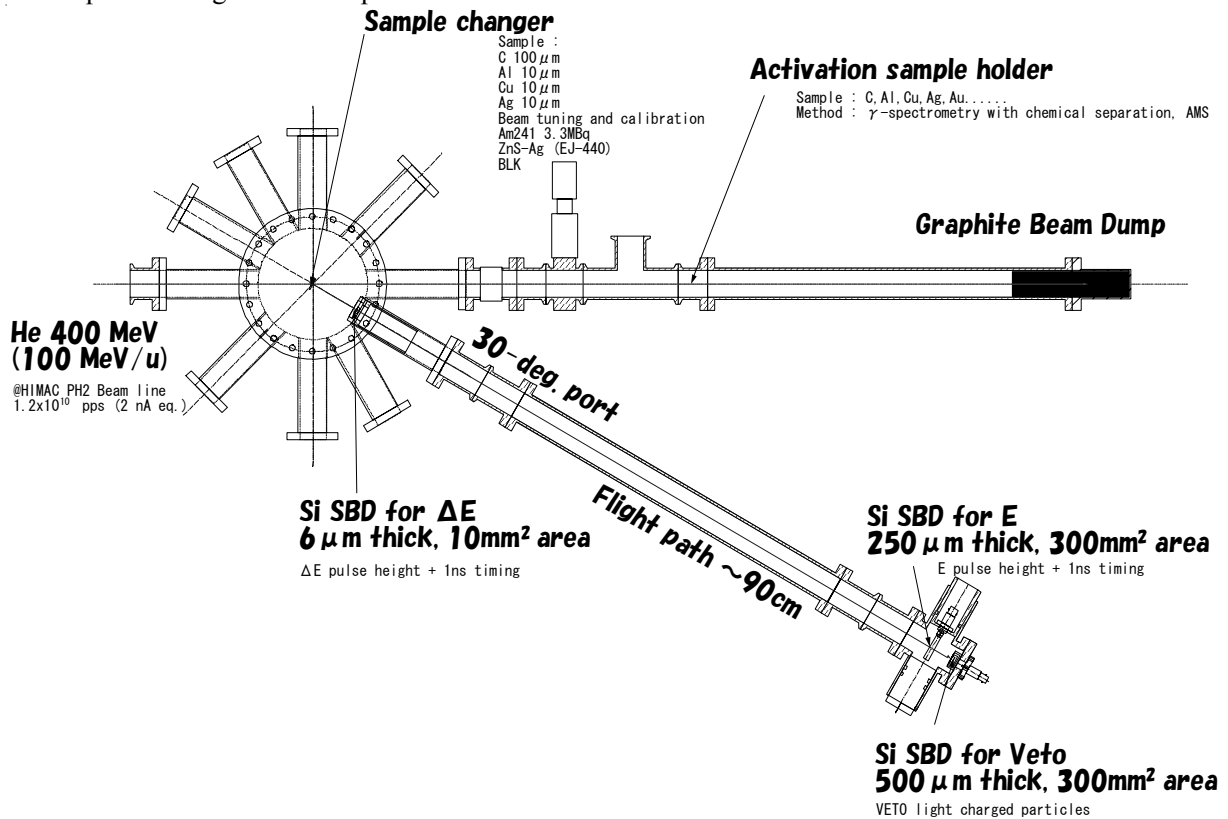


Fig. 1 Experimental arrangement for fragment spectroscopy.

The telescope consisted of three silicon surface barrier detectors (SBDs) of 6 μm , 250 μm and 250 μm thick used as ΔE , E and Veto, respectively. The SBD for ΔE is placed at 7 cm from the sample, which is important to maximize detector efficiency because an active area of the thin SBD is small (10 mm 2). The SBD for E is placed at the 90 cm position from the ΔE . The active area of the SBD is 300 mm 2 .

The SBD for Veto is placed just behind the one for E. The distance is determined with considering mass resolution. The solid angle of this telescope is determined by counting α particles placed at the sample changer. By this array, mass and Z number of a fragment can be identified by ΔE -E and Time-of-flight method, simultaneously. As a ΔE detector, a thin-film scintillator combined with double photo-multiplier readout also tested. An energy resolution of the combination is not sufficient to identify z-number however a timing resolution sufficient.

The outputs from the SBDs are fed to a fast-preamplifiers after pass through Bias-tees. The fast-preamplifier provides an output pulse, rise time of which is less than 5 ns, typically. A digital storage oscilloscope (DSO) is connected with the outputs of the pre-amplifiers to record the waveforms from each SBDs, because the signal is too fast to analyze pulse height using a conventional amplifier module. Trigger signal for DSO is generated from output signal of the pre-amplifier using a constant fraction discriminator to pickup events with a low pulse height. To enhance data accumulation rate, the DSO is operated with a segment recording mode. The data are sent to PC through Ethernet when its memory filled up. Typical dead time rate is 0.6~0.8 which is corrected using the ratio of real triggers to accumulated events. Owing to close position of ΔE counter, only 2 hours are needed to obtain following results for each samples. It is important because the period is enough as irradiation time of the activation sample. Products of the activation sample are determined using γ -spectrometry with chemical separation and AMS. Details of the procedures are described at other paper [3].

3. Data Analysis

From the waveform data, pulse height and arrival time are determined for each events. Pulse height is obtained from integration of the pulse. Arrival time is determined as the time when the signal reaches 20 % of the peak value. These values are booked as column-wise-ntuple data for PAW event by event. Coincidence analysis and particle identification are performed using PAW. Figures 2 and 3 show scatter plots of ΔE -E and E-TOF, respectively. As shown in these figures, separation of Z and mass number is clear except for low energy particles. The relationship between energy and pulse height is determined using deposit energy of punch through particle at E SBD. Using the relationship between mass, energy and time-of-flight, a mass-E scatter plot is made as shown in figure 4. Energy loss corrections in ΔE detector and the sample are performed using range-energy curves obtained from SRIM code [4]. Normalization factors are determined by normalizing about beam current, number of sample atoms and solid angle.

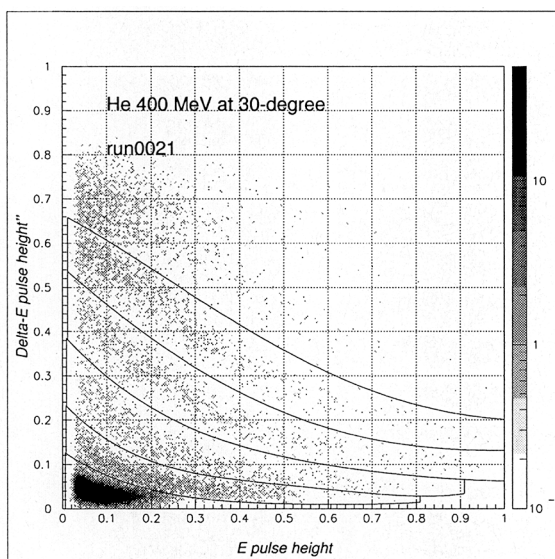


Fig. 2 ΔE -E spectrum for Al sample.

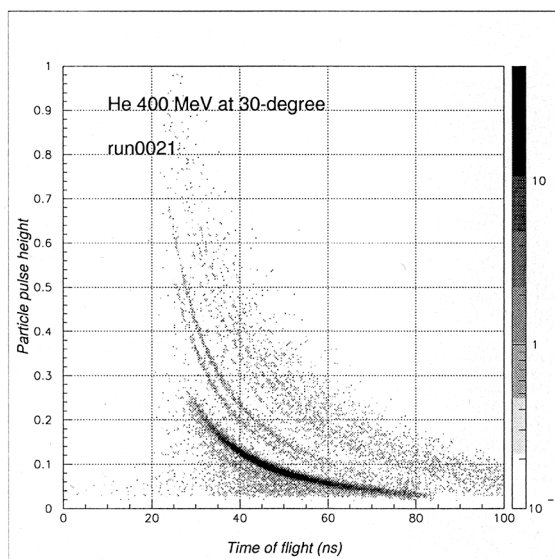


Fig. 3 E-TOF spectrum for Al sample.

4. Result

Figure 5 shows results of double differential cross sections for isotopes of Lithium, Beryllium, Boron and Carbon for each samples at 30 degree on laboratory frame. Upper energies of these spectrum are limited from the thickness of SBD. For Lithium, the energy corresponds to ≈ 60 MeV. In these figures, there are still problems since Z and mass resolution are not enough to identify fragments below ≈ 20 MeV. For example, there are a few ^8Be events which should not be observed owing to its short life. As shown in figure 4, these events are originated by timing walk. The almost all spectra will be still affected by the walk at low energy. Since the ΔE -E separation is also not enough in low E region, this method should be improved with focusing on the measurement of low energy fragments.

From fig 5, statistics of main products are in fairly sufficiency such as Lithium 6,7, Beryllium 7,9,

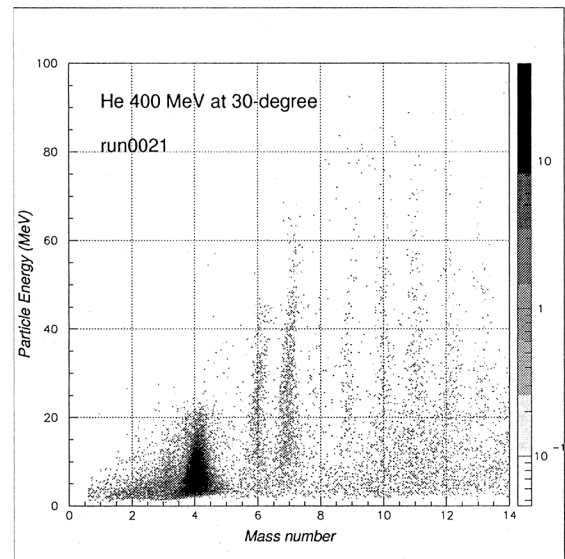


Fig. 4 Mass-E spectrum for Al sample.

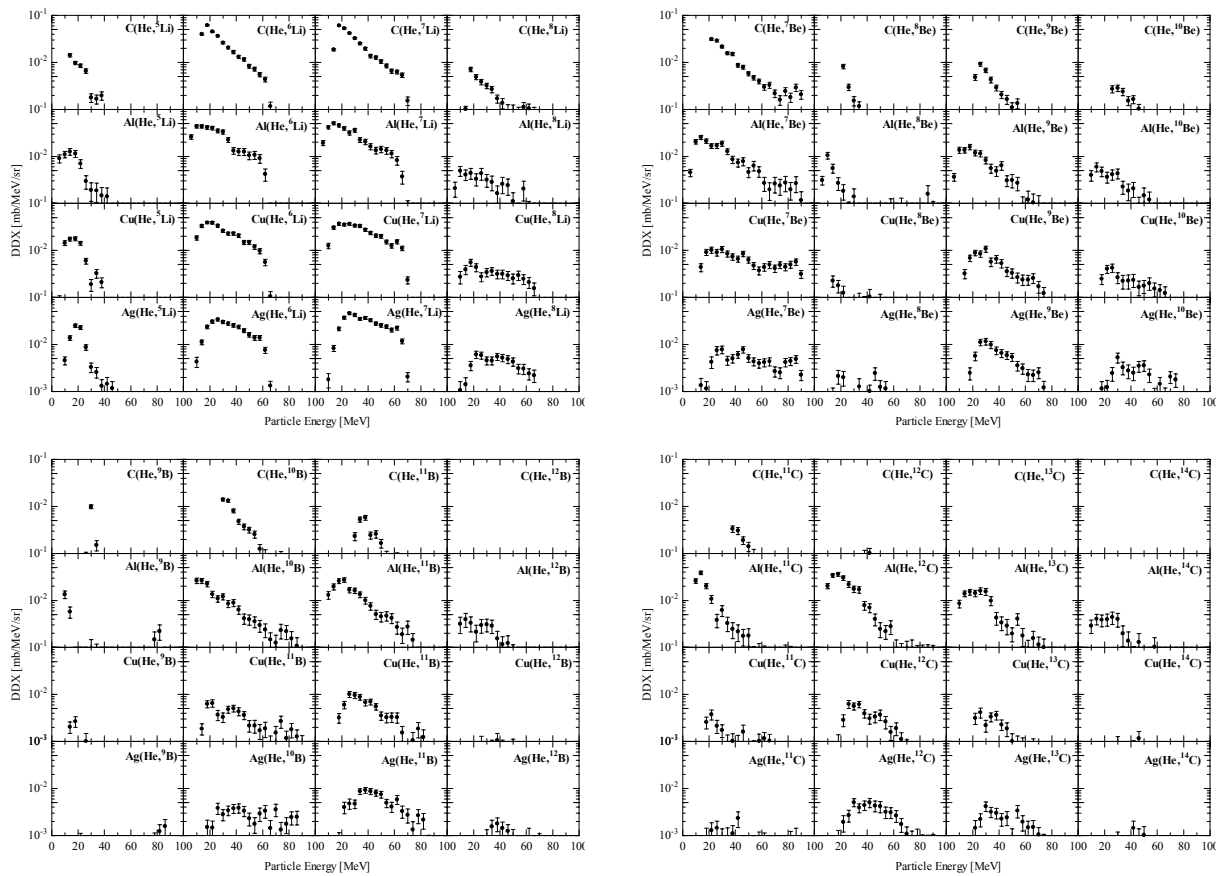


Fig. 5, Fragment production cross section at 30-degree for C, Al, Cu, Ag sample.

Boron 10,11 and Carbon 12,13, however counting time and beam current are not so much. For these fragments, target dependencies in energy spectrum are roughly observed. Thresholds of the system are too high to observe evaporation peak because of relatively high energy losses in the target for the Cu and Ag case. The target thickness can be reduced to half of its thickness since it will be compensated by dead time reduction using a high speed DSO.

5. Conclusion

In the present work, a counter telescope which can determine fragment mass and Z number by using time-of-flight and ΔE -E method is prepared for an experimental setup which enables fragment spectroscopy and mass yield study, simultaneously, in intermediate energy. By using this setup, fragment spectra with mass and Z number separation are obtained for C, Al, Cu and Ag samples with only two hour measurement with 1.2×10^{10} pps incident helium beam. The mass and Z resolution of the spectra are not sufficient in low energy region. Nevertheless, target dependencies in energy spectrum are observed for isotopes of Lithium, Beryllium, Boron and Carbon. These results have led to next experiments; incident energy and angular dependence are intended with the improvement of the low energy fragment measurement.

References

1. R.E.L.Green et al., Phys.Rev.C29 (1984) 1806
2. R.Barna et al., Nucl. Instrm. Meth. A519 (2004) 610
3. H.Matsumura et.al, Radiochim. Acta 93, 497-501 (2005)
4. J.F.Ziegler et al., The stopping and Range of Ions in Solids. Pargamon, New York (1985)

3.4 Measurements of cross-sections of producing short-lived nuclei with 14 MeV neutrons

- $^{27}\text{Al}(n, \alpha)^{24\text{m}}\text{Na}$, $^{144}\text{Sm}(n, 2n)^{143\text{m}}\text{Sm}$, $^{206}\text{Pb}(n, 2n)^{205\text{m}}\text{Pb}$, $^{208}\text{Pb}(n, 2n)^{207\text{m}}\text{Pb}$ -

Kazumasa Arakita¹, Toshiaki Shimizu¹, Kiyoshi Kawade¹,
Michihiro Shibata², Kentaro Ochiai³, Takeo Nishitani³

¹*School of Engineering, Nagoya University*

²*Radioisotope Research Center, Nagoya University*

³*Japan Atomic Energy Agency*

e-mail: k-arakita@ees.nagoya-u.ac.jp

The activation cross-sections producing short-lived nuclei whose half-lives are shorter than a second were measured by the in-beam method. The neutron collimator installed in Fusion Neutronics Source (FNS) at the Japan Atomic Energy Agency (JAEA) was used. The scattering of the collimated neutron was calculated by the Monte-carlo simulation code MCNP-4C, and an appropriately geometrical condition for the in-beam method was considered. The cross-sections of $^{27}\text{Al}(n, \alpha)^{24\text{m}}\text{Na}$ ($T_{1/2}=20.20$ ms), $^{144}\text{Sm}(n, 2n)^{143\text{m1}}\text{Sm}$ ($T_{1/2}=66$ s), $^{144}\text{Sm}(n, 2n)^{143\text{m2}}\text{Sm}$ ($T_{1/2}=30$ ms), $^{206}\text{Pb}(n, 2n)^{205\text{m}}\text{Pb}$ ($T_{1/2}=5.54$ ms) and $^{208}\text{Pb}(n, 2n)^{207\text{m}}\text{Pb}$ ($T_{1/2}=806$ ms) reactions were measured with uncertainties of 4.4 to 23%. The $^{144}\text{Sm}(n, 2n)^{143\text{m2}}\text{Sm}$ reaction was measured for the first time. The systematics for isomer ratios for 14.2 MeV neutrons, that is the ratio between the cross-section for the isomeric state (σ_{m}) and that for the ground state (σ_{g}) were proposed within accuracies a half to two times the ratio itself.

1. Introduction

There are a lot of data of activation cross-sections with 14 MeV neutrons from a viewpoint of the DT fusion reactor design. In general, most of data are long-lived nuclei whose half-lives are longer than several minutes. However, there are few data for short-lived nuclei whose half-lives are equal to or shorter than a few seconds. These data are also important for the nuclear database and improvement of accuracies for the evaluation value. Hence, we aimed to measure the cross-sections producing the short-lived nuclei with 14 MeV neutrons by using the in-beam method [1]. The systematics for the isomer ratio was studied by using the present and the previous results (e.g. [2,3]).

2. Experiment

The d-T neutrons were generated by bombarding a tritiated titanium (Ti-T) target with a 350 keV d^+ -beam at the 0 degree beam line of the FNS at the JAEA. The induced activities were measured with a 36% HPGe detector. Samples were ^{27}Al , ^{144}Sm and $^{206,208}\text{Pb}$, these were 1 mm thick rectangular (10 mm \times 20 mm) or disk-shape (15 mm ϕ), and weights were 0.045 to 0.95 g. In Table1, the chemical form, the isotopic abundance and the weight of samples are listed.

In order to reduce the background at the measuring position, the neutron collimator at the 0 degree beam line was used (Fig.1). The angle between the d^+ -beam and the axis of the collimated neutron beam was 80 degree, which resulted in a 14.2 MeV neutron energy [4]. The diameter of the collimator was 2 cm. The experimental arrangement is shown in Fig.2. The distance between an exit of the collimator and the sample was 15 cm. And the distance between the sample and the HPGe detector surface was 5 cm. The typical neutron fluence rates at the irradiation positions were measured with the standard reaction of $^{27}\text{Al}(n, \alpha)^{24}\text{Na}$ [5]. The typical value at the sample position was $6.5 \times 10^5 \text{ n}\cdot\text{cm}^{-2}\cdot\text{s}^{-1}$. The fast neutron does not damage the HPGe detector by the neutron collimator. However the effect of the scattered neutron from the sample, the sample folder and the atmosphere has to be taken into account. The amount of the scattered neutron was calculated by the MCNP-4C [6]. The result of the calculation is shown in Fig.3. It was found that the neutron fluence rate at the HPGe detector surface was 4.0×10^{-4} times against the sample position.

3. Result

The spectrum for the $^{144}\text{Sm}(n, 2n)^{143\text{m}2}\text{Sm}$ which were measured by the in-beam method are shown in Fig.4. The cross-sections of $^{27}\text{Al}(n, \alpha)^{24\text{m}}\text{Na}$, $^{144}\text{Sm}(n, 2n)^{143\text{m}1}\text{Sm}$, $^{144}\text{Sm}(n, 2n)^{143\text{m}2}\text{Sm}$, $^{206}\text{Pb}(n, 2n)^{205\text{m}}\text{Pb}$ and $^{208}\text{Pb}(n, 2n)^{207\text{m}}\text{Pb}$ reactions were obtained. The results are shown in Fig.5. Uncertainties which are 4.4 to 23% are mainly caused by statistics.

- (1) $^{144}\text{Sm}(n, 2n)^{143\text{m}2}\text{Sm}$ ($T_{1/2} = 30 \text{ ms}$, $E_\gamma = 208 \text{ keV}$); The cross-section was measured for the first time.
- (2) $^{144}\text{Sm}(n, 2n)^{143\text{m}1}\text{Sm}$ ($T_{1/2} = 66 \text{ s}$, $E_\gamma = 754 \text{ keV}$); The cross-sections had been measured with other methods [7,8] for comparison, the present are agreement with those value.
- (3) $^{27}\text{Al}(n, \alpha)^{24\text{m}}\text{Na}$ ($T_{1/2} = 20.20 \text{ ms}$, $E_\gamma = 472 \text{ keV}$); Because the scattered neutron reacts the Al housing of the HPGe detector, the γ -rays from the $^{27}\text{Al}(n, \alpha)^{24\text{m}}\text{Na}$ reaction become a background. Hence, it was found that the counting rate of the 472 keV γ -ray as the background was 0.5 cps, the effect were corrected properly (Fig.6). The evaluated data for this reaction listed in FENDL/A-2.0 [9] were underestimated 0.63 times as small as the present result, approximately.
- (4) $^{206}\text{Pb}(n, 2n)^{205\text{m}}\text{Pb}$ ($T_{1/2} = 5.54 \text{ ms}$, $E_\gamma = 988 \text{ keV}$); The broken line shows the evaluated data of FENDL/A-2.0 for the ground state. It was found that σ_{m} is half σ_{g} .
- (5) $^{208}\text{Pb}(n, 2n)^{207\text{m}}\text{Pb}$ ($T_{1/2} = 806 \text{ ms}$, $E_\gamma = 1064 \text{ keV}$); The evaluated data for this reaction listed in FENDL/A-2.0 were overestimated 1.37 times as large as the present result, approximately. Re-evaluations except for the $^{144}\text{Sm}(n, 2n)^{143\text{m}1}\text{Sm}$ reaction are strongly recommended.

4. Systematics

The isomer ratio was obtained by using the data set of the cross-section with 14.2 MeV neutrons, and the systematics was proposed. The value of $(\sigma_{\text{high}} / \sigma_{\text{low}})$ were plotted as a function of $(J^{\text{m}} - J^0)$ as shown in Fig.7, where σ_{high} is the cross-section producing higher isomeric state and σ_{low} is the cross-section producing lower one, and $(J^{\text{m}} - J^0)$ is the difference of spin between the isomeric state of the product

nucleus and the ground state of the target one. In the case of Al shown in Fig.8, $(J^m - J^0) = 1 - 5/2 = -3/2$, $(\sigma_{\text{high}} / \sigma_{\text{low}}) = (\sigma_g / \sigma_m)$. The solid line was obtained by fitting the data, and it could predict the ratio within accuracies a half to two times the ratio itself.

5. Conclusion

We measured the cross-sections producing short-lived nuclei whose half-lives are between 5.54 and 806 ms by the in-beam method. We proposed the systematics for the isomer ratio for 14.2 MeV neutrons, which could predict the ratio within accuracies a half to two times the ratio itself.

Acknowledgement

The authors would like to express their thanks to Messrs. C. Kutsukake, S. Tanaka, Y. Abe, M. Seki, and Y. Oginuma for the stable operation of the accelerator at FNS.

References

- [1] T. Shimizu, I. Miyazaki, K. Arakita, M. Shibata, K. Kawade, J. Hori, T. Nishitani; Annals of Nuclear Energy 32 (2005) 949-963
- [2] C.Konno, Y.Ikeda, K.Oishi, K.Kawade, H.Yamamoto, H.Maekawa; JAERI-1329 (1993)
- [3] Y. Kasugai, Y. Ikeda, Y. Uno, H. Yamamoto, K. Kawade; JAERI-Research 2001-025
- [4] H. Sakane, Y. Kasugai, F. Maekawa, Y. Ikeda, K. Kawade; JAERI-Conf 99-002
- [5] H. Maekawa, Y. Ikeda, Y. Oyama, S. Yamaguchi, T. Nakamura; JAERI-M 83-219
- [6] J. F. Briesmeister, Ed, "MCNP-4 General Monte Carlo N-Particle Transport Code, Version 4C" LA-13709-M (2000)
- [7] I. A. Reyhancan, M. Bostan, A. Durusoy, A. Elmali, A. Baykal, Y. Oezbir; Annals of Nuclear Energy 30 (2003) 1539-1547
- [8] H. Sakane, Y. Kasugai, M. Shibata, T. Iida, K. Kawade, A. Takahashi, T. Fukahori; Annals of Nuclear Energy 28 (2001) 1175-1192
- [9] A. B. Pashchenko, Summary Report for IAEA Consultants' Meeting on Selection of Evaluations for the FENDL/A-2.0 Activation Cross Section Library. INDC (NDS)-341, International Atomic Energy Agency (1996)

Table 1. Chemical form, weight and abundance of the samples.

Target nuclei	Chemical form	Typical weight [mg]	Abundance [%]
²⁷ Al (Natural)	Al	949.6	²⁷ Al : 100
¹⁴⁴ Sm (Enriched)	Sm ₂ O ₃	45.01	¹⁴⁴ Sm : 96.47
²⁰⁶ Pb (Enriched)	Pb	138.0	²⁰⁶ Pb : 99.56
²⁰⁸ Pb (Enriched)	Pb	123.1	²⁰⁸ Pb : 99.86

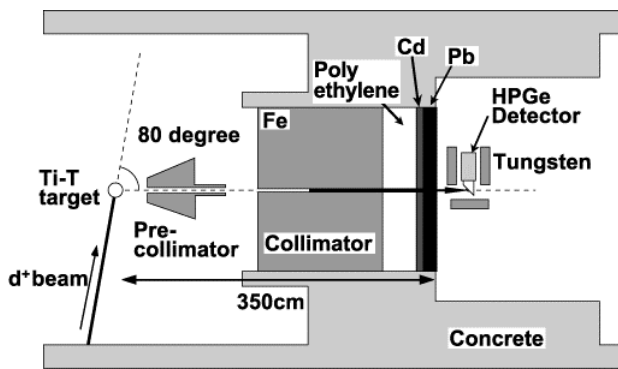


Fig.1. The schematic view of the 14 MeV neutron source and the neutron collimator system. The collimator is composed of Fe, Polyethylene, Cd and Pb.

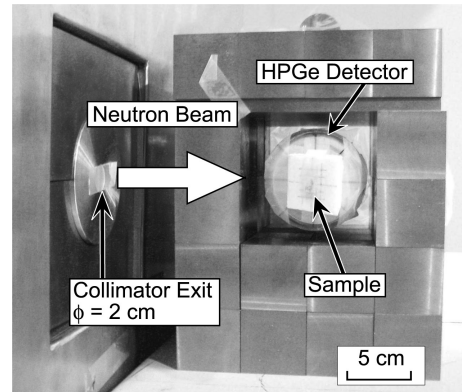


Fig.2. The schematic view of the experimental arrangement. Tungsten blocks are used to prevent the HPGe detector from the background γ -rays.

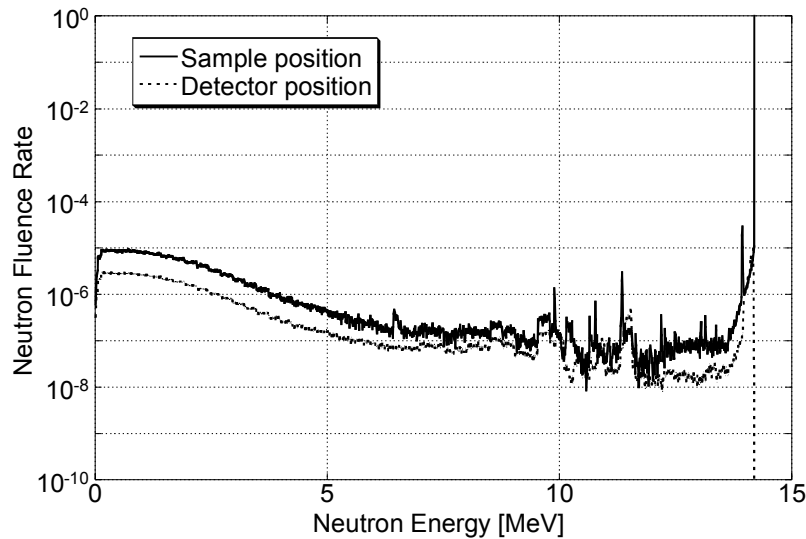


Fig.3. Neutron spectrum calculated by the MCNP-4C. The solid and broken lines indicate the neutron spectrum at the sample position and the detector position, respectively.

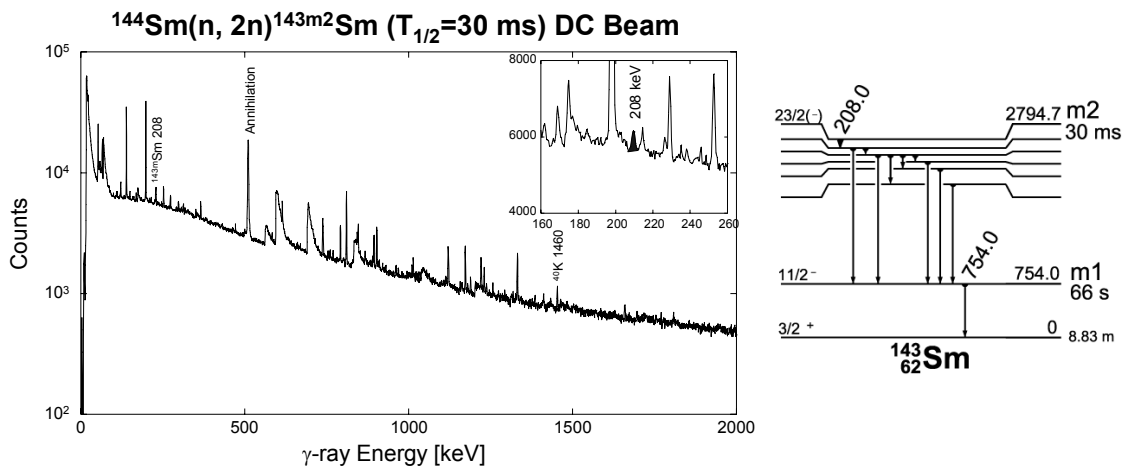


Fig.4. The measured HPGe spectrum for γ -rays from $^{144}\text{Sm}(n, 2n)^{143m2}\text{Sm}$ reaction with the in-beam method and a partial level scheme of the ^{143}Sm .

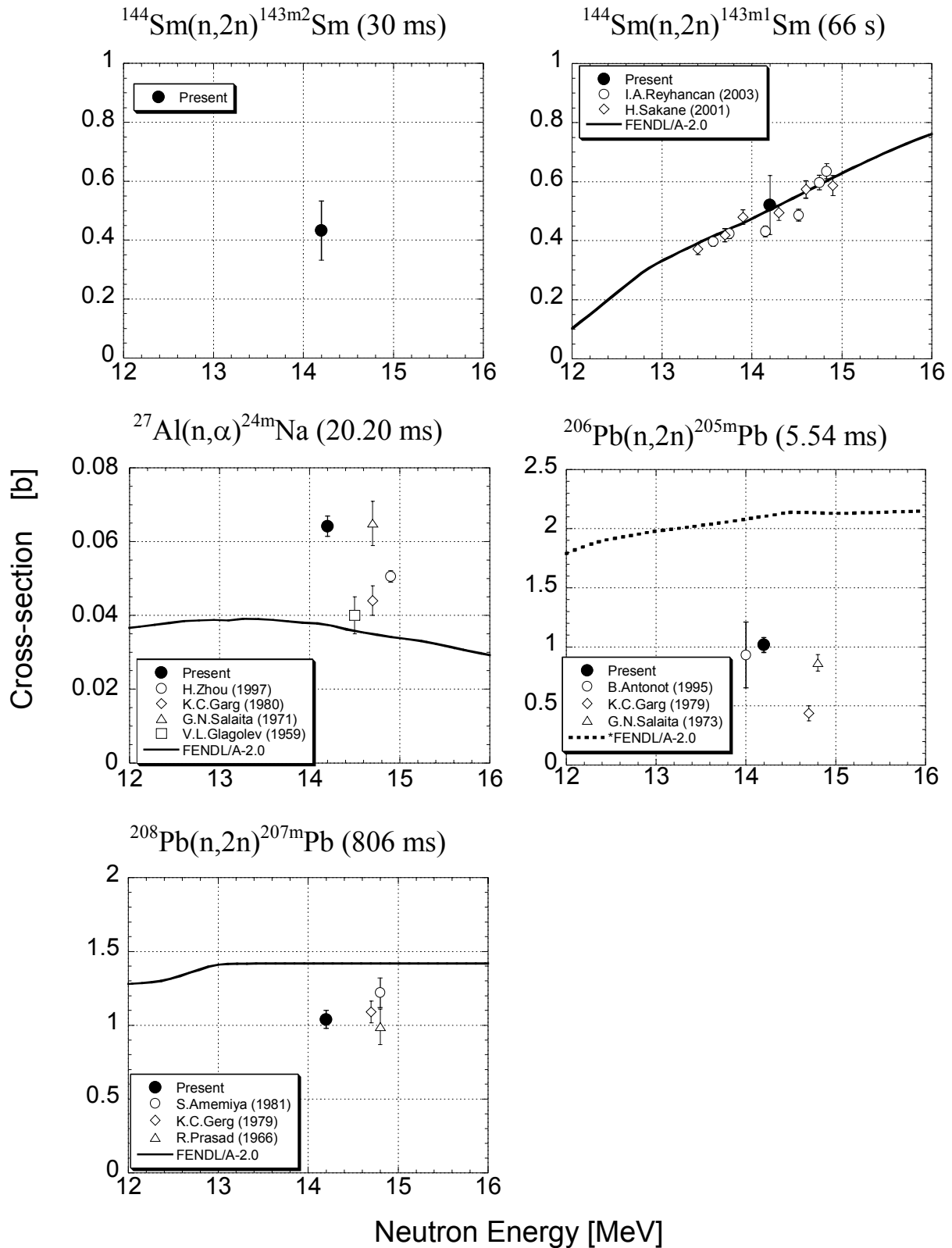


Fig.5. The experimental cross-section data compared with the previous ones and the evaluated data in FENDL/A-2.0.

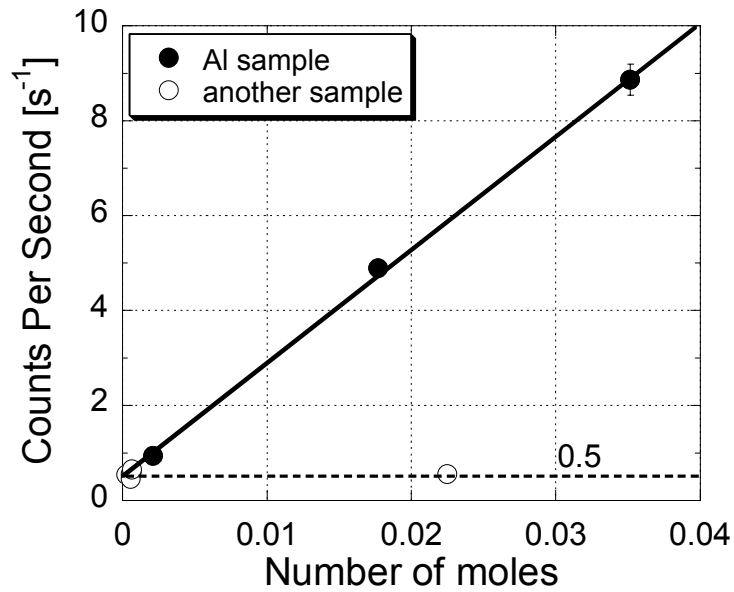


Fig.6. The relationship between the number of moles of the sample material and the background counting rate (cps). The solid and open circles indicate the cps of the 472 keV γ -ray from the Al samples and the other samples, respectively.

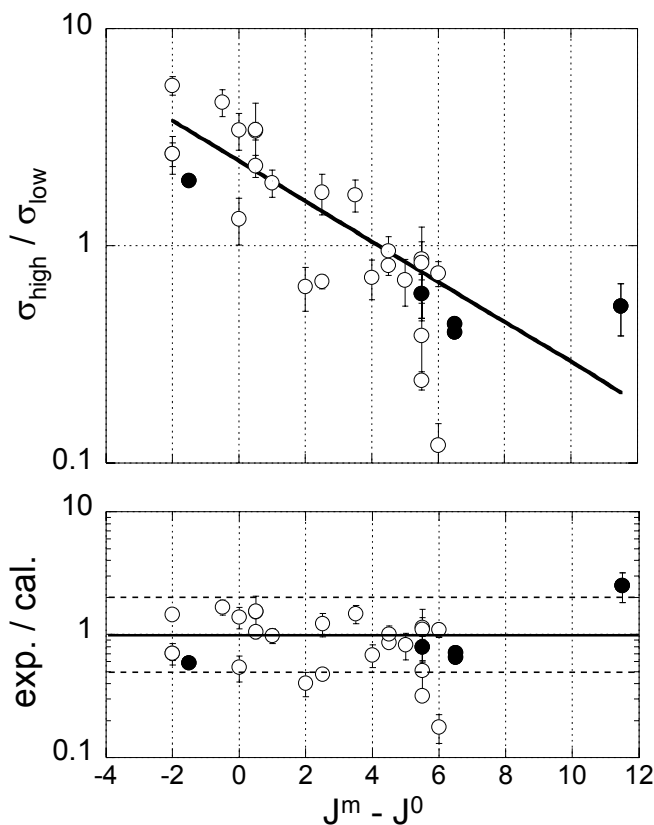


Fig.7. The relationship between $(J^m - J^0)$ and $(\sigma_{\text{high}}/\sigma_{\text{low}})$. The solid line was obtained by fitting the data.

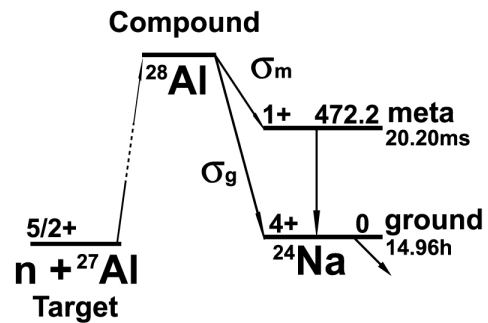


Fig.8. The schematic diagram for the isomer cross section of $^{27}\text{Al} (n, \alpha) ^{24}\text{Na}$ reaction.

3.5 Measurement of Angle-correlated Differential (n,2n) Reaction Cross Section with Pencil-beam DT Neutron Source

S. Takaki, K. Kondo, S. Shido, H. Miyamaru, I. Murata, K. Ochiai* and T. Nishitani*

Division of Electric, Electronic and Information Engineering,
Graduate School of Engineering, Osaka University, Suita, Japan

*Japan Atomic Energy Agency, Tokai-mura, Ibaraki, Japan

e-mail: takagi@ef.eie.eng.osaka-u.ac.jp

Angle-correlated differential cross-section for ${}^9\text{Be}(n,2n)$ reaction has been measured with the coincidence detection technique and a pencil-beam DT neutron source at FNS, JAEA. Energy spectra of two emitted neutrons were obtained for azimuthal and polar direction independently. It was made clear from the experiment that there are noise signals caused by inter-detector scattering. The ratio of the inter-detector scattering components in the detected signals was estimated by MCNP calculation to correct the measured result. By considering the inter-detector scattering components, the total ${}^9\text{Be}(n,2n)$ reaction cross-section agreed with the evaluated nuclear data within the experimental error.

1. Introduction

${}^9\text{Be}(n,2n)$ reaction cross-section is quite important value in order to design fusion reactor. However, because ${}^9\text{Be}(n,2n)$ reaction makes no radioactive isotopes, the foil activation method cannot be used. The cross-section can be measured by the detection of α -particles. But it is impossible by the method to obtain emitted neutron energy spectrum of emitted neutron directly, which is very important in the case of light nuclei because the evaporation process may not be directly applied to evaluate the spectrum. Up to now, the method using coincidence detection technique was established.^[1] In the present study, this method was applied to measure energy and angular dependent distributions of ${}^9\text{Be}(n,2n)$ reaction.

2. Experimental procedure

In present experiment, we used a pencil-beam DT neutron source of Fusion Neutronics Source (FNS) in Japan Atomic Energy Agency (JAEA). It is the only existing pencil-beam DT neutron source in the world, which supplies an excellent experimental condition, i.e., 10^6 n/cm²/sec inside the beam and several hundred n/cm²/sec outside. One can thus arrange neutron detectors very close to the sample to get a very good signal to noise (S/N) ratio.

The schematic experimental arrangement around detectors is shown in Fig.1. The distance between the neutron source and a beryllium sample (2cm in diameter, 2cm long) was 485cm. Two spherical

NE213 (4cm in diameter) detectors to detect neutrons emitted simultaneously by the (n,2n) reaction were used and located at 18.8cm from the beryllium sample. An ^{238}U fission chamber was located on the beam line behind the sample to monitor the neutron flux. As shown in Fig.2, three angular parameters (θ_0, θ, ϕ) with respect to the detector position were defined in which θ_0 and θ are polar angles of emitted two neutrons and ϕ is the azimuthal angle of detector 2 from detector 1. Measurement points were determined by the combination of these angle parameters.

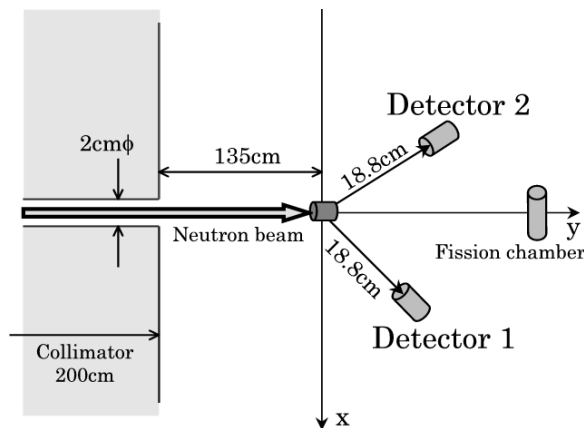


Fig.1 Schematic experimental arrangement

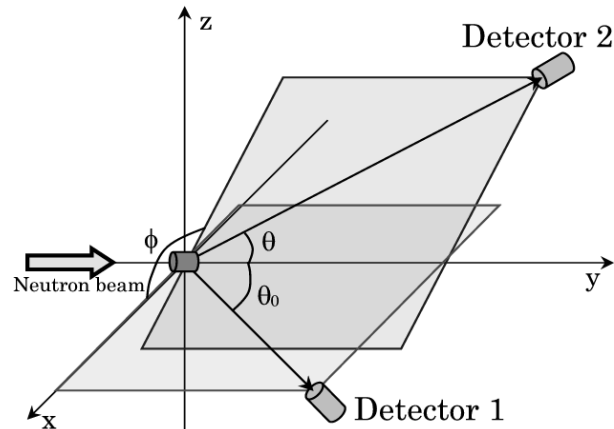


Fig.2 Arrangement around sample and detectors

Because two detectors are positioned very close with each other, there are neutrons, which can pass through both detectors in turn by inter-detector scattering. The existence of such a signal was confirmed by the measurement with a carbon sample, in which (n,2n) reaction cannot take place with 14MeV neutron, and could not be neglected. A polyethylene shielding block up to 10.16cm in thickness was located between two detectors depending on the measurement points to prevent inter-detector scattering components.

Because NE213 detectors are sensitive also to gamma ray, n/ γ discrimination was applied by the pulse shape discrimination technique. Two amplifiers with different gains were used to cover a wider measurable energy range. Timing difference spectrum of anode signals of the two detectors was used to extract the coincidence signals. In the time difference spectrum, time-dependent signals, i.e., coincidence signals make a peak on a flat spectrum of time-independent signals, i.e., chance coincidence signals. The region including the peak was gated and defined as Foreground (FG), and the region of time-independent signals was defined as Background (BG). Eight pulse height spectra were measured for one case considering two detectors (1/2), two gains (high/low) and FG and BG. Details of the electric circuit of the measurement is described in ref.[1].

3. Data processing

Obtained pulse height spectra were transformed into light output spectra. Examples of measured pulse height spectra are shown in Fig.3. The position of Compton edge made by 1.275MeV gamma ray emitted from ^{22}Na was used in the light unit calibration. The BG spectra (y_{BG}) were subtracted from FG spectra (y_{FG}) by following equation.

$$y = y_{FG} - \alpha y_{BG} \quad (1)$$

where, α is the ratio of the gate widths between FG and BG spectra.

The net light output spectra were unfolded using FORIST^[2] unfolding code. Necessary response function was calculated with SCINFUL^[3]. And the energy spectra were obtained by the following equations,

$$y(\theta_0, \theta, \phi, E) = R \cdot x(\theta_0, \theta, \phi, E) \quad (2)$$

$$\sigma_i(\theta_0, \theta, \phi, E) = \frac{x_i(\theta_0, \theta, \phi, E)}{N \cdot FC \cdot C \cdot d\Omega_i \cdot d\Omega_j \cdot f_j} \quad (3)$$

where, subscript in eq.(3) represent either detector 1 or detector 2, R is the response matrix of the NE213 detector, x_i is the unfolded spectrum, σ_i is the energy spectrum, N is the number of nuclei of the sample, FC is the integrated counts of the fission chamber monitor, C is the conversion factor of FC into the neutron flux at the sample, $d\Omega_i$, $d\Omega_j$ is the solid angle of each detector, f_j is the efficiency of detector j . The efficiency of the other detector was considered in the response matrix. The conversion factor C was determined by the activation method using aluminum foil. The angle-correlated differential cross-section was obtained by integrating the energy spectrum.

As for the correction of the inter-detector scattering effect, the detection rate of inter-detector scattering component was estimated by Monte Carlo calculation with MCNP^[4] and a precise model of the experimental arrangement.

4. Results and discussion

Figure4 shows the obtained energy spectra. In the spectra, the inter-detector scattering

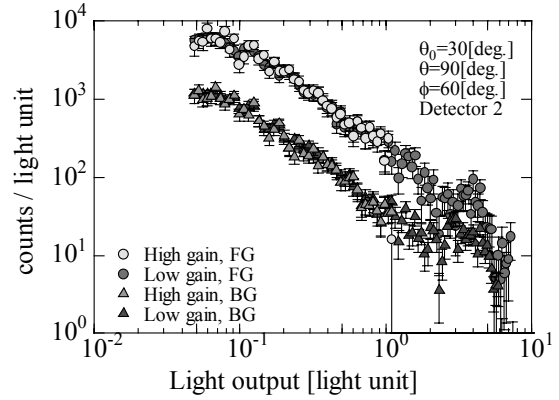


Fig.3 Measured light output spectra at described measurement point

components are included. The error bar in Fig.4 contains only statistical error. As show in the figure, the oscillation due to poor statistics is observed especially in the high energy region above 7MeV. Since there are no evaluated data, which can be compared with the spectra in Fig.4, it is difficult to discuss the validity of the nuclear data. But these data will be helpful to study the mechanism of ${}^9\text{Be}(n,2n)$ reaction in the future.

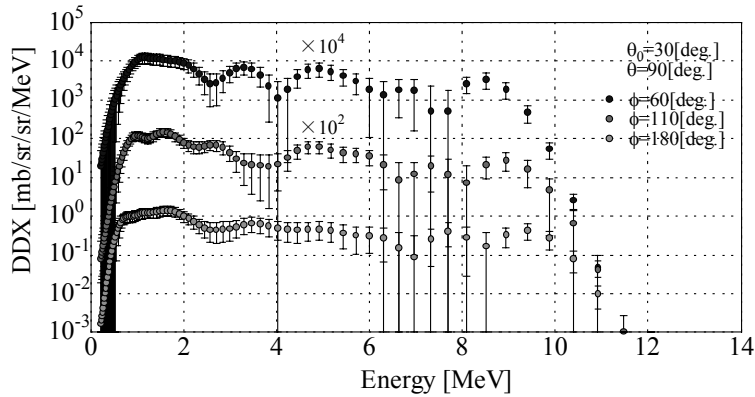


Fig.4 Obtained energy spectra at each angle

From results of the MCNP calculation, the rate of the inter-detector scattering component in the angle-correlated differential cross-section was estimated to be about 5 to 40% as shown in Fig.5. The rate increases as the distance between two detectors becomes closer. And it was found that the component was effectively suppressed by the polyethylene shield.

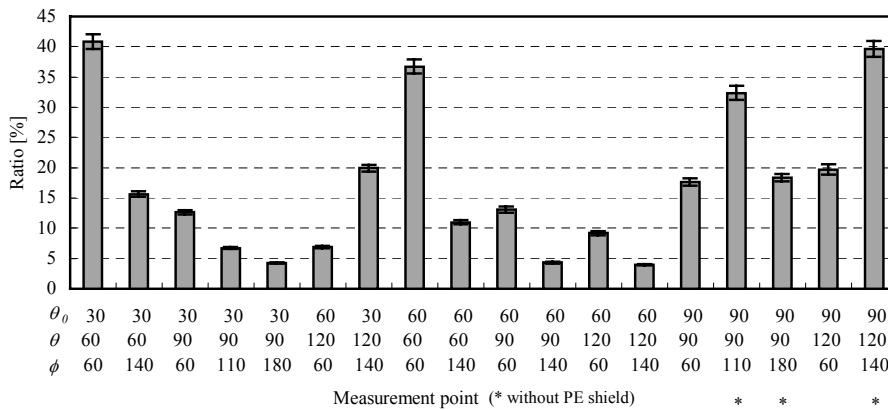


Fig.5 The ratio of the inter-detector scattering component

Figure 6 shows the azimuthal distribution at $\theta_0=90$ deg. and Fig.7 shows the polar distribution at each scattering angle (θ_0 and ϑ) of the angle-correlated differential cross-section after subtraction of the inter-detector scattering component.

There was some azimuthal structure although it is not taken into consideration in the evaluated data. And there was a strong forward oriented polar distribution. These distributions would mainly reflect reaction kinematics according to many reaction processes included in ${}^9\text{Be}(n,2n)$ reaction.

The angular differential cross-section for the polar angle θ_0 was obtained by integrating the distribution over the polar angle θ . Figure 8 shows the comparison of the angular distribution of cross-section with JENDL-3.3^[5]. The angular distribution measured by Takahashi et al.^[6] is also shown in Fig.8. It was measured by the TOF method. And it agrees well with this experiment. Especially in forward scattering angle, agreement between this experiment and the evaluated data was excellent, although there was underestimation in the JENDL-3.3 at a backward angle. Obtained total cross-section is $418 \pm 5.4\text{mb}$, which is a little larger than the value evaluated in JENDL-3.3 of 380.85mb (lower energy limit was 800keV). This difference would result from the underestimation at the backward angle. Therefore further detail measurements at back scattering angles are needed.

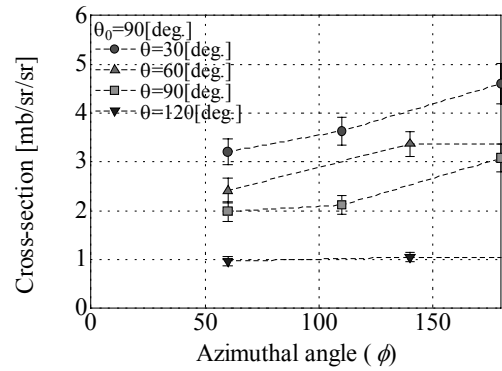


Fig.6 The azimuthal distribution of ${}^9\text{Be}(n,2n)$ reaction cross-section at $\theta_0=90$ deg.

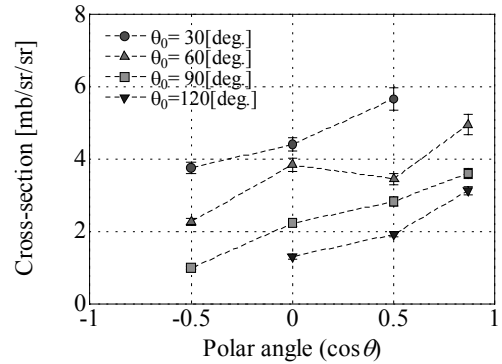


Fig.7 The polar distribution of ${}^9\text{Be}(n,2n)$ reaction cross-section at each scattering angle

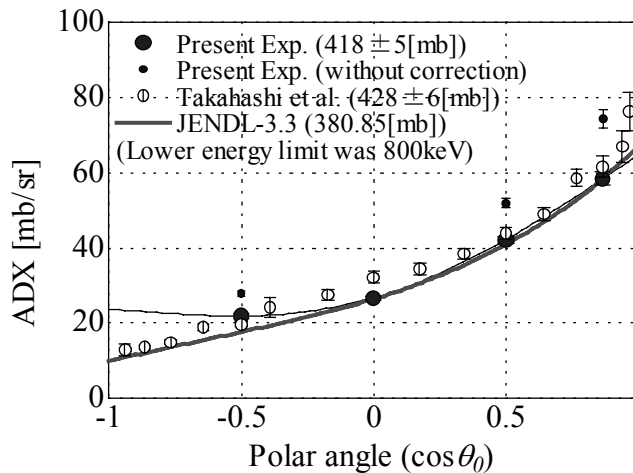


Fig.8 The angular differential cross-section for ${}^9\text{Be}(n,2n)$ reaction compared with JENDL-3.3

5. Conclusion

Using the pencil-beam DT neutron source and the coincidence detection technique, angle-correlated energy differential cross-section for ${}^9\text{Be}(n,2n)$ reaction was measured successfully. Noise signals caused by the inter-detector scattering component were taken into consideration and subtracted according to the calculation. As for in the energy spectra, measurement with better statistics is required to discuss the validity. However, the integral value of the energy spectrum, that is the total cross-section, has an acceptable accuracy, and could be compared with the evaluation to give an excellent agreement with JENDL-3.3. Since the longitudinal distribution of ${}^9\text{Be}(n,2n)$ reaction and its energy spectrum was quite new measurement value, which has been measured very few, more investigation will be required in order to find out the nuclear reaction of beryllium precisely.

Acknowledgements

The authors wish to acknowledge the FNS staff for their excellent operation of the FNS accelerator: Mr. Kutsukake, Mr. Tanaka, Mr. Abe, Mr. Seki and Mr. Oginuma.

References

- [1] I. Murata et al., *J. Nucl. Sci. Technol.*, **Sup. 2**, 433 (2002)
- [2] R. H. Johnson: "FORIST:Neutron Spectrum UnfoldingCode - Iterative Smoothing Technique", PSR-92, ORNL/RSIC (1975).
- [3] J. K. Dickens: "A Monte Carlo Based Computer Program to Determine a Scintillator Full Energy Response to Neutron Detector for En Between 0.1 and 80 MeV:User's Manual and FORTRAN Program Listing", ORNL-6462 (1988).
- [4] J. F. Briesmeister, Ed.: "MCNP – A General Monte Carlo N-Particle Transport Code, Version 4C", LA-13709-M (2000).
- [5] K. Shibata et al. "Japanese Evaluated Nuclear Data Library Version 3 Revision-3: JENDL-3.3", *J. Nucl. Sci. Technol.*, **39**, 1125 (2002).
- [6] A. Takahashi et al. "Double differential neutron emission cross sections at 14.1MeV –Volume-I-," *OKTAVIAN Report*, **A-87-03**, Osaka University, Japan (1987)

3.6

Study on keV-neutron capture cross sections and capture γ -ray spectra of $^{117, 119}\text{Sn}$

J. Nishiyama^{1,*}, M. Igashira¹, T. Ohsaki¹, G. N. Kim², W. C. Chung³ and T. I. Ro³

1) *Research Laboratory for Nuclear Reactors, Tokyo Institute of Technology, 2-12-1-N1-26*

Okayama, Meguro-ku, Tokyo 152-8550, Japan

**)E-mail: jun-nishiyama@nr.titech.ac.jp*

2) *School of Physics and Energy Science, Kyungpook National University, 1370 Sankyok-dong,*

Buk-gu, Daegu 702-701, Korea

3) *Department of Physics, Dong-A University, 840 Hadan 2-dong, Saha-gu, Busan 604-714, Korea*

The capture cross sections and capture γ -ray spectra of $^{117, 119}\text{Sn}$ were measured in an incident neutron energy region from 10 to 100 keV and at 570 keV, using a 1.5-ns pulsed neutron source by the $^7\text{Li}(p,n)^7\text{Be}$ reaction and a large anti-Compton NaI(Tl) γ -ray spectrometer. A pulse-height weighting technique was applied to observed capture γ -ray pulse-height spectra to derive capture yields. The capture cross sections of $^{117, 119}\text{Sn}$ were obtained with the error of about 5% by using the standard capture cross sections of ^{197}Au . The present cross sections were compared with previous experimental data and the evaluated values in JENDL-3.3 and ENDF/B-VI. The capture γ -ray spectra of $^{117, 119}\text{Sn}$ were derived by unfolding the observed capture γ -ray pulse-height spectra. The calculations of capture cross sections and capture γ -ray spectra of $^{117, 119}\text{Sn}$ were performed with the EMPIRE-II code. The calculated results were compared with the present experimental ones.

1. Introduction

Recently, a great interest has been taken in the study on the nuclear transmutation of Long-Lived Fission Products (LLFPs: ^{79}Se , ^{93}Zr , ^{99}Tc , ^{107}Pd , ^{126}Sn , ^{129}I , ^{135}Cs) generated in nuclear fission reactors. The neutron capture cross sections of LLFPs are important physical quantities for the study on the transmutation of LLFPs, because performance of transmutation system using neutron capture reaction mainly depends on these quantities. However, there is no experimental data for neutron capture cross section of ^{126}Sn , because the preparation of high-purity sample is difficult and, moreover, γ -ray radiation from a sample causes a serious background.

On the other hand, keV-neutron capture cross sections and capture γ -ray spectra of stable Sn isotopes contain important information useful for the theoretical calculation of the capture cross sections of ^{126}Sn . Thus, we started a systematic measurement of keV-neutron capture cross sections and capture γ -ray spectra of stable Sn isotopes. In the present contribution, the results for $^{117, 119}\text{Sn}$ are shown.

2. Experimental procedure and data processing

The capture cross sections and capture γ -ray spectra of $^{117, 119}\text{Sn}$ were measured in an incident neutron energy region from 10 to 100 keV and at 570 keV, using the 3-MV Pelletron accelerator of the Research Laboratory for Nuclear Reactors at the Tokyo Institute of Technology. Pulsed keV neutrons were produced from the $^7\text{Li}(p,n)^7\text{Be}$ reaction by bombarding a Li-evaporated copper disk with a 1.5-ns bunched proton beam from the accelerator. The pulse-repetition rate was 4 MHz. The $^{117, 119}\text{Sn}$ samples were highly isotopically enriched metal plates with the net weight of about 1 g. Capture γ rays were detected with a large anti-Compton NaI(Tl) spectrometer¹⁾ by means of a time-of-flight method.

A pulse-height weighting technique²⁾ was applied to the observed capture γ -ray pulse-height spectra to obtain capture yields. The capture cross sections of $^{117, 119}\text{Sn}$ were derived using the standard capture cross sections of ^{197}Au ³⁾. The capture γ -ray spectra were derived by unfolding the observed capture γ -ray pulse-height spectra.

3. Calculations

The calculation of capture cross sections and capture γ -ray spectra of $^{117, 119}\text{Sn}$ were performed with the Empire-II code⁴⁾ in an incident neutron energy region from 10 to 1000 keV using three global optical model parameter sets (Koning-Delaroche, Wilmore-Hodgson, and Moldauer) and three different level densities (Empire-specific, Gilbert-Cameron, and Hartree-Fock-BCS).

4. Results and discussion

The capture cross sections of $^{117, 119}\text{Sn}$ were derived with the error of about 5%. The present results of ^{119}Sn are compared in Fig.1 with previous experimental data^{5, 6)} and the evaluated values in JENDL-3.3⁷⁾ and ENDF/B-VI⁸⁾.

The capture γ -ray spectrum of ^{119}Sn in incident neutron energy region from 15 to 100 keV is shown in Fig.2. The characteristic primary transitions from the capture states to the ground and first excited states are observed.

The calculated results of capture cross sections of ^{119}Sn are shown Fig.3 and those of capture γ -ray spectrum are shown Fig.4. As seen from Figs.3 and 4, Gilbert-Cameron level density is better than others, but it is not enough to reproduce the present experimental results.

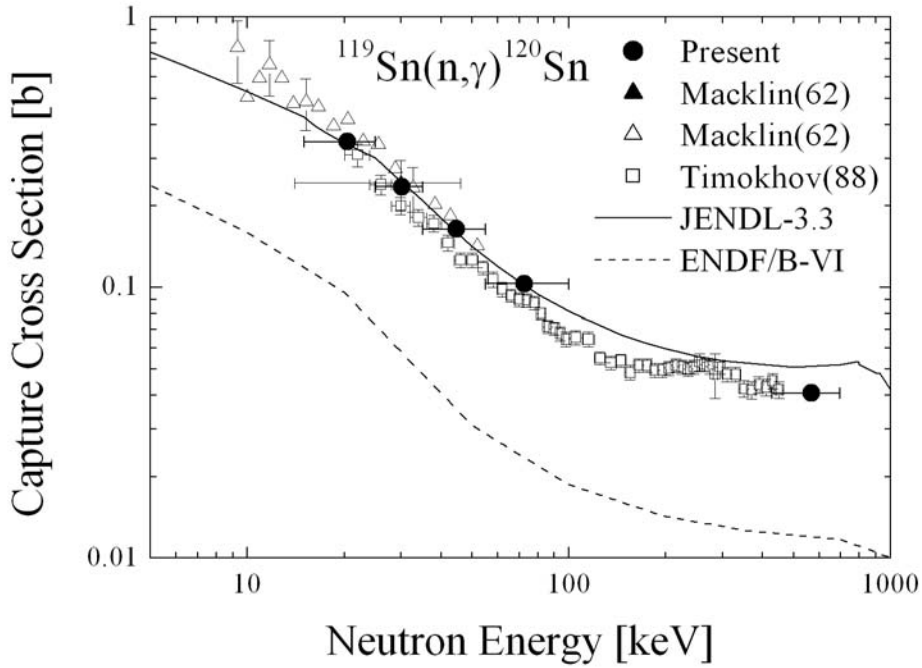


Fig. 1 Neutron capture cross sections of ^{119}Sn
 The solid circles show the present results. Other measurements^{5, 6)} and the evaluations of JENDL-3.3⁷⁾ and ENDF/B-VI⁸⁾ are compared with the present results.

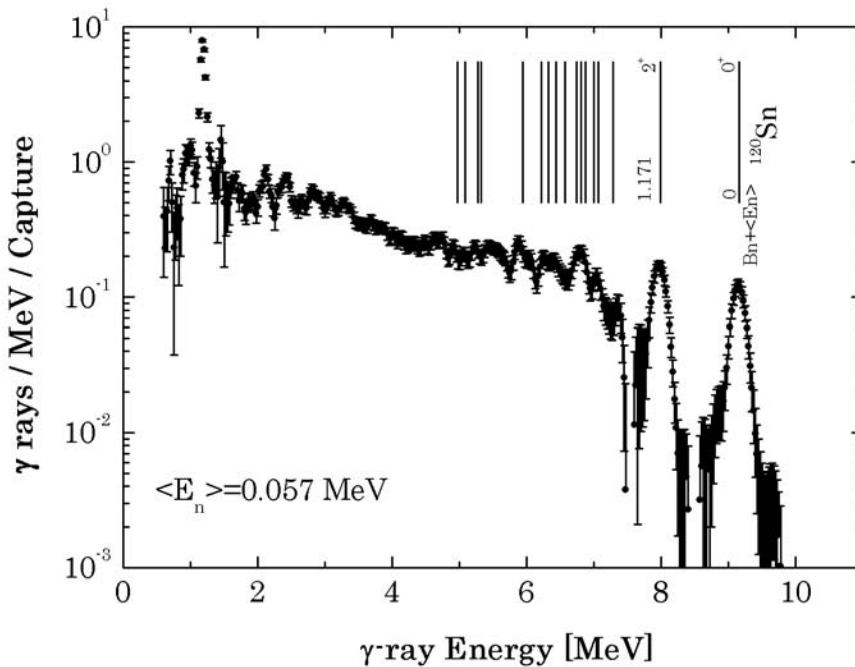


Fig. 2 Neutron capture γ -ray spectrum of ^{119}Sn
 The solid circles show the present spectrum. Low lying states of ^{120}Sn are shown in figure, where ground state is placed at 9.17 MeV : the excitation energy of the 57 keV neutron capture states.

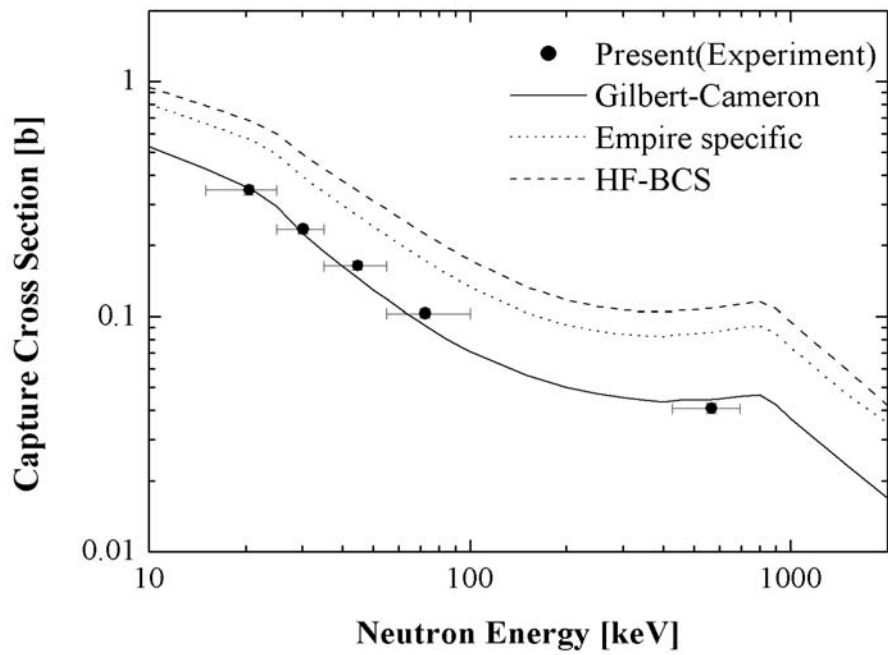


Fig. 3 Neutron capture cross sections calculated with three different level densities.

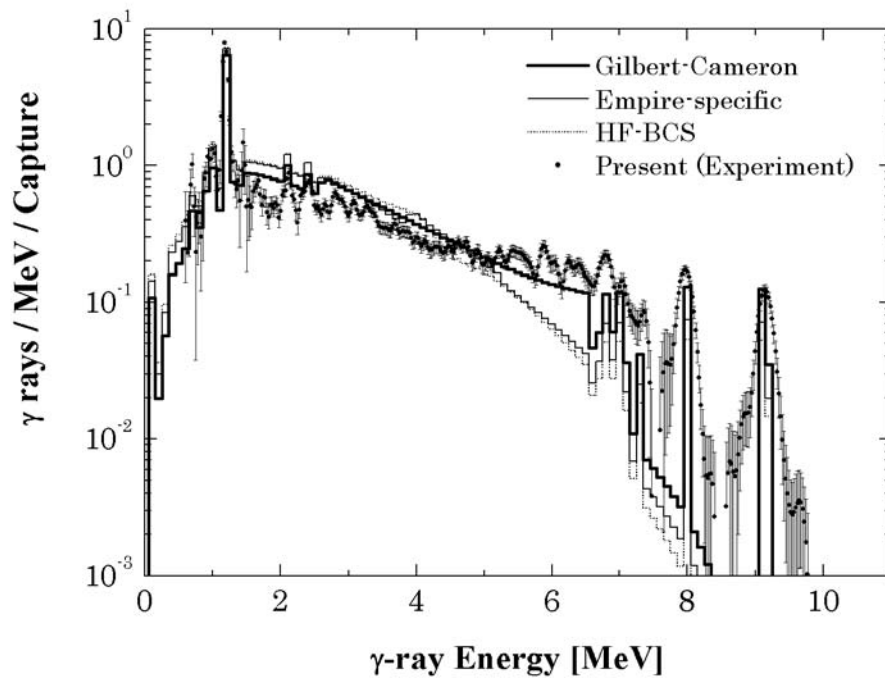


Fig. 4 Neutron capture γ -ray spectra calculated with three different level densities.

5. Conclusions

The capture cross sections and capture γ -ray spectra of $^{117, 119}\text{Sn}$ were measured in the incident neutron energy region from 10 to 100 keV and at 570 keV, using a 1.5-ns pulsed neutron source by the $^7\text{Li}(p,n)^7\text{Be}$ reaction and the large anti-Compton NaI(Tl) γ -ray spectrometer. A pulse-height weighting technique was applied to observed capture γ -ray pulse-height spectra to derive capture yields. The capture cross sections of $^{117, 119}\text{Sn}$ were obtained with the error of about 5% by using the standard capture cross sections of ^{197}Au . The present cross sections were compared with previous experimental data and the evaluated values in JENDL-3.3 and ENDF/B-VI. The capture γ -ray spectra of $^{117, 119}\text{Sn}$ were derived by unfolding the observed capture γ -ray pulse-height spectra.

The calculations of capture cross sections and capture γ -ray spectra of $^{117, 119}\text{Sn}$ were performed with the EMPIRE-II code in an incident neutron energy region from 10 to 1000 keV. The calculated results were compared with the present experimental results. In this comparison, Gilbert-Cameron level density was better than others, but it is not enough to reproduce the present experimental results. It is necessary to analyze the present experimental results in more detail.

Acknowledgments

The present study was supported by a Grant-in-Aid of the Japan Ministry of Education, Culture, Sports, Science and Technology.

References

- 1) S. Mizuno, M. Igashira and K. Masuda, *J. Nucl. Sci. Technol.*, **36**, 493-507 (1999).
- 2) R. L. Macklin and J. H. Gibbons, *Phys. Rev.*, **159**, 1007-1012 (1967).
- 3) ENDF/B-VI data file for ^{197}Au (MAT=7925), evaluated by P. G. Young (1991).
- 4) M. Herman, EMPIRE-II, [Http://www-nds.iaea.org/empire/](http://www-nds.iaea.org/empire/)
- 5) R. L. Macklin, T. Inada and J. H. Gibbons, *Nature.*, **194**, 1272(1962); EXFOR11958.005 (1976), EXFOR11981.006 (1976).
- 6) V. M. Timokhov et al., *Sov. J. Nucl. Phys.*, **50**, 375-380 (1989); EXFOR40960.008 (1988).
- 7) JENDL-3.3 data file for ^{119}Sn (MAT=5046), evaluated by JNDC FP Nuclear Data W. G. (1990)
- 8) ENDF/B-VI data file for ^{119}Sn (MAT=5046), evaluated by R. E. Schenter and F. Schmittroth (1974).

3.7 Measurement of Fission Cross-Sections with Lead Slowing-down Spectrometer using Digital Signal Processing

Wataru TAKAHASHI, Takuji OISHI, Mohammad NAKHOSTIN, Takeshi YAMAUCHI
Mamoru BABA, Junichi HORI*, Hideyuki YUKI**, Tsutomu OHTSUKI**

Cyclotron and Radioisotope Center (CYRIC), Tohoku University

Aoba6-3, Aramaki, Aoba-ku, Sendai-shi, Miyagi-ken, 980-8578, Japan

**Research Reactor Institute (KURRI), Kyoto University*

Asasironishi2, Kumatori-cho, Sennan-gun, Osaka-fu, 590-0494, Japan

***Laboratory of Nuclear Science (LNS), Tohoku University*

Mikamine1-2-1, Taihaku-ku, Sendai-shi, Miyagi-ken, 982-0826, Japan

Email: wataru@cyric.tohoku.ac.jp

The energy range of fission cross-section measurement with the lead slowing-down spectrometer at KURRI was extended to about 1 MeV by reducing the electromagnetic noise with a digital signal processing (DSP) technique. We report the results of measurement of neutron induced fission cross-sections of ^{237}Np and ^{241}Am .

1. Introduction

For effective transmutation of minor actinide (MA) in nuclear waste and generation of electricity by Accelerator Driven Systems (ADS), a variety kind of nuclear data are needed. The nuclear data are essential for calculation of reactor characteristics such as critical safety, kinetics, decay heat and so on. Especially, neutron induced fission cross-sections are crucial because the transmutation of the nuclear waste is based on a fission reaction [1].

However, the nuclear data of MA are not enough in quality and quantity. For example, evaluated neutron induced fission cross-sections of ^{237}Np show marked discrepancies each other. Therefore, new measurement is required to improve the data status [2, 3].

A lead slowing-down spectrometer has been used very effectively for measurement of neutron induced fission cross-sections of MA [1-3]. However, the energy range of the measurement was limited below ~10 keV because accelerator-correlated electromagnetic noise piled up on high-energy events. Therefore, we tried and succeeded to extend the energy range of measurement to about 1 MeV by the reduction of the electromagnetic noise with a digital signal processing (DSP) technique [4].

The present study aims to measure neutron induced fission cross-sections of ^{237}Np and ^{241}Am using DSP and to contribute the improvement of these nuclear data. These nuclei account for the greater part of the nuclear waste.

2. Lead slowing-down spectrometer

2.1. The principle and properties of a lead slowing-down spectrometer

The lead isotopes are characterized by a very small capture cross-section, and lead behaves as a non-absorptive substance. Besides, elastic scattering is essentially isotropic and kinetic energy loss is ~1 % per collision. The neutron mean free path is about 2.8 cm. Under these conditions, neutrons slow-down very progressively spreading in space. As a result there is a statistical correlation between slowing-down time t and the mean kinetic energy E that can be expressed as

$$E = \frac{K}{(t + t_0)^2} \quad (5)$$

The value of K is bound to the neutronic properties of lead whereas t_0 is related to the initial kinetic energy of the neutrons [5].

The lead slowing-down spectrometer is very effective for the measurement of small amount of samples with low cross-sections and that of radioactive materials with a high background level, because the neutron intensity is as high as more than thousands times than those in conventional neutron time-of-flight (TOF) method owing to short distance from the source [6]. However the energy resolution of lead slowing-down spectrometer is about 40 % and is lower than those in the TOF method [6].

2.2. Kyoto university lead slowing-down spectrometer

The present measurement was performed using Kyoto University lead slowing-down spectrometer driven by an electron linac (KULS) at KURRI. KULS is a cube of 1.5 × 1.5 × 1.5 m³ and composed of lead blocks (10 × 10 × 20 cm³, and purity: 99.9%) and set on a steel platform cart in the linac target room. All surfaces of KULS are covered with cadmium sheets of 0.5 mm thick to shield from low energy neutrons. The cross sectional view of KULS is shown in Fig.1 [6].

At the center of KULS, pulsed fast neutrons are produced by a photoneutron target of tantalum (8 cm in diameter and 6 cm in effective thickness) in cylindrical titanium case, which is air-cooled with compressed air [6].

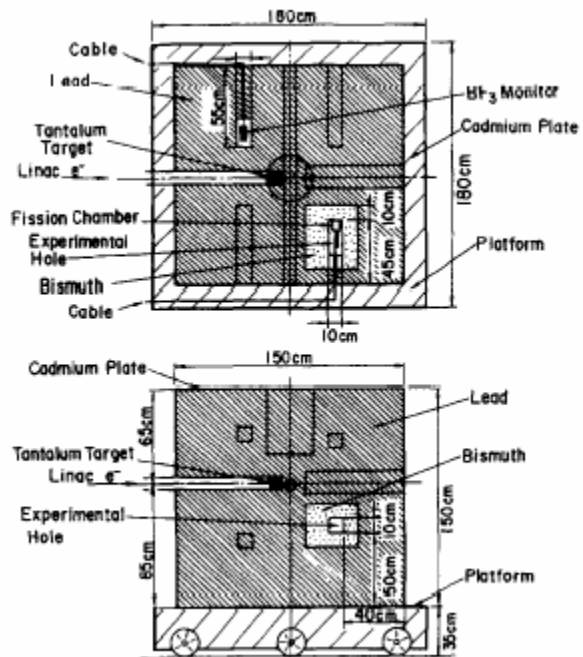


Fig.1 The cross sectional view of KULS [5]

There are eight experimental holes ($10 \times 10 \text{ cm}^2$, 55 or 45 cm in depth) in KULS. The experiment was carried out in one of the experimental holes, which was covered with bismuth layers of 10 to 15 cm in thickness to reduce high energy γ -rays (6 to 7 MeV) produced by the $\text{Pb}(n,\gamma)$ reaction in KULS. Accordingly, the background by the photo-fission events could be ignored in this measurement because the energy of the prompt γ -rays produced by the $\text{Bi}(n,\gamma)$ reaction are lower than the threshold energy for photo-fission reaction [1].

2.3. Energy Calibration of KULS

The energy calibration of KULS was done by using two types of detectors; one was a BF_3 counter for the neutron transmission measurement through a resonance filter that is indium or cobalt, and the other was an Ar gas counter for the capture γ -ray measurement with a resonance filter of gold, copper or aluminum.

The present result for calibration, E vs. t is shown Fig.2. The slowing-down constant K is $193 \times 10^2 \text{ (keV } \mu\text{s}^2)$ and the initial energy constant t_0 is $0.3 \mu\text{s}$. The present values of K and t_0 are in agreement with those reported by Kobayashi et al. [6] However it is probable that the correlation (δ) between t and E dose not stand above 100 keV because the inelastic scattering occurs above 0.57 MeV [5]. Therefore now we are promoting calculation for t vs. E , by use of a Monte Carlo code MCNP.

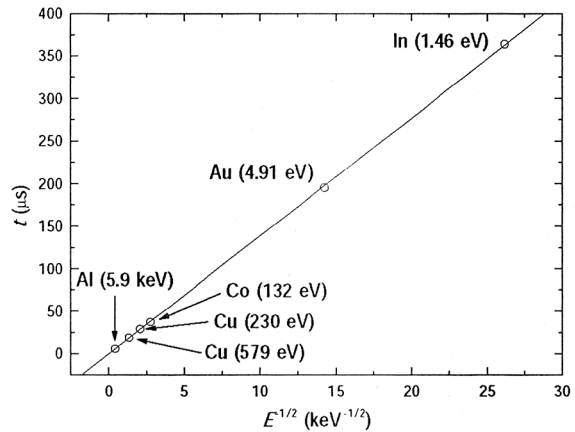


Fig.2 The relation between t and E

2.4. Back-to-back fission chamber

An ionization chamber with two parallel plate electrodes was employed for the detection of fission events. The chamber is made of aluminum, 2 mm thick, and is 40 mm in diameter and 43 mm in length as seen in Fig.3. Since the backsides of MA and ^{235}U deposits face each other, the chamber is called a back-to-back (BTB) type double fission chamber. The distance between the electrode and the deposit layer is 8 mm. The electrodes act as anodes at 300 V from which the fission fragment

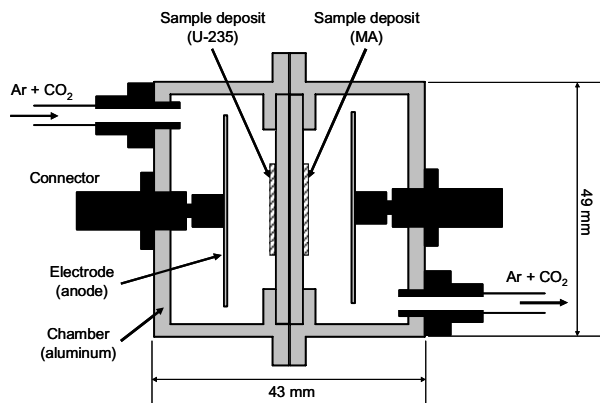


Fig.3 The figure of the BTB chamber

pulses are taken. An Ar + CO₂ gas is flowed through the BTB chamber. The number of atoms for sample deposits was determined through low-geometry α -counting as shown in Table 1.

The signal from the chamber was input into charge-sensitive preamplifier (ORTEC 142PC) and then shaped with a spectroscopy amplifier. The chamber, preamplifier and the cables between the chamber and the preamplifier were heavily wrapped with aluminum foils reduction of electromagnetic noise.

Table 1 The number of atoms for sample deposits

Material	The number of atoms
²³⁵ U (10 μ g)	$(2.80 \pm 0.10) \times 10^{16}$ [7]
²³⁷ Np	$(1.99 \pm 0.02) \times 10^{17}$ [8]
²³⁵ U (5 μ g)	$(1.51 \pm 0.03) \times 10^{16}$ [9]
²⁴¹ Am	$(1.73 \pm 0.02) \times 10^{16}$ [1]

3. Experimental procedure

The pulse width of electron beam was generally 33 ns in FWHM and the frequency was 100 Hz as the optimum value for KULS [5]. The beam current on the target was around 10.5 to 12.4 μ A. The waveform data of the fission fragment pulses were taken from the linear amplifier and digitized and recorded by a digital storage oscilloscope (DSO), LeCroy.

4. Data analysis

Data analysis was performed with the DSP method. The pulse height data and the slowing-down time data were acquired by processing the waveform data. The fission fragment pulses were discriminated from the α -particles pulses by the pulse height [4].

The electromagnetic noise in high-energy region was almost independent of time. Therefore subtraction of the typical waveform data of electromagnetic noise from that of fission fragments enabled great reduction of the electromagnetic noise and extension of the neutron energy range to higher energy. As a result, we could extend the energy range of measurement to about 1 MeV [4].

5. Results and discussion

The present results for neutron induced fission cross-sections of ²³⁷Np and ²⁴¹Am are shown in Fig.4 and Fig.5, respectively. The reference cross-section data of ²³⁵U was taken from JENDL-3.3. The present data are compared with the evaluated nuclear data in JENDL-3.3, ENDF/B- ν and JEFF-3.1 and other experimental data. The evaluated data are broadened by

40 % in the energy resolution of the KULS to compare with the experimental data.

About the result of ^{237}Np , the present data below 1 keV are in good agreement with the data by Yamanaka et al. [7] and JENDL-3.3. JENDL-3.3 and other experimental data between 1 and 100 keV are 5-30% larger than the present data. The present data above 100 keV differ from JENDL-3.3 markedly probably because the experimental energy resolution becomes gradually worse and the inelastic scattering in lead occurs [8, 10]. For the data in this region, further analysis is needed considering the problem of correlation between t and E .

About the result of ^{241}Am , the present data below 10 keV are in good agreement with JEFF-3.1, but JENDL-3.3, ENDF/B- ν and other experimental data are smaller than the present data by 5-20 %. The data above 10 keV are 20-80% larger than the evaluated nuclear data probably due to the same reason for ^{237}Np .

References

- [1] T. Kai et al., *Annals of Nuclear Energy*, 28, 723-739 (2001)
- [2] K. Kobayashi et al., *Journal of Nuclear Science and Technology*, 36, 1, 20-28 (1999)
- [3] K. Kobayashi et al., *Journal of Nuclear Science and Technology*, 36, 6, 549-551 (1999)
- [4] T. Oishi et al., *Journal of Radiation Protection Bulletin* (to be published)
- [5] T. Granier et al., *Nucl. Instr. and Meth. in Phys. Res. A* 506, 149-159 (2003)
- [6] K. Kobayashi et al., *Nucl. Instr. and Meth. in Phys. Res. A* 385, 145-156 (1997)
- [7] A. Yamanaka et al., *Journal of Nuclear Science and Technology*, 30, 9, 863-869 (1993)
- [8] S. Yamamoto et al., *Nucl. Sci. Eng.*, 126, 201-212 (1997)
- [9] Y. Ikeuchi, *Proceedings of the 34th symposium at KURRI*, 30 (Japanese)
- [10] D. Rochman et al., *Nucl. Instr. and Meth. in Phys. Res. A* 550 (2005) 397-413

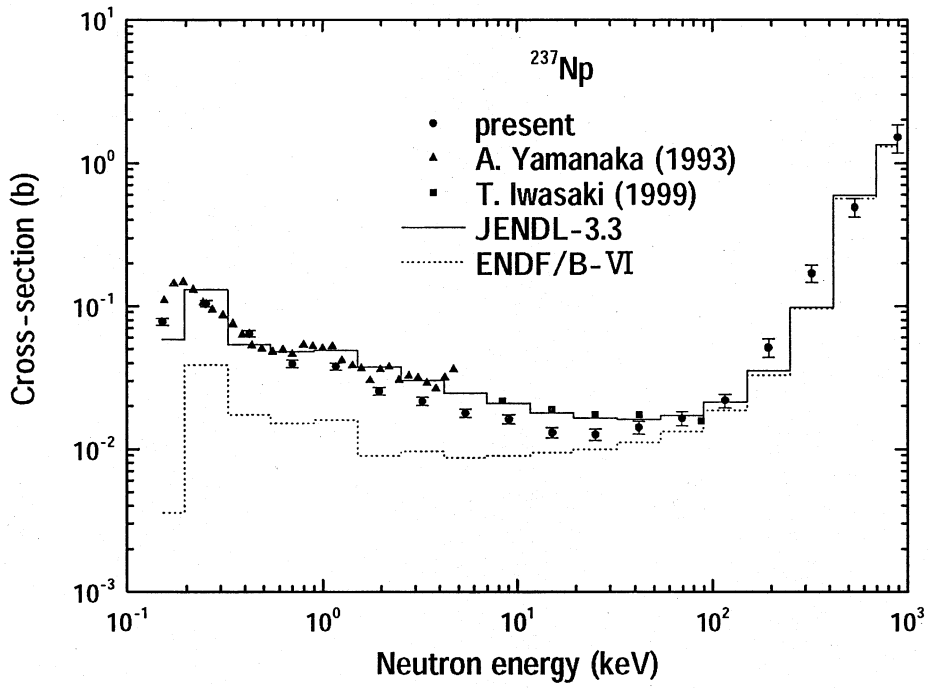


Fig.4 Neutron induced fission cross-section of ^{237}Np

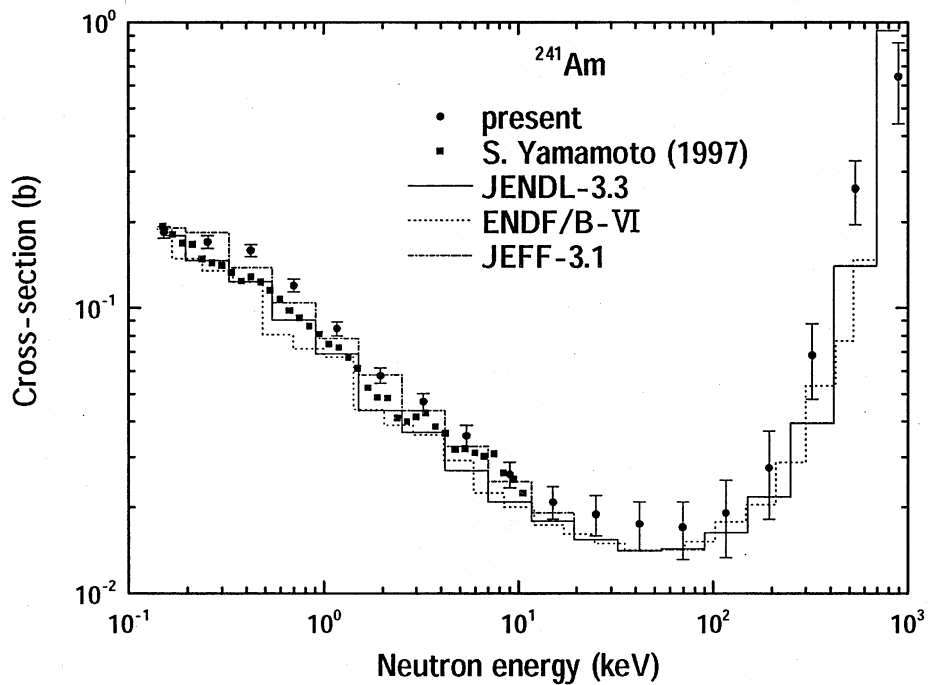


Fig.5 Neutron induced fission cross-section of ^{241}Am

3.8 Effect of ^{140}Ba Fission Yield on Fission Rate Distribution Measurements in UO₂-MOX Mixed Core of REBUS Program

Toru YAMAMOTO, Katsuyuki KAWASHIMA, Katsuichiro KAMIMURA

Reactor Core and Fuel Reliability Group, Safety Standard Division

Japan Nuclear Energy Safety Organization (JNES)

Fujita Kanko Toranomon Bldg. 7F, 3-17-1, Toranomon, Minato-ku, Tokyo 105-0001

E-mail: yamamoto-toru@jnes.go.jp

Japan Nuclear Energy Safety Organization (JNES) has been participating in the REBUS international program⁴⁾ organized by Belgonucleaire and SCK/CEN and analyzing the experimental data. This paper presents a study of an effect of the ^{140}Ba fission yield on measured fission rate distribution through the analysis of a UO₂ - MOX fuel mixed core of the REBUS program.

1. Introduction

In core physics experiments a fission rate distribution is one of the essential data that is used to validate the core analysis methods. The measurements of this parameter have been adopting spectroscopy of specific gamma-rays from fission products, such as 1,596.5 keV gamma-rays from ^{140}Ba ($T_{1/2}=12.752\text{d}$) - ^{140}La ($T_{1/2}=1.6781\text{d}$) after short period irradiation of experimental cores. When this method is applied to UO₂ - MOX fuel mixed cores, it is necessary to take into account the difference of the fission yield of ^{140}Ba in the UO₂ and the MOX fuel. For instance, the JNDC Nuclear Data Library of Fission Products¹⁾ shows that the cumulative fission yield of ^{140}Ba is 6.295 % for ^{235}U -thermal fission and 5.545 % for ^{239}Pu -thermal fission.

Recent studies^{2, 3)} of the UO₂ - MOX fuel mixed cores of VENUS-2 and VIP experimental programs show that the ratios of the analysis result to the measurement result (C/E) of the fission rate tend to be larger than 1.0 in the MOX fuel region and less than 1.0 in the UO₂ fuel region.

Japan Nuclear Energy Safety Organization (JNES) has been participating in the REBUS international program⁴⁾ organized by Belgonucleaire and SCK/CEN. The aim of the participation is to obtain measured reactivity change with burn-up of MOX fuel and UO₂ fuel and the fission rate and the flux distribution of the cores containing burned MOX and UO₂ fuel and to analyze these data in order to validate nuclear core analysis methodologies for burned MOX and UO₂ cores. The program partly contains UO₂ - MOX mixed cores and a fission rate distribution has been measured with the gamma-ray spectroscopy of 1,596.5 keV gamma-rays from ^{140}La .

This paper presents a study of an effect of the ^{140}Ba fission yield on the measured fission rate distribution through the analysis of a UO₂ - MOX fuel mixed core of the REBUS program.

2. Fresh BR3 MOX Core in REBUS Program

Table 1 summarizes core configurations and measurement items of the REBUS (PWR fuel) program. The REBUS cores commonly consist of a 7x7 fuel test bundle in a core center and a driver region of 3.3% (eight lows) and 4.0% (two lows) UO2 rods in the VENUS critical facility of SCK/CEN. A diameter of those fuel rods is about 9.5 mm, an effective fuel length is about 100cm and a fuel rod pitch is 1.26cm. The test region is changed by four different bundles consisting BR3 MOX (fresh and burned) and GKN (a Germany commercial PWR) UO2 (fresh and burned). Fig. 1 shows a schematic diagram of a core configuration consisting of the fresh BR3 MOX (6.8% Puf enrichment) core.

Table 1 Summary of Core Configurations and Measurement Items of REBUS (PWR Fuel)

	Reference Core	BR3 MOX		GKN UO2	
		Fresh	Irradiated	Fresh	Irradiated
Central test bundle configuration	7x7 3.3%VENUS UO2 rods	24 MOX rods 21 Water channels	24 MOX rods (about 20GWd/t) 21 Water channels	5x5 3.8%UO2 20 3.3%VENUS UO2 rods	5x5 3.8%UO2 (about 51GWd/t) 20 3.3%VENUS UO2 rods
Critical height	M	M	M	M	M
Water level reactivity effect	M	M	M	M	M
Fission rate distribution	—	Test bundle Driver region	Driver region	Test bundle Driver region	Driver region
Neutron flux distribution	—	Sc activation	Co activation	Sc activation	Co activation

3. Fission Rate Distribution Measurement

In the measurements of the REBUS program, a relative fission rate of a fuel rod is obtained as:

$$F \propto C / Y \quad (1)$$

Here, C is a measured count rate of the 1,596.5 keV gamma-ray peak after necessary corrections of decay and gamma-ray self shielding in the fuel rod. Y is an effective cumulative fission yield of ¹⁴⁰Ba for the fuel rod that is expressed as:

$$Y = \frac{\sum_i (F^{fast} Y^{fast} + F^{th} Y^{th})_i}{\sum_i (F^{fast} + F^{th})_i} \quad (2)$$

Here,

i: nuclides contributing fission such as ²³⁵U, ²³⁸U, ²³⁹Pu, ²⁴⁰Pu, ²⁴¹Pu and ²⁴²Pu,

F^{fast}, Fth: relative contribution of fast fission and thermal fission for nuclide i,

Y^{fast}, Yth: cumulative fission yields of ¹⁴⁰Ba of fast fission and thermal fission for nuclide i.

4. Calculation of Effective Fission Yield

Since Y is not a measured parameter, a core analysis result is used to obtain it. For the effective fission

yield of the fuel rods, for which the fission rates were measured in the fresh BR3 MOX core, F^{fast} and F^{th} were calculated as a part of the core analysis using SRAC system⁵⁾ with JENDL-3.2⁶⁾. Fig. 2 shows the calculated fission rate distribution with the measured one along the Y axis of the core. The figure also shows measurement data that are reported by the organizer (BN) of the REBUS program. Table 2 shows the relative contributions of heavy nuclides to the fast fission (neutron energy: 9.12 keV to 10 MeV) and the thermal fission (0 to 9.12 keV) for several fuel rods. It is seen that the six major nuclides cover more than 99.6% of total fission even for the MOX fuel rod. Table 3 shows the fission yields, Y^{fast} and Y^{th} in JENDL-3.2, ENDF/B-VI and JEF-2.2 for the six major nuclides. The fission yields of Pu isotopes is smaller than U isotopes and the values slightly change depending on the nuclear libraries.

Table 2 Relative Contributions of Heavy Nuclides to Fissions in Fast and Thermal Energy Regions

(X, Y)	MOX (-2, -3)			3.3% UO ₂ (-4,-4)			3.3% UO ₂ (-7,-7)			3.3% UO ₂ (-11,-11)			4.0% UO ₂ (-12,-12)		
Nuclide	Fast	Th	Total	Fast	Th	Total	Fast	Th	Total	Fast	Th	Total	Fast	Th	Total
U-234	0.0	0.0	0.0	0.0	0.0	0.0	0.0	0.0	0.0	0.0	0.0	0.0	0.0	0.0	0.0
U-235	0.1	2.2	2.4	1.4	93.5	95.0	1.3	94.0	95.3	1.3	94.0	95.3	1.9	92.6	94.6
U-236	0.0	0.0	0.0	0.0	0.0	0.0	0.0	0.0	0.0	0.0	0.0	0.0	0.0	0.0	0.0
U-238	6.1	0.0	6.1	5.0	0.0	5.0	4.7	0.0	4.7	4.7	0.0	4.7	5.4	0.0	5.4
Pu-238	0.1	0.1	0.1												
Pu-239	3.8	79.6	83.3												
Pu-240	0.8	0.0	0.8												
Pu-241	0.3	6.6	6.9												
Pu-242	0.1	0.0	0.1												
Am-241	0.2	0.1	0.2												
Total	11.4	88.6	100.0	6.5	93.5	100.0	6.0	94.0	100.0	6.0	94.0	100.0	7.4	92.6	100.0
6 Nucl	11.2	88.5	99.6	6.4	93.5	100.0	6.0	94.0	100.0	6.0	94.0	100.0	7.3	92.6	100.0

Fast: 9.12keV~10MeV, Th (Thermal): 0~9.12keV, 6 Nucl (Nuclides): U-235, U-238, Pu-239, Pu-240, Pu-241, Pu-242

Table 3 Cumulative Fission Yields of ¹⁴⁰Ba for Six Major Nuclides in Three Nuclear Libraries

Library	JENDL-3.2		ENDF/B-VI		JEF-2.2	
	Fast	Th	Fast	Th	Fast	Th
U-235	6.119	6.295	5.978	6.215	5.782	6.276
U-238	5.988		5.815		5.743	
Pu-239	5.317	5.545	5.323	5.355	5.119	5.285
Pu-240	5.110		5.502	5.701	5.462	
Pu-241	5.378	6.215	5.306	5.766	5.395	5.743
Pu-242	5.005		5.449	6.022	5.682	5.462

Table 4 Effective fission Yields of ¹⁴⁰Ba for MOX and UO₂ fuel rods

	JENDL-3.2	ENDF/B-VI	JEF-2.2
MOX (-2, -3)	5.621 (1.0)	5.430 (1.0)	5.362 (1.0)
3.3% UO ₂ (-4,-4)	6.277 (1.117)	6.191 (1.140)	6.242 (1.164)
3.3% UO ₂ (-7,-7)	6.278 (1.117)	6.193 (1.141)	6.245 (1.165)
3.3% UO ₂ (-11,-11)	6.278 (1.117)	6.193 (1.141)	6.245 (1.165)
4.0% UO ₂ (-12,-12)	6.267 (1.115)	6.178 (1.138)	6.223 (1.161)

From these data, the effective fission yields, Y, were evaluated based on the relative contributions of the six major nuclides in Table 2 and shown in Table 4. The Table also shows ratios of the effective fission yield of UO₂ rods to that of the MOX fuel rod in brackets for each library. The ratios of 3.3% UO₂ to MOX are 1.117 for JENDL-3.2, 1.140 for ENDF/B-VI and 1.165 for JEF-2.2.

The organizer (BN) of the REBUS program have evaluated and used 1.123 ± 0.012 for $3.3\text{UO}_2/\text{MOX}$ to the measured radial fission rate distribution, which is 0.6 % larger than that of this study with JENDL-3.2.

Those effective fission yields were applied to the measured fission rates and comparison between the SRAC analysis (C) and the measured fission rates (E) were shown in Fig. 3.

5. Discussion and Conclusion

The ratio of the measured fission rates of MOX fuel rods to UO_2 fuel rods is expressed as:

$$\frac{F_M}{F_U} \propto \frac{C_M}{C_U} \frac{Y_U}{Y_M} \quad (3)$$

Here, the suffix, M, means MOX fuel rods and U UO_2 fuel rods. Generally the change of Y_U is negligible small among the UO_2 fuel rods and also among the MOX rods. The uncertainty of Y_U/Y_M directly influences on the ratios of the measured fission rates of the MOX fuel rods to the UO_2 fuel rods so that the ratios depend on the nuclear data library adopted in the measurements. Some difference in the cumulative fission yield of ^{140}Ba is seen for the Pu isotopes as shown in Table 3. Table 5 shows a comparison of the fission yields among the libraries for the thermal fission of ^{235}U and ^{239}Pu and their ratio of ^{235}U to ^{239}Pu . The ratio of ^{235}U to ^{239}Pu is a major part of Y_U/Y_M and therefore F_M/F_U . It is seen that the F_M/F_U change up to 4 % depending on the nuclear library.

When the Y_U/Y_M of this study with JENDL-3.2 is used in place of the REBUS organizer (BN), the F_M/F_U will decrease by 0.6 % and then the C/E is almost increase by 0.6 % in the MOX test bundle as shown in Fig. 3, which is not significant. However, when the Y_U/Y_M in this study with ENDF/B-VI or JEF-2.2 is used, the F_M/F_U will increase by 1.5 % or 3.7 % and then the C/E is almost decrease by about 1.5 % or about 3.7 % in the MOX test bundle.

Table 5 Comparison of Cumulative Fission Yields (%) of ^{140}Ba for Thermal Fission of ^{235}U and ^{239}Pu

	JENDL-3.2	ENDF/B-VI	JEF-2.2
U-235	6.295 (1.0)	$6.215 \pm 1.0\%$ (0.987)	$6.276 \pm 1.2\%$ (0.998)
Pu-239	5.545 (1.0)	$5.355 \pm 1.4\%$ (0.966)	$5.285 \pm 1.0\%$ (0.953)
U-235/Pu-239	1.135 (1.0)	$1.161 \pm 1.7\%$ (1.022)	$1.188 \pm 1.6\%$ (1.046)

For conclusions: (1) The ratios of fission rates of the MOX and the UO_2 fuel rods depend on the cumulative fission yields of ^{140}Ba that is used in the process of the experimental data, (2) The difference in the ^{140}Ba fission yield for the ^{239}Pu thermal fission among the libraries is up to 5 % and not negligible. (3) The fission yield data of ^{140}Ba used in the process of the experimental data should be precisely reviewed in order to evaluate the calculation errors for the ratio of the fission rate of the MOX and the UO_2 fuel rods in the UO_2 - MOX mixed cores, (4) The Effort to decrease uncertainty of the fission yield data of ^{140}Ba for ^{239}Pu (Thermal fission) is requested for the precise evaluation of the calculation errors of fission rate distribution in the UO_2 - MOX mixed cores.

References

- 1) K. Tasaka *et al.*, " JNDC Nuclear Data Library of Fission Products - Second Version -," JAERI 1320 (1990).
- 2) Y. Nagaya, K. Okumura and T. Mori, "Analysis of VENUS-2 MOX Core Measurements with a Monte Carlo Code MVP," Proc. Int. Conf. PHYSOR 2002, Seoul, Korea, October 7-10, 2002.
- 3) T. Shiraki, H. Matsumoto and M. Nakano, "Analysis of MOX Critical Experiments with JENDL-3.3," Proc. the 2004 Symposium on Nuclear Data, Nov. 11-12, 2004, JAERI, Tokai, Japan, JAERI-Conf, 2005-3 (2005).
- 4) P. Baeten *et al.*, "The REBUS Experimental Programme for Burn-up Credit," Proc. Int. Conf. on Nuclear Critical Safety (ICNC 2003), Oct. 20-24, 2003, Tokai, Japan (2003).
- 5) K. Tsuchihashi, Y. Ishiguro, K. Kaneko, M. Ido, Revised SRAC Code System, JAERI-1302, Japan Atomic Energy Research Institute (JAERI), (1986).
- 6) T. Nakagawa, K. Shibata, S. Chiba, *et al.*, "Japanese Evaluated Nuclear Data Library Version 3 Revision-2," J. Nucl. Sci. Technol., 32, 1259 (1995).

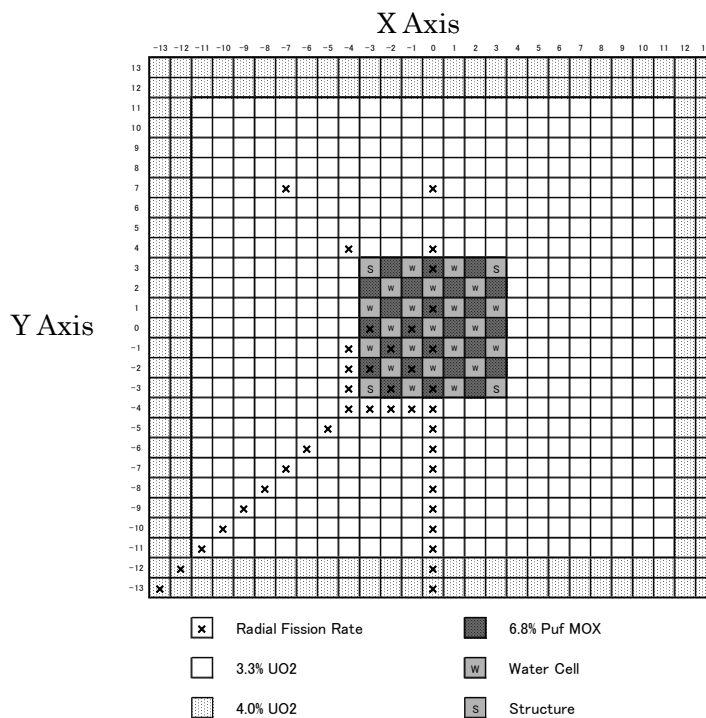


Fig. 1 Schematic Radial Core Configuration of Fresh BR3 MOX Core in REBUS Program

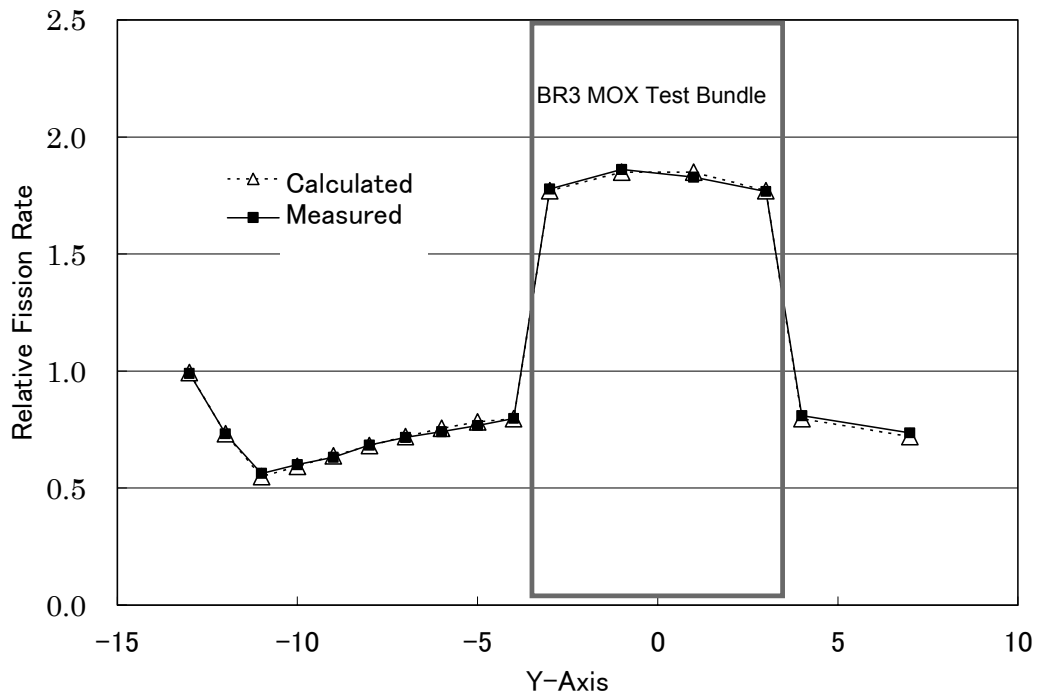


Fig. 2 Relative Fission Rate Distribution along Y Axis and Difference between Calculation and Measured Values for Fresh BR3 MOX Core in REBUS Program

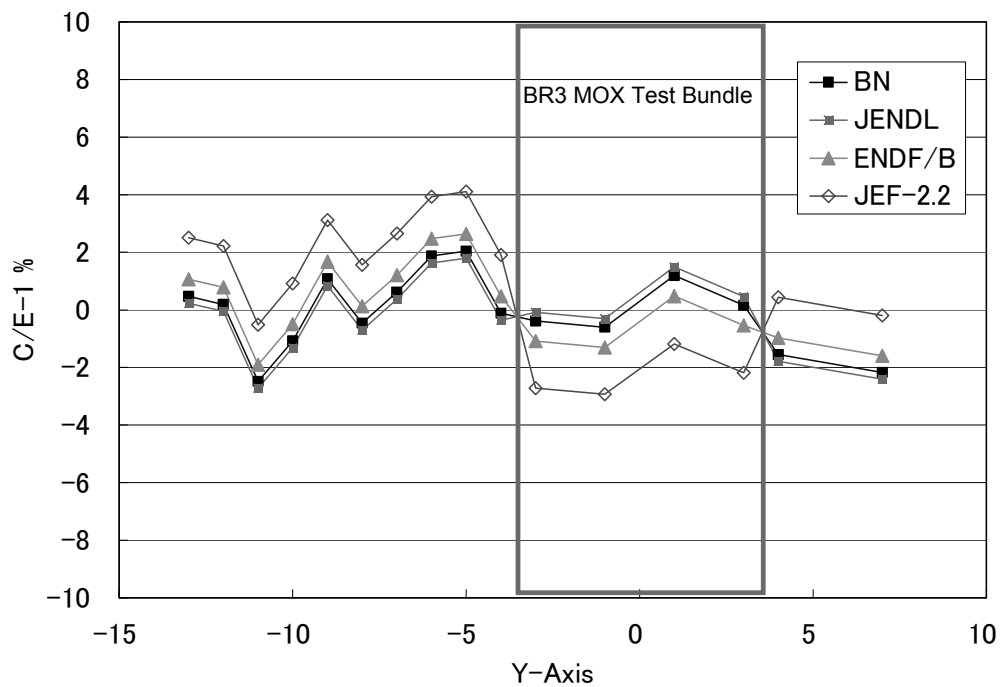


Fig. 3 Comparison between the SRAC analysis (C) and the measured fission rates (E) with effective fission yields by the different nuclear libraries

3.9 Measurement of Neutron Production Spectra at the Forward Direction from Thick Graphite, Aluminum, Iron and Lead Targets Bombarded by 250 MeV Protons

Yosuke IWAMOTO¹, Shingo TANIGUCHI², Noriaki NAKAO³, Toshiro ITOGA⁴, Takashi NAKAMURA⁴,
Yoshihiro NAKANE¹, Hiroshi NAKASHIMA¹, Daiki SATOH¹, Hiroshi YASHIMA⁵,
Hiroshi YAMAKAWA⁶, Koji OISHI⁶, Atsushi TAMII⁷, Kichiji HATANAKA⁷

1 Japan Atomic Energy Agency, 2 Japan Synchrotron Radiation Research Institute,
3 Stanford Linear Accelerator Center, 4 Cyclotron and Radioisotope Center, Tohoku University,
5 Research Reactor Institute, Kyoto University, 6 Shimizu Corporation,
7 Research Center of Nuclear Physics, Osaka University

e-mail: iwamoto.yosuke@jaea.go.jp

Neutron energy spectra at the forward direction produced from stopping-length thick graphite, aluminum, iron and lead targets bombarded by 250 MeV protons were measured at the neutron TOF course at RCNP of Osaka University. The experiments were performed by the time-of-flight technique with the flight path length of 11.4m and 67.8m, and neutron energy spectra were obtained in the energy range from 10 MeV to 250 MeV. To compare the experimental data, Monte Carlo calculations by PHITS, MCNPX, and JQMD+INC codes were performed. It was found that these calculation results at 0-degree generally underestimated the experimental data for all targets in the energy range above 20 MeV.

1. Introduction

Various Monte Carlo transport calculation codes have been widely employed for the shielding designs of proton accelerator facilities. In such designs, it is important to estimate the energy spectra of the secondary particles, especially neutrons, produced by beam losses in thick materials of beam line modules and the beam dump as source terms. The accuracy of calculated results has been verified by the benchmark experimental data. The double differential neutron energy spectra at 0-degree by bombarding 210 MeV protons on a thick iron target were measured at RIKEN [1]. No other experimental data are available from other thick targets. We have measured neutron energy spectra from thick graphite, aluminum, iron and lead targets at the forward direction bombarded by 250 and 350 MeV protons at the TOF course of the RCNP (Research Center of Nuclear Physics) ring cyclotron of Osaka University. We already reported results of the 350 MeV measurement [2]. In this work, the 250 MeV measurements and the calculation results of the PHITS [3], MCNPX [4] and JQMD+INC [5] codes are reported.

2. Experiment

The experiments were carried out at the neutron TOF course of the RCNP ring cyclotron of Osaka University. A schematic view of the experimental arrangement is illustrated in **Figs. 1**. The characteristics of the targets used in this work are summarized in **Table 1**. The targets were covered with aluminum foil to absorb secondary electrons emitting from the targets. The neutrons produced at 0-degree direction were transported to the TOF course through the 150-cm-thick iron collimator of a 12-cm high and 10-cm wide opening, while charged particles were rejected by a vertical bending magnet equipped in the collimator. The neutron TOF measurements were performed using an NE213 organic liquid scintillator (12.7-cm-diameter by 12.7-cm-long) placed at either 11.4 m (short path) or 67.8 m (long path) from the beam-incident surface of the target. The long path measurement was carried out to get good time resolution in higher energy region. In the measurements, the currents of the proton beam were kept in the range of 0.2 nA for the short path and 5 nA for the long path.

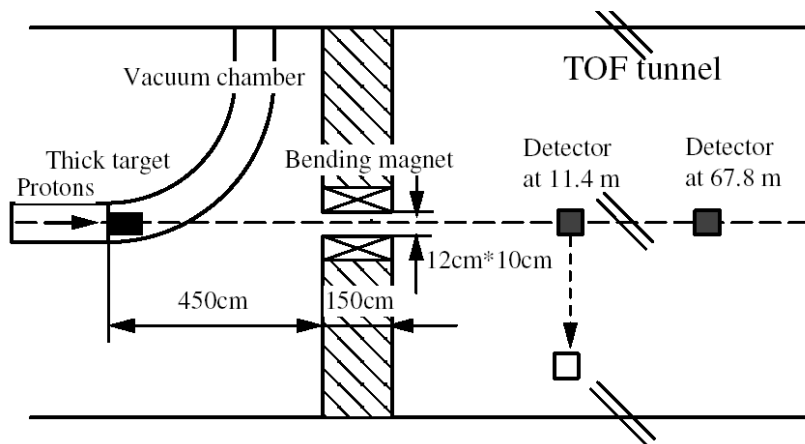


Fig. 1 Illustration of experimental setup at RCNP.

Table 1 Target characteristics and stopping range of 250 MeV protons in the target

Material	Density (g/cm ³)	Size (cm)	Stopping range (cm)
Graphite	1.76	6.0 × 6.0 × 27.5	25.0
Al	2.72	φ6.0 × 20.0	18.0
Fe	9.12	φ6.5 × 7.5	6.93
Pb	11.3	6.0 × 6.0 × 7.5	6.76

3. Analysis

The TOF distributions of neutrons were converted to the neutron energy spectra. In the TOF distribution analysis, neutron events above the Am-Be (4.2 MeVee) bias were summed up and neutron TOF distributions in wide energy range above 10 MeV were obtained.

Neutron detection efficiencies were obtained from calculation results of the CECIL code [6]. The results of CECIL agree with the measurements within 15 % in the energy region between 10 and 206.8 MeV for 4.2 MeVee bias [7]. To get better energy resolution results, the long path measurements were used for the energy range above 100 MeV.

The statistical uncertainties at the neutron spectra determination varied from 0.5 to 5 %. The systematic error comes mainly from neutron detection efficiency, which was determined to 15 %. The energy resolution depends on the time and the geometrical component. The time component estimated from FWHM of the flash gamma-ray peak was 1.2 ns. The geometrical component comes from the target thickness and from the size of the sensitive area of the detector. The typical neutron energy resolutions of 200 MeV with the graphite target are 12.7 MeV at 11.4 m and 2.1 MeV at 67.8 m, respectively.

4. Monte Carlo Calculation

The Monte Carlo particle transport code, the PHITS, MCNPX and JQMD+INC codes with the Bertini model [8] based on intranuclear cascade model were used. In the PHITS and MCNPX calculations, the JENDL/HE2004 [9] and the LA150 [10] evaluated neutron data libraries were employed for energies up to 150 MeV. In the JQMD+INC calculation, QMD model was employed above 50 MeV and the Bertini model under 50 MeV. In all calculations, neutrons produced within an angle of 3-degrees were collected.

5. Results

(1) Intercomparison with each calculation result

Figure 2 shows the calculated neutron energy spectra from the graphite target. The difference of calculation results using between JENDL/HE2004 and LA150 is very small. A discrepancy of the results with Bertini model between PHITS and MCNPX above 200 MeV may come from the difference of the using parameter in Bertini model.

(2) Experimental results and the comparison with the calculation

Figure 3 shows the measured and the calculated neutron energy spectra from thick targets. All calculation results underestimate the experimental

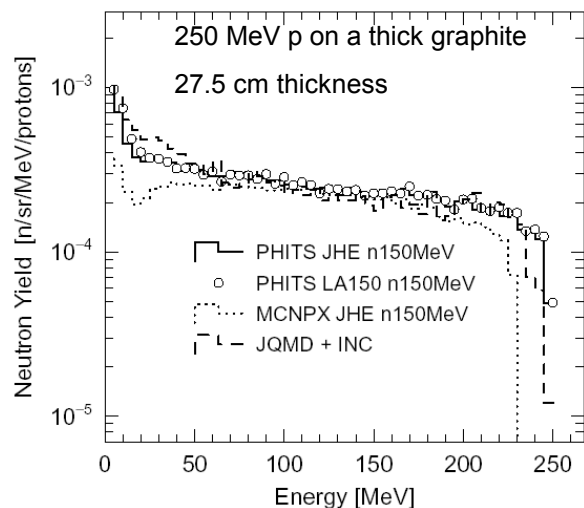


Fig. 2 Calculated results for graphite target. JHE shows JENDL/HE2004. n 150 MeV indicates the use of neutron data library below 150 MeV.

ones in the neutron energy range from 30 MeV to 200 MeV. The underestimations of the calculations are also found in 210 MeV proton incident experiment at RIKEN [1] and 350 MeV experiment at RCNP [2]. Those may result from the underestimation of neutron-production cross sections at small angles and the strong self-shielding in target nucleus.

Figure 4 shows that The results of neutron yields integrated at the forward direction of 250 MeV proton incidence as a function of the target mass. 10 – 50 MeV neutrons and 50 – 250 MeV neutrons are corresponding roughly to evaporation-preequilibrium and cascade neutrons, respectively.

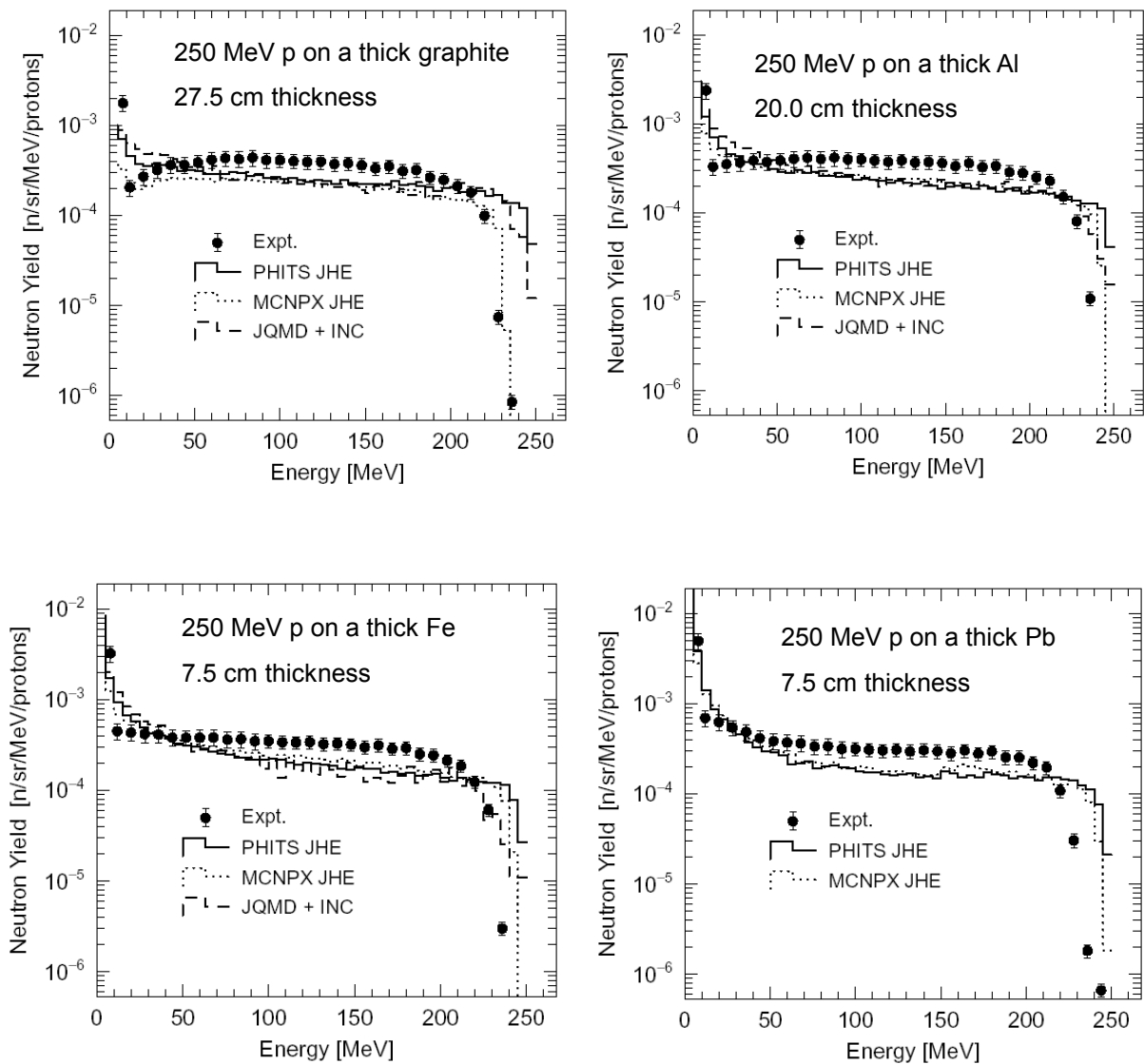


Fig. 3 Measured and calculated neutron energy spectra at 0-degree.

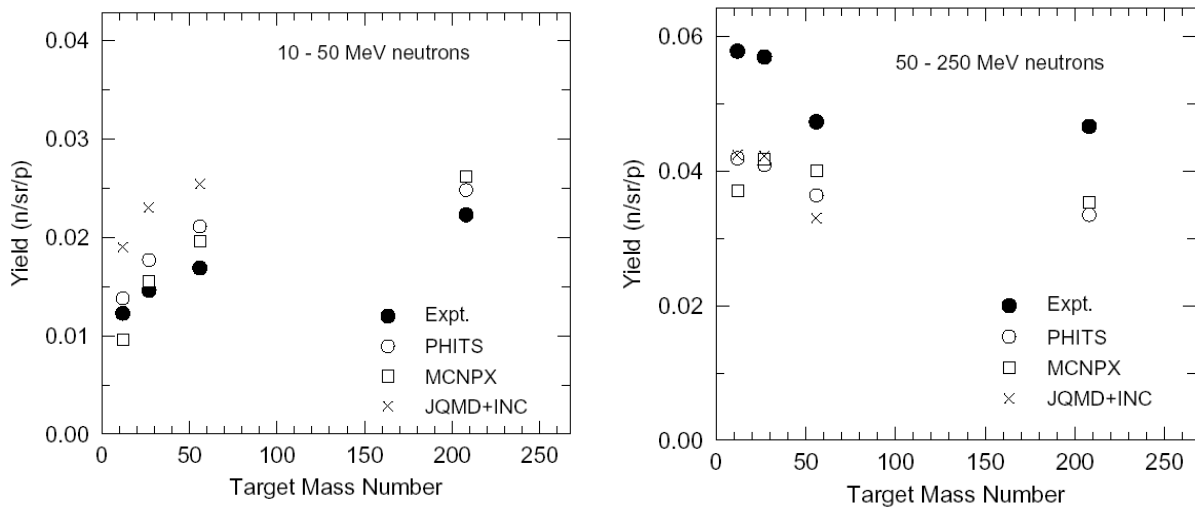


Fig. 4 Neutron yields integrated at the forward direction of 250 MeV proton incidence as a function of the mass of the thick targets. Left: 10 – 50 MeV neutron yield; right: 50 – 250 MeV neutron yield.

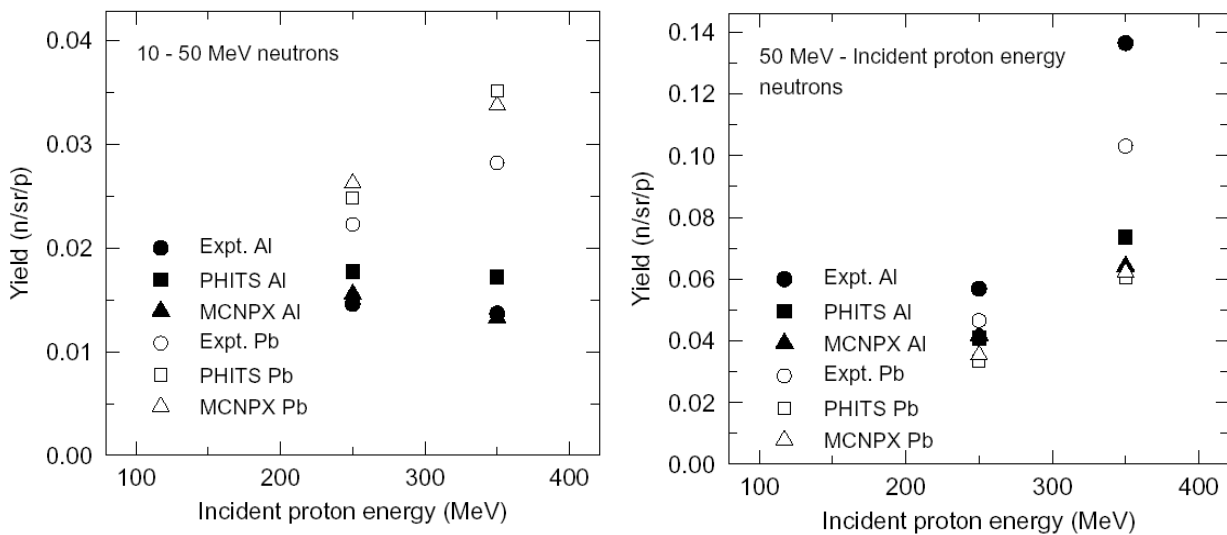


Fig. 5 Neutron yields integrated at the forward direction for the aluminum and lead thick targets as a function of incident energy. Left: 10 – 50 MeV neutron yield; right: 50 – incident energy neutron yield.

For 10 – 50 MeV neutrons in the figure, all results increase with mass number, gradually. On the other hand, the dependency to the mass is less for 50 – 250 MeV neutrons. For the comparison of the experimental and calculated yields in the figure, the calculated 50 – 250 MeV neutrons tend to be less emitted than the experimental ones, and the calculated 10 – 50 MeV neutrons are more emitted. These may indicate that the calculated energy of residual nucleus is higher than the experimental one.

The results of neutron yields integrated at the forward direction as a function of incident proton energy are shown in **Figs. 5** for the aluminum and lead targets. The results of 350 MeV proton incidence have been reported [2].

10 – 50 MeV neutrons increase with incident proton energy for the lead, on the other hand, those for the aluminum is not depend on incident energy. For 50 – 350 MeV neutrons at 350 MeV proton incidence, the discrepancy between the experimental results and calculated ones are larger than that of 250 MeV proton incidence.

6. Summary

Neutron energy spectra produced at the forward direction from thick graphite, aluminum, iron and lead targets bombarded by 250 MeV protons were measured by the TOF method at RCNP of Osaka University. The experimental data were compared with the calculated results of the PHITS, MCNPX and JQMD+INC codes. All calculations give lower neutron energy spectra than the experimental ones for all targets above 20 MeV and must be improved for neutron production at 0-degree. These experimental data will be useful as benchmark data for investigating the accuracy of the Monte Carlo simulation and for the shielding design of accelerator facilities.

Acknowledgment

The authors express their gratitude to the accelerator staff of RCNP for generous support of this experiment.

References

- [1] S. Yonai, T. Kurosawa, H. Iwase, et al., Nucl. Instr. and Meth. A 515 (2003) 733.
- [2] Y. Iwamoto, S. Taniguchi, N. Nakao, et. al., the AccApp05 Proceedings, Venice, Italy, Aug. 29 – Sep. 1 2005.
- [3] H. Iwase, K. Niita, T. Nakamura, J. Nucl. Sci. Technol. 39 (2002) 1142.
- [4] L.S. Water (Ed.), MCNPX User's Manual version 2.4.0, LA-CP-02-408, Los Alamos National Laboratory, Los Alamos, New Mexico, 2002.
- [5] K. Niita et al., Phys. Rev. C 52 (1995) 2620
- [6] R.A. Cecil, B.D. Anderson, R. Madey, Nucl. Instr. And Meth. 161 (1979) 439.
- [7] N. Nakao, T. Kurosawa, T. Nakamura, Y. Uwamino, Nucl. Instr. and Meth. A 463 (2001) 275.
- [8] H.W. Bertini, Phys, Rev. 188 (1969) 1711.
- [9] Y. Watanabe., et al., AIP Conference proceedings, 769 (2005) 1646.
- [10] M.B. Chadwick, P.G. Young, S. Chiba, S.C. Frankle, G.M. Hale, H.G. Hughes, A.J. Koning, R.C. Little, R.E. MacFarlane, R.E. Prael, L.S. Waters, Nucl. Sci. Eng. 131 (1999) 293.

3.10

Measurement of 40 MeV Deuteron Induced Reaction on Fe and Ta for Neutron Emission Spectrum and Activation Cross Section

Toshiro Itoga, Masayuki Hagiwara, Takuji Oishi, So Kamada, Mamoru Baba

Cyclotron and Radioisotope Center, Tohoku University, Aramaki, Aoba-ku, Sendai 980-8578, Japan

With a view to improve the data accuracy, the neutron emission spectra and the activation cross section for the deuteron interaction with ^{nat}Ta , ^{nat}Fe which will be used as the structural materials in IFMIF (International Fusion Materials Irradiation Facility), we have measured the 1) differential thick target neutron yields from thick tantalum and iron targets bombarded by 40 MeV deuterons, and the 2) excitation functions of activation cross sections for deuteron interaction with tantalum and iron up to 40 MeV, at the K=110 AVF cyclotron facility of Tohoku University.

1. Introduction

The International Fusion Material Irradiation Facility (IFMIF) project has been proposed to establish an accelerator-based d-Li neutron source in order to produce the intense fluence for test irradiations of fusion reactor candidate materials [1]. In IFMIF, high current (250 mA) deuteron beam is accelerated to 40 MeV and transported to the liquid lithium target so as to generate a neutron field that simulates a fusion reactor neutron field.

For the safety design and management of IFMIF, detailed knowledge is required on the neutron emission spectrum and the activation cross-section. The neutron flux and spectral data play an important role for accurate estimation of the neutron shielding, and the activation cross-section is indispensable for the estimation of radioactivity induced in the accelerator components and shielding materials. Although some studies had already been undertaken on these subjects, the data are scarce and the data accuracy is not good enough at present [2].

To improve the accuracy of the neutron energy-angular distribution data and the predictability of the radioactivity accumulation in IFMIF, we have been conducting a series of experiments on the neutron emission spectrum of the (d,xn) reaction and the activation cross-section and radioactivity induced in the accelerator components with the AVF cyclotron at the Tohoku University Cyclotron and Radioisotope Center (CYRIC). So far, we have obtained data on lithium targets for 25 and 40 MeV deuterons [3][4] and on carbon and aluminum targets for 40 MeV deuterons [5].

Here, we present the experiments on 1) neutron emission spectra from thick iron and tantalum, and 2) activation cross-sections of the $^{nat}\text{Fe}(d,x)^{51}\text{Cr}$, $^{nat}\text{Fe}(d,x)^{52}\text{Mn}$, $^{nat}\text{Fe}(d,x)^{56}\text{Co}$, $^{nat}\text{Fe}(d,x)^{57}\text{Co}$ and $^{nat}\text{Fe}(d,x)^{58}\text{Co}$ reactions. These data are required for shielding design and radioactivity estimation since

these elements are one of the main accelerator components, especially in the beam tube. The neutron spectra were measured at seven laboratory angles between 0- and 110- deg. The stacked target technique was applied to obtain the activation cross-section from 40 MeV down to the threshold energy.

2. Experimental apparatus

The experiments were carried out using the AVF cyclotron at the Tohoku University CYRIC. The experimental apparatus is almost the same as one employed in Refs. 3-5. A deuteron beam accelerated to 40 MeV by means of cyclotron was transported to the NO.5 target room which was equipped with a beam-swinger system and a neutron flight channel that enabled angular distribution measurements without changing the detector arrangement [6]. The frequency of the deuteron beam was reduced to 2.3 MHz with a beam chopper to avoid a frame-overlap in the time-of-flight (TOF) measurements.

The thick iron and tantalum targets were set on a remotely-controllable target changer together with a beam viewer of a ZnS(Ag) scintillation sheet. The support frame was isolated from ground to read a beam charge induced on the thick target. To measure the number of incident particles accurately, a copper mesh biased to -500 V was installed around the target to suppress secondary electrons emission from the targets.

We adopted a two-detector method to obtain the data over almost the entire energy range of secondary neutrons [4-5,7]. Neutrons emitted from the targets were detected by an NE213 organic liquid scintillation detector, 14-cm-diam \times 10-cm-thick or 2-inch-diam \times 2-inch-thick, through a 1.5 m thick concrete-iron collimator which reduced the background events due to neutron scattering and γ -rays from activated components and the beam dump. The larger and smaller detectors were placed around 11.0 m and 3.5 m from the target, respectively. In the measurements with the longer flight path, an NE213 scintillation detector coupled with a Hamamatsu R1250 photo-multiplier and a tube base specially designed for high energy range neutrons [8] was employed to measure emitted neutrons over the whole energy region with high energy resolution. The shorter flight path was adopted to measure the low energy part of the neutron spectra with high gain avoiding the frame-overlap. The long and short path measurements covered 4.0 – 80 MeV and 0.5 – 5 MeV regions, respectively, of secondary neutron energy range. Using this technique, we obtained the data over almost the entire energy range of secondary neutrons with sufficient energy resolution and good signal-to-noise ratio.

The measurements of the neutron spectra were conducted at seven laboratory angles (0, 5, 15, 30, 60, 90 and 110 deg.) with the beam swinger system. In each measurement, the TOF, pulse-shape-discrimination (PSD) and pulse-height data were collected event by event as three parameter list data for off-line analysis [3-5,7].

3. Target dimensions

The stacked targets were prepared to measure not only thick target neutron spectra but also the activation cross-section of (d,x) reactions for iron and tantalum. The stacked targets consist of twenty elemental iron (purity: 99.5 %) foils of approximately 30 mm \times 30 mm \times 100 μ m thick. The total

thickness (2 mm) is greater than the range calculated with the SRIM code [9] (1.72 mm in iron for 40 MeV deuteron) and thick enough to stop the incident beam.

4. Experimental procedures

First, the neutron measurements were performed for 0-110 degree laboratory angles. During the irradiation, the beam current on the targets was continuously recorded using a multi-channel scalar (MCS) for normalization of the neutron TOF spectra and for the later activation measurements of the stacked targets. The beam current on the targets was around 2 nA and its pulse width was 2-3 ns is FWHM.

After the irradiation, the activities of ^{51}Cr , ^{52}Mn , ^{56}Co , ^{57}Co , ^{58}Co accumulated in each stacked targets were measured by detecting 320.08 keV, 935.52 keV, 1238.26 keV, 122.06 keV and 810.76 keV, γ -rays, respectively, at 5 cm from the detector with a high-pure Ge detector (EURICIS MESURESE GPC50 -195-R) and a multi-channel analyzer. The dead times during the γ -ray counting were less than 2 %.

5. Data analysis

5.1 Neutron Spectra

Neutron TOF spectra were obtained by gating the neutron events with a pulse-height bias on two-dimensional pulse pulse-height vs. PSD graphical plots and by removing random background events to eliminate γ -ray events. The TOF spectra were converted into neutron energy spectra according to the Lorentz conversion [3-5,7].

The energy spectra were divided by the solid angle of the experimental arrangements, an integrated charge of the incident beam and the detection efficiency calculated by the Monte Carlo code SCINFUL-R [10]. Finally, the data were corrected for the attenuation in the air and the wall of a vacuum chamber by means of the total cross-section data of LA150 [11].

5.2 Activation cross-section

The activation cross-section was determined from the peak counts of the γ -ray spectra and the number of projectile with data corrections for the decay, the peak efficiency of the Ge detector, the self-absorption effect in the samples and the beam current fluctuation during irradiation [3]. The efficiency curves were determined experimentally with standard γ -ray sources. The data were corrected for the energy degradation and the attenuation of incident particles through the targets. The incident energy for each stacked foil was estimated by the SRIM code [9].

6. Results and Discussion

6.1 Neutron spectra

For 40 MeV deuterons, the present results for the $^{nat}\text{Fe}(d,xn)$ and $^{nat}\text{Ta}(d,xn)$ neutron spectra at seven laboratory angles are shown in Fig.1. Figure 2, show the comparison of experimental data with the corresponding MCNPX calculation [12]. The data clarified secondary neutron production spectra for whole energy range. The lower energy limit is approximately 0.6 MeV. The error bars of the spectra

represent mainly the statistical errors. The 0-15 deg. spectra show main peaks centered around 15 MeV, similarly with the cases of previous experiments such as $^{nat}\text{Li}(d,xn)$ reaction. Generally, these spectra have very strong angular dependence. It can be concluded that the neutrons are produced by similar reaction mechanisms on the main neutron peak region.

The $^{nat}\text{Ta}(d,xn)$ spectra extended up to approximately 50 MeV though the $^{nat}\text{Fe}(d,xn)$ spectra are limited to around 45 MeV. This is consistent with the reaction Q-value of 9.52 and 3.8 MeV for the $^{nat}\text{Ta}(d,n)$ reaction and $^{nat}\text{Fe}(d,n)$ reaction, respectively. Figure 2 shows the comparison with the results of MCNPX. The results of MCNPX underestimate the experimental data in whole energy region. In the case of 60 degree, the figure is almost same except for lower energy region. Figure 3 shows the comparison of neutron emission spectra from thick Li, C and Al with present data. In this figure, the neutrons from break-up reaction becomes lower while low energy neutrons increase with the increasing target mass. For the reason, lithium seems to be best for the neutron source due to its high neutron yield. Carbon is better material for beam dump due to low activities, although, neutron yield for carbon is larger than the other heavier nuclides.

6.2 Activation cross-section

The cross-section acquired for the $^{nat}\text{Fe}(d,x)^{51}\text{Cr}$, $^{nat}\text{Fe}(d,x)^{52}\text{Mn}$, $^{nat}\text{Fe}(d,x)^{57}\text{Co}$ and $^{nat}\text{Fe}(d,x)^{58}\text{Co}$ reactions are compared with other experimental data [13-18] with the evaluated data by the IAEA group [19] and calculations by a recent code TALYS [20]. Figure 4 shows the comparison for the $^{27}\text{Fe}(d,x)^{51}\text{Cr}$ and ^{52}Mn reaction. The present data is generally consistent with other experimental data. The TALYS results are similar to the experimental data in higher energy region, but they are much lower in magnitude. The present data for the $^{nat}\text{Fe}(d,x)^{56}\text{Co}$, ^{57}Co and ^{58}Co reactions are consistent with other experimental data and the evaluated data except for the TALYS results as shown in Fig.5. To estimate radioactivity induced by deuterons with TALYS, improvements will be required for cross-section calculation models.

7. Summary

This paper described the experiments of (1) neutron energy-angular distribution from the Fe; Ta(d,xn) reactions and (2) cross-sections of the $^{nat}\text{Fe}(d,x)^{51}\text{Cr}$, $^{nat}\text{Fe}(d,x)^{52}\text{Mn}$, $^{nat}\text{Fe}(d,x)^{56}\text{Co}$, $^{nat}\text{Fe}(d,x)^{57}\text{Co}$ and $^{nat}\text{Fe}(d,x)^{58}\text{Co}$ reaction performed using 40 MeV deuterons at Tohoku University CYRIC. In the neutron measurement, the spectra data for seven laboratory angles between 0-110 deg. were measured over almost the entire energy range from the maximum energy down to 0.7 MeV. These experimental results will be used as the basic data to check the accuracy of the Monte Carlo simulation and for the shielding design of tens of MeV accelerator facility such as IFMIF.

The activation cross-section data were acquired for iron from the threshold energy to 40 MeV. The data were generally consistent with other experimental data and evaluated data. However, the results by TALYS were generally much smaller than experimental values, while the shapes were similar to experimental values. The

presented results will be helpful for improvement of the calculation models.

Reference

- [1]IFMIF CDA TEAM, IFMIF Conceptual Design Activity Final Report edited by Marcello Martone, Report 96.11, Enea, Dipartimento Energia, Frascati (1996)
- [2]M.A.Lone et al., Nucl. Instrum. and Meth., 143 (1977) 331
- [3]M. Baba, T. Aoki, M. Hagiwara et al., J. Nucl. Materials 307-311 (2002) 1715.
- [4]M., Hagiwara, et al., J. Nucl. Materials, 329-333, (2004) 218-222
- [5]T. Aoki, M. Hagiwara, M. Baba et al., J. Nucl. Sci. and Technol. 41 No.4 (2004) 399
- [6]Terakawa et al., Nucl. Instrum. Meth. A 491 (2002) 419.
- [7]T. Aoki, M. Baba, S. Yonai, N. Kawata, M. Hagiwara, T. Miura, T. Nakamura, Nucl. Sci. Eng., 146 (2004) 200
- [8]M. Baba, H. Wakabayashi, M. Ishikawa, T. Ito and N. Hirakawa, J. Nucl. Sci. and Technol., 27(No.7) (1990) 601
- [9]J. F. Ziegler, J. P. Biersack, U. Littmark, Pergamon Press, New York (1984).
- [10]S.Meigo Nucl. Instrum. Meth. A 401 (1997) 365
- [11]M. B. Chadwick, P. G. Young et al., Nucl. Sci. Eng. 131 (1999) 293
- [12]L.S. Waters (Ed.), MCNPX User's Manual version 2.4.0, LA-CP-02-408, Los Alamos National Laboratory, Los Alamos, New Mexico, 2002.
- [13]P. Jung, Conf. on Nucl. Data for Sci. and Technol., Juelich, 1991
- [14]J.W. Clark et al., Phys. Rev., 179, 1104
- [15]A. Hermanne et al., Nucl. Instrum. Meth. B, 161-163, 178
- [16]Zhao Wenrong et al., Chinese J. of Nuclear Physics Res., Sect. B, 17, 2, 163
- [17]J.W. Clark et al., Phys. Rev., 179, 1104
- [18]S.Takacs, et al., Conf.on Appl.of Accel.in Res.and Ind.,Denton,USA,1996
- [19]IAEA, Charged-particle cross section database for medical radioisotope production,
<http://www-nds.iaea.org/medical/>
- [20]A.J. Koning, et al., TALYS: Comprehensive nuclear reaction modeling, Conf. on Nucl. Data for Sci. and Technol., Santa Fe, 2005

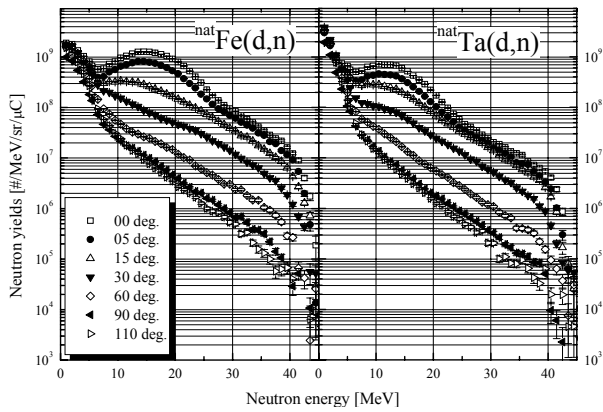


Fig. 1 Neutron spectrum for Fe and Ta

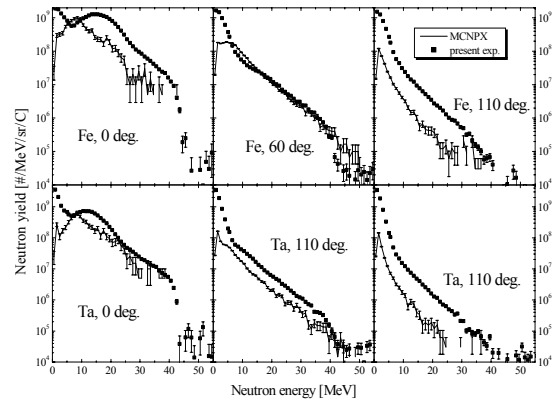


Fig. 2 Comparison with MCNPX

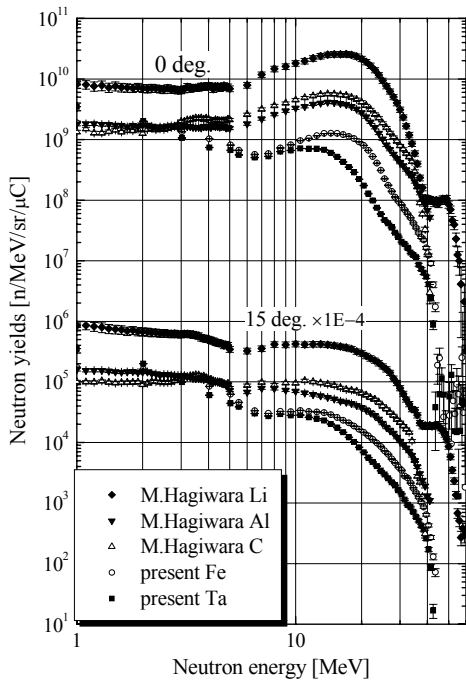


Fig. 3 Neutron spectrum for (d,n) reactions at 40 MeV

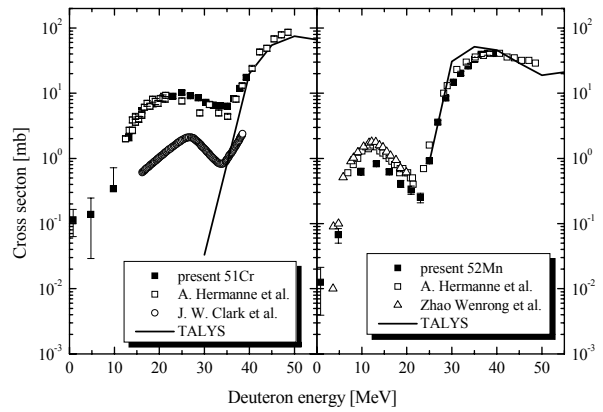


Fig. 4 Activation cross-section for $^{nat}\text{Fe}(d, x)^{51}\text{Cr}, ^{52}\text{Mn}$

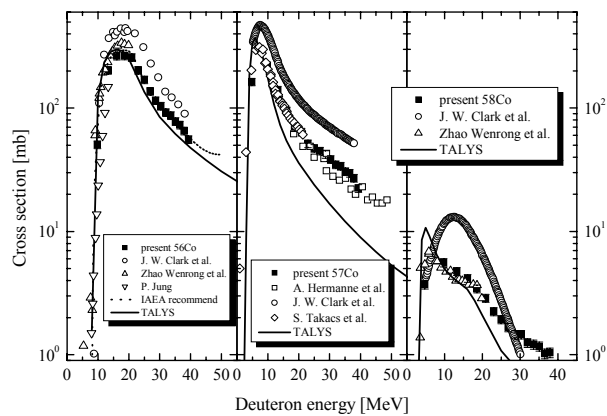


Fig. 5 Activation cross-section for $^{nat}\text{Fe}(d, x)^{56}\text{Co}, ^{57}\text{Co}$ and ^{58}Co

3.11 Analysis of Induced-radioactivity using DCHAIN-SP for Iron, Copper and Niobium at a Mercury Target Irradiated by 2.83 and 24 GeV Protons

Tetsuya Kai, Yoshimi Kasugai, Fujio Maekawa, Shin-ichiro Meigo, Hiroshi Takada, Yujiro Ikeda
 Quantum Beam Science Directorate, Japan Atomic Energy Agency
 Tokai-mura, Naka-gun, Ibaraki-ken 319-1195
 e-mail: tetsuya.kai@j-parc.jp

Reliability estimation was carried out on a radioactivity calculation code system consisting of PHITS, MCNP/4C and DCHAIN-SP 2001 by analyzing an activation experiment performed by using AGS (Alternative Gradient Synchrotron) accelerator at Brookhaven National Laboratory. For induced radioactivity in iron, copper and niobium samples, calculations and experiments were compared indicating that both agreed by a factor of 2 on the average over produced nuclides although the calculation had a tendency to underestimate.

1 Introduction

Many kinds of radioactive nuclides are produced in materials in high-energy intense proton accelerator facilities such as J-PARC [1] conducted by Japan Atomic Energy Agency (JAEA) and the High Energy Accelerator Research Organization (KEK). For calculations of such radioactivity, a high-energy particle induced radioactivity calculation code DCHAIN-SP was developed [2, 3] to combine with such particle transport codes as NMTC/JAM [4, 5] and MCNP[6]. NMTC/JAM estimates nuclide yields produced in target materials mainly by neutrons with energies higher than 20 MeV and protons. MCNP simulates neutron transport phenomena below 20 MeV to provide neutron flux spectra. DCHAIN-SP combines the nuclide yields calculated by NMTC/JAM and those below 20 MeV by folding the activation cross section data with the flux spectra calculated by MCNP, and estimates time-evolution of decaying nuclides by Beteman equation and a decay data library. Physical quantities of radioactivity, decay heat and decay γ -ray spectrum are obtained.

Reliability estimation for this code system was already carried out focusing on either the activation cross section data library below 20 MeV or the nuclide yields calculated by NMTC/JAM. The former was performed using experimental activation data in a 14-MeV neutron field [7, 8], the latter using experimental cross section data in literatures [8]. Although, the reliability estimation was performed using the experimental data in ideal radiation fields, it is also important to estimate the reliability in rather complicated fields including incident protons and spallation neutrons. We utilized an induced-radioactivity experiment[9] performed in a framework of ASTE (AGS Spallation Target Experiment) collaboration [10]. In the experiment, fourteen kinds of materials were activated around the mercury target irradiated by 2.83 and 24 GeV protons. The radioactivity was measured at cooling times from 2 hours to 200 days. In this paper, the radioactivity in iron, copper and niobium is analyzed in order to estimate the reliability of the code system consisting of DCHAIN-SP 2001, PHITS[11] (an upgrade version of NMTC/JAM) and MCNP/4C.

2 Experiment

Figure 1 shows schematic views of the target and the activation samples. Mercury was contained in a cylindrical target container ($\phi=200$ mm, $L=1300$ mm) having a hemisphere beam incident surface

made of stainless steel with 2.5 mm in thickness. The samples of boron-10, boron-11, carbon, aluminum, iron, copper, niobium, mercury-oxide, lead, bismuth, acrylic resin, SS-316, Inconel-625 and Inconel-718 were activated by proton (2.83 and 24 GeV) injection on the target. Sample stacks were set at the on-beam and off-beam position as shown in Fig. 1. The on-beam position samples were irradiated with the incident protons and the spallation neutrons, and off-beam samples were irradiated

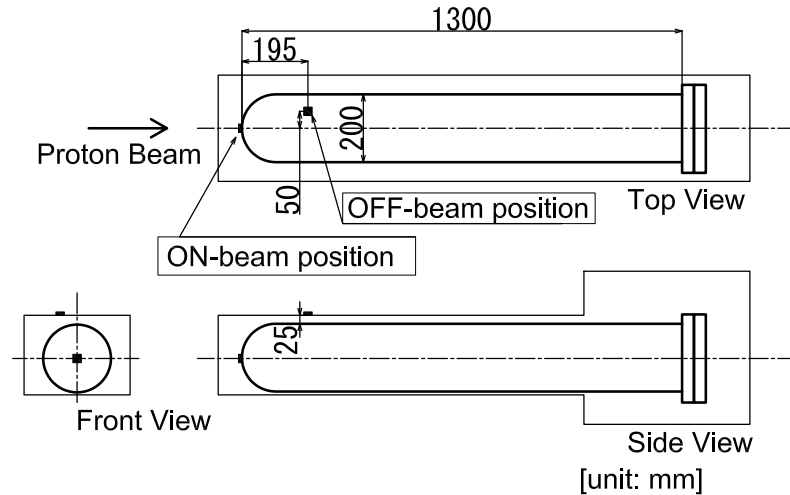


Fig. 1: Side, top and front views of the mercury target. ‘On-beam’ and ‘Off-beam’ positions of activation sample stacks are indicated in the top view.

ated mainly with the spallation neutrons. An integrating current transformer (ICT) was utilized to measure the total number of protons injected onto the mercury target. The imaging plate (IP) technique was employed for monitoring the incident proton beam profile. A thin aluminum foil was exposed to the proton beam. After the irradiation and cooling, foil was attached to an IP to obtain the image of the distribution of radioactivity mainly induced by the $\text{Al}(p,x)^{24}\text{Na}$ reaction. To obtain the numbers of protons bombarded the on-beam samples precisely, we measured ^{24}Na activity in copper foil in the stacks induced by the $^{\text{nat}}\text{Cu}(p,x)$ reaction. After the irradiation, γ -rays of activated samples were measured with HPGe detectors at cooling times between 0.1 and 200 days. Details are shown in reference [9].

3 Analysis

Figure 2 shows a flow diagram of the radioactivity calculation. At first, full geometry calculations with PHITS were carried out. The target container, the all samples, concrete walls of a irradiation room were included in the calculation model. The proton beam profiles were assumed to exhibit Gaussian distributions judging from the IP measurements. The resultant full widths at half maxima (FWHMs) were $(W_x, W_y, E_p) = (40 \text{ mm}, 19 \text{ mm}, 2.83 \text{ GeV})$ and $(27 \text{ mm}, 27 \text{ mm}, 24 \text{ GeV})$, where W_x and W_y were FWHMs in horizontal and vertical directions, E_p the incident proton beam energy. The first PHITS calculations produced proton ($>1 \text{ MeV}$) and neutron ($>20 \text{ MeV}$) energy spectra at the samples. Using the proton and the neutron energy spectra, nuclear production yields were calculated again by PHITS. Although the nuclide yields are produced in the first PHITS calculation, this two-step calculation method was indispensable to achieve adequate uncertainty associated with the Monte Carlo calculation. Since there are many calculation options to select reaction models in PHITS, default parameters are determined to obtain reasonable results through such benchmark calculations as analyses of neutron spectra produced by the spallation reactions. We utilized the default parameters except for INMED option in the calculation of nuclide yields by PHITS. By default, INMED indicates to use the nucleon-nucleon elastic scattering cross sections in medium [12], while that in free-space was utilized for the present nuclide yields calculations. In DCHAIN-SP, we also adopted non-default parameter for ISOMER, which indicates how to treat isomers in the nuclide yields

file. DCHAIN-SP reads the isomer data as is shown in the files by default, however, the current version of PHITS outputs only nuclides in ground state. To avoid serious underestimation of some important nuclides, we adopted a parameter which assumed that nuclides in the ground state and all isomers were produced with equal probabilities. Assuming the

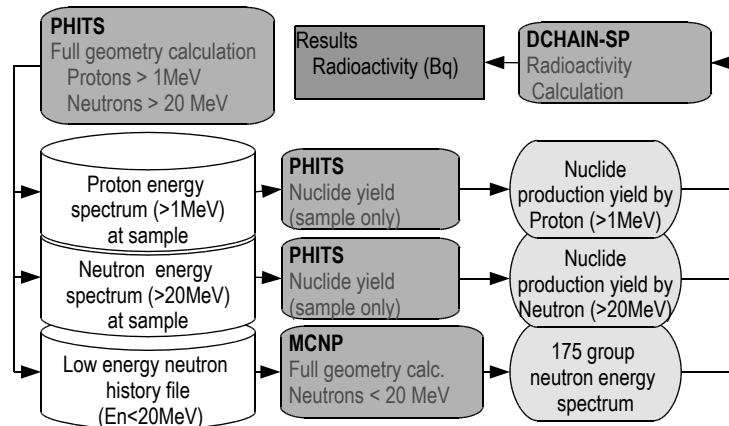


Fig. 2: Flow diagram of radioactivity calculation.

number of isomer is two, underestimation of nuclide production is limited by a factor of 3 although it may cause large overestimation for a nuclide having small production yield in practical.

The number of protons in the off-beam samples and the number of neutrons (both below and above 20 MeV) were normalized to the incident protons measured by ICT. For the number of protons injected into the on-beam samples, we considered it was more reliable to utilize the results by the copper activation method using the foil with same size to the samples since not all protons were injected in the on-beam samples.

4 Results

4.1 Energy Spectra

Figure 3 shows calculated neutron and proton energy spectra in the iron samples at the on-beam and off-beam positions for the $E_p=2.83$ GeV case. At the on-beam position, the incident proton and the secondary neutrons produced in the Hg target are dominant. Spallation reactions, which produce many nuclides having quite different mass from the sample material, are mainly caused by incident protons. The dominant neutrons around 1 MeV initiate reactions producing nuclides having mass numbers close to the sample nuclides. At the off-beam position, the contribution of proton is almost negligible.

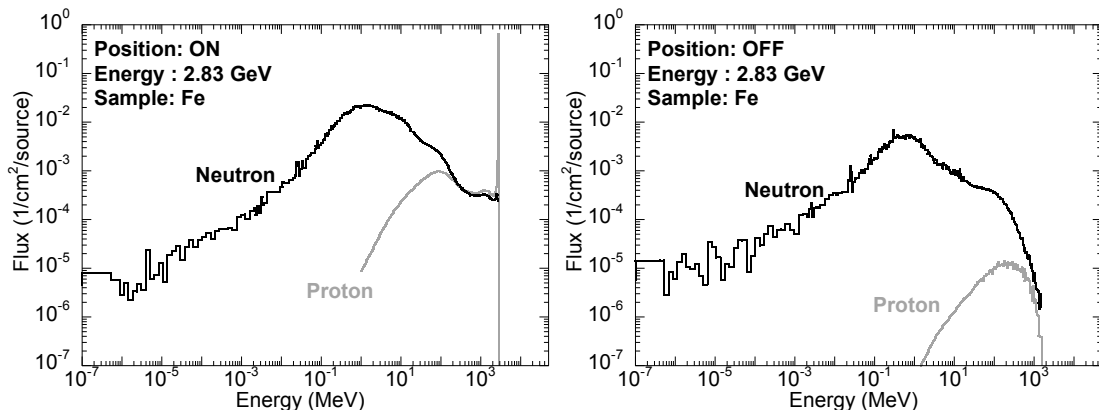


Fig. 3: Proton and neutron energy spectra at the on- and off-beam positions in the iron samples for the $E_p = 2.83$ GeV case.

4.2 Radioactivity

Figure 4 shows time evolution of radioactivity in the iron sample with $E_p=2.83$ GeV. Although most of the calculation results are lower than the experimental ones, the time evolution is almost consistent between them. Therefore, it is appropriate to take average over the cooling-time in discussions about ratios of the calculation to the experiment (C/E). Figure 5 shows C/E values for various radioactivity taking the average considering inverse squares of the experimental errors as weights. Minimum relative error among the original data was adopted as the error of the averaged C/E. Upper four figures in Fig. 5 show C/E of radioactivity in the iron samples at the on-beam and off-beam positions for the $E_p=2.83$ and 24 GeV cases. The measured nuclides are analogous among these results. Except for the $E_p=24$ GeV case at the off-beam position, the calculated radioactivity agrees with the experimental results by a factor of 2~3 although the calculation trended to underestimate. The radioactivity of ^{24}Na is underestimated by one order of magnitude only in the $E_p=24$ GeV case at the off-beam position. For other nuclides, the C/E values are between 0.3 and 1.0. The reason why only the estimation of ^{24}Na in this case exhibited such large discrepancy is not understood. Excluding this data, the averages of C/E are 0.67, 0.84, 0.66 and 0.49 for the cases of $E_p=2.83$ GeV at the on-beam, $E_p=24$ GeV at the on-beam, $E_p=2.83$ GeV at the off-beam and $E_p=24$ GeV at the off-beam positions, respectively.

In middle of Fig. 5, C/E values are shown for the radioactivity in the copper samples. The results are only for the on-beam position since no copper sample was put at the off-beam position in the experiment. The calculated radioactivity agrees with the experimental results almost by a factor of 2~3 although rather large discrepancies are found in ^{52}Mn . The averages of C/E are 0.58 and 0.80 for the $E_p=2.83$ and 24 GeV cases, respectively. The calculated cross sections by PHITS were compared with existing experimental ones for further discussions. The $^{nat}\text{Cu}(p,x)^{24}\text{Na}$ reaction was utilized as a reference to obtain the number of protons in the experiment. In $E_p=2.83$ GeV case, the cross section of 3.5 ± 0.5 mb was adopted [9] while those of 2.4 mb was calculated by PHITS. The C/E value of 0.52 for ^{24}Na is reasonable considering the difference of the cross section, the error of the cross section (15%) and the uncertainty of ^{24}Na activity (5%).

In bottom four figures of Fig. 5, C/E values are shown for the radioactivity in the niobium samples. In all cases, good agreement is shown for ^{92m}Nb indicating that the calculated neutron fluences were reasonable between 11 and 20 MeV, in which the $^{93}\text{Nb}(n,2n)^{92m}\text{Nb}$ reaction is sensitive. However, exceptional underestimation is recognized for ^{67}Cu , ^{76}As and ^{82}Br at the on-beam position, and for ^{46}Sc , ^{57}Co and ^{60}Co at the off-beam position by one to three order of magnitude. On the other hand, ^{44}Sc and ^{76}Br in the $E_p=24$ GeV case at the on-beam

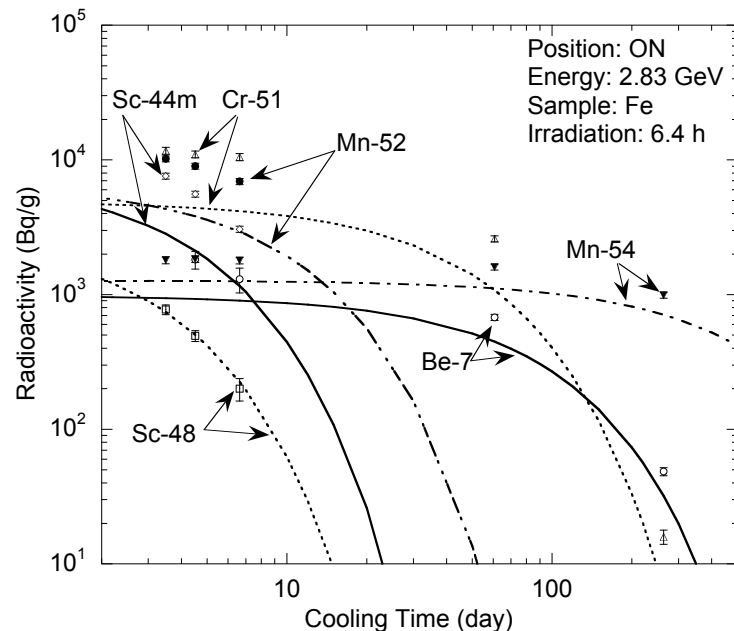


Fig. 4: Time evolution of radioactivity in the iron sample at the on-beam position in case of $E_p=2.83$ GeV. Symbols are the measured ones, lines are the calculated ones.

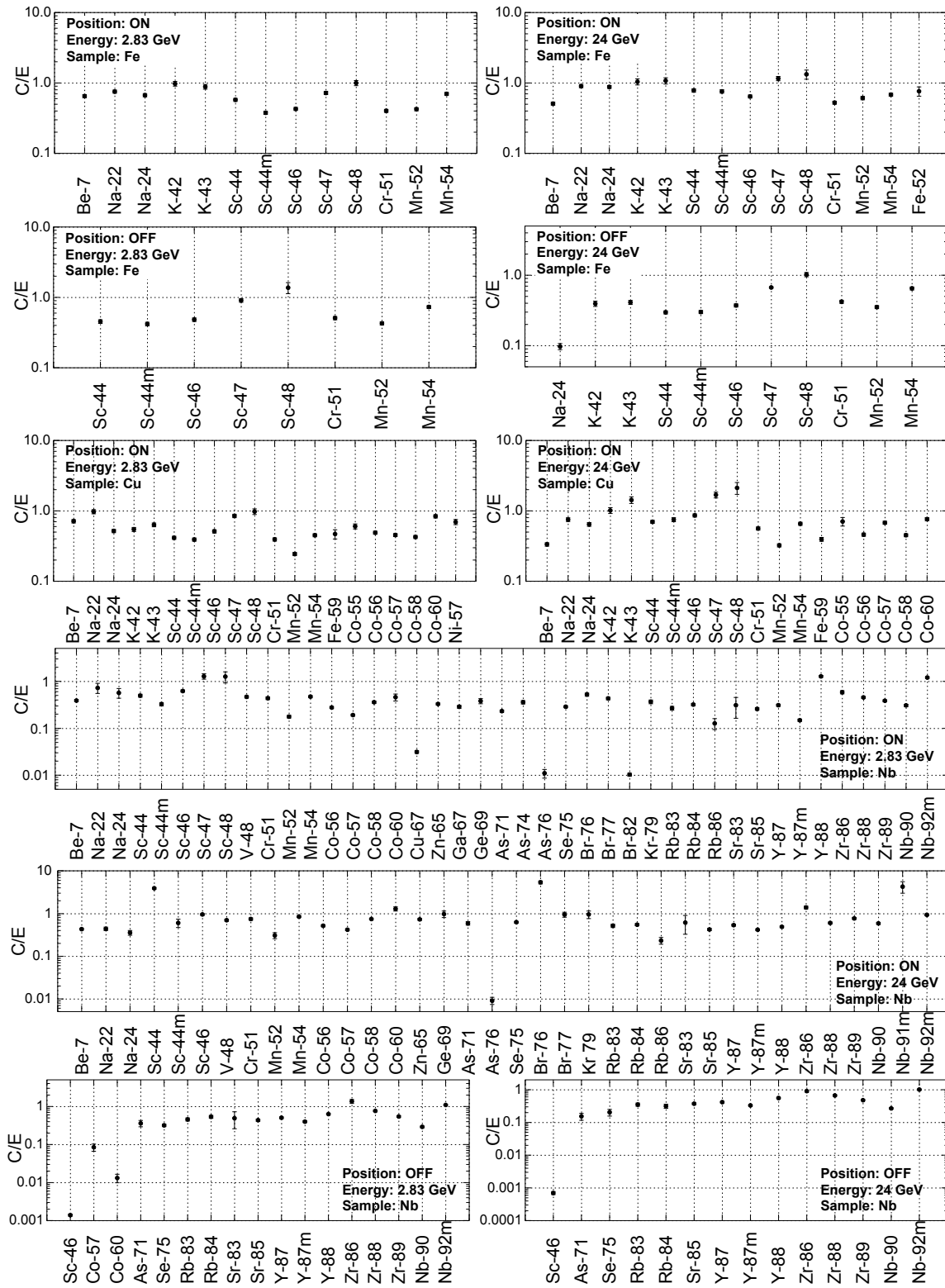


Fig. 5: C/E values for radioactivity in iron, copper and niobium samples. Sample positions, incident proton energies and sample materials are shown in figures.

position are overestimated by a factor of 4 and 5, respectively. The reason for the overestimation was found to be large C/E values at the shortest cooling time. Excluding such data, the C/E values are improved to be 0.56 for ^{44}Sc and 1.1 for ^{76}Br . Although C/E for $^{91\text{m}}\text{Nb}$ is also large, there is not such a discrepancy as in the above case. Assuming all nuclides were produced in the grand state by selection of the ISOMER parameter in DCHAIN-SP, C/E for $^{91\text{m}}\text{Nb}$ was underestimated by a factor of forty. As mentioned in the section 3, one of the reasons for the overestimation is considered to be that nuclides in the grand state and all isomers were assumed to be produced with equal probabilities. Excluding the exceptional data, the averages of C/E are 0.47, 0.78, 0.59 and 0.46 for the cases of $E_p=2.83$ GeV at the on-beam, $E_p=24$ GeV at the on-beam, $E_p=2.83$ GeV at the off-beam and $E_p=24$ GeV at the off-beam positions, respectively.

5 Conclusion

The radioactivity experiment was analyzed to estimate the calculation reliability of the code system. The calculations were consistent with the experiments within a factor of 2 on the average over the produced nuclides excluding the data exhibiting the exceptional discrepancies although the calculations were lower than the experiment on the whole. The overestimation for $^{91\text{m}}\text{Nb}$ produced from the niobium sample was caused by the assumption that a nuclide in the grand state and all isomers were produced with equal probabilities. Further discussions are important to improve the calculation reliability, however, we concluded that the code system was available to estimate the radioactivity in iron, copper and niobium. We considered this conclusion was also valid for other nuclides having middle mass number.

Acknowledgements

The authors would like to thank Drs. K. Niita, C. Konno and H. Katoh for their useful comments.

Reference

- [1] The Joint Project Team of JAERI and KEK, *JAERI-Tech 99-056*, JAERI (1999).
- [2] H. Takada, K. Kosako, *JAERI-Data/Code 99-008*, JAERI (1999).
- [3] T. Kai, et al., *JAERI-Data/Code 2001-016*, JAERI (2001) [in Japanese].
- [4] K. Niita, et al., *Nucl. Instrum. Meth. B* **184** (2001) 406.
- [5] Y. Nara, et al., *Phys. Rev. C* **61** (2000) 024901.
- [6] J. F. Briesmeister (Ed.), *LA-13709-M*, Los Alamos National Laboratory (2000).
- [7] T. Kai, et al., *JAERI-Research 2002-005*, JAERI (2002).
- [8] T. Kai, et al., *Proc. ICANS-XVI*, Düsseldorf-Neuss, Germany, May 12 - 15, 2003, 1041.
- [9] Y. Kasugai, et al., *JAERI-Research 2003-034 (2004)*.
- [10] H. Nakashima, et al., *J. Nucl. Sci. Technol.*, **Supplement 2**, (2002) 1155.
- [11] H. Iwase, K. Niita, T. Nakamura, *J. Nucl. Sci. Technol.* **39** (2002) 1142.
- [12] J. Cugnon, et al., *Nucl. Phys. A* **352** (1981) 505 ; J. Cugnon, *Phys. Rev. C* **22** (1980) 1885.

3.12 Analysis of Induced-radioactivity using DCHAIN-SP for Pb and Hg at a Mercury Target Irradiated by 2.8 and 24 GeV Protons

Yoshimi Kasugai, Tetsuya Kai, Fujio Maekawa, Shinichiro Meigo, Hiroshi Takada, Yujiro. Ikeda

Japan Atomic Energy Agency
 Tokai-mura, Naka-gun, Ibaraki-ken 319-1195
 e-mail: kasugai.yoshimi@jaea.go.jp

The high energy particle induced radioactivity calculation code system consisting PHITS, MCNP4C and DCHAIN-SP 2001 was validated for mercury and lead samples by the experimental activation data obtained using AGS (Alternative Gradient Synchrotrons) accelerator at Brookhaven National Laboratory. As a result, we found that the calculation is consistent with the experimental data within a factor of 2 on the average. Mass yield curves of the spallation reactions were approximately deduced using the experimental activation data.

1. Introduction

Radioactivity estimation in spallation neutron field including incident high-energy protons is essential for designing spallation neutron target and accelerator driven nuclear transmutation system. In particular, the estimation for heavy material such as mercury and lead is important since those elements are used as target materials. However, the radioactivity estimation for such heavy material has not been easy and reliable, because the products cover wide range of nuclei, consideration of huge kinds of reaction paths is required, and the most of reaction cross sections for high energy incident particles are unknown or unreliable.

A radioactivity calculation code consisting PHITS, MCNP4C and DCHAIN-SP 2001 [1] has been used for the radioactivity estimation for design of the J-PARC facilities. It is important to know the safety margin of the calculation code for efficient and reliable design. The code validation has been carried out using the experimental activation data for 14 MeV neutron field, and the nuclide production calculation by PHITS has been validated using the experimental cross section data in literature. However the code validation for mixed radiation field including incident protons and spallation neutrons has not been performed yet. Therefore, we carried out the activation experiment for such kinds of mixed field using AGS (Alternative Gradient Synchrotrons) accelerator at Brookhaven National Laboratory. Using these data, we validated the code system for the major structural materials irradiated in the mixed radiation field. In this paper, we present the analytical results for mercury and lead samples.

2. Experiment

Schematic drawing of the AGS accelerator complex and the mercury target used in the experiment are shown in Figs. 1 and 2, respectively. In the experiment, the samples of mercury-oxide, lead and others were irradiated around the mercury target, which was bombarded with 2.83 and 24 GeV protons. The samples were placed at the top and side of the target; the top and side samples were called "On-" and "Off-beam" samples, respectively. The on-beam samples were irradiated by incident protons in addition to secondary neutrons, and the off-beam samples were mainly irradiated by the spallation neutrons from the target. The number of protons injected to each on-beam sample were determined by the foil activation method using the reference reaction of $\text{Cu}(p, x)^{24}\text{Na}$. Using the previous experimental data, the cross section values were evaluated to be 3.5 ± 0.5 mb and 3.5 ± 0.2 mb at the proton energies of 2.83 GeV and 24 GeV, respectively. The total incident protons were measured by an integrating current transformer (ICT) and separated electron chamber (SEC). The neutron flux at the off-beam samples were validated using $^{93}\text{Nb}(n, 2n)^{92m}\text{Nb}$ reaction. After the irradiation, the radioactivities of samples were measured with HPGe detectors at the cooling time between 2 h and 267 d. The detail of the experimental procedure and

the experimental data were shown in the reference [2].

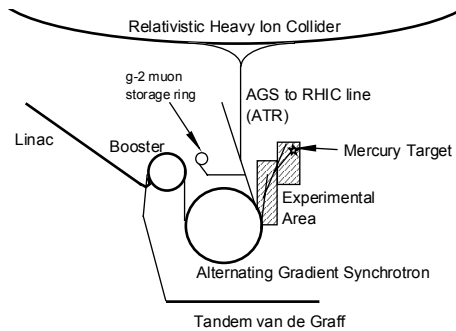


Fig. 1 A schematic drawing of the AGS accelerator complex.

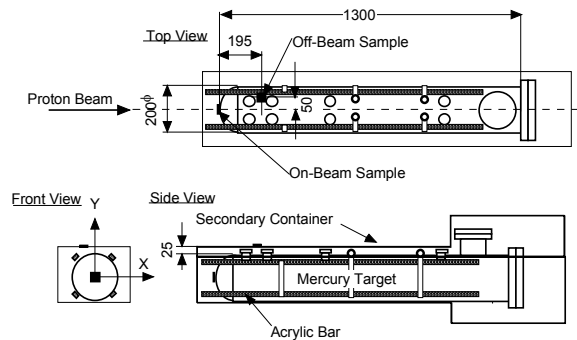


Fig. 2 Top, front and side view of the mercury target. The target container was made of stainless steel with 2.5 mm in thickness. The acrylic bar was used to set the activation detectors for measurement of neutron performance of the mercury target.

3. Analysis

In the analysis, we used the calculation model including the mercury target, a target container of stainless steel, all samples and concrete walls of the irradiation room. Proton beam profile was assumed to be a Gaussian distribution which was measured parameters of a full width at half maximum (FWHM) and the center of proton beam. For each sample, proton spectrum was calculated by PHITS, and neutron spectrum was obtained by PHITS (>20 MeV) and MCNP/4C(<20 MeV). Using the proton energy spectra and the neutron energy spectra above 20 MeV, nuclear production yields were calculated by PHITS. DCHAIN-SP calculated the radioactivity of the samples by using the nuclear production yields and the neutron energy spectra below 20 MeV. For the off-beam samples, the proton energy spectra were normalized to the number of protons obtained by the activation method using the copper foil. The proton energy spectra of the samples on the side surface and the neutron energy spectra were normalized to the number of incident protons measured by ICT. The calculation procedure is described in the reference presented in this conference [3].

4. Result and Discussion

Decay curves of induced radioactivities were calculated for each sample. Figure 3 shows the calculated decay curves and the experimental data for mercury-oxide samples irradiated at on-beam position for 2.83 GeV protons. This figure shows that the calculation well-reproduces the decay feature of major products such as ^{203}Hg , $^{197\text{m}}\text{Hg}$, $^{198\text{g}}\text{Au}$, ^{185}Os and $^{182\text{m}}\text{Re}$. C/E-values for each radioactive product are shown for mercury-oxide and lead samples in Fig. 4 and 5, respectively. If we had multiple

experimental data with different cooling time, the average values were adopted as representative values. These figures show that the calculation is consistent with the experimental data within a factor of 2 on the average. However, the calculated values are lower than the experimental data on the whole. In addition the C/E-values have the mass-number dependence, which implies that the calculated yield curve for spallation reactions shows different tendency from the real curve. In order to make it clear, the experimental-basis mass yield curves for Pb were deduced under the assumptions as follows:

- Proton-number (Z) dependence of calculated spallation yield at a fixed mass number (A) is approximately reasonable.
- The differences between the calculated and experimental radioactivities are largely due to the calculated mass yield.

On the basis of these assumptions, the experimental-basis mass yields were deduced from (Calculated total yield)/(C/E). The upper figures in Fig. 6 show the mass yield curves for Pb samples irradiated at on-beam position on 2.83 and 24 GeV incident protons. The calculated production yield for proton- and neutron-incidents and the total yield curves are shown in the figure. The lower figures show the C/E-values for radioactivities as a function of mass number of products. Experimental-basis yields are shown by circles in the upper figures. Considering the distribution of the circles, the yield curves should be drawn in between the two dotted lines indicated by two-headed arrows in order to obtain more consistency between the calculation and the experimental data. The calculation curves at $A \sim 20$ and 170 show underestimation by a factor of more than 10 and 2, respectively.

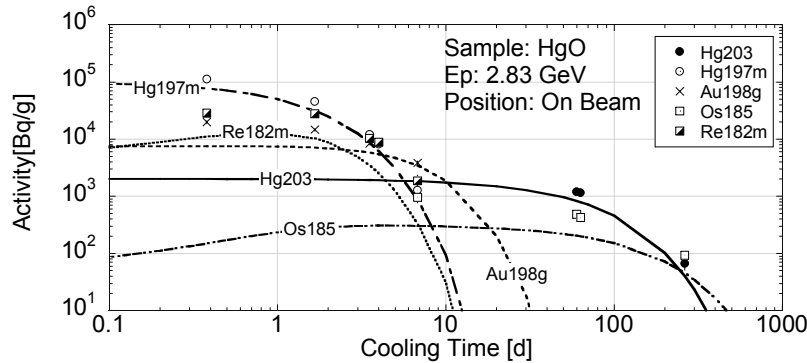


Fig. 3 Radioactivity of the HGO sample irradiated at on-beam position for 2.83 GeV incident protons. Circles, squares and crosses show the measured data, and lines show the decay curve calculated using DCHAIN-SP.

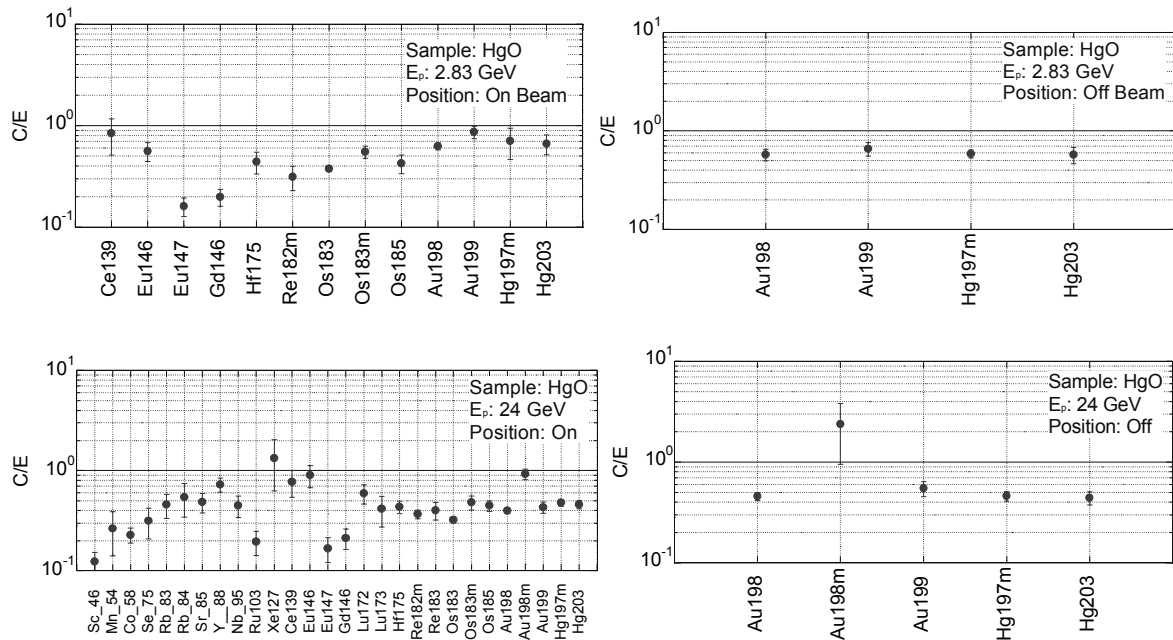


Fig. 4 C/E for the radioactivity of HgO samples.

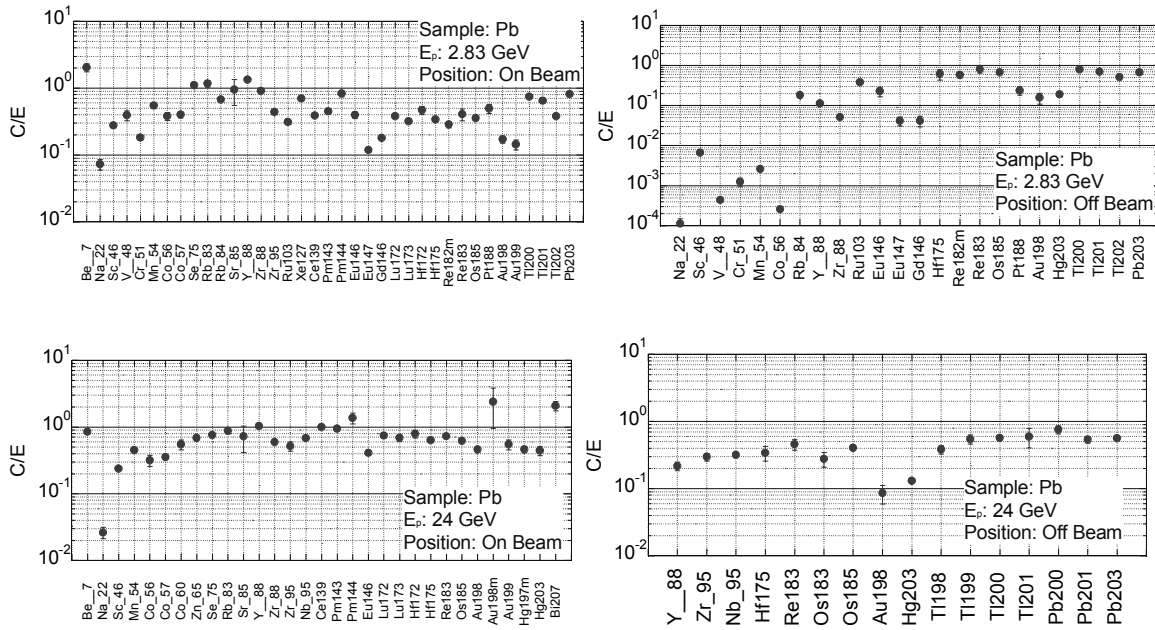


Fig. 5 C/E for the radioactivity of Pb samples.

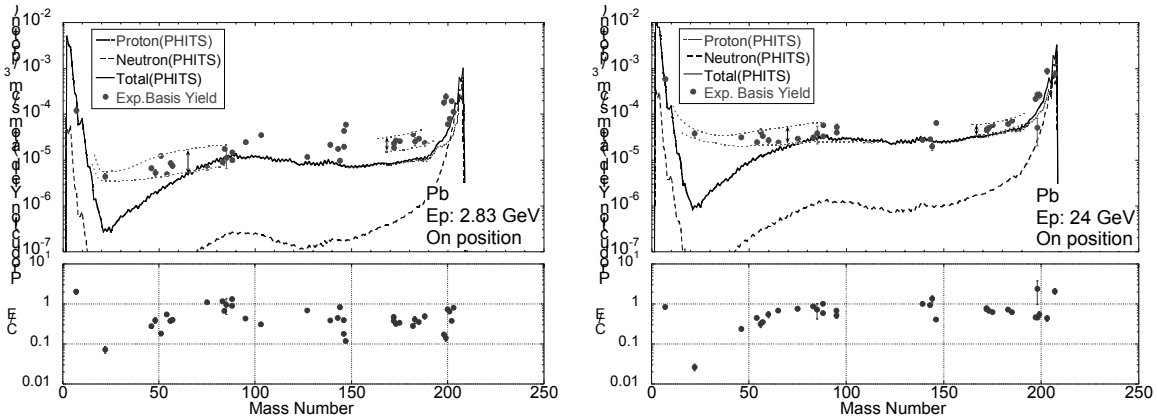


Fig. 6 The upper figures show the mass yield curves for the Pb sample irradiated at on-beam position on 2.83 and 24 GeV incident protons. In the figures the dotted lines show the production yield for protons and neutrons, and the solid lines show the total yield curve. The lower figures show the C/E values of radioactivities as a function of mass number of products. The closed circles in the upper figures are experimental-basis yield deduced by dividing the calculated total yield by the C/E-value. On the basis of the present experimental data, the yield curves should be drawn in between the two dotted lines indicated by two-headed arrows.

In order to check the calculation in detail, proton-induced cross sections for 2.8 and 24 GeV were estimated using the present activation data of the on-beam samples by neglecting the contribution of neutrons. Since the radioactive products in the on-beam samples were almost induced by incident protons except at $A \sim 200$, we supposed to obtain the reasonable proton-induced cross sections using the present activation data. In Fig. 7, the cross sections deduced using the present data are plotted as a function of the mass number of products. Previous reported data of Gloris et al. [4] for 1.6 GeV protons are shown in the figure for reference. The mass-yield cross sections calculated by PHITS were also plotted. At $A \sim 170$, the Gloris' data for 1.6 GeV shows 20~30 mb and the present data for 2.83 and 24 GeV are 20~30 mb and 10~20 mb, respectively. The present values are reasonable considering the typical shape of the excitation curves in this mass region. The experimental cross sections, which is cumulative yields of spallation products, can be interpreted as the minimum value of the mass yield cross section. The mass yield curve should always be larger than the experimental data. In this context, the calculation curve of PHITS shows

underestimation at $A \sim 20$ and 170.

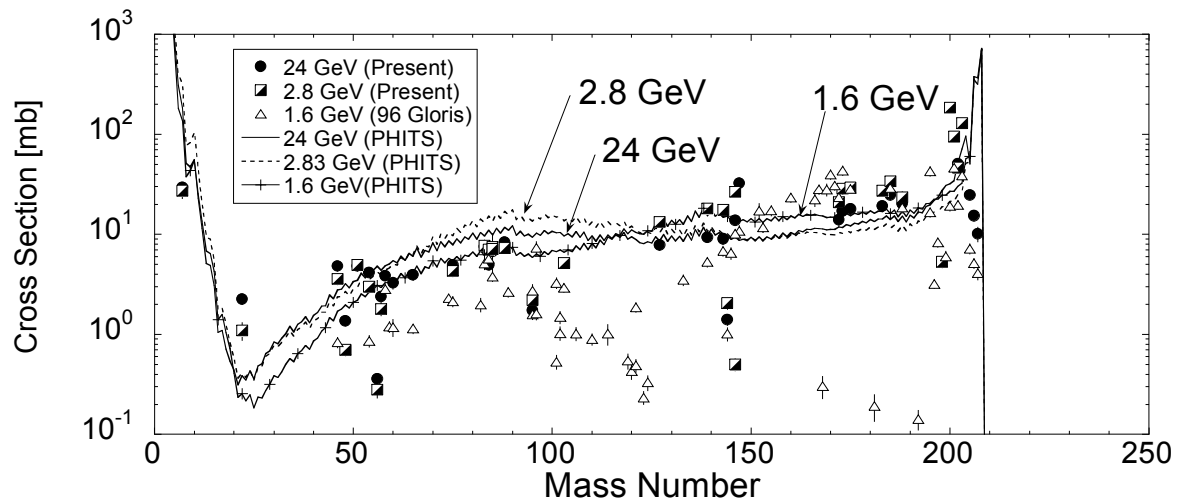


Fig. 7 Proton induced cross sections for 2.8 and 24 GeV were deduce using the present experimental data for the on-beam samples by neglecting the contribution of neutrons. The closed and open circles show the present data for 24 and 2.83 GeV protons, respectively. The experimental data for 1.6 GeV protons, which were reported by Gloris et al.[4], are plotted by triangles. The lines show the calculation curves by PHITS for 1.6, 2.83 and 24 GeV incident-protons.

5. Summary

The high energy particle induced radioactivity calculation code system was validated for mercury and lead samples by using the experimental activation data. As a result, the calculation is consistent with the experimental data within a factor of 2 on the average, and calculated values are lower than the experimental data on the whole. Mass yield curves of the spallation reactions could be approximately deduced using the experimental activation data. By comparing between the experimental-basis mass yield curve and the calculation curve, we found that the calculation show underestimation by a factor about 2 around $A \sim 170$. The calculated production yield should be larger by a factor more than 10 at $A \sim 20$.

Acknowledgements

The authors would like to thank Drs. K. Niita, C. Konno and T. Katoh for their useful comment.

References

- [1] T. Kai, F. Maekawa, K. Kosako, Y. Kasugai, T. Takada and Y. Ikeda: "DCHAIN-SP 2001: High Energy Particle Induced Radioactivity Calculation Code", JAERI-Data/Code 2001-016 (2001) (In Japanese).
- [2] Y. Kasugai, T. Kai, F. Maekawa, H. Nakashima, H. Takada, C. Konno, M. Numajiri, T. Ino and K. Takahashi: "Measurement of Radioactivity induced by GeV-Protons and Spallation Neutrons using AGS Accelerator.", JAERI-Research 2003-034 (2004).
- [3] T. Kai, Y. Kasugai, F. Maekawa, S. Meigo, H. Takada, Y. Ikeda: "Analysis of Induced-radioactivity using DCHAIN-SP for Light Nuclei at a Mercury Target Irradiated by 2.8 and 24 GeV Protons", in this proceedings.
- [4] M. Gloris, R. Michel, U. Herpers and F. Sudbrock and F. Filges: Nucl. Instrum. and Methods, B113, 429 (1996).

3.13 Resonance Analysis Combined with Optical Model

Toru Murata* and Tsuneo Nakagawa**

*former Toshiba, **JAEA Nuclear Data Center

e-mail: t.murata@ma.point.ne.jp

For the resonance analysis of neutron total and elastic scattering cross sections of light nuclides, combined model with the optical model is presented, and as an example, total cross section of the $^{18}\text{O}+n$ reaction was analyzed.

1. Introduction

Cross sections of light nucleus show composite resonance structures in the incident energy range over 10 MeV. Ordinary method of resonance analysis requires frequently some wide resonance levels in the outside of the objective resonance region. These background resonance levels would not be explained physically. These background resonance levels could be predicted by the optical model, as some dispersed single particle states, using adequate potential parameters. So, combination of resonance formula and the optical model will be useful to analyze resonance region cross sections and effective to obtain continuation of nuclear data between resonance region and higher energy region that will be analyzed with the optical model.

2. Analysis method

In the present model, the collision matrix U which describes the neutron elastic scattering channel is assumed to be given by the sum of optical model U^{opt} and resonance formula U^{res} of the same spin-parity state, such as

$$U_{J\pi} = kU_{J\pi}^{\text{opt}} + (1-k)U_{J\pi}^{\text{res}} \quad (1)$$

where k is the optical model weight factor and resonance term weight was determined to hold U unitary approximately and normalized so as to $|U_{J\pi}|^2 = 1$. The collision matrix of R-matrix is given by, under assumption that the same spin parity resonance levels have same ratio of reduced width between each channel¹⁾.

$$U_{cc' J\pi}^{res} = \exp i(\omega_c - \phi_c) \left[\delta_{cc'} + \frac{\sum_{\lambda} i\Gamma_{\lambda c}^{1/2} \Gamma_{\lambda c'}^{1/2} / (E_{\lambda} - E)}{1 + \sum_{\lambda} (\Delta_{\lambda} - i\Gamma_{\lambda} / 2) / (E_{\lambda} - E)} \right]_{J\pi} \exp i(\omega_{c'} - \phi_{c'}) \quad (2)$$

where notations are given in article by Lane and Thomas²⁾ and energy dependence of resonance widths are given by using barrier penetration factor P_l

$$\Gamma_{\lambda a}(E) = P_l(E) \Gamma_{\lambda a}(E_{\lambda}) / P_l(E_{\lambda}) \quad (3)$$

The optical model collision function U_{opt} is given by

$$U_{J\pi}^{opt} = \exp(2i\delta_{J\pi}), \text{ and } \delta_{J\pi} = \alpha_{J\pi} + i\beta_{J\pi} \quad (4)$$

Real and imaginary part of phase shift $\alpha_{J\pi}$ and $\beta_{J\pi}$ are calculated with optical model code such as ELIESE-3³⁾.

Cross sections of total and elastic scattering and angular distribution of scattered neutrons are calculated using the combined collision function given by Eq. (1) with ordinary formula²⁾;

Total cross section

$$\sigma_{tot} = \frac{\pi}{k_n^2} \sum_{Jl} 2g_J [1 - \text{Re}(U_{Jl})] \quad (5)$$

Elastic scattering cross section

$$\sigma_{el} = \frac{\pi}{k_n^2} \sum_{Jl} g_J [1 - \text{Re}(U_{Jl})^2 + \text{Im}(U_{Jl})^2] \quad (6)$$

Angular distribution (general case)

$$d\sigma_{aa'} = \sum_{s,\tau} \frac{k_a^{-2}}{(2s+1)} \sum_L B_L(a's'; as, \tau) P_L(\cos \theta) d\Omega \quad (7)$$

$$B_L(a's'; as, \tau) = \frac{(-1)^{s'-s}}{4} \sum_{J_1 J_2 l_1 l_2 l_1' l_2'} i^{l_1 - l_2 - L} Z(l_1 J_1 l_2 J_2, sL) \times i^{l_1' - l_2' - L} Z(l_1' J_1 l_2' J_2, s'L) \times$$

$$\text{Re}[(\delta_{aa'} \delta_{l_1 l_1'} \delta_{s s'} - U_{a's'l_1', asl_1, J_1 \tau})^* (\delta_{a'a} \delta_{s's} \delta_{l_2 l_2'} - U_{a's'l_2', asl_2, J_2 \tau})]$$

3. Result of application and discussion

We are now evaluating the nuclear data for the $^{18}\text{O}+n$ reaction and analyzing the experimental total cross sections measured by Vaughn et al.⁴⁾ and by Salisbury et al.⁵⁾. Koehler et al.⁶⁾ measured angular distributions of elastic and inelastic ($E_x=1.98\text{MeV}$) scattered neutrons and the analysis was made in detail with a multilevel-multichannel R-matrix code and resonance parameters were obtained in the incident neutron energy region

$E_n = 0 \sim 7.5$ MeV. For the analysis, they assumed seven broad background resonance levels in the region $E_n \approx 10 \sim 15.5$ MeV. To examine the effect of the background resonance levels, we reanalyze the total cross section below $E_n = 5.0$ MeV with the resonance formula given in Eq.(2) by adjusting the resonance parameters given by Koehler et al.. Result of the reanalysis is shown in Fig.1. If no background resonance levels included, calculated cross section (dashed line) is fairly larger than experimental one. The background resonance levels seem to be set to reproduce the average experimental cross sections.

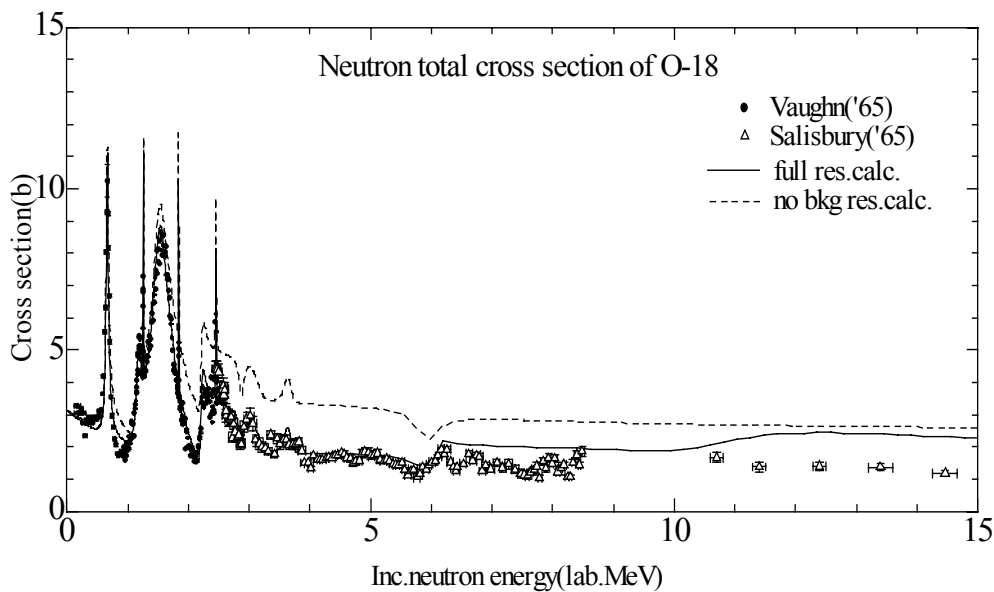


Fig.1 Effect of the seven background resonance levels assumed in $E_n > 10$ MeV by Koehler et al.⁶⁾ Solid line shows the calculated cross section using full resonance levels and dashed line shows calculated one without the background resonance levels.

Figure 2 shows the total cross section in the incident energy region $E_n \leq 5.0$ MeV with the present model comparing with the experimental data. The dashed line shows the optical model total cross section calculated with ELIESE-3 code using potential parameters given by Wilmore and Hodgson⁷⁾. The optical model U^{opt} was calculated with the same code and same potential parameters. The resonance U^{res} was calculated using 14 resonances of almost same resonance parameters of the calculation in Fig.1 and the optical model weight factor $k=0.35$.

Though the present model will be applied to analyze the cross section of resonance region without background resonance levels, simple weighted sum of collision functions given by Eq. (1) will reduce somewhat pure resonance amplitude and there is possibility to mis-assign the spin-parity of resonance levels. Further study shall be made for the combination of the optical model and resonance formula from more fundamental stand points.

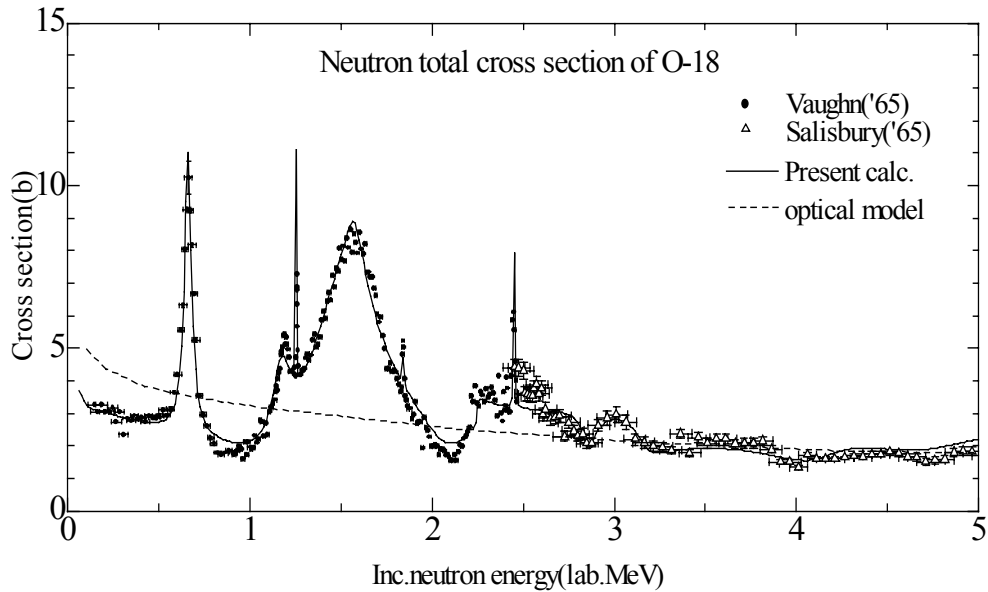


Fig.2 Comparison between the experimental cross sections and those calculated with the present model (solid line) and with the optical model (dashed line).

References

- 1) Murata, T. : Proc. Int. Conf. on Nuclear Data for Sci. and Tech.(Mito,1998),p.557
- 2) Lane, A., Thomas, R.G.: Rev.Mod.Phys.30,257(1958)
- 3) Igarasi, S. JAERI 1224 (1972)
- 4) Vaughn,F.J. Grench, H.A., Imhof, W.L, Rowland, J.H., Walt, M.: Nucl. Physics 64,336(1965)
- 5) Salisbury, S.R. Fossan, D.B., Vaughn ,F.J.: Nucl. Physics 64,343(1965)
- 6) Koehler, P.E., Knox, H.D., Resler, D.A., Lane, R.O.: Nucl. Physics A453,429(1986)
- 7) Wilmore, D., Hodgson, P.E. Nucl. Physics 55,673(1964)

3.14 Analysis of Fission with Selective Channel Scission Model

Masayuki OHTA and Shoji NAKAMURA

Japan Atomic Energy Agency

2-4 Shirakata-Shirane, Tokai-mura, Naka-gun, Ibaraki, 319-1195, Japan

E-mail: ohta.masayuki@jaea.go.jp

The mass distributions of fission product yields for neutron-induced fissions of ^{232}Th , ^{235}U , ^{239}Pu and ^{241}Pu were calculated by the selective channel scission model with simple assumptions. Although the present calculation is a rough estimation, it is applicable to the wide range of fissionable nuclei without the adjustable parameters for each fission channel.

1. Introduction

The multimodal random-neck rupture model [1], which based on the assumption of the existence of few fission paths (modes), has been used for fission analyses as the standard. Recently, the five-dimensional analysis [2] revealed the existence of symmetric and asymmetric paths of fission. There are some improvements and developments for fission analysis. However, there still remain difficulties in prediction of the fission product (FP) yields about which there are no experimental data. Therefore, the selective channel scission (SCS) model [3-5] has been proposed to calculate the fission product yield. This model deals with the fission process for each channel. The fission product yields are calculated from the penetrabilities of the channel-dependent fission barriers. Since the channel-dependent fission barrier has not been calculated theoretically yet, the adjustable parameters which are concerned with the elongation and the deformation of the nucleus and the Coulomb potential between two fission fragments have been introduced to calculate the channel-dependent fission barrier.

This paper gives the results for fission product yields obtained by SCS model with the simple assumptions, and discusses the correlation between the parameter and the fission modes on the multimodal random-neck rupture model.

2. Model Assumptions and Calculations

The fission process and the potential are shown in **Fig. 1**. The excited nucleus is deformed, and induces tandem (dumbbell) oscillation collectively. It starts scission to form two fission fragments (FP1 and FP2). Here, the following fission potentials are considered for all fission channels. The channel-dependent fission barrier E_f is estimated from the difference between the Q -value and the potential at the saddle point

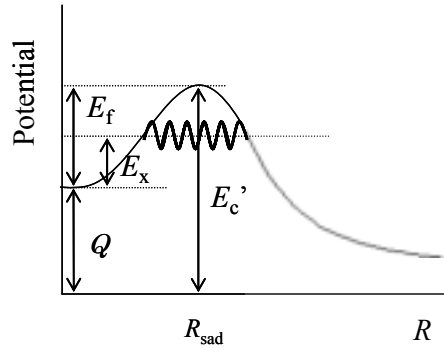
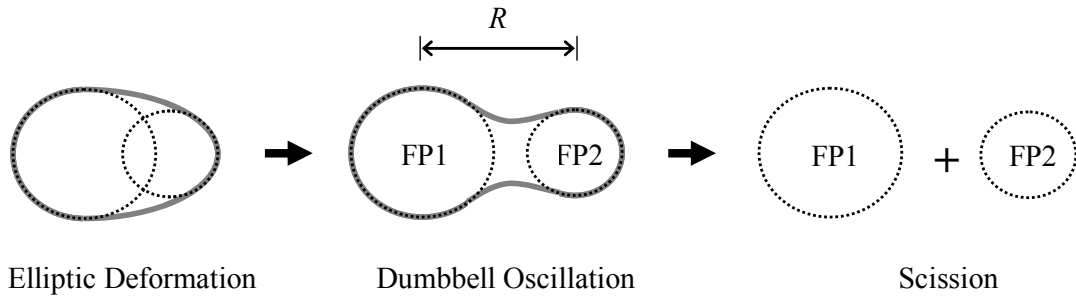


Fig. 1 Fission process and potential.

R_{sad} . In this work, the E_f is calculated with simple assumptions described below.

The potential at R_{sad} is estimated from the Coulomb potential between two fission fragments of the certain channel. It assumes that the R_{sad} is given by the sum of the radii of two fragments at the grand state (R_1' and R_2') and the distance of the nuclear interaction ($\Delta \approx 2$ fm).

$$R_{\text{sad}} = R_1' + R_2' + \Delta. \quad (1)$$

For the deformations of nuclei, the data of KTUY mass formula [6] were used in this analysis. The value of R_{sad} approximately corresponds to the interaction distance of the nuclear reaction. The Coulomb barrier is given by Eq. (2),

$$E_c' = \frac{1.44 Z_1 Z_2}{R_{\text{sad}}}, \quad (2)$$

in MeV and fm units, where Z_1 and Z_2 are the atomic number of the fragments FP1 and FP2, respectively.

The channel-dependent barrier E_f is defined as follows,

$$E_f = E_c' - Q. \quad (3)$$

It assumes that the potential height at the saddle point is nearly equal to the Coulomb barrier of fusion as the reversal process of fission.

The fission probability for the certain channel is given by the tunnel probability P of the channel-dependent potential for the excitation energy E_x ,

$$P = \frac{1}{1 + \exp\left[\frac{2}{\hbar} \int_a^b \sqrt{2M(s)(V(s) - E_x)} ds\right]}, \quad (4)$$

where s is the distance along the fission path, $V(s)$ is the potential energy, a and b are the points at which $V(s) = E_x$ and $M(s)$ is the mass parameter of the system. The potential near the saddle point is approximated by the inverted parabola and the curvatures α is assumed as a constant for all channels for simplicity. Then the tunnel probability P is reduced as

$$P \approx \frac{1}{1 + \exp[0.218\alpha\sqrt{\mu} \Delta E]}, \quad (5)$$

in MeV and fm units, where $\mu = A_1 A_2 / (A_1 + A_2)$, $\Delta E = E_f - E_x$ and A_1 and A_2 are the mass number of FP1 and FP2, respectively. The FP yields are obtained by summing up these probabilities all over fission channels.

Furthermore, the η is introduced to discuss how much the nucleus deviates from the spherical shape. The η is defined as the elongation at the saddle point from the point-to-point distance of the fission fragment of spherical shapes which is given by

$$R_{\text{sad}} = \eta(R_1 + R_2), \quad (6)$$

where R_1 and R_2 are the radii of FP1 and FP2, respectively, and given as $R_1 = r_0 A_1^{1/3}$, $R_2 = r_0 A_2^{1/3}$ and $r_0 = 1.2$ fm.

3. Results and Discussion

The FP yields for the neutron-induced fissions of ^{232}Th , ^{235}U , ^{239}Pu and ^{241}Pu were obtained as shown in **Figs. 2-a, 3-a, 4-a** and **5-a**, respectively. Prompt neutron emission was considered only for the FP yields for ^{235}U . Others show the FP yields without the consideration of the prompt neutron emission. The position of the humps coincided with the data of JENDL-3.3 [7] except for the dips in the mass region of $A = 140-150$ (also $A = 85-95$). The channel-dependent fission barriers E_f for ^{233}Th , ^{236}U , ^{240}Pu and ^{242}Pu were shown in **Figs. 2-b, 3-b, 4-b** and **5-b**, respectively. The dips of E_f corresponding to the yields of mass region of $A = 140-150$ (also $A = 85-95$) were found.

Figures 2-c, 3-c, 4-c and **5-c** shows the η for ^{233}Th , ^{236}U , ^{240}Pu and ^{242}Pu , respectively. The dips of the FP yields and E_f in $A = 140-150$ (also $A = 85-95$) may depend on the differences between the real distance at saddle point and the assumption of R_{sad} . The upper part of the η increases around $A = 130-140$ with the mass number of fragments. The η is discussed in connection with the shape elongation at scission. Y.L. Zhao *et al.* [8] showed the existence of symmetric and asymmetric fissions with the factor β , which is the ratio of the elongation from sphere nuclei at scission configurations, by evaluation from the total kinetic energy (TKE) data. The β changed the trend at mass of fragments $A \sim 130$. The behavior of η also changes its trend around $A = 130-140$ like that of the β .

4. Conclusions

The channel-dependent fission barrier was calculated for the neutron-induced fissions of ^{232}Th , ^{235}U , ^{239}Pu and ^{241}Pu by the SCS model with simple assumptions. The mass distributions of FP yields were calculated and compared with the data of JENDL-3.3 [7]. These mass yields were in agreement with the data of JENDL-3.3 except for discrepancies at the mass regions of $A = 140\text{--}150$ (also $A = 85\text{--}95$). To improve the discrepancies, further studies should be needed for the model calculation and assumptions.

The elongation factor at saddle point η was calculated and compared with that at scission point β in Ref. [8]. Though the deviation was wide, the trend of η was similar to that of the β . It might mean the existence of the symmetric and asymmetric fission modes for the η as well as that for the β .

References

- [1] U. Brosa, S. Grossmann and A. Müller: *Phys. Rep.*, **197**, 167 (1990).
- [2] P. Möller, D.G. Madland, A.J. Sierk and A. Iwamoto: *Nature*, **409**, 785 (2001).
- [3] A. Takahashi, M. Ohta and T. Mizuno: *Jpn. J. Appl. Phys.*, **40**, 7031 (2001).
- [4] M. Ohta, M. Matsunaka and A. Takahashi: *Jpn. J. Appl. Phys.*, **40**, 7047 (2001).
- [5] M. Ohta and A. Takahashi: *Jpn. J. Appl. Phys.*, **42**, 645 (2003).
- [6] H. Koura, M. Uno, T. Tachibana and M. Yamada: *Nucl. Phys.*, **A674**, 47 (2000).
- [7] K. Shibata, T. Kawano, T. Nakagawa, O. Iwamoto, J. Katakura, T. Fukahori, S. Chiba, A. Hasegawa, T. Murata, H. Matsunobu, T. Ohsawa, Y. Nakajima, T. Yoshida, A. Zukeran, M. Kawai, M. Baba, M. Ishikawa, T. Asami, T. Watanabe, Y. Watanabe, M. Igashira, N. Yamamuro, H. Kitazawa, N. Yamano and H. Takano: *J. Nucl. Sci. and Technol.*, **39**, 1125 (2002).
- [8] Y.L. Zhao, I. Nishinaka, Y. Nagame, M. Tanikawa, K. Tsukada, S. Ichikawa, K. Sueki, Y. Oura, H. Ikezoe, S. Mitsuoka, H. Kudo, T. Ohtsuki and H. Nakahara: *Phys. Rev. Lett.*, **82**, 3408 (1999).

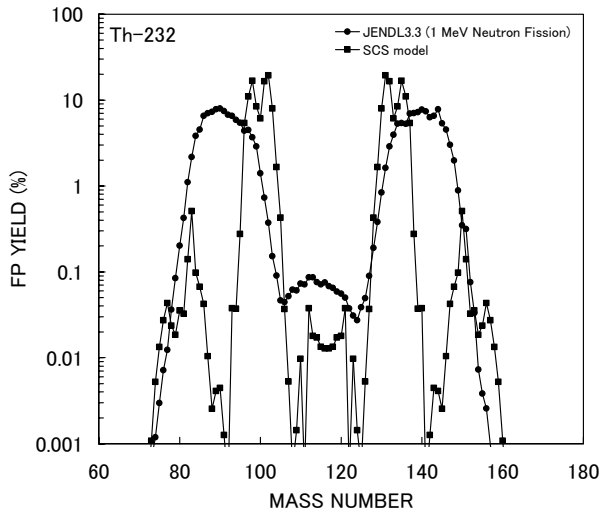


Fig. 2-a Fission product yield of $n+^{232}\text{Th}$

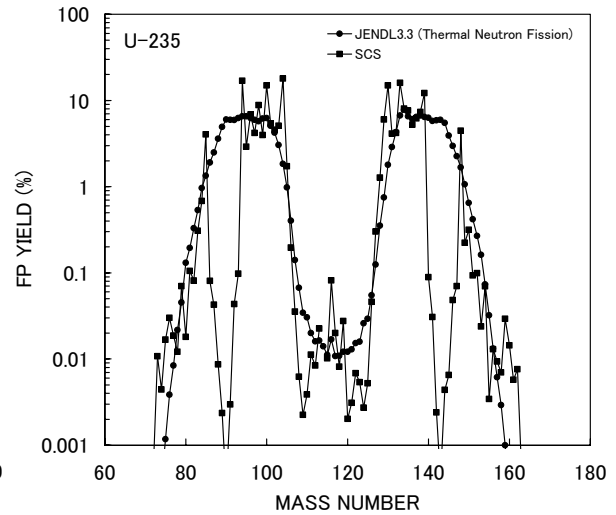


Fig. 3-a Fission product yield of $n+^{235}\text{U}$

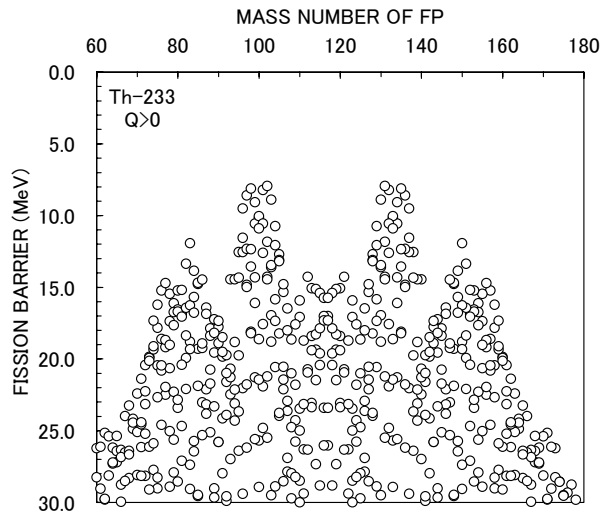


Fig. 2-b Fission barriers of ^{233}Th

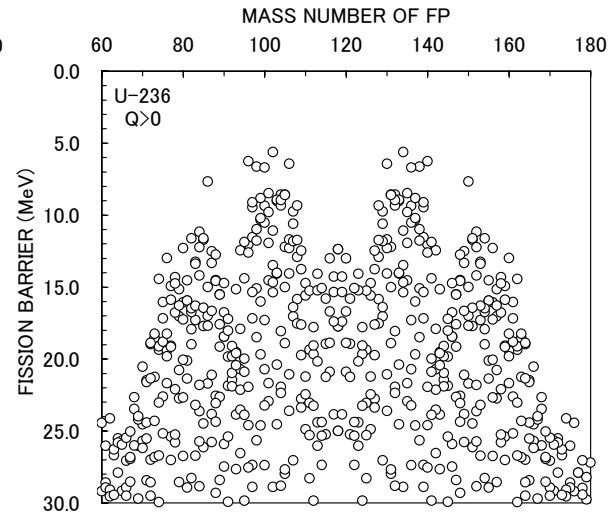


Fig. 3-b Fission barriers of ^{236}U

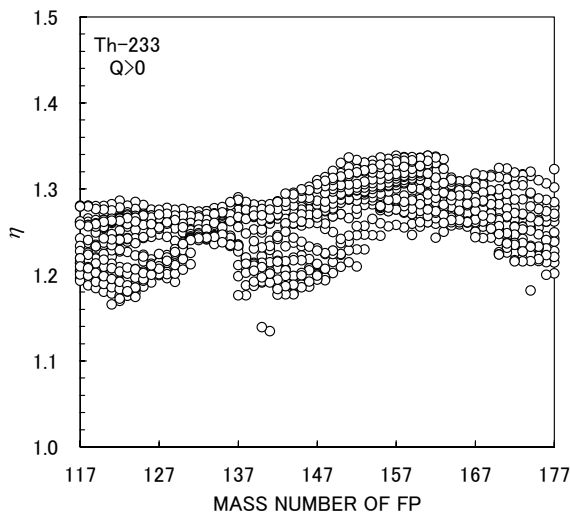


Fig. 2-c η of ^{233}Th

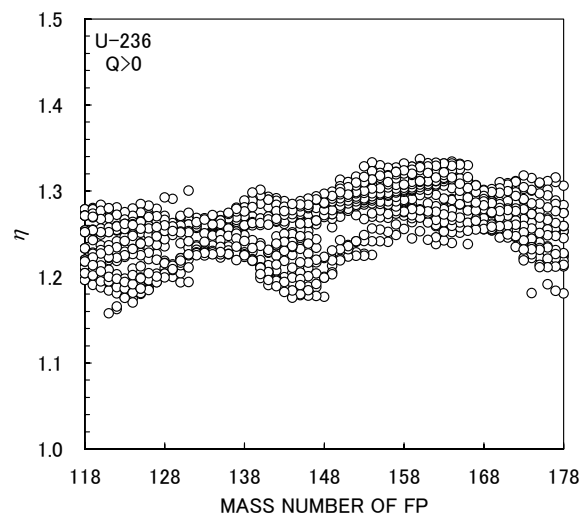


Fig. 3-c η of ^{236}U

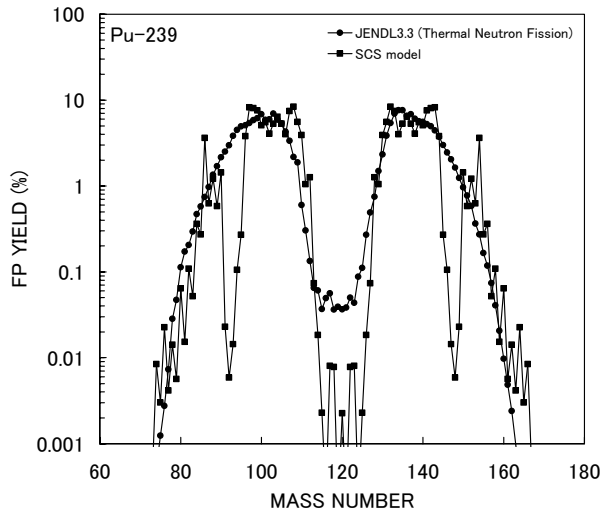


Fig. 4-a Fission product yield of $n+^{239}\text{Pu}$

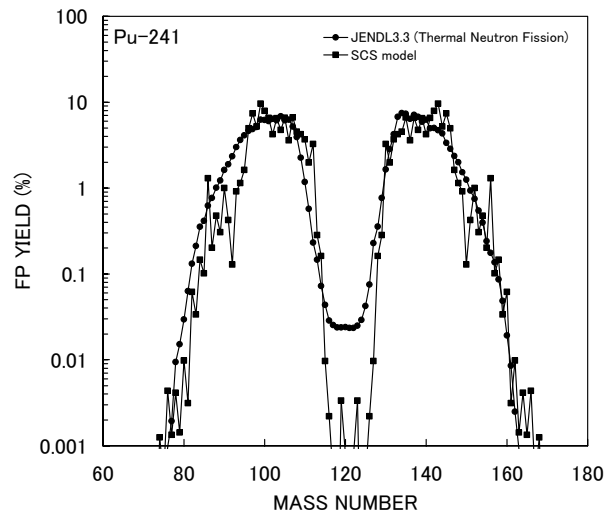


Fig. 5-a Fission product yield of $n+^{241}\text{Pu}$

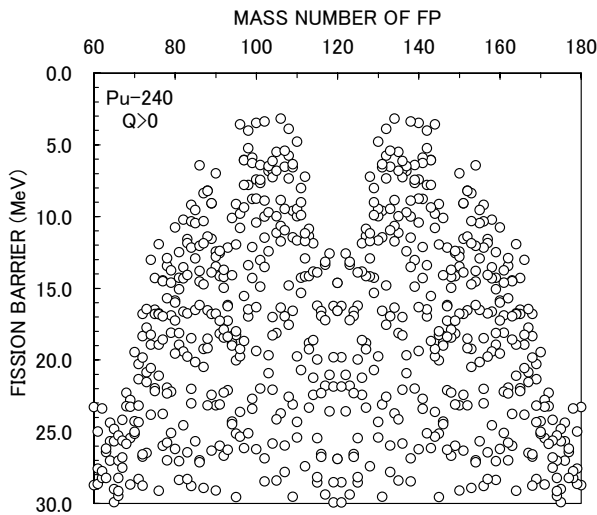


Fig. 4-b Fission barriers of ^{240}Pu

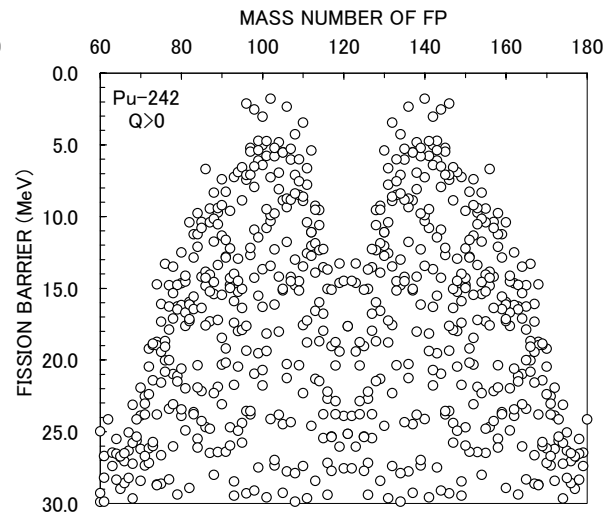


Fig. 5-b Fission barriers of ^{242}Pu

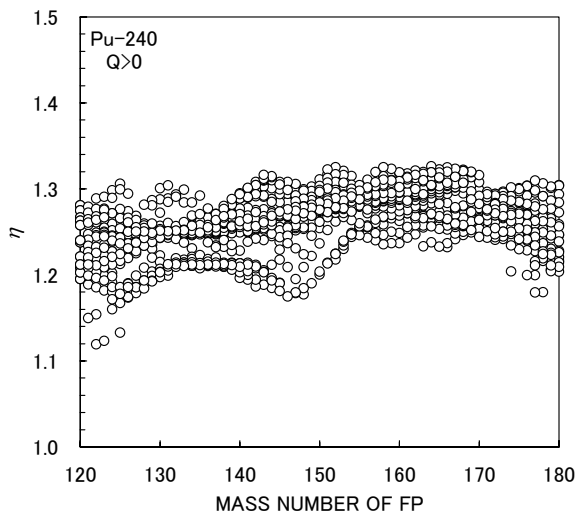


Fig. 4-c η of ^{240}Pu

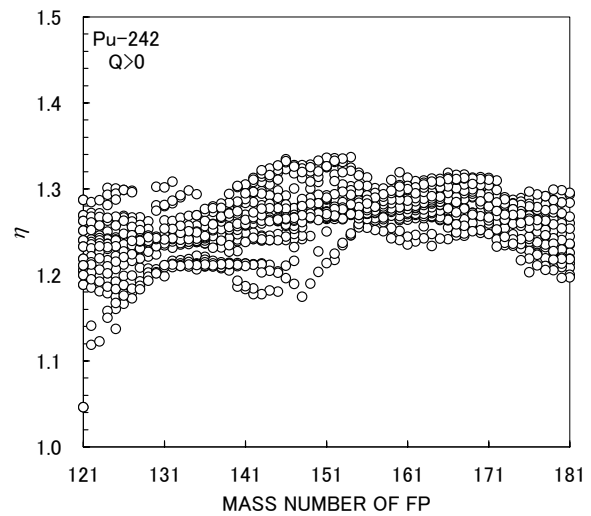


Fig. 5-c η of ^{242}Pu

3.15 Investigation of Nuclear Reaction Data for Analyses of Single-Event Effects in Semiconductor Devices

Akihiro Kodama, Kouta Nishijima, Yukinobu Watanabe
*Department of Advanced Energy Engineering Science, Kyushu University,
 Kasuga, Fukuoka 816-8580, Japan*
 Corresponding email: watanabe@aes.kyushu-u.ac.jp

We have investigated the effect of simultaneous multiple ions emission in neutron-induced reactions on single-event upsets (SEUs) and the relative importance of elastic scattering in SEUs in order to develop a nuclear reaction database of Si suitable for SEU microscopic simulation. Proton-induced SEU cross sections are calculated using a simplified empirical model that uses experimental heavy-ion induced SEU cross-sections and nuclear data for proton-induced reactions. In addition, an integral test of the proton nuclear data used is carried out through analyses of the energy deposition spectrum measured by bombardment of protons on a fully depleted surface barrier detector.

1. Introduction

In recent years, nucleon-induced single-event upsets (SEUs) have been a serious concern for microelectronic devices used in various radiation environments. For instance, terrestrial cosmic-ray neutrons hitting the earth have the wide energy range from MeV to GeV, and are regarded as one of the major sources of SEUs in the devices used at the ground level or in airplanes. Also, cosmic-ray protons are known to have a serious influence on SEUs in the devices installed in artificial satellites.

The nucleon-induced SEU is initiated by an interaction of incident cosmic-ray particles with materials in microelectronics devices. Light-charged particles and heavy recoils are generated via a nuclear reaction with a constituent atomic nucleus, mainly ^{28}Si , and then deposit the charge in a small sensitive volume (SV) of the device. The charge is collected at one of the nodes keeping the memory information and the resulting current transient generates an SEU. Therefore, reliable nuclear reaction data are required in estimating the SEU rate by numerical simulation methods.

So far we have created a dedicated nuclear reaction database using available nuclear data and theoretical model calculations, and have applied it to the calculation of neutron-induced SEU cross sections using a simplistic model [1]. The cross section data stored in the database consist of “inclusive” energy spectra of each secondary ion, and the angular distribution was assumed to be isotropic. Use of the inclusive data means ignorance of an event that multiple ions are emitted simultaneously, which becomes important with increasing incident energy. In the calculation of upset cross sections, we have used a simplified geometry having a spherical SV and a step-like critical energy required to flip a logical state.

Sophistication of the nuclear reaction database will be necessary for more reliable SEU simulations. In the present work, we pay attention to two nuclear processes, simultaneous multiple ions emission and elastic scattering, and investigate these effects on SEUs quantitatively. Since neutron elastic scattering cross sections of Si are larger than reaction cross sections at intermediate incident energies where cosmic-ray neutrons are expected to provide a large sensitivity to SEU rate, it is of interest to estimate the relative contribution using recent reliable nuclear data [2]. For SEU cross-section calculations, we extend the spherical SV geometry to a rectangular parallelepiped geometry widely used. In addition, intra-cell variation of charge collection is taken into account using experimental heavy ion SEU cross sections under an assumption that their dependence of the deposition energy reflects the variation [3]. Our semi-empirical model is applied to calculations of proton induced SEU cross-sections and comparisons with experimental data and the other model calculation are presented. Finally, an integral test of the nuclear reaction data used in the calculation is also performed by analyses of an energy deposition spectrum obtained by proton bombardment on a fully depleted surface barrier detector (SBD).

2. Monte Carlo simulator based on sensitive volume concept

Our model uses a well-known memory cell geometry having a sensitive volume (SV) of rectangular

parallelepiped shape as shown in Fig.1. The SV is defined as the volume containing all the charges deposited by secondary ions generated from the interaction between an incident nucleon and ^{28}Si , which are ultimately collected by a memory node and induce an SEU. One of the important physical quantities relevant to the SEU is the distribution function of the energy E_d deposited in the SV. It is hereinafter denoted by $f(E_{in}, E_d)$, where E_{in} is the incident energy. It is characterized by the nuclear reaction, particularly energy and angular distributions of the generated secondary ions, and ion penetration and linear energy transfer (LET) into the device. Note that the deposited charge Q_d can be reduced to the deposited energy E_d using the expression, E_d (in MeV) = 0.0225 Q_d (in fC).

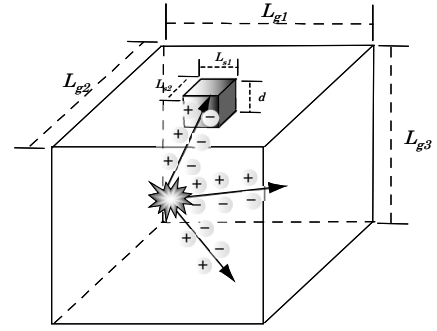


Fig. 1 Schematic illustration of memory cell geometry including the sensitive volume

Using $f(E_{in}, E_d)$, the nucleon-induced SEU cross section is expressed by

$$\sigma_{SEU}(E_{in}) = N_{Si} V_{int} \sigma_N(E_{in}) \int_0^\infty f(E_{in}, E_d) h(E_d) dE_d, \quad (1)$$

where N_{Si} is the number density of silicon atoms, V_{int} the volume size of the region (“interaction volume”) where nuclear reactions occur in the memory cell, $\sigma_N(E_{in})$ the cross section to describe the interaction between an incident nucleon and ^{28}Si , which is given by the sum of elastic scattering cross section and reaction cross section, $h(E_d)$ the normalized heavy-ion SEU cross section expressed by the following Weibull fitting function:

$$h(E_d) = \sigma_{HI}(E_d) / \sigma_{HI}^\infty = 1 - \exp\left\{-\left[\frac{E_d - E_0}{W}\right]^s\right\}, \quad (2)$$

where W and s are shape parameters, σ_{HI}^∞ is the saturation value of the heavy-ion SEU cross section and E_0 the SEU threshold. Since experimental heavy-ion SEU data are usually given as a function of LET, we need to convert it to the energy using the relation $E_d = d \times LET$, where d represents the sensitive depth. If we assume a step function $h(E_d) = \Theta(E_d - E_c)$, where E_c is called the critical energy required to cause an SEU, then Eq.(1) reduces to

$$\sigma_{SEU}(E_{in}, E_c) = N_{Si} V_{int} \sigma_N(E_{in}) F(E_c), \quad (3)$$

where $F(E_c) = \int_{E_c}^\infty f(E_{in}, E_d) dE_d$.

The distribution function $f(E_{in}, E_d)$ is calculated by a Monte Carlo method using a nuclear reaction database and a range and energy loss database of secondary ions. In the present work, two kinds of neutron and proton databases from 20 MeV to 1 GeV are prepared using the JQMD/GEM code [4,5]. One consists of so-called “inclusive” double-differential cross sections of all secondary ions including light ions. Another contains the “event-by-event” information, *i.e.*, the kind of secondary ions and their emission energy and angle, so that simultaneous multiple ions emission can be correctly taken into account.

When the former “inclusive” database is used, a secondary ion j is firstly generated in a position chosen randomly in the interaction volume by sampling its energy and emission direction in terms of the double-differential cross sections. Then, the energy deposited by the ion in the SV is calculated numerically using the data of range and energy loss computed by the SRIM code [6]. In this case, $\sigma_N(E_{in}) f(E_{in}, E)$ used in Eqs.(1) and (3) is replaced by $\sum_j \sigma_j(E_{in}) f_j(E_{in}, E)$ where $\sigma_j(E_{in})$ is the production cross section of the ion of type j . Consequently, Eq.(3) can be re-written by

$$\sigma_{SEU}(E_{in}, E_c) = N_{Si} V_{int} \sum_j \sigma_j(E_{in}) F_j(E_c) = N_{Si} V_{int} \sum_j \int_{E_c}^\infty \sigma_j(E_{in}) f_j(E_{in}, E_d) dE_d, \quad (4)$$

It should be noted that Eq.(4) was used to calculate SEU cross sections in our earlier work [1].

In case of using the latter “event-by-event” database, a position where a nuclear reaction occurs is chosen randomly in the interaction volume shown in Fig.1. Then the total energy deposited in the SV by all secondary ions generated in a certain reaction event is calculated using the above-mentioned way.

3. Influence of nuclear data on neutron-induced SEU analysis

First, we have investigated the effect of simultaneous multiple ions emission on SEUs by comparing the energy deposit calculated using the above-mentioned two different nuclear reaction databases consisting of the “inclusive” data (denoted hereinafter Cal. 1) and the “event-by-event” data (Cal.2), respectively. Next, the relative importance of elastic scattering has been examined in the incident energy region below 150 MeV. It should be noted that Eq.(3) was used in both analyses.

3.1 Simultaneous multiple ions emission

In Fig. 2(a), the SEU cross sections calculated by Eq. (3) are plotted as a function of E_c for the case of a small sensitive volume with $V_s = 1 \times 1 \times 1 \mu\text{m}^3$. There is no obvious difference between two calculations with different nuclear reaction data sets. This implies that simultaneous multiple ions emission has negligible effect on SEUs if the size of SV is small. To see the reason, we have obtained the mean number of emitted ions as functions of the atomic number of generated ions and the incident neutron energy. As shown in Fig.3, light ions, particularly protons and deuterons, are mainly included in the simultaneous multiple ions emission and the total fraction of heavy ions is nearly equal to unity. Even if many light ions are generated by a nuclear reaction, the energy deposited in the small SV is negligibly small because of their low LET. Also, the probability that more than one ion passes through the SV simultaneously is reduced as the size of SV becomes small. From this analysis, we have found that it is a quite good approximation to use the “inclusive” nuclear data in the calculation of SEU rates for a device having as small SV as this, and therefore it is not necessary to revise the results obtained in our previous work [1] not considering the multiple ions emission.

Figure 2(b) shows the result for a larger SV size ($V_s = 20 \times 20 \times 2 \mu\text{m}^3$) than that used in Fig.2 (a), because we will discuss SEU for a device of the similar size in the following section. There is an appreciable difference between two calculations as the critical energy is over 2 MeV corresponding to $Q_c=89 \text{ fC}$. Also, a significant difference is seen near $E_c=0$. Since the sensitive area is much wider than the above case, light ions emitted in the lateral direction can deposit considerable energy along the path in spite of low LET. Thus, the emitted light-ions become involved in SEU as well. If one uses the “inclusive” data, contributions from these light ions are added incoherently, which results in larger value at very small E_c than Cal.2. In the calculation with the “event-by-event” data, the total energy deposited by all the ions generated in a nuclear reaction is tallied. This leads to enhancement at larger E_c compared to the result of Cal.1.

From this investigation, it was found that the simultaneous multiple ions emission that is predominant at high incident energies does not influence seriously on SEUs for the devices having the small SV size. However, it should be noted that the multiple ions emission is expected to have some sort of effects on multiple bits upsets (MBUs).

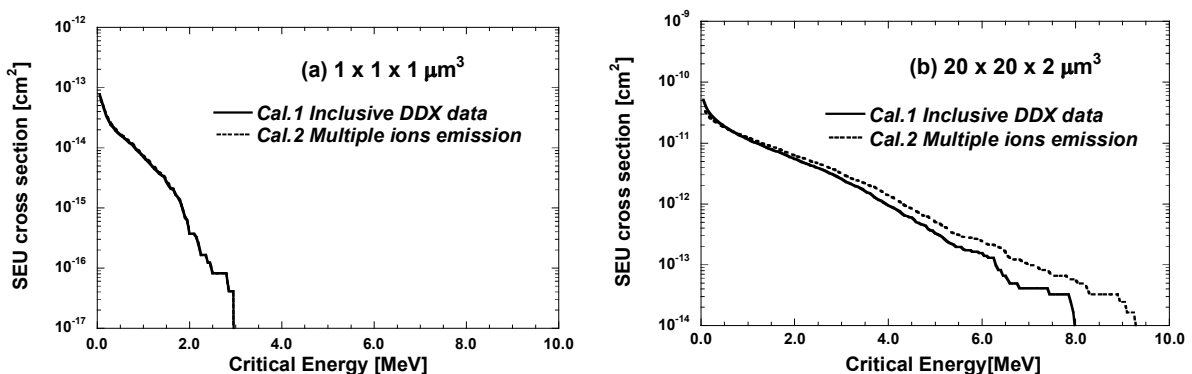


Fig.2 Calculated neutron SEU cross section as a function of critical energy E_c for the following sensitive volume: (a) $V_s = 1 \times 1 \times 1 \mu\text{m}^3$ and (b) $V_s = 20 \times 20 \times 2 \mu\text{m}^3$

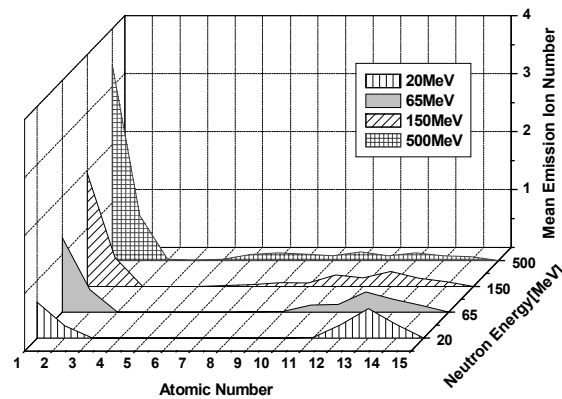


Fig.3 Average number distribution of secondary ions obtained by the QMD calculation

3.2 Elastic scattering

We have examined the effect of elastic scattering on SEU using JENDL/HE-2004 data [2], because the elastic scattering is not included in the QMD calculation. As shown in Fig.4, the elastic cross section is much larger than the reaction cross section in the energy range between 20 and 120 MeV. Therefore, it is of importance to know how the elastic scattering influences on SEU in the energy range of interest.

Relative contribution of the elastic scattering to SEU is calculated as functions of incident energy and critical charge for a device having the sensitive volume $V_s = 1 \times 1 \times 1 \mu\text{m}^3$. The ratio of the elastic SEU cross-section to the total SEU cross section is plotted as a function of incident neutron energy in Fig.5. Paying attention to the energy range above 20 MeV, one finds that the contribution of the elastic scattering increases as the critical charge is reduced and the maximum fraction is at most 20 % near 20 MeV. This supports a similar estimation by Barak et al.[7] made in their proton-induced SEU analysis. Less important role of the elastic scattering can be explained by the fact that the average kinetic energy of the recoiled ^{28}Si becomes smaller, because the angular distribution of elastically scattered neutron becomes steeper with increasing incident energy. On the other hand, the ratio increases suddenly up to unity at a certain energy corresponding to the SEU threshold energy below 10 MeV except at $Q_c=50 \text{ fC}$. In this energy range, the elastic scattering becomes dominant as seen in Fig.5 and the other reaction channels are suppressed. From the present analysis, therefore, the elastic scattering is expected to play an important role near the SEU threshold energy for memory devices with small Q_c .

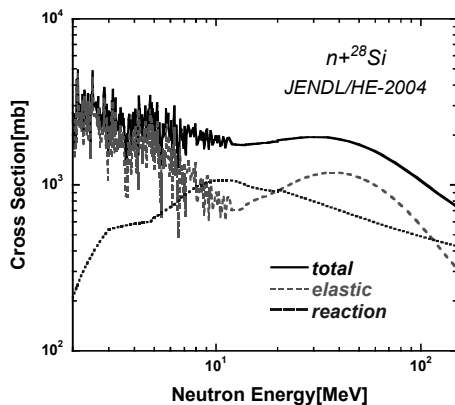


Fig.4 Neutron total, elastic, and reaction cross-section of ^{28}Si taken from JENDL/HE-2004

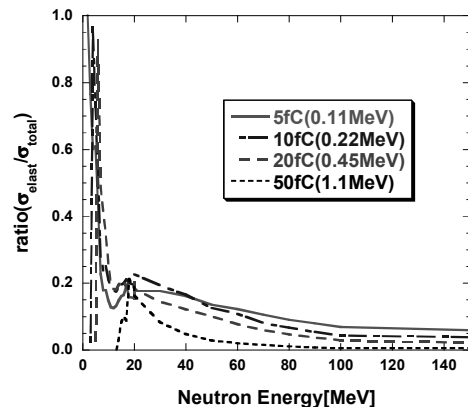


Fig.5 Ratio of the elastic SEU cross section to the total SEU cross section

4. Calculation of proton-induced SEU cross sections

We have applied the present semi-empirical model expressed by Eqs.(1) and (2) to the calculation of proton induced SEU cross-sections for some memory devices at incident energies below 200 MeV. In the calculations, the “event-by-event” nuclear reaction data and the JENDL/HE-2004 data for elastic scattering were used. In addition, the experimental spectrum of the energy deposited by protons in a fully depleted

surface barrier detector (SBD) has been analyzed using our Monte Carlo calculation. The results and discussion are given below.

4.1 Results and comparisons

Proton SEU cross sections were calculated using the Weibull function parameters of heavy-ion SEU cross sections for some memory devices whose parameters and experimental data are compiled in Ref.[8]. The dimension of the SV was determined by the sensitive area saturation cross section, σ_{HI}^{∞} , in Eq.(2) and a “standard” value of the sensitive depth, $d=2$ mm. The interaction volume surrounding the SV ($50 \times 50 \times 50 \mu\text{m}^3$.) was taken to be so large that the calculated proton SEU cross-section is saturated

In Fig.6, the result for three devices is shown in comparison with measured data and the other empirical model calculation using an analytic expression proposed by Barak [9,10]. Our model calculation is generally in good agreement with the measured SEU cross sections in shape and magnitude, and particularly shows better agreement than the Barak’s calculation for HM6516. The SV size is a key parameter in SEU cross-section calculations using the models based on the SV concept. Although the sensitive depth used in the present work is the standard value and must have device-dependence, influences of the SV size on the SEU cross section have not been investigated in details because it is beyond the scope of the present work.

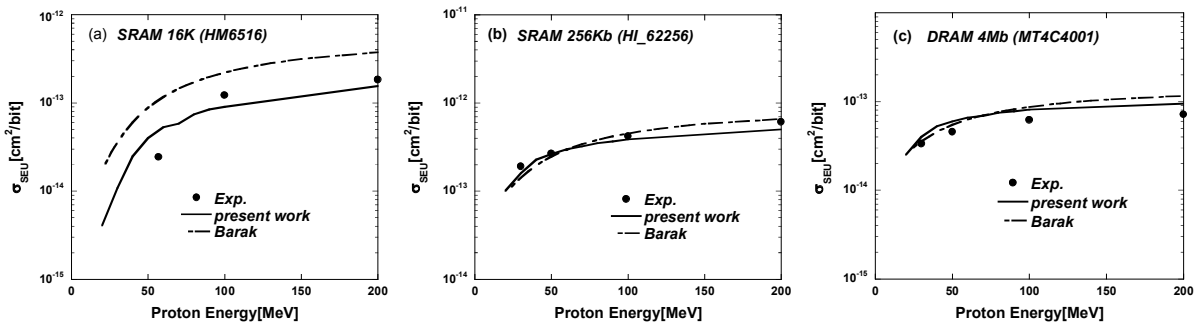


Fig.6 Comparison of calculated proton SEU cross-sections with experimental data and Barak’s work[9,10]

4.2 Analysis of energy deposition spectrum for surface barrier detector

Barak et al.[9,10] have derived an analytic expression of $f(E_{in}, E_d)$ in Eq.(1) based on the experimental spectra of the energy deposited by protons in fully depleted SBDs. Here we compare their experimental data with our Monte Carlo calculation.

Figure 7 show a comparison of experimental and calculated integral spectra for an SBD with thickness of $2 \mu\text{m}$ and the sensitive area 10 mm^2 at incident proton energy of 300 MeV. The integral spectrum represents the total event numbers obtained by integrating the deposition energy spectrum from a given energy to infinity. Our calculation depicted by the solid line underestimates the measurement at deposition energies above 7 MeV. Since the SBD has the large lateral dimension, the energy deposition by light ions is expected to play an important role from discussion in the above section 3.1. The present version of the QMD code underestimates remarkably the high-energy component of light cluster ions such as deuteron and alpha as described in Ref.[11]. To see whether the underestimation seen in Fig.7 is related to the lack of emission of high-energy light cluster ions, a preliminary calculation was performed using the QMD model improved in Ref.[11]. The result is shown by the dotted line in Fig.7. As expected, better agreement is obtained although underestimation is still seen at energies above 10 MeV. From this consideration, we conclude that the disagreement is probably due to insufficient description of light cluster ions production.

Finally, we discuss whether light cluster ions have a serious effect on the proton SEU cross sections in Fig.6. Since the typical sensitive area for these memory devices in Fig.6 is $20 \times 20 \mu\text{m}^2$, which is considerably smaller than the sensitive area of the SBD (10 mm^2), the energy deposited by light cluster ions with large kinetic energy is negligibly small compared to the SEU threshold energy E_0 . Consequently, it is expected that the high-energy components of light cluster ions play a lesser role in SEU in actual memory devices. A variation of the energy spectra of recoils associated with high-energy light cluster ions emission might effect partially on the total energy deposition. A detailed analysis of the effect is in progress.

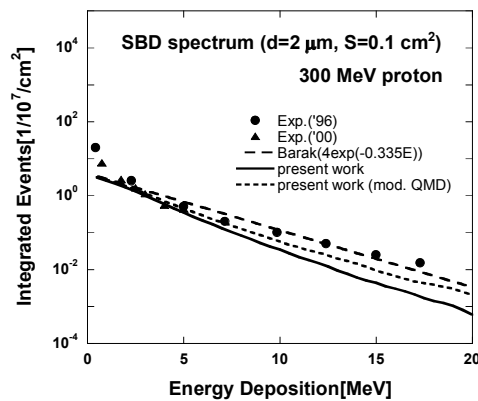


Fig.7 Experimental and calculated integral SBD spectra for $E_p=300$ MeV

5. Summary and conclusions

We have investigated the effect of multiple ions emission on SEU and the relative importance of elastic scattering in SEU. The multiple ions emission was found to have negligible effects in the case where the sensitive volume (SV) size is sufficiently small because the light ions having low LET are primarily produced in the process. However, multiple ions production probably has some impact on multiple-bit upsets (MBUs) for devices with low Q_c [12]. The qualitative estimation will be necessary in the future. It was found that the relative importance of elastic scattering increases when the amount of critical charge Q_c is small, because the averaged kinetic energy of the recoiled ^{28}Si is smaller than the other heavy recoils. Our qualitative evaluation for the memory devices with the small SV indicated that its contribution has at most 20% for $Q_c = 5$ fC.

The proton-SEU cross sections were calculated using the semi-empirical model with the “event-by-event” nuclear reaction data and the JENDL/HE-2004 for the elastic scattering. The result reproduced generally well the incident energy dependence of experimental proton-SEU cross sections in both shape and magnitude. The distribution function of the energy deposited in the SV, which is one of the important physical quantities in this model, was compared with the experimental data for the fully depleted SBD with the large lateral dimension. As a result, the underestimation was seen for high-energy deposition, which is probably attributable to the lack of preequilibrium components of light cluster ions such as deuteron and alpha. This will require further refinement of the present QMD model for light cluster ions production in order to provide more reliable nuclear reaction data for microscopic simulation of SEUs.

Acknowledgement

A part of this work was carried out in cooperation with Institute of Unmanned Space Experiment Free Flyer.

References

- [1] Y. Watanabe et al., Proc. of Int. Conf. on Nuclear Data for Science and Technology, Santa Fe, USA, Sept. 26-Oct. 1, 2004; AIP Conference Proceedings Vol. 769, pp. 1646-1649, (2005).
- [2] Y. Watanabe et al., *ibid.*, pp. 326-331, (2005).
- [3] E.L. Petersen, IEEE Trans. Nucl. Sci., **43**, No. 6, 952-959 (1996); *ibid.*, 2805-2813 (1996).
- [4] K. Niita et al., Phy. Rev. C, **52**, 2620 (1995); JQMD code, JAERI-Data/Code 99-042 (1999).
- [5] S. Furihata, Nucl. Inst. Method in Phys. Res. B **171**, 251 (2000).
- [6] J.F. Ziegler, SRIM-2000 code, URL <http://www.srim.org/>
- [7] J. Barak et al., IEEE Trans. Nucl. Sci., **46**, No. 6, 1342-1353 (1999).
- [8] P. Calvel et al., IEEE Trans. Nucl. Sci., **43**, No.6, 2827-2831 (1996).
- [9] J. Barak et al., IEEE Trans. Nucl. Sci., **43**, No.3, 979-984 (1996).
- [10] J. Barak, IEEE Trans. Nucl. Sci., **47**, No.3, 545-550 (2000).
- [11] Y. Watanabe, to be published in Proc. of Workshop on the Future of Theory- and Experiment-based Nuclear Data Evaluation, Bruyères-le-Châtel, France, Sept. 26-28, 2005.
- [12] F. Wrobel et al., IEEE Trans. Nucl. Sci., **48**, No.6, 1946-1952 (2000).

3.16 Improvement of Prediction Power of FP Summation Calculations by Use of the TAGS Experimental Data

Naoto HAGURA*, Tadashi YOSHIDA, Masahiko KATSUMA**

Musashi Institute of Technology, Tamazutsumi 1-28-1, Setagaya-ku, Tokyo 158-8557, Japan

*E-mail: g0567014@sc.musashi-tech.ac.jp

***Universite Libre de Bruxelles, Campus de la Plaine, Boulevard du Triomphe, B-1050 Bruxelles, Belgium*

The average β - and γ -ray energies per decay were calculated from the Total Absorption γ -ray Spectrometer (TAGS) measurements carried out at Idaho for 45 isotopes to replace the original JEFF-3.1 or JENDL values. As a result, the JEFF-3.1 summation calculation became fairly consistent with the results of the sample-irradiation decay-heat measurements both in the β - and the γ -ray components. This fact implies that the TAGS measurement is free from the so-called pandemonium problem as is expected. We propose a list of the important nuclides to be measured by the TAGS technique in near future.

1. Introduction

When we use the decay-scheme information for the radioactive fission products (FP) in the decay-heat summation calculations as their basis, we have to pay attention to the problem that the β -transitions to the highly-excited levels are apt to be lost from them¹⁾. This problem is known as the pandemonium problem²⁾. The calculated results based on JEFF-3.1, which was released in May 2005, could not reproduce the sample-irradiation experiments performed world wide, where the β - and the γ -ray components are measured separately. On the other hand, the result with JENDL FP Decay Data File 2000 (Hereafter JENDL) is quite consistent with the integral measurements. It is because JEFF-3.1 is generated exclusively based on the decay-schemes constructed from the experimental data. On the contrary, JENDL is made up of experimental data with theoretical supplementation of the gross theory of beta decay, to attain good consistency.

In the early 1990's, a series of Total Absorption γ -ray Spectrometer (TAGS) measurements was carried out at INEL (Idaho National Engineering Laboratory) for 45 FP nuclides³⁾. One of the most important properties of the TAGS measurement is expected to be pandemonium-problem free. In this respect, the TAGS measurement is considered that it may provide a solid basis of the summation calculations⁴⁾. The INEL group, however, terminated their TAGS activity in 1990's and, then, we can no longer expect the relevant new data from the U.S. nowadays. On the contrary, a European group recently started a new collaboration⁵⁾, in which the TAGS technique is fully employed in measuring the β -strength functions of FP region nuclides.

We plan to propose them a list of the nuclides to be measured by the TAGS technique in the

framework of the WPEC (Working Party on International Evaluation Cooperation of the NEA Nuclear Science Committee). For this purpose we select important FP nuclides which are assumed to be suffered from the pandemonium problem among the nuclides contributing largely to the FP decay heat in this paper.

2. TAGS Measurements

In the TAGS measurement, a NaI(Tl) scintillator is used as the γ -ray detector installed at a on-line mass separator. In principle all of the γ -rays emitted in a cascade accompanied by a de-excitation of a certain level deposit all of their energies into the scintillator giving the level (or a group of levels) energy into which the preceding β -transition have taken place. In this way the TAGS gives the level energy as the pulse energy and the β -feeding rate as the pulse height at the same time. These are exactly the data required to calculate the average β - and γ -ray energy releases per one β -decay of the parent nucleus, or E_β and E_γ . Therefore, if the TAGS measurements are carried out in an ideal way, the values of E_β and E_γ obtained from them are free from the pandemonium problem.

3. Calculation Results

Figure 1 shows the γ -ray component of the Pu-239 decay heat after a fission burst calculated with JEFF-3.1 (solid curve) and with JENDL (dotted curve). This figure indicates that JEFF-3.1 underestimates largely the integral measurements between 2 and 3,000 seconds. They are the pandemonium nuclides that cause the pulling down of the JEFF-3.1 result. As the next step, we introduced the TAGS values that were measured by Idaho group into the decay data of JEFF-3.1 and JENDL, respectively (Fig.2). In introducing the TAGS data, E_β and E_γ values were replaced by the TAGS-origin values for the 45 nuclides for which the Idaho-group made measurement. As a result, JEFF-3.1 became fairly consistent with the sample-irradiation measurements. Namely, the JEFF-3.1 curve is pulled up between 10 and 300 seconds and, as a result, part of the curve of JEFF-3.1 is caught in the error bar of the experimental data.

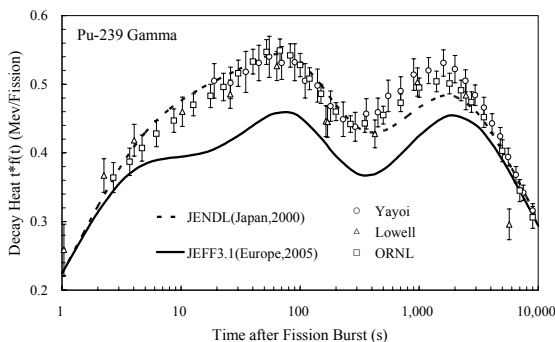


Fig. 1 Decay heat after a burst fission in Pu-239 before the TAGS-correction (γ -ray component)

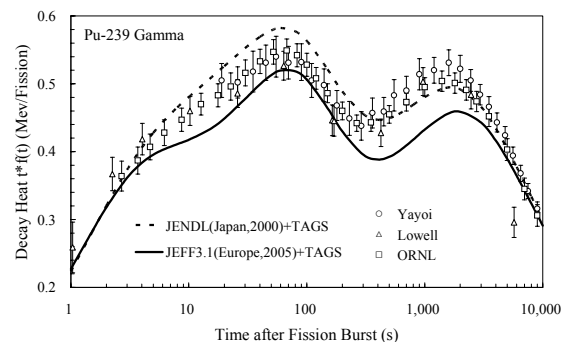


Fig. 2 Decay heat after a burst fission in Pu-239 after the TAGS correction (γ -ray component)

On the contrary, by introducing the TAGS data into the summation calculation, the JENDL curve deviated from the integral measurements. Figures 3 and 4 show the nuclide-wise contributions to the difference between the JENDL and the JEFF-3.1 curves both after the introduction of the TAGS data. Here the nuclides Tc-102, Mo-103, Mo-105, and Xe-139 are big contributors (Fig. 4). These isotopes are important candidates for the nuclides included in the list of nuclide to be measured by TAGS. Recently a series of isotopes of technetium was measured by the European group⁵⁾. The results will be released sooner or later.

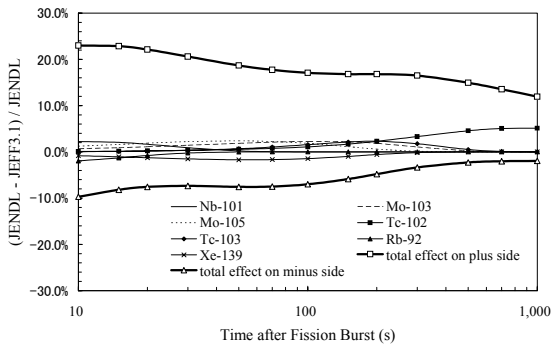


Fig. 3 Nuclide-wise contributions to the fractional difference between JENDL and JEFF-3.1 after introduction of the TAGS energies (γ -ray component of Pu-239 decay heat)

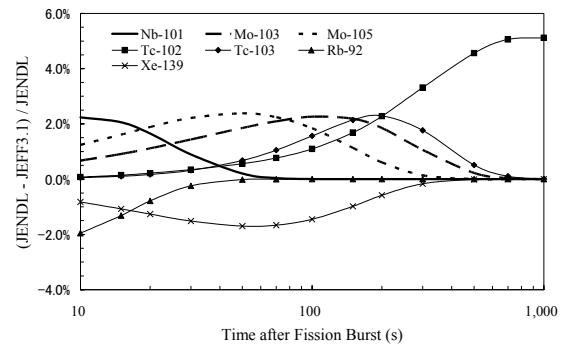


Fig. 4 Nuclide-wise contributions to the fractional difference between JENDL and JEFF-3.1 after introduction of the TAGS energies (the close-up of a few percent regions)

Figure 5 exhibits the contributions from the nuclides on the heavy ($A > 120$, black dotted curve) and the light ($A \leq 120$, dotted curve) humps of the double-humped mass-yield curve to the γ -ray component of the Pu-239 decay heat. This figure suggests that the light group dominates the short-cooling time range and the heavy group does the long cooling-time range. The effect of the introduction of TAGS data (thin curve) into the heavy mass nuclides is bigger than the light group. Therefore, in the future TAGS measurement, the group of the light-mass nuclide should be measured with a higher priority, in the future.

Our present task is to make a high priority request list for the future TAGS measurements. For the same purpose Bersillon listed⁶⁾ Br-87, Rb-92, Sr-89, Sr-97, Y-96, Nb-98, Nb-101, Nb-102, Tc-102, Tc-104, Tc-105, Te-135, Cs-142, Ba-145, La-143, and La-145 as the important nuclides to be studied (Hereafter Bersillon's list).

Table 1 through 4 list the nuclides which contribute appreciably to the difference between JEFF-3.1 and JENDL by more than 0.5% of the total fractional difference. We select the nuclides by the following three criteria:

- a) If its contribution to the difference between JENDL and JEFF-3.1 is over 1.0% of the total fractional difference in the β -ray and γ -ray component of the decay heat often a burst fission in ^{235}U or ^{239}Pu or not,

- b) If Appearing on the Bersillon's list or not,
- c) If the highest known level is smaller than 70% of the Q-value or not.

We here put priority A, AA or AAA to each nuclide according to the number of the criteria which the nuclide in question satisfies. The results are listed in Table 5. As an exception we put a high priority to several technetium isotopes, for we have enough basis to believe that these isotopes are suffered from the pandemonium problem⁷⁾.

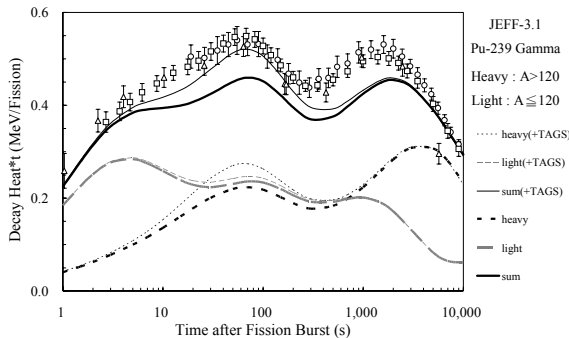


Fig. 5 The contributions from the nuclides on the heavy and the light humps of the double-humped of fission mass-yield curve nuclides to decay heat of γ -ray component of Pu-239 for JEFF-3.1

Table 5 The high priority request list for future TAGS measurement

nuclide				priority	nuclide				priority
Z	A	m	Z		A	m			
41	Nb	98	0	AAA	42	Mo	103	0	AA
41	Nb	101	0	AAA	42	Mo	105	0	AA
43	Tc	102	0	AAA	43	Tc	103	0	AA
43	Tc	104	0	AAA	43	Tc	106	0	AA
43	Tc	105	0	AAA	43	Tc	107	0	AA
37	Rb	92	0	AA	52	Te	135	0	AA
38	Sr	89	0	AA	56	Ba	145	0	AA
38	Sr	97	0	AA	57	La	145	0	AA
39	Y	96	0	AA	35	Br	87	0	A
40	Zr	100	0	AA	55	Cs	142	0	A
41	Nb	99	0	AA	57	La	143	0	A
41	Nb	102	0	AA					

4. Future Plan and Conclusion

We have to pay attention to the so-called pandemonium problem in calculating the average β - and γ -ray energies for decay-heat summation calculations. The successful introduction of the INEL-TAGS data into the decay-heat summation calculation on the basis of JEFF-3.1 decay data file suggests that TAGS data are free from pandemonium problem as has been expected. In this respect, further TAGS measurements for the FP region nuclides are highly encouraged. We selected important FP nuclides, which are assumed to be suffered from the pandemonium problem, among those contributing appreciably to the FP decay heat in rather short cooling-time range, and propose a list of the nuclides to be measured by the TAGS technique with high priority.

References

- 1) T.Yoshida, R.Nakashima, *J.Nucl. Sci. Technol.*: **18**[6], 393 (1981)
- 2) J.C.Hardy, L.C.Carrez, B.Jonson, P.G.Hansen: *Phys. Lett.*, **71B**, 307(1977)
- 3) R.C.Greenwood, R.G.Helmer, M.H.Putnam, K.D.Watts: *Nucl. Instr. and Meth.*, **A390**, 95(1997)
- 4) N.Hagura, T.Yoshida, T.Tachibana, submitted to *J.Nucl. Sci. Technol.*: to be published
- 5) A. Algora, private communication (2005)
- 6) O. Bersillon, private communication (2005)
- 7) T.Yoshida, T.Tachibana, F.Storrer *et al.*: *J.Nucl. Sci. Technol*, **36**[2], 135 (1999)

Table 1 The nuclide contributing to the difference between JEFF-3.1 and JENDL by more than 0.5% of the total sum (U-235 Beta-ray component)

time(s)	nuclide				Q-value [keV]	last level [keV]	★1	★2	JENDL [MeV/fis.]	JEFF-3.1 [MeV/fis.]	★3	priority
	Z	A	m									
20	37	Rb	92	0	8105	7363	○	90.8%	1.49E-03	1.25E-03	0.66%	A
	41	Nb	99	0	3639	236		6.5%	1.10E-03	1.30E-03	-0.55%	A
	41	Nb	101	0	4569	811	○	17.7%	1.49E-03	1.70E-03	-0.57%	AA
	54	Xe	140	0	4060	2324		57.3%	7.23E-04	9.76E-04	-0.69%	A
	41	Nb	98	0	4586	2608	○	56.9%	1.48E-03	1.79E-03	-0.84%	AA
	39	Y	96	0	7087	6232	○	87.9%	1.34E-03	1.77E-03	-1.19%	AA
	52	Te	135	0	5960	4773	○	80.1%	1.19E-03	1.65E-03	-1.26%	AA
100	43	Tc	103	0	2660	1065		40.0%	8.85E-05	1.26E-04	-0.66%	A
	53	I	136	0	6930	6624		95.6%	2.01E-04	2.41E-04	-0.71%	
	41	Nb	98	0	4586	2608	○	56.9%	2.48E-04	3.00E-04	-0.90%	AA
1,000	43	Tc	102	0	4530	2909	○	64.2%	2.24E-05	3.10E-05	-2.07%	AAA

Table 2 The nuclide contributing to the difference between JEFF-3.1 and JENDL by more than 0.5% of the total sum (U-235 Gamma-ray component)

time(s)	nuclide				Q-value [keV]	last level [keV]	★1	★2	JENDL [MeV/fis.]	JEFF-3.1 [MeV/fis.]	★3	priority
	Z	A	m									
20	52	Te	135	0	5960	4773	○	80.1%	8.46E-04	2.60E-04	1.72%	AA
	39	Y	96	0	7087	6232	○	87.9%	6.06E-04	4.43E-05	1.65%	AA
	41	Nb	98	0	4586	2608	○	56.9%	7.77E-04	2.95E-04	1.42%	AAA
	41	Nb	101	0	4569	811	○	17.7%	6.34E-04	2.23E-04	1.21%	AAA
	41	Nb	99	0	3639	236		6.5%	5.36E-04	1.50E-04	1.14%	AA
	40	Zr	100	0	3335	704		21.1%	5.64E-04	1.86E-04	1.11%	AA
	39	Y	96	1	7087	5899	○	83.2%	1.33E-03	1.01E-03	0.95%	A
	35	Br	88	0	8960	7000		78.1%	1.22E-03	1.05E-03	0.53%	
	54	Xe	139	0	5057	4228		83.6%	6.50E-04	1.07E-03	-1.24%	A
37	Rb	92	0	8105	7363	○	90.8%	2.21E-04	7.59E-04	-1.58%	AA	
100	41	Nb	98	0	4586	2608	○	56.9%	1.30E-04	4.95E-05	1.15%	AAA
	41	Nb	99	1	4004	2944		73.5%	1.05E-04	4.15E-05	0.90%	
	42	Mo	103	0	3750	1621		43.2%	1.25E-04	7.33E-05	0.74%	A
	43	Tc	102	0	4530	2909	○	64.2%	4.72E-05	3.23E-06	0.63%	AA
	43	Tc	103	0	2660	1065		40.0%	6.95E-05	3.20E-05	0.53%	A
	51	Sb	133	0	4003	2756		68.8%	1.89E-04	1.54E-04	0.51%	A
	53	I	136	0	6930	6624		95.6%	2.37E-04	2.86E-04	-0.69%	
54	Xe	139	0	5057	4228		83.6%	1.61E-04	2.64E-04	-1.48%	A	
1,000	43	Tc	102	0	4530	2909	○	64.2%	1.88E-05	1.29E-06	3.40%	AAA
	51	Sb	130	1	4960	3413		68.8%	7.67E-06	3.97E-06	0.72%	A

★1: Bersillon's list ★2: $\frac{\text{last level}}{Q - \text{value}}$ ★3: $\frac{\text{JENDL} - \text{JEFF} - 3.1}{\text{JENDL}}$

Table 3 The nuclide contributing to the difference between JEFF-3.1 and JENDL by more than 0.5% of the total sum (Pu-239 Beta-ray component)

time(s)	nuclide				Q-value [keV]	last level [keV]	★1	★2	JENDL [MeV/fis.]	JEFF-3.1 [MeV/fis.]	★3	priority
	Z	A	m									
20	53	I	138	0	7820	5342		68.3%	4.12E-04	2.32E-04	0.63%	A
	43	Tc	106	0	6547	3930		60.0%	8.00E-04	9.52E-04	-0.53%	A
	41	Nb	101	0	4569	811	○	17.7%	1.55E-03	1.76E-03	-0.72%	AA
	41	Nb	99	0	3639	236		6.5%	1.10E-03	1.31E-03	-0.73%	A
	39	Y	96	0	7087	6232	○	87.9%	7.47E-04	1.05E-03	-1.06%	AA
	41	Nb	98	0	4586	2608	○	56.9%	1.46E-03	1.77E-03	-1.07%	AAA
	43	Tc	107	0	4820	2680		55.6%	5.44E-04	8.82E-04	-1.17%	AA
100	43	Tc	102	0	4530	2909	○	64.2%	7.88E-05	1.10E-04	-0.61%	AA
	43	Tc	106	0	6547	3930		60.0%	2.07E-04	2.46E-04	-0.76%	A
	42	Mo	103	0	3750	1621		43.2%	2.84E-04	3.30E-04	-0.89%	A
	41	Nb	98	0	4586	2608	○	56.9%	2.44E-04	2.96E-04	-1.02%	AAA
	43	Tc	103	0	2660	1065		40.0%	2.03E-04	2.82E-04	-1.54%	AA
1,000	55	Cs	139	0	4213	3951		93.8%	3.34E-05	3.58E-05	-0.59%	
	51	Sb	130	1	4960	3413		68.8%	2.88E-06	6.04E-06	-0.77%	A
	43	Tc	104	0	5600	4268	○	76.2%	2.93E-05	3.42E-05	-1.19%	AA
	43	Tc	102	0	4530	2909	○	64.2%	3.14E-05	4.37E-05	-3.02%	AAA

Table 4 The nuclide contributing to the difference between JEFF-3.1 and JENDL by more than 0.5% of the total sum (Pu-239 Gamma-ray component)

time(s)	nuclide				Q-value [keV]	last level [keV]	★1	★2	JENDL [MeV/fis.]	JEFF-3.1 [MeV/fis.]	★3	priority
	Z	A	m									
20	42	Mo	105	0	4950	2766		55.9%	7.89E-04	2.97E-04	1.885%	AA
	52	Te	135	0	5960	4773	○	80.1%	6.34E-04	1.45E-04	1.875%	AA
	41	Nb	98	0	4586	2608	○	56.9%	7.66E-04	2.91E-04	1.82%	AAA
	43	Tc	107	0	4820	2680		55.6%	6.59E-04	2.21E-04	1.68%	AA
	41	Nb	101	0	4569	811	○	17.7%	6.62E-04	2.31E-04	1.65%	AAA
	39	Y	96	1	7087	5899	○	83.2%	1.56E-03	1.13E-03	1.65%	AA
	41	Nb	99	0	3639	236		6.5%	5.36E-04	1.51E-04	1.47%	AA
	40	Zr	100	0	3335	704		21.1%	4.80E-04	1.65E-04	1.21%	AA
	43	Tc	106	0	6547	3930		60.0%	1.39E-03	1.07E-03	1.20%	AA
	39	Y	96	0	7087	6232	○	87.9%	3.39E-04	2.63E-05	1.20%	AA
	42	Mo	103	0	3750	1621		43.2%	6.52E-04	3.61E-04	1.12%	AA
	40	Zr	98	0	2261	0		0.0%	1.36E-04	0.00E+00	0.52%	A
	53	I	136	1	7570	6624		87.5%	4.83E-04	6.54E-04	-0.66%	
	44	Ru	109	0	4160	2270		54.6%	1.46E-04	3.22E-04	-0.67%	A
	37	Rb	92	0	8105	7363	○	90.8%	7.94E-05	2.85E-04	-0.79%	A
	54	Xe	139	0	5057	4228		83.6%	3.80E-04	7.11E-04	-1.27%	A
100	42	Mo	103	0	3750	1621		43.2%	2.87E-04	1.59E-04	2.26%	AA
	42	Mo	105	0	4950	2766		55.9%	1.66E-04	6.26E-05	1.84%	AA
	43	Tc	103	0	2660	1065		40.0%	1.59E-04	7.13E-05	1.57%	AA
	43	Tc	106	0	6547	3930		60.0%	3.59E-04	2.77E-04	1.45%	AA
	41	Nb	98	0	4586	2608	○	56.9%	1.28E-04	4.88E-05	1.41%	AAA
	41	Nb	99	1	3639	2944		80.9%	1.03E-04	3.98E-05	1.12%	A
	43	Tc	102	0	4530	2909	○	64.2%	6.63E-05	4.56E-06	1.10%	AAA
	51	Sb	132	0	5290	3562		67.3%	1.35E-04	8.98E-05	0.81%	A
	45	Rh	108	0	4510	1540		34.1%	5.37E-05	1.29E-05	0.73%	A
	43	Tc	107	0	4820	2680		55.6%	4.88E-05	1.63E-05	0.58%	A
	45	Rh	109	0	2591	1318		50.9%	2.95E-05	5.93E-05	-0.53%	A
	44	Ru	109	0	4160	2270		54.6%	2.92E-05	6.45E-05	-0.63%	A
	45	Rh	110	0	5400	2805		51.9%	2.27E-06	5.20E-05	-0.88%	A
	53	I	136	1	7570	6091		80.5%	1.48E-04	2.00E-04	-0.93%	
54	Xe	139	0	5057	4228		83.6%	9.40E-05	1.76E-04	-1.45%	A	
1,000	43	Tc	102	0	4530	2909	○	64.2%	2.64E-05	1.82E-06	5.12%	AAA
	43	Tc	104	0	5600	4268	○	76.2%	4.68E-05	4.06E-05	1.31%	AA
	45	Rh	108	0	4510	1540		34.1%	5.58E-06	1.34E-06	0.88%	A
	53	I	134	0	4170	3492		83.7%	1.81E-05	1.53E-05	0.59%	

3.17 Density distributions and form factors in neutron-rich nuclei

A. N. Antonov¹, D. N. Kadrev¹, M. K. Gaidarov¹, E. Moya de Guerra², P. Sarriguren², J. M. Udias³, V. K. Lukyanov⁴, E. V. Zemlyanaya⁴, and G. Z. Krumova⁵

¹*Institute for Nuclear Research and Nuclear Energy, Sofia 1784, Bulgaria*

²*Instituto de Estructura de la Materia, CSIC, Serrano 123, 28006 Madrid, Spain*

³*Departamento de Fisica Atomica, Molecular y Nuclear, Facultad de Ciencias Fisicas, Universidad Complutense de Madrid, Madrid E-28040, Spain*

⁴*Joint Institute for Nuclear Research, Dubna 141980, Russia*

⁵*University of Rouse, Rouse 7017, Bulgaria*

Results of charge form factors calculations for several unstable neutron-rich isotopes of light, medium and heavy nuclei (He, Li, Ni, Kr, Sn) are presented and compared to those of stable isotopes in the same isotopic chain. For the lighter isotopes (He and Li) the proton and neutron densities are obtained within a microscopic large-scale shell-model (LSSM), while for heavier ones Ni, Kr and Sn the densities are calculated in deformed self-consistent mean-field Skyrme HF+BCS method. We also compare proton densities to matter densities together with their rms radii and diffuseness parameter values. Whenever possible comparison of form factors, densities and rms radii with available experimental data is also performed. Calculations of form factors are carried out both in plane wave Born approximation (PWBA) and in distorted wave Born approximation (DWBA). These form factors are suggested as predictions for the future experiments on the electron-radioactive beam colliders where the effect of the neutron halo or skin on the proton distributions in exotic nuclei is planned to be studied and thereby the various theoretical models of exotic nuclei will be tested.

1 Introduction

The scattering of particles and ions from nuclei has provided along the years invaluable information on charge, matter, current and momentum distributions of stable isotopes. At present, efforts are devoted to investigate with such probes highly unstable isotopes at radioactive nuclear beam facilities. Concerning the charge distributions of nuclei, it is known that their most accurate determination can be obtained from electron-nucleus scattering. For the case of exotic nuclei the corresponding charge densities are planned to be obtained by colliding electrons with these nuclei in storage rings. As shown in the NuPECC Report [1], a first technical proposal for a low-energy electron-heavy-ion collider made at JINR (Dubna) has been further developed and incorporated in the GSI physics program [2] along with the plan for the electron-ion collider at the MUSES facility at RIKEN [3]. Several interesting and challenging issues can be analyzed by the mentioned electron scattering experiments. One of them is to study how the charge distribution evolves with increasing neutron number (or isospin) at fixed proton number. The question remains up to what extent the neutron halo or skin may trigger sizable changes of the charge root-mean-square (rms) radius, as well as of the diffuseness in the peripheral region of the charge distribution. This point may then be very important for understanding the neutron-proton interaction in the nuclear medium. To this end the preliminary theoretical calculations of the charge form factors of neutron-rich exotic nuclei can serve as a challenge for future experimental works and thus, for accurate determination of the charge distributions in

these nuclei. This can be a test of the different theoretical models used for predicting charge distributions.

In recent years theoretical work has been done along these lines focusing on halo nuclei. Various existing theoretical predictions for the charge distributions in light exotic nuclei ${}^6,8\text{He}$, ${}^{11}\text{Li}$, ${}^{14}\text{Be}$, ${}^{17,19}\text{B}$ have been used for calculations of charge form factors [4] within the PWBA.

In our recent work [5] in comparison with [4] we extend the range of exotic nuclei for which charge form factors are calculated. Along with the new calculations for He and Li isotopes, we present results on charge form factors of several unstable isotopes of medium (Ni) and heavy (Kr and Sn) nuclei and compare them to those of stable isotopes in the same isotopic chain. The isotopes of Ni and Sn are chosen because they have been indicated in Ref. [3] as first candidates accessible for the charge densities and rms radii determination and as key isotopes for structure studies of unstable nuclei at the electron-radioactive-ion collider in RIKEN. We calculate the charge form factors not only within the PWBA but also in DWBA by the numerical solution of the Dirac equation [6, 7, 8] for electron scattering in the Coulomb potential of the charge distribution of a given nucleus. Also, now we do not neglect neutrons, as was done in Ref. [4].

2 The Theoretical Scheme

The nuclear charge form factor $F_{ch}(q)$ has been calculated as follows

$$F_{ch}(q) = \left[F_{point,p}(q)G_{Ep}(q) + \frac{N}{Z}F_{point,n}(q)G_{En}(q) \right] F_{c.m.}(q), \quad (1)$$

where $F_{point,p}(q)$ and $F_{point,n}(q)$ are the form factors which are related to the point-like proton and neutron densities $\rho_{point,p}(\mathbf{r})$ and $\rho_{point,n}(\mathbf{r})$, respectively. These densities correspond to wave functions in which the positions \mathbf{r} of the nucleons are defined with respect to the centre of the potential related to the laboratory system. In PWBA these form factors have the form

$$F_{point,p}(\mathbf{q}) = \frac{1}{Z} \int \rho_{point,p}(\mathbf{r})e^{i\mathbf{q}\mathbf{r}} d\mathbf{r} \quad \text{and} \quad F_{point,n}(\mathbf{q}) = \frac{1}{N} \int \rho_{point,n}(\mathbf{r})e^{i\mathbf{q}\mathbf{r}} d\mathbf{r}, \quad (2)$$

where

$$\int \rho_{point,p}(\mathbf{r})d\mathbf{r} = Z; \quad \int \rho_{point,n}(\mathbf{r})d\mathbf{r} = N. \quad (3)$$

In order that $F_{ch}(q)$ corresponds to density distributions in the centre-of-mass coordinate system, a factor $F_{c.m.}(q)$ is introduced in the standard way [$F_{c.m.}(q) = \exp(q^2/4A^{2/3})$]. In Eq. (1) $G_{Ep}(q)$ and $G_{En}(q)$ are the Sachs proton and neutron electric form factors, correspondingly, and they are taken from one of the most recent phenomenological parametrizations [9].

In addition to PWBA, we also perform DWBA calculations solving the Dirac equation which contains the central potential arising from the proton ground-state distribution [6, 7, 8].

The theoretical predictions for the point-like proton and neutron nuclear densities of the light exotic nuclei ${}^6,8\text{He}$ and ${}^{11}\text{Li}$, as well as of the corresponding stable isotopes ${}^4\text{He}$ and ${}^6\text{Li}$ are taken from the LSSM calculations. For ${}^4,6,8\text{He}$ nuclei they are obtained in a complete $4\hbar\omega$ shell-model space [10]. The LSSM calculations use a Woods-Saxon single-particle wave function basis for ${}^6\text{He}$ and ${}^8\text{He}$ and HO one for ${}^4\text{He}$. The proton and neutron densities of ${}^6\text{Li}$ are obtained within the LSSM in a complete $4\hbar\omega$ shell-model space and of ${}^{11}\text{Li}$ in complete $2\hbar\omega$ shell-model calculations [11]. For ${}^6\text{Li}$ the single-particle HO wave functions have been used in the LSSM calculations and Woods-Saxon ones for ${}^{11}\text{Li}$.

The density distributions of Ni, Kr and Sn isotopes are taken from deformed self-consistent HF+BCS calculations with density-dependent SG2 effective interactions using a large HO basis with 11 major shells [12, 13].

3 Results and Discussion

We calculate charge form factors for a variety of exotic nuclei with both PWBA and DWBA.

In Fig. 1 the point proton and matter density distributions (normalized correspondingly to Z and A) calculated with LSSM for the He and Li isotopes are shown. Matter distribution is taken to be $\rho_m(r) = \rho_{point,p}(r) + \rho_{point,n}(r)$. In addition, we give the “experimental” charge densities of ${}^4\text{He}$ [14, 15] and the “experimental” point-proton density of ${}^6\text{Li}$ [16]. One can see the considerable difference between the “experimental” charge densities of ${}^4\text{He}$ and the point proton densities calculated in LSSM. The calculated matter distributions for the halo nuclei are much more extended than the proton ones. The calculated matter densities for ${}^8\text{He}$ and ${}^{11}\text{Li}$ are in fair agreement with the experimental data obtained in proton scattering on these isotopes in GSI [17] (gray area).

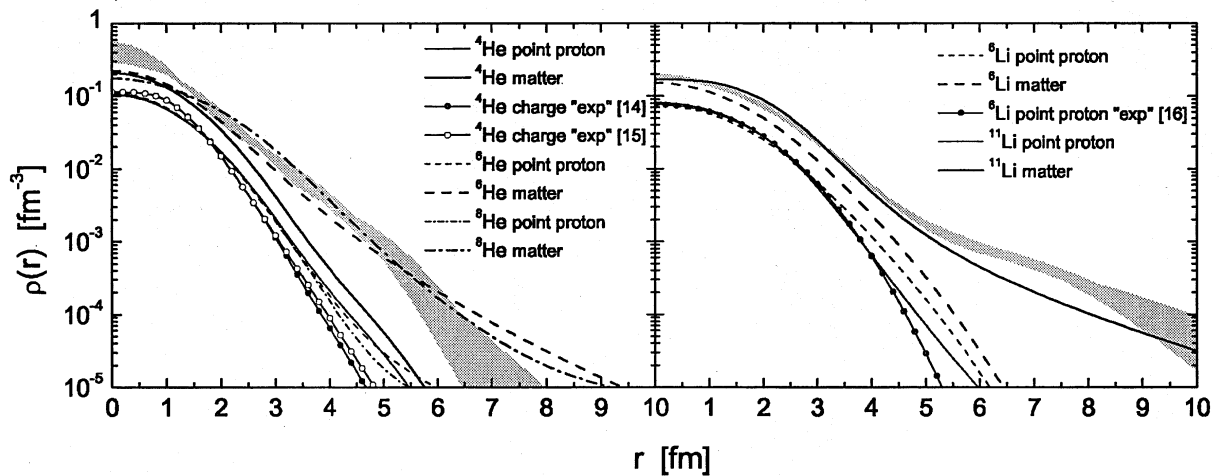


Figure 1: Thin lines are LSSM point proton densities of ${}^4,{}^6,{}^8\text{He}$ and ${}^6,{}^{11}\text{Li}$ compared to the “experimental” charge density from “model-independent” analyses for ${}^4\text{He}$ [14, 15] and ${}^6\text{Li}$ [16]. Thick lines are LSSM matter densities of ${}^4,{}^6,{}^8\text{He}$ and ${}^6,{}^{11}\text{Li}$ compared to matter density of ${}^8\text{He}$ and ${}^{11}\text{Li}$ deduced from the experimental proton scattering cross section data in [17] (grey area).

In Fig. 2 proton density distributions for isotopes of Ni, Kr, and Sn are compared. It can be seen that the point proton densities in a given isotopic chain decrease in the central region and increase in the surface with increasing neutron number.

The charge form factors for the He and Li isotopes in DWBA (at an energy of 540 MeV) and PWBA are shown in Fig. 3. The available experimental data for ${}^4\text{He}$ and ${}^6\text{Li}$ are also shown for comparison. One can see in the left panel the similarity of the LSSM charge form factors of ${}^4\text{He}$ and ${}^6\text{He}$ and their difference from that of ${}^8\text{He}$ and the small deviation of the DWBA from PWBA results in the whole q -range. At the same time there is not a minimum in this q -range in the form factors of ${}^4,{}^6,{}^8\text{He}$ and ${}^6\text{Li}$ in contrast to the experimental data of ${}^4\text{He}$ and ${}^6\text{Li}$ and this leads us to the conclusion that the LSSM densities of these light isotopes do not seem reliable.

In Fig. 4 we present the charge form factors calculated with DWBA at an energy of 250 MeV for the Ni, Kr, and Sn isotopes. A common feature of the charge form factors is the shift of the minima to smaller values of q when the number of neutrons increases in a given isotopic chain. This is due mainly to the enhancement of the proton densities in the peripheral region and also (to a minor extent) to the contribution of the charge distribution of the neutrons themselves. A common feature is also the expected filling of the Born zeros when DWBA is used (instead of PWBA), as well as the shift of the minima to smaller values of q and the increase of the

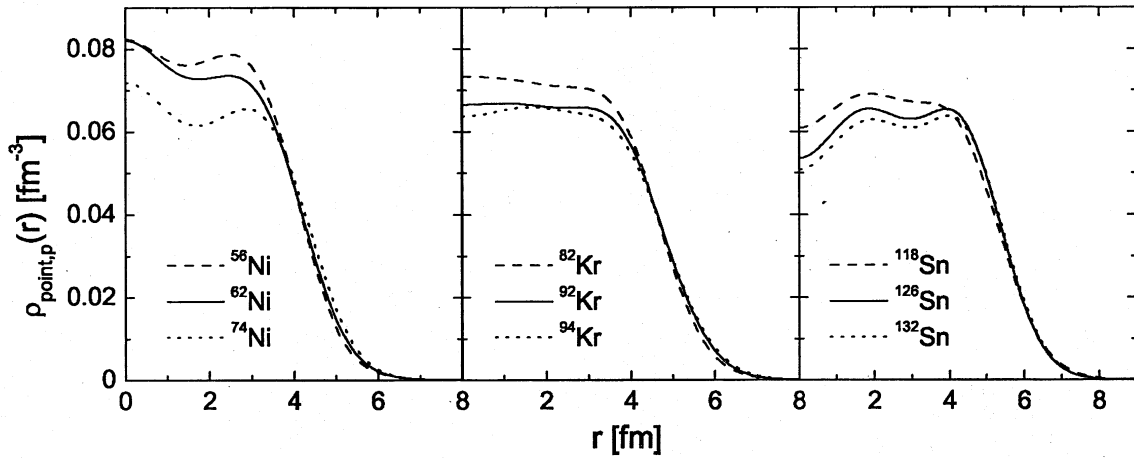
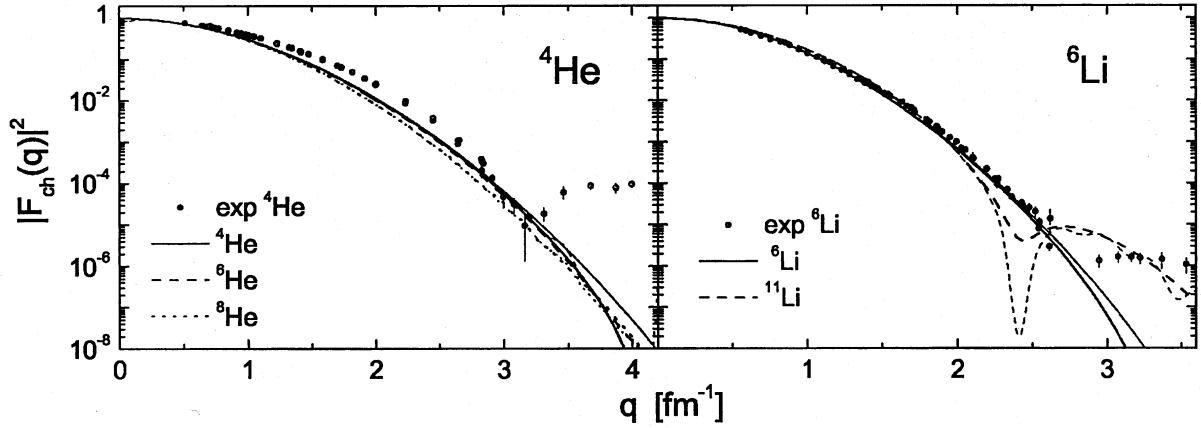


Figure 2: HF+BCS proton densities for isotopes of Ni, Kr, and Sn.


 Figure 3: Charge form factors in DWBA (thick lines) and in PWBA (thin lines) for ${}^4,{}^6,{}^8\text{He}$ and ${}^6,{}^{11}\text{Li}$ using LSSM densities and the experimental data for ${}^4\text{He}$ and ${}^6\text{Li}$.

secondary peaks. We would like to note the reasonable agreement of the results of the DWBA calculations with the experimental charge form factors of ${}^{62}\text{Ni}$ and ${}^{118}\text{Sn}$. The agreement with the empirical data for the stable isotopes is supportive of our results on the exotic nuclei to be used as guidance to future experiments.

In Table 1 we give the rms radii (R_p , R_n , R_{ch} , R_m) corresponding to nuclear proton, neutron, charge and matter distributions, as well as the difference $\Delta R = R_m - R_p$ for the He, Li, Ni, Kr and Sn isotopes which are considered in our work. For comparison we give additionally the charge and matter radii deduced from the electron and proton scattering experiments and from the total interaction cross sections. It is seen that the calculated charge rms radii of ${}^4\text{He}$ and ${}^6\text{Li}$ are larger than the experimental ones and the matter density of ${}^{11}\text{Li}$ exhibits the most extended halo component. The general trend of the difference ΔR between the matter and proton rms radii is to increase with the number of neutrons but for the heavy isotopes this increase is moderate compared to that of the light ones. The common tendency of all predicted rms radii for medium (Ni) and heavy (Kr and Sn) nuclei is the small increase of their values with the increase of the number of neutrons in a given isotopic chain except that R_{ch} of ${}^{126}\text{Sn}$ is practically the same as R_{ch} of ${}^{118}\text{Sn}$. Our theoretical results on R_{ch} of Ni, Kr and Sn isotopes are in good agreement with the available experimental values.

The performed theoretical analyses of the densities and charge form factors can be a step

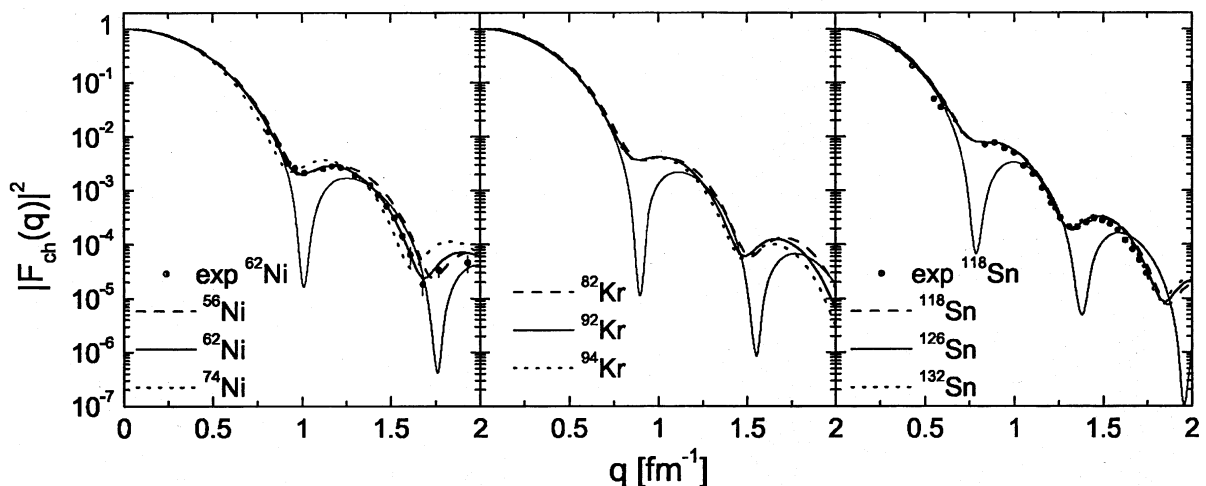


Figure 4: Charge form factors in DWBA for Ni, Kr, and Sn isotopes calculated using the HF+BCS densities and the experimental data for ^{62}Ni and ^{118}Sn . Thin solid lines are PWBA results for ^{62}Ni , ^{92}Kr and ^{126}Sn .

in the studies of the influence of the increasing neutron number on the proton and charge distributions in a given isotopic chain. This is important for understanding the neutron-proton interaction in the nuclear medium. We emphasize also the questions of interest, namely, the necessary both kinematical regions of the proposed experiments and precision to measure small shifts in the form factors.

The theoretical predictions for the charge form factors of exotic nuclei are a challenge for their measurements in the future experiments in GSI and RIKEN and thus, for obtaining detailed information on the charge distributions of such nuclei. The comparison of the calculated charge form factors with the future data will be a test of the corresponding theoretical models used for studies of the exotic nuclei structure.

The work was partly supported by the Bulgarian National Science Foundation under Contracts Φ -1416 and Φ -1501.

References

- [1] Radioactive Nuclear Beam Facilities, NuPECC Report (Europe, 2000).
- [2] Electromagnetic Probes and the Structure of Hadrons and Nuclei, Prog. Part. Nucl. Phys. **44** (2000); G. Shrieder *et al.*, Proposal for GSI RI Beam Factory (2001).
- [3] T. Suda, in *Challenges of Nuclear Structure*, Proceedings of 7th International Spring Seminar on Nuclear Physics, edited by Aldo Covello (World Scientific Publishing Co., Singapore, 2002), p. 13; Proposal for RIKEN RI Beam Factory (2001); T. Katayama, T. Suda, and I. Tanihata, Physica Scripta, **T104**, 129 (2003).
- [4] A. N. Antonov *et al.*, Int. J. Mod. Phys. **E13**, 759 (2004).
- [5] A. N. Antonov *et al.*, Phys. Rev. C **72**, 044307 (2005).
- [6] D. R. Yennie, D. G. Ravenhall, and R. N. Wilson, Phys. Rev. **95**, 500 (1954).
- [7] V. K. Lukyanov *et al.*, Particles and Nuclei, Letters, No. 2[111], 5 (2002); Bull. Rus. Acad. Sci., Phys. **67**, 790 (2003).
- [8] M. Nishimura, E. Moya de Guerra, and D. W. L. Sprung, Nucl. Phys. **A435**, 523 (1985); J. M. Udias, M.Sc. Thesis, Universidad Autonoma de Madrid (unpublished) (1987).

Table 1: Proton (R_p), neutron (R_n), charge (R_{ch}), matter (R_m) rms radii (in fm) and difference $\Delta R = R_m - R_p$ of He and Li isotopes calculated using LSSM densities and Ni, Kr and Sn isotopes using HF+BCS densities. Available data on R_m and R_{ch} are also presented.

	R_p	R_n	R_{ch}	R_m	ΔR	R_m	R_{ch}
^4He	1.927	1.927	2.153	1.927	0.000	1.49(3) [18]	1.696(14) [14] 1.695 [15]
^6He	1.945	2.900	2.147	2.621	0.676	2.30(7) [18] 2.33(4) [19] 2.54(4) [20]	
^8He	1.924	2.876	2.140	2.670	0.746	2.45(7) [18] 2.49(4) [19]	
^6Li	2.431	2.431	2.647	2.431	0.000	2.45(7) 2.32(3) [19]	2.57(10) [16] 2.539 [15]
^{11}Li	2.238	3.169	2.477	2.945	0.707	3.62(19) [18] 3.12(16) [19] 3.53(10) [20]	
^{56}Ni	3.725	3.666	3.795	3.696	-0.029		
^{58}Ni	3.719	3.697	3.794	3.707	-0.012	3.764(10) [16]	
^{62}Ni	3.798	3.855	3.866	3.829	0.031	3.830(13) [16]	
^{74}Ni	3.911	4.130	3.977	4.049	0.138		
^{82}Kr	4.126	4.190	4.189	4.162	0.036		4.192(4) [21]
^{92}Kr	4.224	4.412	4.285	4.340	0.116		4.273(16) [21]
^{94}Kr	4.277	4.496	4.338	4.413	0.136		4.300(20) [21]
^{116}Sn	4.583	4.650	4.646	4.621	0.038	4.626(15) [16]	
^{118}Sn	4.649	4.739	4.705	4.701	0.052	4.679(16) [16]	
^{126}Sn	4.642	4.798	4.698	4.737	0.095		
^{132}Sn	4.685	4.879	4.740	4.807	0.122		

- [9] J. Friedrich and Th. Walcher, *Eur. Phys. J. A* **17**, 607 (2003).
- [10] S. Karataglidis *et al.*, *Phys. Rev. C* **61**, 024319 (2000).
- [11] S. Karataglidis *et al.*, *Phys. Rev. C* **55**, 2826 (1997).
- [12] P. Sarriguren, E. Moya de Guerra, and A. Escuderos, *Nucl. Phys.* **A658**, 13 (1999).
- [13] D. Vautherin, *Phys. Rev. C* **7**, 296 (1973).
- [14] H. De Vries, C. W. De Jager, C. De Vries, *At. Data and Nucl. Data Tables* **36**, 495 (1987).
- [15] V. V. Burov and V. K. Lukyanov, Preprint JINR, R4-11098, 1977, Dubna; V. V. Burov, D. N. Kadrev, V. K. Lukyanov, and Yu. S. Pol', *Phys. At. Nuclei* **61**, 525 (1998).
- [16] J. D. Patterson and R. J. Peterson, *Nucl. Phys.* **A717**, 235 (2003).
- [17] P. Egelhof *et al.*, *Physica Scripta* **T104**, 151 (2003) (and references therein).
- [18] P. Egelhof *et al.*, *Eur. Phys. J.* **A15**, 27 (2002).
- [19] I. Tanihata *et al.*, *Phys. Lett.* **B206**, 592 (1988).
- [20] J. S. Al-Khalili, J. A. Tostevin, and I. J. Thompson, *Phys. Rev.* **C54**, 1843 (1996).
- [21] M. Keim *et al.*, *Nucl. Phys.* **A586**, 219 (1995).

3.18 Burn-up Calculation of Fusion-Fission Hybrid Reactor Using Thorium Cycle

S.Shido¹, Y.Yamamoto², M. Matsunaka¹, K.Kondo¹ I.Murata¹,

¹Division of Electrical, Electronic and Information Engineering,
Graduate School of Engineering, Osaka University, Suita, Osaka, Japan

²Mitsubishi Heavy Industries, Tokyo, Japan

e-mail:shido@ef.eie.eng.osaka-u.ac.jp

A burn-up calculation system has been developed to estimate performance of blanket in a fusion-fission hybrid reactor which is a fusion reactor with a blanket region containing nuclear fuel. In this system, neutron flux is calculated by MCNP4B and then burn-up calculation is performed by ORIGEN2. The cross-section library for ORIGEN2 is made from the calculated neutron flux and evaluated nuclear data.

The 3-dimensional ITER model was used as a base fusion reactor. The nuclear fuel (reprocessed plutonium as the fissile materials mixed with thorium as the fertile materials), transmutation materials (minor actinides and long-lived fission products) and tritium breeder were loaded into the blanket. Performances of gas-cooled and water-cooled blankets were compared with each other. As a result, the proposed reactor can meet the requirement for TBR and power density. As far as nuclear waste incineration is concerned, the gas-cooled blanket has advantages. On the other hand, the water cooled-blanket is suited to energy production.

1. Introduction

A fusion-fission hybrid system is a fusion reactor with a blanket containing nuclear fuel. Even for a relatively lower plasma condition, neutrons can be well multiplied by fission in the nuclear fuel and tritium is thus bred so as to attain its self-sufficiency. Enough energy multiplication is then expected and moreover nuclear waste incineration is possible. A fusion-fission hybrid reactor can play an important role in seamless transition from fission energy to fusion energy.

In our group, a hybrid system with U-Pu cycle has been studied so far. However, acceptable incineration performance for minor actinide (MA) was not expected from the analysis. [1] Hence we started to investigate feasibility of a hybrid system with Th-U cycle.

In the present study, the performance of feasible fusion-fission hybrid reactor with Th-U cycle was examined by a new calculation system, in which a new procedure to prepare cross-section library for burn-up calculation is implemented in order to evaluate more accurate amount of nuclides to be produced or to be incinerated. Target parameters of the blanket of the feasible reactor are in the following;

- TBR > 1.05
- $K_{eff} < 0.95$
- Power Density < 15 W/cc (for gas cooled)
- < 100 W/cc (for water cooled)

2. Calculation System

2.1 Calculation Procedure

The flow chart of this calculation system is shown in Fig. 1. The calculation was performed with the 3-D Monte Carlo code MCNP4-B [2] and point burn-up code ORIGEN2 [3]. These codes are interconnected by a shell script and some C++ codes. The cross-section library of MCNP-4B is based on JENDL-3.2 [4].

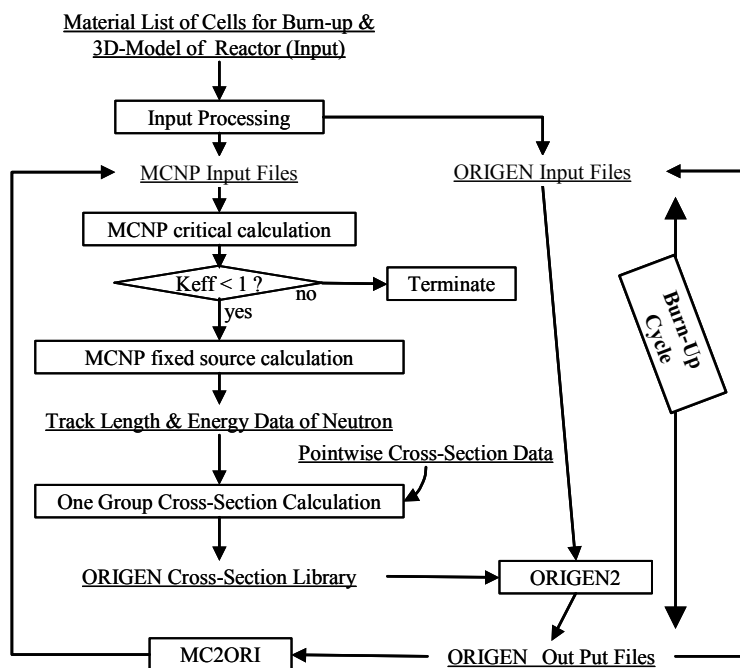


Fig. 1. Flow chart of burn-up calculation

Track length data of neutron for each cell are stored in the MCNP-4B calculation. The data are fed directly to a routine for evaluation of one group cross-section library for burn-up calculation by ORIGEN2. This routine uses JENDL3.3 pointwise files at 300K [4] and JENDL Activation Cross Section File 96 [4]. The one group cross-section is made by the product of the track length data and the pointwise cross-section. Burn-up cycle was repeated for necessary times.

2.2 Calculation Model

The 3-dimensional ITER model [5] was used as a base fusion reactor. The cross section of this model is shown in Fig.2. The nuclear fuel (reprocessed plutonium as the fissile materials mixed with thorium as the fertile materials), transmutation materials (minor actinides and long-lived fission products) and tritium breeder were loaded into the blanket. The blanket consists of five sections, each of which has three layers, i.e., 1st one is on the plasma side, 2nd one is in the middle and 3rd one is in the outer layer.

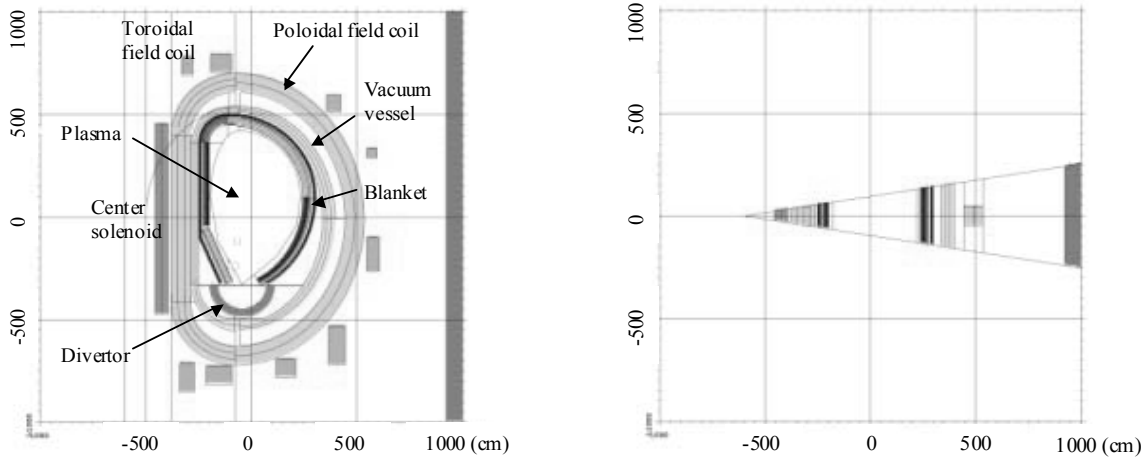


Fig. 2. Vertical (left) and horizontal (right) cross-sections of calculation model

2.3 Plasma Condition

The fusion power of the hybrid reactor was calculated by using parameters listed in Table 1, in which plasma temperature, confinement time and electron density were achieved in JT60 [6]. Other data were cited from recent ITER design.

Table 1 Calculation condition

plasma parameter	
Major radius (m)	6.2
Minor radius (m)	2.1
Plasma volume (m ³)	884
Plasma temperature (KeV)	19
Confinement time (s)	1.1
Electron density (/m ³)	4.80E+19
Fusion power (MW)	646
Neutron yeild (n/s)	2.20E+20
Neutron wall load (MW/m ²)	0.4

3. Results

3.1 Power density and TBR at the beginning of cycle (BOC)

The power density and TBR for gas-cooled (GC) blanket and water-cooled (WC) blanket were calculated for three cases, i.e., nuclear fuel was loaded in 1st, 2nd, or 3rd layer. In two layers other than nuclear fuel, breeding materials which include Li₂ZrO₃ and Be were loaded. The ⁶Li density and Be volume fraction were changed to obtain the optimized result. In the GC blanket with nuclear fuel in 1st layer, water was loaded in 3rd layer instead of Be in order to enhance production of tritium. For example, Fig. 3 shows TBR for WC blanket with the fuel in 2nd layer and Fig. 4 shows its power density.

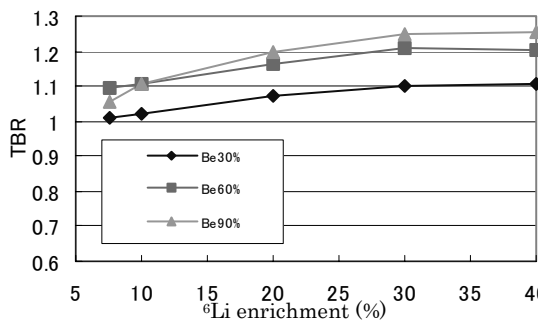


Fig. 3 TBR for WC blanket at BOC

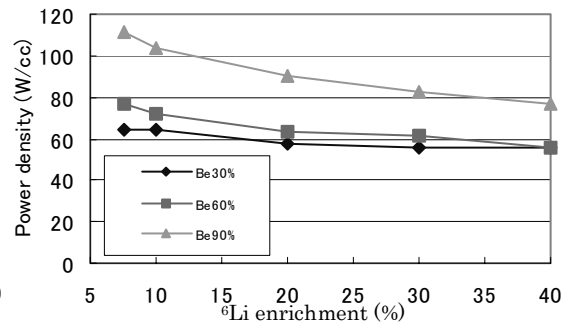


Fig. 4 Power density of WC blanket at BOC

3.2 Burn-up calculation

In the case of GC blanket, two blankets with nuclear fuel loaded in 1st layer (GC1) and 3rd layer (GC3) were feasible. In 5 year burn-up calculation, GC1 was employed because the case doesn't need much plutonium in the fuel layer.

In the case of WC blanket, two blankets with nuclear fuel loaded in 2nd layer (WC2) and 3rd layer (WC3) were feasible. These data are summarized in Table 2. WC2 was employed for 5 year burn up calculation because of its high power density and neutron flux. In all cases, blanket has a transmutation zone that contains long-lived fission products (LLFP). In the present calculation, the period of burn-up is 5 years, in which each year has five burn-up cycles. The plant factor is 70%.

3.2.1 TBR

As shown in Fig.5, GC1 blanket shows a slight increase of TBR over the 5 years burn-up calculation. WC2 blanket shows a decrease of TBR, but the rate of the decrease becomes smaller and TBR >1.05 is achieved in 5 years later, as shown in Fig. 6.

Table 2. Condition of calculation

case	TBR	Power Density W/cc	Fuel material fraction (%)			Breeder (Li ₂ ZrO ₃ +Be)	
			Pu	Th	Be	Li6 enrichment(%)	Be fraction (%)
GC1*	1.06	15.4	0.25	6	63.75	40	90
GC3	1.04	8.8	3	77	0	40	90
WC2	1.25	82.7	8	52	0	30	90
WC3	1.09	31.5	8	52	0	10	60

* Water was employed instead of Be in the 3rd layer. The volume fraction of water and Li₂ZrO₃ are 80% and 20%, respectively.

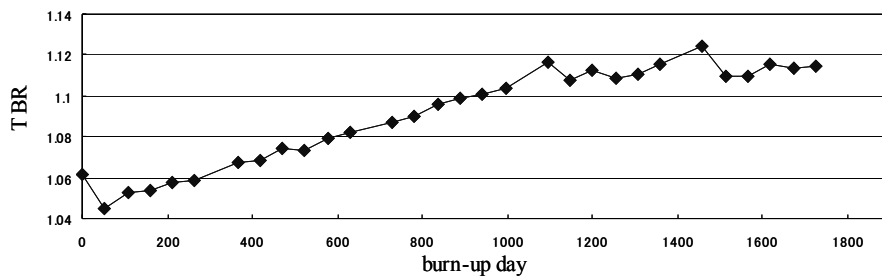


Fig. 5 TBR for GC1

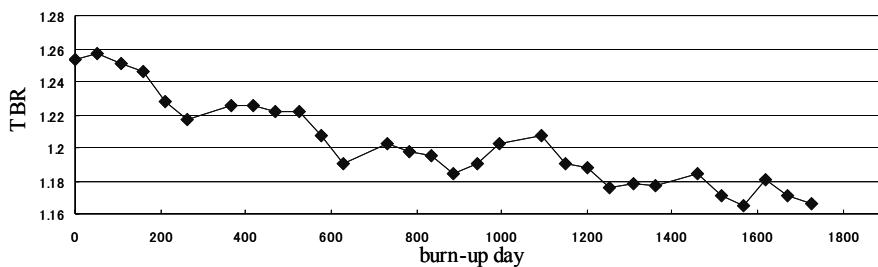


Fig. 6 TBR for WC2

3.2.2 Transmutation of FP

^{93}Zr , ^{99}Tc , ^{107}Pd , ^{129}I and ^{135}Cs were loaded as the LLFP mixed with Be or water in the transmutation zone (FP cell) in the 1st layer of the blanket in the case of WC2 and in the 2nd layer in the case of GC1. The calculation result is shown in Table 3.

Table 3 Performance of incineration

Gwty-PWR	5years			
	Gas Cooled (GC1) in FP cell		Water Cooled (WC2) in FP cell	
	Total	Total	Total	Total
Zr 93	2.8	-3.6	4.0	-16.5
Tc 99	52.1	47.3	76.9	51.7
Pd 107	140.7	133.3	165.5	106.9
I 129	43.4	37.9	66.3	28.6
Cs 135	12.8	-0.7	16.6	-84.6

Because of its high neutron flux, WC2 blanket has a better transmutation performance of FP cell than GC1 blanket. But WC2 blanket contains much more plutonium and generates more FPs, then ^{93}Zr and ^{135}Cs are totally built up. Compared with WC2, ^{135}Cs production was decreased for GC1 blanket

because of less plutonium contained. It is necessary to load more ^{93}Zr and ^{135}Cs in FP cell if they should be incinerated effectively.

3.2.3 Production of MA

As shown in Table 4, the production rate of MA (^{237}Np , ^{241}Am , ^{243}Am) is compared with the calculation result of U-cycle blanket in which only thorium is replaced by uranium in the fuel cell. In the Th-cycle, production of ^{237}Np is much smaller, but production of ^{243}Am is the same as U-cycle because using Pu as nuclear fuel caused generation of ^{243}Am . Pu composition was drastically different from U-cycle because Pu isotopes are produced from a fertile material of ^{238}U in the U-cycle. Subsequent Long-term burn-up calculation will show difference in Am production.

Table 4 MA & Pu production (5 years burn-up)

Production Rate (kg / 5years)		0 - 5 year					
		MA			Pu		
case		Np237	Am241	Am243	Pu239	Pu240	Pu241
GC1	Th-cycle	0.3	11.7	41.2	-643.1	-268.7	44.6
	U-cycle	79.7	30.5	37.0	829.8	-61.9	254.5
WC2	Th-cycle	5.4	659.7	395.5	-8036.1	-810.0	591.3
	U-cycle	257.2	670.6	369.5	-3307.8	-483.2	585.3

4. Long-term Burn-up Calculation

Additional 5 years burn-up calculation without refueling or shuffling was performed to estimate the long-term burn-up characteristics of 10 years. The result of the calculation for MA and Pu is shown in Table 5. In Th-cycle of GC1, Pu and MA except for ^{237}Np are reduced compared to the first 5 years. TBR is stabilized over 1.05 and the FP transmutation performance is almost the same as the first 5 years burn-up calculation. Gas-cooled blanket is suited to incineration of nuclear waste.

Table 5 MA & Pu production (10 years burn-up)

		Production Rate (kg / 5years)		5 – 10 year			
		Np237	MA		Pu		
case			Am241	Am243	Pu239	Pu240	Pu241
GC1	Th-cycle	2.2	-12.1	3.4	-73.5	-21.2	-111.1
	U-cycle	38.2	28.8	23.6	400.9	73.5	89.0
WC2	Th-cycle	8.7	488.5	211.2	-5365.2	-946.1	-89.6
	U-cycle	208.7	534.0	198.7	-2161.7	-450.0	33.6

5. Conclusion

A burn-up calculation system with more accurate estimation procedure of one-group cross section for point burn-up calculation has been developed to estimate the performance of blanket in a fusion-fission hybrid reactor using thorium cycle. In the calculation, reprocessed plutonium and thorium oxide were loaded in the blanket. A 3-D ITER model was used as a base reactor, and the plasma condition achieved in JT60 was used. As a result, it was shown that the proposed reactor can meet the requirement for TBR and power density in both gas-cooled and water-cooled blankets. And Th-cycle has advantages in FP and Pu transmutation compared to U-cycle. As far as nuclear waste incineration is concerned, gas-cooled blanket has advantages. On the other hand, water cooled-blanket is suited to energy production.

References

- [1]I. Murata, Fusion-driven hybrid system with ITER model, Fusion Eng. Des. 75-79 (2005) 871-875.
- [2]J.F. Briesmeister (Ed.), MCNP-A General Monte Carlo N-particle Transport Code, Version 4B, LA-12625-M, 1997.
- [3]A.G. Croff, ORIGEN2: a versatile computer code for calculating the nuclide compositions and characteristics of nuclear materials, Nucl. Technol. 62 (1983)335-352.
- [4]<http://www.ndc.tokai.jaeri.go.jp/nucldata/index.html>
- [5]<http://www.naka.jaeri.go.jp/ITER/FDR/>
- [6]<http://www-jt60.naka.jaea.go.jp/HOME-J.html> (in Japanese)

3.19 Database Retrieval Systems for Nuclear and Astronomical Data

Takuma SUDA¹, Naohiko Otuka², Sergei Korennov¹, Shimako Yamada³, Yutaka Katsuta³,
Akira Ohnishi³, Kiyoshi Katō³, Masayuki Y. Fujimoto³

¹*Meme Media Laboratory, Hokkaido University, 060-8628 Sapporo, Japan*

²*Nuclear Data Evaluation Group, Japan Atomic Energy Agency, 319-1195 Tokai, Japan*

³*Division of Physics, Graduate School of Science, Hokkaido University, 060-0810 Sapporo, Japan*

e-mail: suda@astro1.sci.hokudai.ac.jp

Data retrieval and plot systems of nuclear and astronomical data are constructed on a common platform. Web-based systems will soon be opened to the users of both fields of nuclear physics and astronomy.

1. Introduction

The compilation of nuclear data has played an important role in contributing not only to the scientific research but also to the technological progresses. At the same time, this invokes demands for the utilization of nuclear data. There are some systems in the world that can search and plot the data from enormous database. However, no retrieval system can treat both experimental and evaluated nuclear data simultaneously. Based on the needs for comparisons of evaluated data with experimental data in a more convenient way, we have developed a web-based retrieval system (see <http://www.jcprg.org/>).

On the other hand, we have launched a project of constructing the database of astronomical data that treat the observed properties of stars in the Galactic halo born in the early universe [1]. This project is motivated by the recent growing number of known extremely iron-poor stars and by our recent work on the origin of such stars [2] after the discovery of the most iron-poor object [3], which is more encouraged by the recent break of the record [4]. The purpose of the project is to identify the first generation objects as well as the comprehensive understanding of the history of our universe through the accumulation of observational data. Due to the difficulty of compiling the data from individual papers, the database of this kind has not yet been opened to the astronomical society.

In this paper, we will describe the current status of the development of astronomical database. In the next section, the outline of the system is elaborated. Future development and statistics are discussed and summarized in the third section.

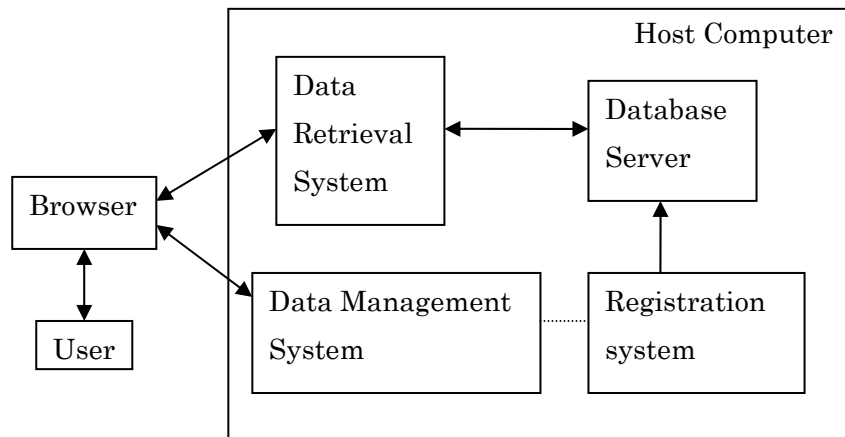


Figure 1: Internal structure of astronomical database

2. Outline of the astronomical database system

The schematic view of the structure of the whole system is illustrated in Figure 1. The system consists of some independent programs in the host computer. While users access the system only through the Internet browser, workers and administrators of the system use both browser and terminal.

Before using this system, the data to be retrieved from the web have to be prepared. We constructed the online system to compile and store the required data in CSV format. The process of data input is done through CGI form of this system. The observational data of extremely metal-poor stars are collected from literatures that focuses on the abundance analyses of field halo stars having low iron content typically one hundred times less than that of the Sun. In order to collect appropriate papers for adding to the database, we have developed the data management system. Candidate papers to be compiled are selected and listed in the management system and their identifier is allocated to each paper. Then the editors who compile the data with the system extract the data from papers and input them into the CSV files.

Stored data files, written in CSV format, are registered into the database server by running the registration system. Since the system is independent from the work via the Internet, the security of the system is ensured. In addition, CSV files can be checked easily during the registration process. At the same time, the program for registration generates text files from CSV files to review the collected data. These files are used as the quick review of data included in each paper and users can easily access the data by tracing the links to the data files of papers and objects.

At present, the database includes 472 stars and 652 records of objects. As the basic data, stellar parameters such as effective temperature, surface gravity, metallicity, and micro-turbulence factor and

The screenshot shows a web browser window titled "Search and Plot - Netscape". The main content area is a form titled "Search" with a "Query" section. The "Graph Options" section includes fields for Xaxis (Atmospheric Parameters), Yaxis (Category), Zaxis (Category), and Criterion (Category), each with a "From" and "To" range. The "Observational Information" section includes fields for Object, Binarity (Binary Nature), and Magnitude (Band). The "Bibliographical Information" section includes fields for Author (First Author), Reference (ALL), and Publication Year. The "Retrieval Options" section includes fields for Display / Page (10), Order by (Object), Output Option (plot by single file for selected data), and Cross Search (Retrieve data across papers). At the bottom of the form are "search", "example", and "reset" buttons.

Figure 2: Snapshot of the query form of the astronomical data retrieval system

photometric data are taken with various bands such as U, B, V, I, J, K, and so on. Positions of target objects are also compiled from the other online database of object catalogues. In these papers, 10179 records of chemical abundances are derived from absorption lines by stellar atmospheres, with increased variation in the elements of derived abundances thanks to the recent observations of detecting more and more atomic lines from only one star. The binary period, the important parameters among the physical quantities, is to be assembled in the database although the number of data is very small due to the difficult detection of binarity. The binary period is determined from the variations in radial velocities between the observations at different time. It is one of the most important quantities to understand the origin of extremely metal-poor stars [2].

The retrieval system works on Internet CGI described by Perl, JavaScript, and MySQL. The snapshots of the retrieval system are shown in Figure 2. Many physical parameters such as chemical composition measured by element relative to hydrogen or iron compared with the solar ratio, number abundances in logarithm scale based on the 10^{12} hydrogen atoms, surface stellar parameters, photometry, and binary period can be used as figure axes to plot 2D and 3D viewgraphs. Users can set the criteria for each physical quantity to extract the data of required range. If only one quantity is chosen, the distribution of required parameter is displayed in the form of histogram with arbitrary size of bin width. Cross match retrieval and plot is also possible like in the case that the object name is common but its data comes from different papers. For element abundances, customized expressions in the abundances are allowed to retrieve and plot

by converting the existing data; for example, [C/N], [C+N/Fe], [Pb+Ba/C], and so on.

The retrieved records from MySQL server are displayed on the browser in table format as shown in Figure 3. Each column represents the checkbox to select data to plot, identifier of the paper, object name, metallicity, the first author of the reference, and the reference code. Each link on entry numbers and object names jumps to the text data extracted from CSV files as mentioned above. The snapshot of plot stage is shown in Figure 4. Viewgraphs drawn in the browser are equipped with simple functions for editing: standard options for Gnuplot such as changing the labels, legends, scales and ranges of the viewgraph. Users can also download figures in various formats (png, eps, ps, and pdf, with color or black and white) and upload data from the form and/or local computers. If you want to edit the viewgraph in detail, the original data and the script for plotting figure can be downloaded from the server. Of course, numerical data are accessible by tracing the link on the data numbers in the left of the list.

Selection

plot restart reset plot_all

Results : 61

<input type="checkbox"/>	#	Object	[Fe/H]	First Author	Reference
<input type="checkbox"/>	A0047	BD185550	-2.87	J.Melendez J.A.Johnson M.Spite R.Cayrel D.L.Burris	J.Melendez+,ApJ, 575, 474, 2002 J.A.Johnson+,ApJ, 139, 219, 2002 M.Spite+,AAP, 430, 655, 2005 R.Cayrel+,AAP, 416, 1117, 2004 D.L.Burris+,ApJ, 544, 302, 2000
<input type="checkbox"/>	A0017	BS16082-129	-2.86	S.Honda	S.Honda+,ApJ, 607, 474, 2004
<input type="checkbox"/>	A0037	BS16085-0050	-3.1	S.Giridhar	S.Giridhar+, 113, 519, 2001
<input type="checkbox"/>	A0017	BS16085-050	-2.91	S.Honda	S.Honda+,ApJ, 607, 474, 2004
<input type="checkbox"/>	A0022	BS16467-062		D.K.Lai M.Spite R.Cayrel P.François	D.K.Lai+,AJ, 128, 2402, 2004 M.Spite+,AAP, 430, 655, 2005 R.Cayrel+,AAP, 416, 1117, 2004 P.François+,AAP, 403, 1105, 2003
<input type="checkbox"/>	A0017	BS16469-075	-3.03	S.Honda	S.Honda+,ApJ, 607, 474, 2004
<input type="checkbox"/>	A0022	BS16477-003		D.K.Lai M.Spite R.Cayrel	D.K.Lai+,AJ, 128, 2402, 2004 M.Spite+,AAP, 430, 655, 2005 R.Cayrel+,AAP, 416, 1117, 2004
<input type="checkbox"/>	A0025	BS17569-049	-2.88	M.Spite R.Cayrel	M.Spite+,AAP, 430, 655, 2005 R.Cayrel+,AAP, 416, 1117, 2004
<input type="checkbox"/>	A0025	CD38245	-4.19	M.Spite J.E.Norris R.Cayrel P.François	M.Spite+,AAP, 430, 655, 2005 J.E.Norris+,ApJ, 561, 1034, 2001 R.Cayrel+,AAP, 416, 1117, 2004 P.François+,AAP, 403, 1105, 2003
<input type="checkbox"/>	A0025	CS22169-035	-3.04	M.Spite S.Giridhar S.Honda R.Cayrel	M.Spite+,AAP, 430, 655, 2005 S.Giridhar+, 113, 519, 2001 S.Honda+,ApJ, 607, 474, 2004 R.Cayrel+,AAP, 416, 1117, 2004

next PAGE : 1 / 7

Figure 3: Snapshot of the retrieval result

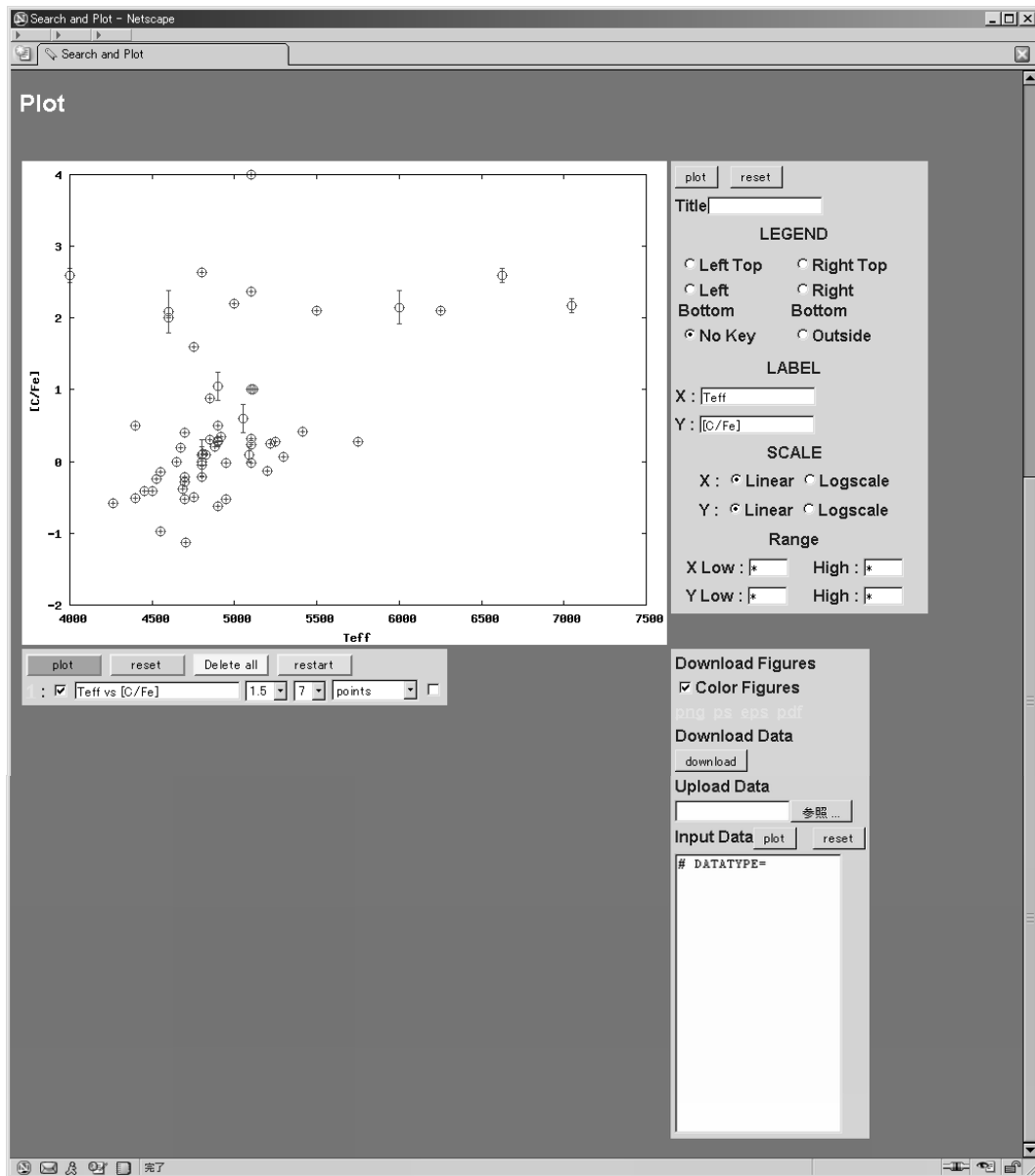


Figure 4: Snapshot of the data plot form

3. Discussion and Future Prospect

Our database system can provide various approaches to the insight into the origin and characteristics of extremely metal-poor stars currently observed by setting possible physical quantities for figure axes. We can see the relations among derived values from different papers, e.g., binary periods from one paper and carbon abundances from another paper, and so on. Some combinations of physical quantities may give new aspects of our understandings of the early universe. Many trials for statistical analyses by using this system are now going on and the test results will be published in a separate paper (Suda et al, in preparation).

This system is expected to contribute to the future observations of metal-poor candidate stars. The

observers can check the current knowledge of individual stars and the data needs for further investigations. The consistency of observational data between different authors and observations can also be checked.

We are planning to collaborate with the Japan Virtual Observatory (JVO) project to extend the users to all over the world. JVO is the unified system of databases to retrieve databases simultaneously in many places and in various formats by using special network technology and unique query language. Our system will be one of the astronomical databases which include almost all kinds of objects like stars, galaxies, quasars, X-ray sources, gamma ray bursts, and so on. Our data will add detailed observational information to known catalogues of stars in the Galactic halo.

References

- [1] T. Suda, T. Suwa, K. Hayasaki, M. Aikawa, and M. Y. Fujimoto, "Database System of the Observed Properties of Stars in the Early Universe", INDC (JPN) -194/U (2005), pp.23
- [2] T. Suda, M. Aikawa, M. N. Machida, M. Y. Fujimoto, and I. Iben Jr., "Is HE 0107-5240 A Primordial Star? The Characteristics of Extremely Metal-Poor Carbon-Rich Stars", *The Astro. Phys. J.*, **611**, 476 (2004)
- [3] N. Christlieb *et al.*, "A stellar relic from the early Milky Way", *Nature*, **419**, 904 (2002)
- [4] A. Frebel, W. Aoki, N. Christlieb *et al.*, "Nucleosynthetic signatures of the first star", *Nature*, **434**, 871 (2005)

3.20 Development of the measurement system of the $^{189}\text{Os}(n,n'\gamma)$ cross section and Re/Os chronometer

Y.Temma, M.Segawa, Y.Nagai, T.Ohta, A.Nakayoshi, S.Fujimoto, H.Ueda, T.Shima,
M.Igashira¹, T.Ohsaki¹, J.Nishiyama, T.Masaki²

Research Center for Nuclear Physics, Osaka Univ.,

¹Research Laboratory for Nuclear Reactors, Tokyo Institute of Technology,

²Kobe University

e-mail: temma@rcnp.osaka-u.ac.jp

Abstract

The keV neutron inelastic scattering reaction off the ground state of ^{189}Os to the 36 keV excited state is important in the study of Re/Os chronometer. So far, the cross section has been measured by detecting neutrons inelastically scattered by ^{189}Os . However, it is not easy to accurately measure the cross section with the mentioned method, because both the inelastically and elastically scattered neutrons from ^{189}Os are detected simultaneously by a neutron detector. Hence, we are now developing a new measurement system to detect the γ -ray from the $^{189}\text{Os}(n,n'\gamma)^{189}\text{Os}$ reaction.

1. Introduction

The age of the universe is one of the most interesting themes in astrophysics. It is known that $^{187}\text{Re}/^{187}\text{Os}$ pair is one of the good chronometers to estimate the age of the universe, since it has unique features described below. First, the parent nucleus ^{187}Re is formed only by a rapid neutron capture process in stars and its half life is quite long 42.3 Gyr. Second, the chemical property of ^{187}Re and ^{187}Os is similar, so the chemical affection for ^{187}Re and ^{187}Os is cancelled in taking the abundance ratio of ^{187}Re to that of ^{187}Os . However there are a few problems in the $^{187}\text{Re}/^{187}\text{Os}$ chronometer. First, ^{187}Os abundance increases by the β decay of ^{187}Re , and also by a slow neutron capture (s-) process of ^{186}Os , and decreases by the s-process of ^{187}Os . Second, inside stars ^{187}Os could be significantly populated at a stellar temperature ($\sim 30\text{keV}$), and ^{187}Os is also depleted by the excited neutron capture process. Therefore the neutron capture cross sections of $^{186,187}\text{Os}$ through the ground- and excited states are very important in order to precisely derive the age of the universe. Since it is not possible to measure the excited neutron capture cross section at a terrestrial laboratory, the cross section should be estimated by a theoretical calculation. For constructing the reliable

theoretical model to calculate the excited neutron capture cross section of ^{187}Os , measurements of the inelastic scattering cross section off the ground state ($J^\pi=1/2^-$) of ^{187}Os to its excited 10keV state ($J^\pi=3/2^-$), and the neutron capture cross section of the ground state ($J^\pi=3/2^-$) for ^{189}Os and inelastic cross section off the ground state ($J^\pi=3/2^-$) of ^{189}Os to its excited 36keV state ($J^\pi=1/2^-$) were suggested firstly by Fowler [1]. Here, it should be noted that the nuclear structure of these two odd-A Os isotopes has the same active nucleon configurations, the same deformation, the same spin-parity for the ground state and 1st excited state in ^{187}Os are $1/2^-$ and $3/2^-$, while those in ^{189}Os are $3/2^-$ and $1/2^-$, respectively (Figure 1).

We are planning to measure the inelastic cross section off the ground state of ^{189}Os to its excited 36keV state, $\sigma_{n,n'}(^{189}\text{Os})$. So far, $\sigma_{n,n'}(^{189}\text{Os})$ was measured by detecting the neutrons inelastically scattered by ^{189}Os with scintillation counters [2]. However, it is not easy to accurately measure $\sigma_{n,n'}(^{189}\text{Os})$ by detecting neutrons, because both the inelastically and elastically scattered neutrons from ^{189}Os are detected simultaneously by neutron detectors. We also made the (n,n') reaction experiment by employing a ^6Li -glass detector, but the obtained signal-to-noise ratio was low 0.0084. Hence, we are now developing a new measurement system to detect the 36 keV γ -ray from the $^{189}\text{Os}(n,n'\gamma)^{189}\text{Os}$ reaction by using Si detectors. This new method is expected to have high sensitivity to detect the γ -ray, but there are a few problems. First, the self-absorption of the 36 keV γ -ray by ^{189}Os sample is large. Second, the 36 keV γ -ray competes with an internal conversion electron process. Third, it is difficult to separate the 36 keV γ -ray signal from the background γ -ray due to the $^7\text{Li}(p,\gamma)^8\text{Be}$ reaction because of the low time resolution of Si detectors. Hence the intensity of the 36 keV γ -ray due to the $^{189}\text{Os}(n,n'\gamma)^{189}\text{Os}$ reaction is estimated to be quite low, and therefore it is crucial to develop a high sensitive system to measure $\sigma_{n,n'}(^{189}\text{Os})$.

2. Experimental procedure

In order to construct the mentioned system we measured γ -ray background by placing Si detectors and Pb shield at various places. The neutrons with an averaged energy of 30 keV were produced by the $^7\text{Li}(p,n)^7\text{Be}$ reaction using a pulsed proton beam provided from the 3.2 MV Pelletron accelerator of the Research Laboratory for Nuclear Reactors at Tokyo Institute of Technology. The produced neutrons were emitted into a cone of about 50° with respect to the proton beam direction. Main γ -ray background was found to be the γ -ray due to the $^7\text{Li}(p,\gamma)^8\text{Be}$ reaction. We measured pulse height and time-of-flight (TOF) spectra to obtain net γ -ray yields as a function of the neutron energy by separating the γ -ray from the $^{189}\text{Os}(n,n'\gamma)^{189}\text{Os}$ reaction from the γ -ray due to the $^7\text{Li}(p,\gamma)^8\text{Be}$ reaction. An experimental setup is shown in figure 2.

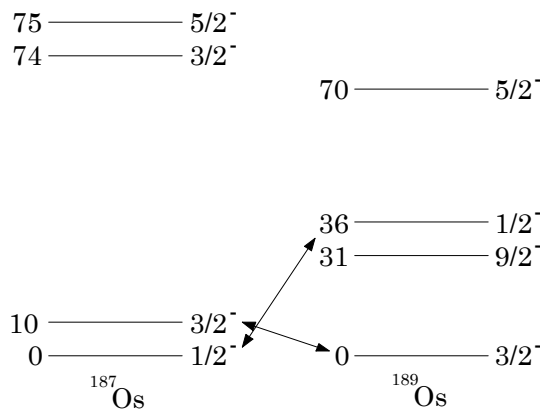


Figure 1 : level scheme of ^{187}Os and ^{189}Os

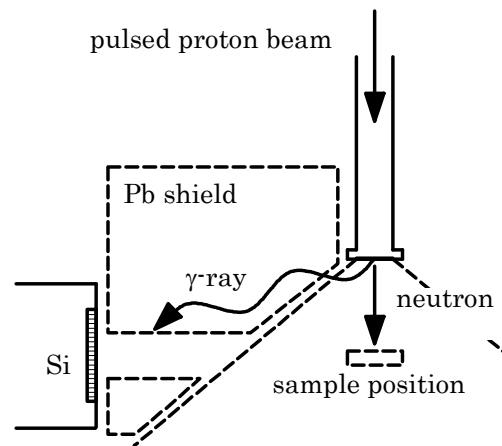


Figure 2 : the measurement geometry

3. Result

We measured the TOF spectra without putting a sample at a sample position by using Pb shield with various thicknesses. A typical TOF spectrum taken without Pb shield around the Si detector is shown in figure 3(a). By covering the Si detector with Pb shield and placing Pb shield with a thickness of 5, or 10, and/or 15 cm (picture 2) between the Li neutron production target and the Si detector, we obtained the spectrum as shown in figure 3(b). It is clearly seen that we needed to put Pb shield with a thickness of 15 cm to construct the system with a large signal-to-noise ratio.

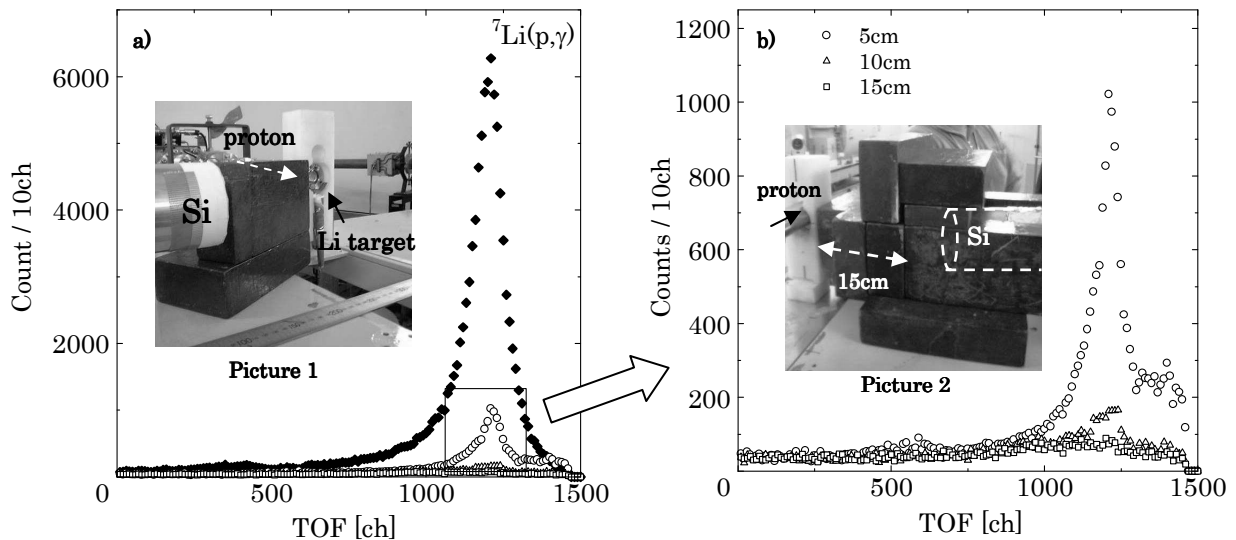


Figure 3 : TOF spectra without sample due to the $^7\text{Li}(p,\gamma)^8\text{Be}$ reaction

In order to study the performance of a system, we measured a TOF and γ -ray spectra taken by bombarding a ^{159}Tb sample. The γ -ray spectrum for the neutron energy range from 36 to 70 keV is shown in Figure 4, where the sharp peaks at around 45 and 75 keV are due to the X-rays from ^{159}Tb and Pb shield, respectively. We estimated the counting rate of the

background around 36 keV region from the obtained γ -ray spectrum by taking into account the energy resolution of Si detector 1.8 keV (FWHM) at 31 keV (Figure 5) to be 84 cph. While the 36 keV γ -ray yield due to the $^{189}\text{Os}(n,n'\gamma)^{189}\text{Os}$ reaction was estimated to be about 8 cph according to a previous result. Therefore, the signal-to-noise ratio could be 0.09, 10 times larger than that for the detection of inelastic neutrons.

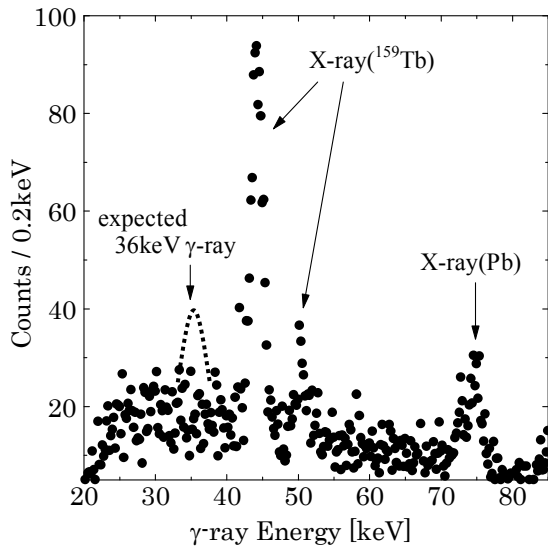


Figure 4 :
 γ -ray spectrum taken with ^{159}Tb sample

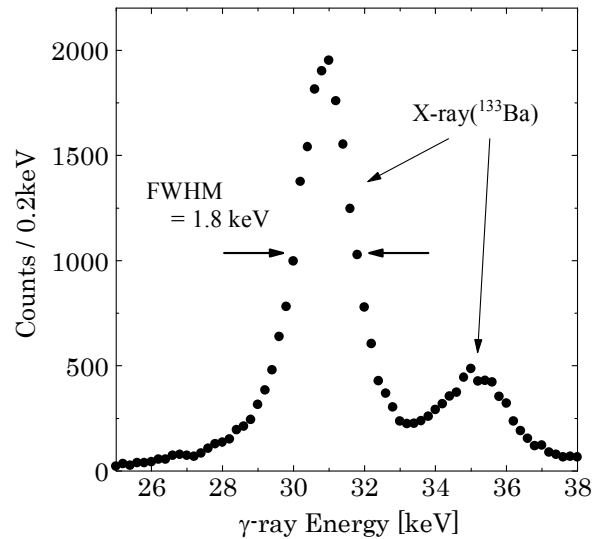


Figure 5 : energy resolution of Si detector

4. Summary

We have made a test experiment to detect the γ -ray due to the inelastic scattering off the ground state of ^{189}Os to its excited 36keV state by means of a Si detector to determine its reaction cross section. We are now making a proper shield based on the present result to measure the $^{189}\text{Os}(n,n'\gamma)^{189}\text{Os}$ cross section using four Si detectors.

Reference

- [1] W. A. Fowler, Rev. Mod. Phys. **56** 149 (1984).
- [2] M. T. McEllistrem, R.R.Winters, R.L.Hershberger, Z.Cao, Phy. Rev. **C40** (1989) 591

3.21

Analysis of Continuum Spectra for Proton Induced Reactions on ^{27}Al , ^{58}Ni , ^{90}Zr , ^{197}Au and ^{209}Bi at Incident energies 42 and 68 MeV-Direct Reaction Model Analysis.

S.A. Sultana¹, T. Kin², G. Wakabayashi²,
Y. Uozumi², N. Ikeda², M. Matoba³ and Y. Watanabe²
e-mail: sadia_afroze@yahoo.com

1. Bangladesh Open University, Gazipur 1705, Bangladesh
2. Kyushu University, Fukuoka, 812-8581, Japan
3. Kyushu Sangyo University, Fukuoka 813-8503, Japan

Abstract

Theoretical analyses of the double differential cross sections for proton induced deuteron pickup reactions are described in this paper. Differential cross sections have been measured in the direct reaction region for various nuclei of mass number from 27-209 (^{27}Al - ^{209}Bi) at incident energies e.g. 42 and 68 MeV (for ^{197}Au , only at 68 MeV and for ^{209}Bi , only at 42 MeV), using an approach based on the DWBA and an asymmetry Lorentzian function having energy-dependent spreading width. The values of the calculated double differential cross sections have been compared with the experimental ones and are in good agreement.

I. Introduction

Nuclear data from several tens of MeV to a few GeV are recently required for some applications, such as, transmutation of nuclear waste, energy production, space development, cancer therapy, etc. Again Accelerator Driven System (ADS) is used for the purpose of transmutation of nuclear waste, energy production, etc. and as for the ADS, for example, proton beam of 1.5 GeV is injected into the sub-critical reactor core, and various kinds of nuclear reactions are induced in the process of proton degradation. So the precise simulation of nuclear reactions is required for the engineering design work. Nuclear reaction data in the energy region from several tens of MeV to a few GeV are the basis of such simulation code and eagerly wanted. However, experimental data for differential cross sections are very scarce and discrepant if data exist.

When experimental data are limited, the calculation code based on the theoretical models becomes a useful tool for evaluating the cross sections. However, the models available for nuclear data analysis are not so well established as those used in the direct reaction regions, i.e., in higher emission energy region because the continuum spectrum in the direct reaction region is not possible to analyse so easily. Theoretical methods to calculate direct reactions are generally to predict excitation of a state having known spin-parities and existing shells of the related nucleons. Therefore, we have developed a new theoretical model, which is based on the first order DWBA model with a strength function of an asymmetric Lorentzian form. Hirowatari et al. [1] and Syafaruddin et al. [2] adopted this model to (p,d) reactions, then applied to both for proton and neutron induced reactions by Sultana et al. [3,4] and demonstrated its reasonable predictive ability.

This paper is concerned with the analysis of continuum spectra for (p,d) reactions on ^{27}Al , ^{58}Ni and ^{90}Zr , at 42 and 68 MeV, on ^{197}Au at 68 MeV and on ^{209}Bi at 42 MeV incident energies by the same method of calculation with some modifications, i.e. the application of seniority scheme to the present model for odd target nucleus makes this model more feasible. Finally, there is an increasing interest to see whether this present model can successfully analyse the cross sections data in a wide range of mass number, i.e., from ^{27}Al to ^{209}Bi . The experimental data that used at the analyses in this paper were measured at the TIARA facility of JAERI [5].

II. Analyses

1. Theoretical Calculations

(1) Direct Reaction Calculations

In the present method, the theoretical calculations of the double differential cross-sections have been done by considering a direct reaction model as an incoherent sum of the direct reaction components, which are based on DWBA predictions and expressed as below:

$$\frac{d^2\sigma}{d\Omega dE} = 2.30 \sum_{\ell,j} \left[\frac{C^2 S_{\ell,j}(E)}{2j+1} \times \left(\frac{d\sigma}{d\Omega} \Big|_{\ell,j}^{DW} (E) \right) \right] \quad (1)$$

where $d\sigma/d\Omega|_{\ell,j}^{DW}(E)$ is the cross-section calculated by the DWBA code DWUCK4 [6] and $C^2 S_{\ell,j}(E)$, the spectroscopic factor expressed as

$$C^2 S_{\ell,j}(E) = \left(\sum C^2 S_{l,j} \right) \times f_{l,j}(E) \quad (2)$$

where $\sum C^2 S_{l,j}$ is the sum of the spectroscopic factors of all the predicted states and the distribution of strength function over the spectra is obtained by using an asymmetric Lorentzian function [7-9]

$$f_{l,j} = \frac{n_0}{2\pi} \frac{\Gamma(E)}{(|E - E_F| - E_{l,j})^2 + \Gamma^2(E)/4} \quad (3)$$

and

$$\int_0^\alpha f_{l,j}(E) dE = 1 \quad (4)$$

where n_0 is the renormalization constant and E_F the Fermi energy. The Fermi energy can be calculated by using an empirical formula given in [10]. The sums of spectroscopic factors and the centroid energies ($E_{l,j}$) for $J = l \pm \frac{1}{2}$ shell orbits have been estimated by using BCS calculations. In these calculations, single particle energies required to calculate the centroid energy are calculated by the prescription of Bohr and Motelson [11]. Spreading width (Γ) is expressed by a function proposed by Brown and Rho [12] and by Mahaux and Sartor [9], as,

$$\Gamma(E) = \frac{\epsilon_0 (E - E_F)^2}{(E - E_F)^2 + E_0^2} + \frac{\epsilon_1 (E - E_F)^2}{(E - E_F)^2 + E_1^2} \quad (5)$$

where ϵ_0 , ϵ_1 , E_0 and E_1 are constants which express the effects of nuclear damping in the nucleus [8]. The estimated parameters [8] are

$$\begin{aligned} \epsilon_0 &= 19.4 \text{ (MeV)}, & E_0 &= 18.4 \text{ (MeV)}, \\ \epsilon_1 &= 1.40 \text{ (MeV)}, & E_1 &= 1.60 \text{ (MeV)}. \end{aligned} \quad (6)$$

The sum rule of the spectroscopic factors of nucleon orbits for $T \pm \frac{1}{2}$ isospin states above a closed shell core is estimated with a simple shell model prescription [13]

$$\sum C^2 S_{l,j} = \begin{cases} n_n(l,j) - \frac{n_p(l,j)}{2T+1} & \text{for } T_< = T - \frac{1}{2} \\ \frac{n_p(l,j)}{2T+1} & \text{for } T_> = T + \frac{1}{2} \end{cases} \quad (7)$$

here $n_{n(l,j)}$ and $n_{p(l,j)}$ are the numbers of neutrons and protons respectively for each (l,j) orbit and T is the isospin of the target nucleus.

(2) Seniority Scheme:

Calculation of Spectroscopic Factor for Odd Target Nucleus in Continuum Spectrum for Direct Reaction Model.

1. Direct reaction model calculation

$$\frac{d^2\sigma}{d\Omega dE} = 2.30 \sum_{\ell,j} \left[\frac{C^2 S_{\ell,j}(E)}{2j+1} \times \left(\frac{d\sigma}{d\Omega} \Big|_{\ell,j}^{DW} (E) \right) \right] \quad (8)$$

2. Coefficient of fractional parentage in seniority scheme

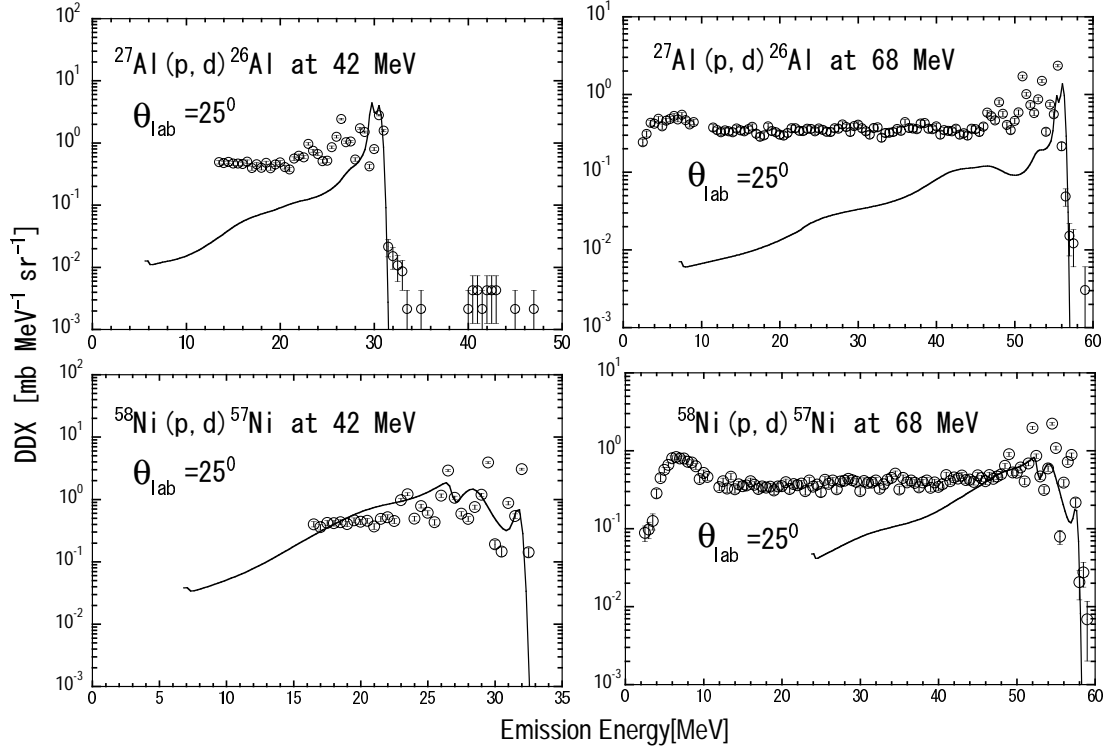


Fig. 1 $^{27}\text{Al}(p, d)^{26}\text{Al}$ and $^{58}\text{Ni}(p, d)^{57}\text{Ni}$ double differential cross section (DDX) data at 42 and 68 MeV incident energies for 25° Laboratory angle are shown in this fig. The open circles show the result of experimental data. Solid curves refer to the prediction due to present work.

1) Seniority scheme:

Generally two identical particles connect each other as a pair. Seniority is defined as number of nucleons appeared from breakdown of nucleon pairing.

2) Spectroscopic factor for one nucleon separation from n particles in a shell

$$\begin{aligned} C^2S &= n && \text{for even particle system in a shell} \\ C^2S &= \frac{2j+2-n}{2j+1} && \text{for odd particle system in a shell} \end{aligned} \quad (9)$$

3) Our estimation:

We calculate C^2S from BCS equation. It is proper to multiply a constant to the strength function as follows,

The C^2S for the ground state and low lying states resulted from n particle system can be estimated by multiplying a constant (χ) as

$$\chi = \frac{\frac{2j+2-n}{2j+1}}{n} \quad (10)$$

III. Results and Discussion

This present work is concerned with the (p,d) reactions on ^{27}Al , ^{58}Ni , ^{90}Zr at 42 and 68 MeV, on ^{197}Au at 68 MeV and on ^{209}Bi at 42 MeV. The comparisons between the theoretical and experimental double differential cross sections are presented in Figs. 1-2. Solid lines and circles stand for the calculated results and for the experimental ones respectively. No theoretical data of the above mentioned nucleus in the direct reaction region are available for comparison with the data calculated by our model. Koning and Delaroche [14] potential is used here for protons and the corresponding adiabatic potentials for deuterons to analyze the double differential cross section spectra.

From figs. 1 and 2, we can see that the theoretical results are in good agreement with the experimental data for ^{90}Zr , ^{197}Au and ^{209}Bi , while for the ^{27}Al and ^{58}Ni , are in fair agreement as in these cases the theoretical results

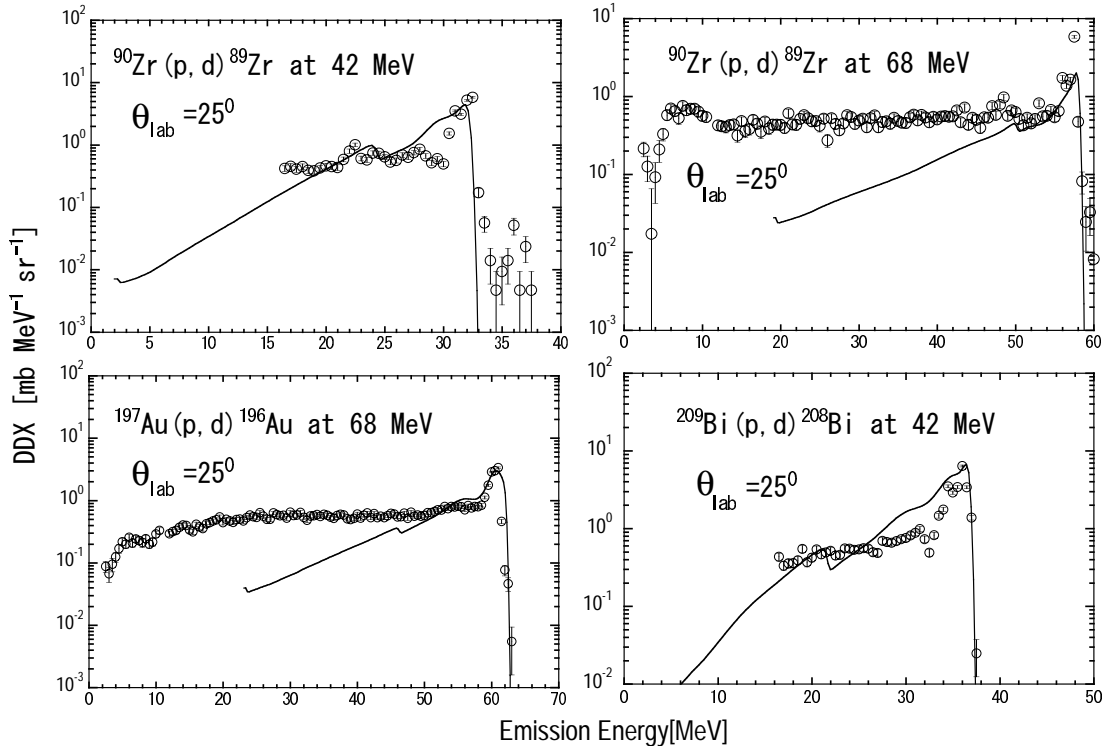


Fig. 2 $^{90}\text{Zr}(p, d)^{89}\text{Zr}$ double differential cross section (DDX) data at 42 and 68 MeV incident energies, $^{197}\text{Au}(p, d)$ DDX data at 68 MeV incident energy and $^{209}\text{Bi}(p, d)$ DDX data at 42 MeV for 25° Laboratory angle are shown in this fig. The open circles show the result of experimental data. Solid curves refer to the prediction due to present work.

are little underestimated. The use of different optical model potentials may solve the problem of underestimation because the absolute values of the spectroscopic factors have systematic errors arising, for example, from the optical model parameters for DWBA analysis. It should be noted from Figs. 1-2 that for all spectra from ^{27}Al to ^{209}Bi at 42 and 68 MeV, the calculated spectra agree with experimental data only above tens of MeV incident energies, because our calculated energy spectrum regions are treated in direct reaction scheme.

IV. Conclusion

Proton induced reactions on ^{27}Al , ^{58}Ni , ^{90}Zr , ^{197}Au and ^{209}Bi have been analyzed here. The incident energies are 42 and 68 for ^{27}Al , ^{58}Ni and ^{90}Zr while for ^{197}Au , it is 68 MeV and for ^{209}Bi , it is 42 MeV at 25° Laboratory angle. The application of seniority scheme to the present model for odd target nucleus makes this model more feasible. The calculated DDXs show an overall good agreement with the experimental data both in magnitude and shape. Successful application of this model on a wide range of mass nuclei, e.g. from ^{27}Al to ^{209}Bi proves the suitability of the present model as a reliable one.

References

- [1] S. Hirowatari et al., Nucl. Phys. A 714, (2003)3.
- [2] Syafarudin et al., J. Nucl. Sci. Technol., Suppl.2, Vol.1, (August 2002) P.377.
- [3] S. A. Sultana et al., Proceedings of the 2003 Symposium on Nuclear Data, JAERI-Conf 2004-005, P.133.
- [4] S. A. Sultana et al., Proceedings of the 2004 Symposium on Nuclear Data, JAERI-Conf 2005-003, P.143.
- [5] M. Harada et al, J. Nucl. Sci. Technol., Suppl.2, Vol.1, P.393 (August 2002).
- [6] P. D. Kunz, Code DWUCK4, University of Colorado (Unpublished).
- [7] M. Matoba et al., Phys. Rev. C53 (1996) 1792.
- [8] M. Matoba et al., Nucl. Phys. A581 (1995) 21.
- [9] C. Mahaux and R. Sartor, Nucl. Phys. A 493 (1989) 157; Adv. Nucl. Phys. 20 (1991) 1.
- [10] K. Hisamochi et al, Nucl.Phys. A564 (1993) 227.
- [11] A. Bohr and B. R. Motelson, "Nuclear Structure" (W. A. Benjamin, INC., 1996, New York, Amsterdam)

Vol. 1, Appendix 2D.

- [12] G. E. Brown and M. Rho, Nucl. Phys. A372 (1981) 397.
- [13] J. B. French and M. H. Macfarlane, Nucl. Phys. 26 (1961) 168.
- [14] A.J. Koning and J.P. Delaroche, Nucl. Phys. A713, (2003)231.

Appendix: Participant Lists

NAME	Abbreviation	NAME	Abbreviation
AKIE Hiroshi	JAEA	NAKAMURA Shoji	JAEA
ARAKITA Kazumasa	Nagoya Univ.	NAKAO Makoto	JAEA
ARUGA Takeo	JAEA	NAUCHI Yasushi	CRIEPI
ASAI Masato	JAEA	NIITA Koji	RIST
BABA Mamoru	Tohoku Univ.	NISHITANI Takeo	JAEA
CHIBA Satoshi	JAEA	NISHIYAMA Jun	Tokyo Inst. of Tech.
FUKAHORI Tokio	JAEA	OCHIAI Kentaro	JAEA
FURUTAKA Kazuyoshi	JAEA	OHSAKI Toshiro	Tokyo Inst. of Tech.
GOTO Minoru	JAEA	OHSAWA Takaaki	Kinki Univ.
HAGURA Naoto	Musashi Inst. of Tech.	OHTA Masayuki	JAEA
HARADA Hideo	JAEA	OISHI Takuji	Tohoku Univ.
HARADA Masahide	JAEA	OKUMURA Keisuke	JAEA
HASEGAWA Akira	JAEA	OKUNO Hiroshi	JAEA
HAZAMA Taira	JAEA	OTSUKA Naohiko	JAEA
HINO Tetsushi	Hitachi Ltd.	Pham Ngoc Son	JAEA
HIRANO Go	TEPSYS	SANAMI Toshiya	KEK
HOHARA Sin-ya	AIST	SHIBATA Keiichi	JAEA
IGASHIRA Masayuki	Tokyo Inst. of Tech.	SHIBATA Michihiro	Nagoya Univ.
IIMURA Hideki	JAEA	SHIBATA Takemasa	JAEA
ISHIKAWA Makoto	JAEA	SHIDO Shoichi	Osaka Univ.
ITO Takuya	NFI	SHIMAKAWA Satoshi	JAEA
IWAMOTO Nobuyuki	JAEA	SUDA Takuma	Hokkaido Univ.
IWAMOTO Yosuke	JAEA	SUGINO Kazuteru	JAEA
KADREV, Dimitre N.	Kyushu Univ.	SUGITA Takeshi	SSL
KAI Tetsuya	JAEA	SUYAMA Kenya	JAEA
KAMATA So	Tohoku Univ.	TAHARA Yoshihisa	EDC
KASUGAI Yoshimi	JAEA	TAKAHASHI Wataru	Tohoku Univ.
KATAKURA Jun-ichi	JAEA	TAKAKI Satoshi	Osaka Univ.
KAWAI Masayoshi	KEK	TAKEMURA Morio	JAEA
KIMURA Atsushi	JAEA	TANAKA Susumu	NAT
KIN Tadahiro	UOEH	TEMMA Yasuyuki	Osaka Univ.
KODAMA Akihiro	Kyushu Univ.	TSUJI Masatoshi	TEC
KONDO Keitaro	JAEA	TSUJIMOTO Kazufumi	JAEA
KONNO Chikara	JAEA	UNO Yoshitomo	JAEA
KOSAKO Kazuaki	Shimizu co.	WATANABE Shouichi	JAEA
KOURA Hiroyuki	JAEA	WATANABE Yukinobu	Kyushu Univ.
KUGO Teruhiko	JAEA	YAMAMOTO Toru	JNES
KUNIEDA Satoshi	JAEA	YAMAMOTO Toshihiro	JAEA
MARUYAMA Hiromi	GNFJ	YAMAMOTO Toshihisa	Osaka Univ.
MATSUDA Norihiro	JAEA	YAMANE Tsuyoshi	JAEA
MATSUMURA Tetsuo	CRIEPI	YAMANO Naoki	Tokyo Inst. of Tech.
MIZUMOTO Motoharu	JAEA	YASHIMA Hiroshi	Kyoto Univ.
MORI Takamasa	JAEA	YOKAYAMA Kenji	JAEA
MURATA Toru	AITEL	YOSHIDA Tadashi	Musashi Inst. of Tech.
NAGAYA Yasunobu	JAEA	ZUKERAN Atsushi	NAIS
NAKAGAWA Tsuneo	JAEA		

国際単位系 (SI)

表1. SI 基本単位

基本量	SI 基本単位	
	名称	記号
長さ	メートル	m
質量	キログラム	kg
時間	秒	s
電流	アンペア	A
熱力学温度	ケルビン	K
物質の量	モル	mol
光度	カンデラ	cd

表2. 基本単位を用いて表されるSI組立単位の例

組立量	SI 基本単位	
	名称	記号
面積	平方メートル	m ²
体積	立方メートル	m ³
速度	メートル毎秒	m/s
加速度	メートル毎秒毎秒	m/s ²
波数	毎メートル	m ⁻¹
密度 (質量密度)	キログラム毎立方メートル	kg/m ³
質量体積 (比体積)	立方メートル毎キログラム	m ³ /kg
電流密度	アンペア毎平方メートル	A/m ²
磁界の強さ	アンペア毎メートル	A/m
(物質量の)濃度	モル毎立方メートル	mol/m ³
輝度	カンデラ毎平方メートル	cd/m ²
屈折率	(数の) 1	1

表5. SI 接頭語

乗数	接頭語	記号	乗数	接頭語	記号
10 ²⁴	ヨタ	Y	10 ⁻¹	デシ	d
10 ²¹	ゼタ	Z	10 ⁻²	センチ	c
10 ¹⁸	エクサ	E	10 ⁻³	ミリ	m
10 ¹⁵	ペタ	P	10 ⁻⁶	マイクロ	μ
10 ¹²	テラ	T	10 ⁻⁹	ナノ	n
10 ⁹	ギガ	G	10 ⁻¹²	ピコ	p
10 ⁶	メガ	M	10 ⁻¹⁵	フェムト	f
10 ³	キロ	k	10 ⁻¹⁸	アト	a
10 ²	ヘクト	h	10 ⁻²¹	ゼプト	z
10 ¹	デカ	da	10 ⁻²⁴	ヨクト	y

表3. 固有の名称とその独自の記号で表されるSI組立単位

組立量	SI 組立単位			
	名称	記号	他のSI単位による表し方	SI基本単位による表し方
平面角	ラジアン ^(a)	rad		m ² ・m ⁻¹ =1 ^(b)
立体角	ステラジアン ^(a)	sr ^(c)		m ² ・m ⁻² =1 ^(b)
周波数	ヘルツ	Hz		s ⁻¹
力	ニュートン	N		m ² ・kg ² ・s ⁻²
圧力, 応力	パスカル	Pa	N/m ²	m ² ・kg ² ・s ⁻²
エネルギー, 仕事, 熱量	ジュール	J	N・m	m ² ・kg ² ・s ⁻²
工率, 放射束	ワット	W	J/s	m ² ・kg ² ・s ⁻³
電荷, 電気量	クーロン	C		s ² ・A
電位差 (電圧), 起電力	ボルト	V	W/A	m ² ・kg ² ・s ⁻³ ・A ⁻¹
静電容量	ファラド	F	C/V	m ⁻² ・kg ⁻¹ ・s ⁴ ・A ²
電気抵抗	オーム	Ω	V/A	m ² ・kg ² ・s ⁻³ ・A ⁻²
コンダクタンス	ジーメン	S	A/V	m ⁻² ・kg ⁻¹ ・s ³ ・A ²
磁束	ウェーバ	Wb	V・s	m ² ・kg ² ・s ⁻² ・A ⁻¹
磁束密度	テスラ	T	Wb/m ²	kg ² ・s ⁻² ・A ⁻¹
インダクタンス	ヘンリー	H	Wb/A	m ² ・kg ² ・s ⁻² ・A ⁻²
セルシウス温度	セルシウス度 ^(d)	°C		K
光照射度	ルーメン	lm	cd・sr ^(c)	m ² ・m ⁻² ・cd=cd
(放射性核種の)放射能	ベクレル	Bq	lm/m ²	m ² ・m ⁻⁴ ・cd=m ⁻² ・cd
吸収線量, 質量エネルギー当量	グレイ	Gy	J/kg	s ⁻¹
線量当量, 周辺線量当量, 方向性線量当量, 個人線量当量, 組織線量当量	シーベルト	Sv	J/kg	m ² ・s ⁻²

- (a) ラジアン及びステラジアンの使用は、同じ次元であっても異なった性質をもった量を区別するときの組立単位の表し方として利点がある。組立単位を形作る際のいくつかの用例は表4に示されている。
- (b) 実際には、使用する時には記号rad及びsrが用いられるが、習慣として組立単位としての記号“1”は明示されない。
- (c) 測光学では、ステラジアンの名称と記号srを単位の表し方の中にそのまま維持している。
- (d) この単位は、例としてミリセルシウス度m°CのようにSI接頭語を伴って用いても良い。

表4. 単位の中に固有の名称とその独自の記号を含むSI組立単位の例

組立量	SI 組立単位		
	名称	記号	SI 基本単位による表し方
粘着力のモーメント	パスカル秒	Pa・s	m ⁻¹ ・kg ² ・s ⁻¹
表面張力	ニュートンメートル	N・m	m ² ・kg ² ・s ⁻²
角速度	ニュートン毎メートル	N/m	kg ² ・s ⁻²
角加速度	ラジアン毎秒	rad/s	m ² ・m ⁻¹ ・s ⁻¹ =s ⁻¹
熱流密度, 放射照度	ラジアン毎平方メートル	rad/s ²	m ² ・m ⁻¹ ・s ⁻² =s ⁻²
熱容量, エントロピー	ワット毎平方メートル	W/m ²	kg ² ・s ⁻³
質量熱容量 (比熱容量), 質量エントロピー	ジュール毎キログラム	J/K	m ² ・kg ² ・s ⁻² ・K ⁻¹
質量エネルギー (比エネルギー)	ジュール毎キログラム	J/(kg・K)	m ² ・s ⁻² ・K ⁻¹
熱伝導率	ジュール毎メートル毎ケルビン	J/(m・K)	m ² ・kg ² ・s ⁻³ ・K ⁻¹
体積エネルギー	ジュール毎立方メートル	J/m ³	m ⁻¹ ・kg ² ・s ⁻²
電界の強さ	ボルト毎メートル	V/m	m ² ・kg ² ・s ⁻³ ・A ⁻¹
体積電荷	クーロン毎立方メートル	C/m ³	m ⁻³ ・s ² ・A
電気変位	クーロン毎平方メートル	C/m ²	m ⁻² ・s ² ・A
誘電率	ファラド毎メートル	F/m	m ⁻³ ・kg ⁻¹ ・s ⁴ ・A ²
透磁率	ヘンリー毎メートル	H/m	m ² ・kg ² ・s ⁻² ・A ⁻²
モルエネルギー	ジュール毎モル	J/mol	m ² ・kg ² ・s ⁻² ・mol ⁻¹
モルエントロピー, モル熱容量	ジュール毎モル毎ケルビン	J/(mol・K)	m ² ・kg ² ・s ⁻² ・K ⁻¹ ・mol ⁻¹
照射線量 (X線及びγ線)	クーロン毎キログラム	C/kg	kg ⁻¹ ・s ² ・A
吸収線量率	グレイ毎秒	Gy/s	m ² ・s ⁻³
放射強度	ワット毎ステラジアン	W/sr	m ⁴ ・m ⁻² ・kg ² ・s ⁻³ =m ² ・kg ² ・s ⁻³
放射輝度	ワット毎平方メートル毎ステラジアン	W/(m ² ・sr)	m ² ・m ⁻² ・kg ² ・s ⁻³ =kg ² ・s ⁻³

表6. 国際単位系と併用されるが国際単位系に属さない単位

名称	記号	SI 単位による値
分	min	1 min=60s
時	h	1 h =60 min=3600 s
日	d	1 d=24 h=86400 s
度	°	1°=(π/180) rad
分	'	1'=(1/60)°=(π/10800) rad
秒	"	1"=(1/60)'=(π/648000) rad
リットル	l, L	1 l=1 dm ³ =10 ⁻³ m ³
トン	t	1 t=10 ³ kg
ネーパ	Np	1 Np=1
ベル	B	1 B=(1/2) ln10 (Np)

表7. 国際単位系と併用されこれに属さない単位でSI単位で表される数値が実験的に得られるもの

名称	記号	SI 単位であらわされる数値
電子ボルト	eV	1 eV=1.60217733(49)×10 ⁻¹⁹ J
統一原子質量単位	u	1 u=1.6605402(10)×10 ⁻²⁷ kg
天文単位	ua	1 ua=1.49597870691(30)×10 ¹¹ m

表8. 国際単位系に属さないが国際単位系と併用されるその他の単位

名称	記号	SI 単位であらわされる数値
海里		1 海里=1852m
ノット		1 ノット = 1 海里毎時=(1852/3600)m/s
アール	a	1 a=1 dam ² =10 ² m ²
ヘクタール	ha	1 ha=1 hm ² =10 ⁴ m ²
バール	bar	1 bar=0.1MPa=100kPa=1000hPa=10 ⁵ Pa
オングストローム	Å	1 Å=0.1nm=10 ⁻¹⁰ m
バール	b	1 b=100fm ² =10 ⁻²⁸ m ²

表9. 固有の名称を含むCGS組立単位

名称	記号	SI 単位であらわされる数値
エル	erg	1 erg=10 ⁻⁷ J
ダイン	dyn	1 dyn=10 ⁻⁵ N
ポアズ	P	1 P=1 dyn・s/cm ² =0.1Pa・s
ストークス	St	1 St =1cm ² /s=10 ⁻⁴ m ² /s
ガウス	G	1 G =10 ⁴ T
エルステッド	Oe	1 Oe =1000(4π) A/m
マクスウェル	Mx	1 Mx =10 ⁻⁸ Wb
スチル	sb	1 sb =1cd/cm ² =10 ⁴ cd/m ²
ホト	ph	1 ph=10 ⁴ lx
ガリ	Gal	1 Gal =1cm/s ² =10 ⁻² m/s ²

表10. 国際単位に属さないその他の単位の例

名称	記号	SI 単位であらわされる数値
キュリー	Ci	1 Ci=3.7×10 ¹⁰ Bq
レントゲン	R	1 R = 2.58×10 ⁻⁴ C/kg
ラド	rad	1 rad=1cGy=10 ⁻² Gy
レム	rem	1 rem=1 cSv=10 ⁻² Sv
X線単位		1 X unit=1.002×10 ⁻⁴ nm
ガンマ	γ	1 γ=1 nT=10 ⁻⁹ T
ジャンスキー	Jy	1 Jy=10 ⁻²⁶ W・m ⁻² ・Hz ⁻¹
フェルミ	fem	1 femi=1 fm=10 ⁻¹⁵ m
メートル系カラット		1 metric carat = 200 mg = 2×10 ⁻⁴ kg
トル	Torr	1 Torr = (101 325/760) Pa
標準大気圧	atm	1 atm = 101 325 Pa
カリ	cal	
マイクロン	μ	1 μ =1um=10 ⁻⁶ m

